



**HAL**  
open science

# Unified theory of spin, heat and charge transport

David Luc

► **To cite this version:**

David Luc. Unified theory of spin, heat and charge transport. Condensed Matter [cond-mat]. Université Grenoble Alpes, 2016. English. NNT : 2016GREAY007 . tel-01425553

**HAL Id: tel-01425553**

**<https://theses.hal.science/tel-01425553>**

Submitted on 3 Jan 2017

**HAL** is a multi-disciplinary open access archive for the deposit and dissemination of scientific research documents, whether they are published or not. The documents may come from teaching and research institutions in France or abroad, or from public or private research centers.

L'archive ouverte pluridisciplinaire **HAL**, est destinée au dépôt et à la diffusion de documents scientifiques de niveau recherche, publiés ou non, émanant des établissements d'enseignement et de recherche français ou étrangers, des laboratoires publics ou privés.

## THÈSE

Pour obtenir le grade de

### DOCTEUR DE L'UNIVERSITÉ DE GRENOBLE

Spécialité : **Nanophysique**

Arrêté ministériel : 25 mai 2016

Présentée par

**David Luc**

Thèse dirigée par **Xavier Waintal**

préparée au sein **CEA/DSM/INAC/SPSMS/GT**  
et de **Ecole doctorale de physique**

## Unified theory of spin, heat and charge transport

Thèse soutenue publiquement le **15/06/2016**,  
devant le jury composé de :

**M. Aurélien Manchon**

Professeur - King Abdullah University of Science and Technology, Rapporteur

**M. André Thiaville**

Chercheur - Laboratoire de Physique du Solide, Université Paris Sud, Rapporteur

**M. Henri Jaffrès**

Chercheur - Unité Mixte de Physique Thales/CNRS, Examineur

**M. Chris Bäuerle**

Chercheur - Institut Néel Grenoble, Président

**M. Xavier Waintal**

Chercheur - CEA Grenoble, Directeur de thèse

**M. Mair Chshiev**

Professeur - Université Joseph Fourier, Co-Directeur de thèse





---

# CONTENTS

---

<b>Contents</b>	<b>vii</b>
<b>ACKNOWLEDGEMENTS</b>	<b>ix</b>
<b>INTRODUCTION</b>	<b>xi</b>
1. Collinear systems: the Valet-Fert theory . . . . .	xi
2. Non-collinear systems: Slonczewski's spin-transfer torque . . . .	xii
3. Novel thermoelectric effects . . . . .	xiii
4. This thesis' work . . . . .	xiii
4.1. Extending our semi-classical theory . . . . .	xiii
4.2. Transverse behavior . . . . .	xv
4.3. Thermoelectric effects . . . . .	xvi
4.4. A theory and a numerical simulation tool . . . . .	xvi
<b>A STATE-OF-THE-ART IN SPINTRONICS AND THERMOELECTRICITY</b>	<b>1</b>
<b>I. MAGNETISM</b>	<b>5</b>
I - 1. Magnetism in solid state physics . . . . .	5
I - 1.1. Description of ferromagnetic metals . . . . .	5
I - 1.2. Long-range interactions in ferromagnets . . . . .	6
I - 1.3. Magnetic domains and domain walls . . . . .	7
I - 2. Magnetic Dynamics . . . . .	8
I - 2.1. Landau-Lifshitz-Gilbert equation . . . . .	8
I - 2.2. Effective field . . . . .	9
I - 2.3. Levels of description . . . . .	11
I - 2.4. Applications . . . . .	11
I - 2.5. Magnetization reversal . . . . .	11
I - 2.6. Current-induced magnetization reversal . . . . .	12
I - 2.7. Spin-Torque Oscillator . . . . .	14
<b>II. THE GIANT MAGNETO-RESISTANCE</b>	<b>15</b>
II - 1. History of a Nobel Prize . . . . .	16

## Contents

II - 2.	The Valet-Fert theory . . . . .	16
II - 3.	First example: GMR of a minimal spin-valve . . . . .	18
II - 4.	Second example: GMR of a more realistic spin-valve . . . . .	19
II - 4.1.	Some useful notations . . . . .	21
II - 4.2.	Derivation example: the spin accumulation and spin currents in the antiparallel state of spin-valve . . . . .	22
II - 5.	Modern GMR devices . . . . .	23
II - 6.	Spin-orbit coupling and spin-flip . . . . .	25
<b>III.</b>	<b>SPIN-TRANSFER TORQUE</b>	<b>27</b>
III - 1.	Overview and consequences in spintronics . . . . .	27
III - 2.	History of spin-transfer torque . . . . .	28
III - 3.	Torque and spin filtering . . . . .	29
III - 3.1.	Spin filtering of an unpolarized current . . . . .	29
III - 3.2.	Spin filtering of a polarized current . . . . .	30
III - 4.	Illustration with a toy model . . . . .	31
III - 5.	In-plane and out-of-plane torques . . . . .	33
III - 6.	Angular dependence of the torque . . . . .	33
<b>IV.</b>	<b>THERMOELECTRICITY</b>	<b>37</b>
IV - 1.	Seebeck and Peltier effect . . . . .	37
IV - 1.1.	History of discovery . . . . .	37
IV - 1.2.	Thermocouples . . . . .	39
IV - 1.3.	Microscopic origin . . . . .	40
IV - 1.4.	Figure of merit $ZT$ . . . . .	45
IV - 2.	Spin-dependent Seebeck effect . . . . .	47
IV - 2.1.	Justification of the theory . . . . .	47
IV - 2.2.	Experimental demonstration . . . . .	49
IV - 2.3.	Outlook . . . . .	50
IV - 2.4.	Spin Seebeck effect: a clash of vocabulary . . . . .	51
<b>B</b>	<b>DESCRIPTION OF OUR SEMI-CLASSICAL THEORY</b>	<b>53</b>
<b>V.</b>	<b>THE STATE OF THE THEORY BEFORE THIS THESIS</b>	<b>59</b>
V - 1.	Origin of the theory . . . . .	59
V - 2.	Scattering Formalism . . . . .	61
V - 2.1.	Description of the formalism . . . . .	61

V - 2.2.	Addition law for two scatterers in series . . . . .	62
V - 2.3.	Semi-classical limit . . . . .	63
V - 3.	Random matrix approach . . . . .	64
V - 3.1.	Definition of the “hat” matrices . . . . .	65
V - 3.2.	Mixing coefficients . . . . .	66
V - 3.3.	Properties of the $\hat{S}$ matrix . . . . .	67
V - 4.	Rotations of $\hat{S}$ matrices . . . . .	69
V - 4.1.	Rotations in spin space . . . . .	70
V - 5.	Equivalence of CRMT with the circuit theory . . . . .	70
V - 5.1.	Interface equations . . . . .	72
V - 6.	From discreet to continuous . . . . .	74
<b>VI.</b>	<b>THE STATE OF THE THEORY AFTER THIS THESIS</b>	<b>77</b>
VI - 1.	Recovering classical variables and obtaining drift-diffusion equations . . . . .	77
VI - 1.1.	Matrix basis . . . . .	77
VI - 1.2.	Rotation properties . . . . .	79
VI - 1.3.	1D continuous equations . . . . .	79
VI - 2.	From 1D to 3D . . . . .	80
VI - 3.	Expanding the theory to include thermoelectric effects . . . . .	83
VI - 4.	3D thermoelectric interface equations and boundary conditions at the reservoirs . . . . .	88
VI - 4.1.	Interfaces . . . . .	88
VI - 4.2.	Boundary conditions at the reservoirs . . . . .	89
VI - 5.	Effective parameters . . . . .	90
<b>C</b>	<b>APPLICATIONS TO TRANSVERSE SPIN CURRENTS IN VARIOUS MAGNETIC LANDSCAPES</b>	<b>93</b>
<b>VII.</b>	<b>TRANSVERSE PENETRATION AND PRECESSION</b>	<b>97</b>
VII - 1.	Penetration and precession of spins transverse to the magnetization . . . . .	98
VII - 1.1.	<i>Ab initio</i> calculations . . . . .	98
VII - 1.2.	Measurement setup . . . . .	100
<b>VIII.</b>	<b>TORQUES IN A DOMAIN WALL</b>	<b>103</b>
VIII - 1.	In-plane and out-of-plane torques . . . . .	103

## Contents

VIII - 2.	$\beta_{\tau}$ , a bridge between transport and micromagnetism . . . . .	104
<b>IX.</b>	<b>SPIN-VALVE ON YIG</b>	<b>109</b>
IX - 1.	Experimental measurements and results . . . . .	109
IX - 1.1.	Description of the system . . . . .	110
IX - 1.2.	Non-local spin-valves . . . . .	110
IX - 1.3.	Experimental measurements . . . . .	111
IX - 2.	Physical model . . . . .	114
IX - 2.1.	Perfect interface model . . . . .	115
IX - 2.2.	Dirty interface model . . . . .	115
IX - 3.	Simulations and numerical results . . . . .	117
IX - 3.1.	Case of a perfect interface . . . . .	117
IX - 3.2.	Dirty interface . . . . .	119
IX - 4.	Effects of the geometry . . . . .	120
<b>D</b>	<b>APPLICATIONS TO SPIN CALORITRONICS</b>	<b>123</b>
<b>X.</b>	<b>SPIN-TRANSFER TORQUE IN A SPIN-VALVE SUBJECTED TO A TEMPERATURE GRADIENT</b>	<b>127</b>
X - 1.	Description of the system and its configurations . . . . .	128
X - 2.	Derivation of an expression for the torque . . . . .	129
X - 3.	Waviness of the thermally-induced torque . . . . .	135
X - 4.	Critical temperature for switching . . . . .	137
<b>XI.</b>	<b><math>\beta_{\tau}</math> IN A DOMAIN WALL SUBJECTED TO A TEMPERATURE GRADIENT</b>	<b>141</b>
XI - 1.	Long walls: the adiabatic limit . . . . .	141
XI - 2.	Short walls . . . . .	142
<b>XII.</b>	<b>COMPARING SIMULATIONS TO SPIN-DEPENDENT SEEBECK MEASUREMENTS</b>	<b>145</b>
XII - 1.	Description of the experiment . . . . .	145
XII - 2.	Simulations and comparison . . . . .	147

<b>E ALGORITHM AND NUMERICS</b>	<b>151</b>
<b>XIII. ALGORITHM</b>	<b>155</b>
XIII - 1. Description of the base algorithm . . . . .	155
XIII - 2. Architecture of the framework . . . . .	157
XIII - 2.1. Package CRMT . . . . .	157
XIII - 2.2. Package CRMT1D . . . . .	157
XIII - 2.3. Package CRMT3D . . . . .	159
XIII - 3. Package Tools . . . . .	160
XIII - 4. Sample code . . . . .	161
XIII - 4.1. CRMT1D . . . . .	161
XIII - 4.2. CRMT3D . . . . .	162
XIII - 5. Performance . . . . .	164
<b>Conclusion</b>	<b>168</b>
<b>Appendices</b>	<b>169</b>
<b>MATERIAL PARAMETERS DATABASE</b>	<b>171</b>
<b>Bibliography</b>	<b>172</b>
<b>List of figures</b>	<b>185</b>
<b>List of tables</b>	<b>187</b>



---

## ACKNOWLEDGEMENTS

---

Je tiens tout d'abord à remercier mon directeur de thèse, Xavier Waintal, pour son encadrement, sa disponibilité, et sa patience ô combien nécessaire. J'ai beaucoup appris à son contact, en physique bien sûr, mais aussi sur d'autres domaines comme l'informatique. Je tiens aussi à le remercier d'avoir su orienter notre recherche en fonction de mes goûts, pas toujours très orthodoxes.

Je voulais aussi présenter toute ma gratitude aux membres de mon jury, d'avoir accepté d'être présents à ma soutenance ainsi que pour leur lecture de ce manuscrit. Tout particulièrement, je tiens à remercier chaleureusement Maïr Chschiev pour son soutien tout à long de ces trois ans, ainsi que pour les lumières qu'il a su projeter sur certains questionnements et les idées originales dont il m'a fait part.

Merci à Cyril Petitjean, qui a su m'éclairer sur son travail dont je suis le successeur, avec clarté, chaleur et bonne humeur.

Ensuite, ces trois ans auraient été bien tristes et longs sans les autres membres du Groupe Théorie. Merci en particulier à Benoit pour nos nombreuses discussions et conseils, à Elio pour avoir apporté un peu d'animation dans le bureau solitaire que j'occupais avant son arrivée, à mes collègues russes, Vladimir, Tania et Kostya pour nos nombreuses discussions qui ont su ouvrir mes horizons à de nouvelles manières de penser, à Roman et Lars pour leur éternelle bonne humeur et les nombreux jeux de mots (parfois pas aussi drôle que nous l'aurions voulu) que nous avons commis. Merci aussi à tous les autres que je ne mentionne pas, mais à qui je ne pense pas moins.

Un grand merci à ceux qui, bien que ne faisant pas partie du laboratoire, m'ont aidé à travers ces trois ans. Les plus importants sont bien sûr mon binôme, Vincent, tout aussi capable de me faire rire même à distance que de me prodiguer de précieux conseils, toute ma famille et leur soutien indéfectible, et du fond de mon coeur, merci à Emmanuelle, ma meilleure moitié, qui a réussi d'une part à me supporter, mais aussi à me fournir un soutien de tous les instants dont elle ne réalise pas toute l'importance.

Enfin, pour finir, je tiens à remercier ceux auxquels on ne pense pas assez souvent, et sans qui la recherche à travers le monde ne serait pas là où elle en est aujourd'hui : merci à tous les producteurs de café de par le monde. Votre récolte est notre plaisir, notre soutien, et parfois même notre addiction.



---

## INTRODUCTION

---

In this thesis, we are interested in gathering and extending the knowledge acquired for the past thirty years in the field of spintronics into one unifying theory. The goal is to have the tools to describe systems made up of several layers of ferromagnetic and non-ferromagnetic metals with any magnetization orientation or texture and understand the electronic transport driven by a voltage bias and/or a temperature gradient.

Valet-Fert's equations [1] have been very successful in describing so-called collinear systems, where the magnetizations of the various layers in the device lie all along the same axis. In particular, it captures very well the giant magnetoresistance (GMR) of such a system. However it fails at giving any information on systems where the magnetizations are non-collinear.

The concept of spin-transfer torque (STT) introduced in 1996 by Berger [2] and Slonczewski [3] addressed this issue by giving a description of the effect of a spin-polarized current on a magnetization with a different orientation. This spin-polarized current however was taken for granted, and not the result of the surrounding system.

More recently, the discovery of spin-dependent thermoelectric effects [4, 5, 6], raised the question whether obtaining the same effects (GMR and STT) is possible and technically feasible.

Our theory regroups all these effects and provides a framework to answer those questions. And because the more interesting systems are not easily studied on paper, we brought our theory to the numerical realm by implementing a fast and easy-to-use simulation framework based on it.

### 1 COLLINEAR SYSTEMS: THE VALET-FERT THEORY

The giant magnetoresistance was the first to be discovered in 1988 by Albert Fert [7] and Peter Grünberg [8], which resulted in their Nobel Prize in 2007. This effect, where a stack of ferromagnetic and non-ferromagnetic metal layers exhibits a difference of resistance according to its magnetic configuration, is of quantum origin and requires the spin of the electrons to be taken into account and not only its charge.

This effect is at the heart of the very fast growing storage capacity in hard drive disks in the past fifteen years.

The Valet-Fert theory was developed to describe such systems in a semi-classical manner. The resulting equations are an Ohm-like equation (i) and a (non-)conservation equation (ii) for each spin specie  $\sigma$ . The non-conservation is due to spin-flip, resulting from the spin-orbit interaction.

$$e\rho_\sigma J_\sigma = -\partial_z \mu_\sigma \quad (\text{i})$$

$$4\rho_* e \partial_z J_\sigma = \frac{\mu_\sigma - \mu_{-\sigma}}{\ell_{sf}^2} \quad (\text{ii})$$

These equations link the spin current  $J_\sigma$  for the specie  $\sigma$  to its spin-resolved electrochemical potential  $\mu_\sigma$  through the spin-dependent resistivity  $\rho_\sigma = 2\rho_*(1 \pm \beta)$  of the material. The length  $\ell_{sf}$  is the characteristic length, corresponding to the mean free path between two spin-flipping scattering events.

Although these equations were originally derived for a 1D system, it can easily be extended to 3D without much more work. However, it is inherently 1D in spin space. This has been the main limitation of this theory.

## 2 NON-COLLINEAR SYSTEMS: SLONCZEWSKI'S SPIN-TRANSFER TORQUE

In order to describe non-collinear systems, Berger [2] and Slonczewski [3] proposed in 1996 the concept of spin-transfer torque. It explains how a spin current (polarized for example with the  $z$  axis) arriving on a magnetization making an angle  $\theta$  with the  $z$  axis behaves. An effect called spin-filtering will make the spin current after the layer polarized along the same direction, while the difference in magnetic moment is deposited on the layer (given to its magnetization). This difference of magnetic moment is what is called the spin-transfer torque.

This torque has very important consequences, most notably on the magnetic dynamics of the system. Without this term, the Landau-Lifshitz-Gilbert equation states that the magnetization will precess around some axis (given by a combination of the applied external magnetic field, the anisotropies and a few other factors), and relax towards it because of the Gilbert damping. Because it is collinear to the damping direction, the torque can either enhance it, or compensate it. This means that the spin-transfer torque allows for switching the magnetic direction without relying on an external magnetic field, but also if tuned properly exactly compensate the damping, and allow for a steady-state precession motion.

### 3 NOVEL THERMOELECTRIC EFFECTS

Thermoelectricity is a topic that has been known for over a century, with the work of Seebeck, Peltier, Thompson etc. Effects involving magnetic fields have also been studied. However, the ones that are of particular interest to us have been theorized for quite a while [4]. In the same way as the conductivity is spin-dependent in ferromagnets, the thermoelectric coefficients are too. We therefore take into consideration the so-called spin-dependent Seebeck and spin-dependent Peltier effects. The main point to study them is that they allow for the easy creation of pure spin currents (spin transport without charge transport). For this reason, a hope arose that they could be at the origin of a thermally induced spin-transfer torque. In the best of scenarios, nanoscale spintronics devices could be powered by harnessing a difference of temperature in the surrounding environment.

### 4 THIS THESIS' WORK

We presented so far the various topics that were of interest to us. We now give the work done during this thesis in order to bring together these topics, and what resulted from that unification. There are four parts to this thesis, corresponding to the last four parts of the manuscript, the first one being dedicated to providing the necessary theoretical background.

#### 4.1 *Extending our semi-classical theory*

The first task (Part B) was to continue developing the theory of spin and charge transport that was already available [9]. We introduced in this theory the effect of the spin-dependent thermoelectric effects, and finally obtained a theory describing electron transport (charge spin and heat) in ferromagnetic metals. This theory is in particular synthesized into six equations reminiscent of the Valet-Fert equations, and incorpo-

rating the spin-transfer torque as well as the thermoelectric effects (spin-dependent and regular):

$$-\ell_* \partial_\alpha \mu_c = j_\alpha^c - \beta \mathbf{j}_\alpha \cdot \mathbf{m} + \frac{\ell_*}{\ell_H} s (s j_\alpha^c + \Delta s \mathbf{j}_\alpha \cdot \mathbf{m}) - \frac{\ell_*}{\ell_H} s j_\alpha^q \quad (\text{iii})$$

$$\begin{aligned} -\ell_* \partial_\alpha \boldsymbol{\mu} = & \mathbf{j}_\alpha - \beta j_\alpha^c \mathbf{m} + \frac{\ell_*}{\ell_H} \Delta s (s j_\alpha^c \mathbf{m} + \Delta s \mathbf{j}_\alpha) - \frac{\ell_*}{\ell_H} \Delta s j_\alpha^q \mathbf{m} \\ & + \frac{\ell_*}{\ell_\perp} (\mathbf{m} \times \mathbf{j}_\alpha) \times \mathbf{m} - \frac{\ell_*}{\ell_L} (\mathbf{m} \times \mathbf{j}_\alpha) \end{aligned} \quad (\text{iv})$$

$$-\ell_H \partial_\alpha \theta = -s j_\alpha^c - \Delta s \mathbf{j}_\alpha \cdot \mathbf{m} + j_\alpha^q \quad (\text{v})$$

$$\sum_\alpha \partial_\alpha j_\alpha^c = 0 \quad (\text{vi})$$

$$\sum_\alpha \partial_\alpha j_\alpha^q = 0 \quad (\text{vii})$$

$$\sum_\alpha \partial_\alpha \mathbf{j}_\alpha = -\frac{\ell_*}{\ell_{sf}^2} \boldsymbol{\mu} - \frac{1}{\ell_\perp} (\mathbf{m} \times \boldsymbol{\mu}) \times \mathbf{m} + \frac{1}{\ell_L} (\mathbf{m} \times \boldsymbol{\mu}) \quad (\text{viii})$$

We provide in Part B the original steps used to obtain the state of this theory before this thesis started. We introduce first the fully quantum Landauer-Büttiker scattering theory, where all the conduction channels are described individually through transmission and reflection probability amplitudes to enter the system from one channel and spin state and exit in another. Then, by applying a Random Matrix Theory (RMT), we go to the semi-classical limit. The theory at this point is described through a reduced  $8 \times 8$  scattering matrix  $\hat{S}$  where instead of describing all the channels, we now only have the probability to be transmitted and reflected from one spin state to another. The only quantum features remaining are the spin description and the Sharvin resistance at the leads.

A change of variable allowed us to prove the equivalence of this theory with the Circuit Theory [10], by introducing currents and potentials. The Circuit Theory is based on the concept of nodes where those currents and potentials are defined, connected to each other (or to the leads) by links, containing the actual information on the materials (the  $\hat{S}$  in our case).

This was the state of the theory before this thesis. Our work consisted in taking this theory to the continuous limit. Instead of having links describing a whole piece of material, they described thin slices of material, easily parametrized by (for the most part) measurable parameters, such as the spin-dependent mean free paths  $\ell_\uparrow$  and  $\ell_\downarrow$ , the spin-flip length  $\ell_{sf}$ , as well as a few others. By introducing some rota-

tion properties, the theory that was written so far only in the local magnetization basis could be expressed for any magnetization orientation. Applying them and separating the charge and spin part allowed us to obtain differential equations. For simplicity those were first derived for unidimensional systems, and the extension to 3D followed naturally. Finally, the introduction of the thermoelectric effects was the final step to obtain Eq. (iii) to Eq. (viii).

## 4.2 Transverse behavior

The main advantage our theory has over the Valet-Fert equations is that it takes into account any magnetization orientation, and therefore includes the behavior of spins transverse to the magnetization. In a bulk material, such a spin will precess around the magnetization axis, and be quickly absorbed by the magnetization. These damped oscillations are parametrized by two lengths, the Larmor precession length  $\ell_L$  and the transverse penetration length  $\ell_\perp$ . These lengths can be extracted from *ab initio* calculations of the mixing conductance (or transmission  $T_{\text{mx}}$ ). We use the following relation for the mixing transmission of a bulk layer of thickness  $d$ :

$$T_{\text{mx}}(d) \approx e^{-d/\ell_\perp + id/\ell_L} \quad (\text{ix})$$

Articles such as Ref [11, 12, 13, 14] provide such calculations, and we extracted the values of  $\ell_\perp$  and  $\ell_L$  for the materials under consideration. We also provide the design of a device that can be used to measure these lengths, as well as simulations to show expected results.

Then, we study the case of domain walls. It has been proven [15] that the torque introduced by Slonczewski and Berger is insufficient to explain domain wall motion under a voltage bias. When a current flows through a domain wall, it gets polarized and deposits magnetic moment on the wall, and allows it to move along the direction of the current if the density is strong enough. However currents much lower than predicted are enough to initiate the movement. The reason behind this is that the torque actually has two components: the in-plane one predicted by Slonczewski and Berger, and a smaller one, out-of-plane. Its destabilizing role is of major importance to describe accurately domain wall motion, and has been introduced in the Landau-Lifshitz-Gilbert equation as a small dimensionless parameter  $\beta$ , the ratio of the out-of-plane to the in-plane component of the torque. Although it was so far purely phenomenological, we give in the limit of long ( $> 10$  nm) domain walls an analytical expression. What is even more interesting is that this micromagnetic parameter depends on transport properties, namely the transverse lengths  $l$  and  $\ell_\perp$ ,

as well as the spin-flip length  $\ell_{sf}$  and the mean free path  $\ell_*$ . We therefore introduce a bridge between the two community, and show that transport has a strong impact on the magnetic dynamics.

Finally, in collaboration with van Wees *et al.*, we studied a device aiming at probing the mixing properties of a magnetic insulator, the YIG. We created a minimal model and performed simulations to explain their experimental results[16].

### 4.3 *Thermoelectric effects*

The introduction of the thermoelectric effects in our theory gave us an additional degree of freedom to generate a torque, for example. We investigate in particular an effect called torque waviness, and prove it is much stronger under a temperature gradient than a voltage bias.

Usually, the torque has always the same sign regardless of the angle between the current polarization and the magnetization direction. However in some cases, the torque may change sign once (see [17] for example). In such a case, the torque is said to be wavy. Under a voltage bias, this effect occurs when the fixed layer is weakly spin polarized compared to the free layer. Our theory allowed us to derive a waviness condition, proving again this known result, and extending it to systems subjected to any voltage and temperature gradient. With this result, we show that a thermal torque can be very easily wavy, especially if the system is in (electrical) open circuit. We explore numerically such a behavior for the torque in three cases: under a voltage bias, and under a temperature gradient in both closed an open circuit.

Since there is a critical current density to initiate switching, there is also a critical temperature difference. We use numerics again to estimate this temperature difference. With good materials, we show that only a few degrees may be enough.

### 4.4 *A theory and a numerical simulation tool*

Finally, in Part E we present the simulation tool we developed. It is written mainly in Python, with the time-critical parts (the solver) in C++. It is made up of several modules. One containing the physics (material parameters database) and the structures coming from the theory (the implementation of the  $\hat{S}$  matrices for example). One module gives powerful tools dedicated to the simulation of 1D systems (most notably pillars and domain walls). Another module is dedicated to simulating systems with any dimensionality, including in particular their geometrical description, as well as the iterative solver used to obtain the various observables. In this part, we

go into details about the architecture of this tool, and give proofs that it is powerful, fast and reliable.



Part A

STATE-OF-THE-ART IN SPINTRONICS AND  
THERMOELECTRICITY



## Summary of Part A

This thesis intends on describing the behavior of spintronics devices. But before doing that, what is spintronics ?

Spintronics is the field of physics aiming at exploiting the spin of the electrons as well as its charge, using magnetic fields as well as electric fields. To do so, spintronics systems usually involve ferromagnetic metals, such as iron, cobalt, nickel and their alloys. A metal is ferromagnetic when the balance of the kinetic energy and the Coulomb interaction favors having electrons at higher energy levels, with the same spin.

The time-dependent properties of a spintronic devices often rely on its magnetic dynamics, described by the Landau-Lifshitz-Gilbert equation. In particular, the magnetization of one of the layers of a stack can be reversed, either by applying an external magnetic field, or by flowing a polarized current through it.

The resistance of a device including ferromagnets depend on the orientation of their respective magnetization. This Nobel-awarded effect, called the giant magnetoresistance is at the core of modern-day digital memory storage. The Valet-Fert theory describes very well cases where all the magnetizations are along the same axis.

A magnetization can be switched with an applied polarized current thanks to a process called the spin-transfer torque. It corresponds to magnetic moment given to magnetization by the spin current. The study of this quantity is at the heart of this thesis, and in particular its dependence with the orientation of the free magnetization with respect to the fixed direction imposed by the others. Two types of dependence are under consideration: the normal one, where the sign of the torque does not depend on the orientation of the layer's magnetization, and the wavy dependence, where the sign changes beyond some critical angle.

Electron transport involves charge and spin, but is also the main source of heat transport in metals, as indicated by the Wiedemann-Franz law. It has also been well-known for more than a century that charge and heat can couple to give the thermoelectric effects (notably the Peltier and Seebeck effects). More recently, it has been discovered that heat and spin couple too to give spin-dependent thermoelectric effects.

**Résumé de la Partie A**

Cette thèse a pour but de décrire le comportement des circuits spintroniques. Mais avant tout, qu'est-ce que la spintronique ?

La spintronique, ou électronique de spin, est le domaine de la physique cherchant à exploiter le spin des électrons en plus de leur charge, en utilisant des champs aussi bien magnétiques qu'électriques. Pour ce faire, la spintronique a souvent recours aux métaux ferromagnétiques comme le fer, le cobalt, le nickel et leurs alliages. Un métal est dit ferromagnétique lorsque l'équilibre entre l'énergie cinétique et l'interaction Coulombienne favorise d'avoir des électrons sur des orbitales de plus haute énergie, mais avec les mêmes spins.

L'évolution temporelle des systèmes spintroniques est souvent basée sur la dynamique magnétique, décrite par l'équation de Landau-Lifshitz-Gilbert. Plus spécifiquement, l'aimantation d'une des couches magnétiques peut être inversée soit en appliquant un champs magnétique externe, soit en faisant passer un courant polarisé à travers.

La résistance d'un circuit mettant en jeu des métaux ferromagnétiques dépend de l'orientation de leur aimantation respective. Cet effet primé aux Nobel, appelé magnétoresistance géante, est à la base des systèmes de stockage de données digitales modernes. La théorie de Valet-Fert décrit très bien les cas où toutes les aimantations sont alignés selon le même axe.

Une aimantation peut être inversée grâce à un courant polarisé grâce à processus appelé le torque par transfert de spin. Il correspond à un moment magnétique donné à l'aimantation par le courant de spin. L'étude de cette quantité est le coeur de cette thèse, et en particulier sa dépendance avec l'orientation entre l'aimantation de la couche libre et celle des couches fixes. Deux types de dépendances ont été rapportées : le cas normal, où le signe du torque est le même quelque soit l'orientation de l'aimantation, et une dépendance appelée "wavy", où le sign du torque change au delà d'un certain angle critique.

Le transport électronique concerne la charge et le spin, mais est aussi le mécanisme principal de transport de chaleur dans les métaux, comme la loi de Wiedemann-Franz le suggère. Cela fait aussi plus d'un siècle que l'on sait que la chaleur et un courant peuvent être couplés à travers les effets thermoélectriques (particulièrement les effets Seebeck et Peltier). Plus récemment, il a été découvert que la chaleur et le spin peuvent être aussi couplés à travers ce que l'on appelle les effets thermoélectriques dépendant du spin.

---

## MAGNETISM

---

Although this thesis focuses on spin transport, a basic understanding of ferromagnetism and of magnetic dynamics is needed to open the discussion and put our results in their context. Indeed any reasonably realistic description of any spintronics device must take into account some level of magnetism, like the notions of (anti-)ferromagnetic coupling, the influence of the thickness of a layer on its coercive field, and so on.

Part 1 will give a few clues about the origin of ferromagnetism, and the related concepts such as domain and domain walls. Part 2 then introduces the equation of micromagnetic dynamics, a description of its constituents, and what practical consequences it yields.

### I - 1 MAGNETISM IN SOLID STATE PHYSICS

We introduce a few useful concepts. First we give an informal explanation about the origin of ferromagnetism. We then introduce the concept of domains and domain walls in magnetic materials, and we conclude by reviewing the most common source of spin relaxation in metals, the spin-orbit coupling.

#### I - 1.1 *Description of ferromagnetic metals*

Materials (and metals in particular) can be classified by their response to an external magnetic field. They can be either diamagnetic if they tend to cancel the external field, or paramagnetic if their response is to add to the field. This can be determined by evaluating (or measuring) the susceptibility  $\chi$  of the material, where  $\chi$  is defined by:

$$\chi = \frac{\partial M}{\partial H} = -\frac{1}{V} \frac{\partial^2 F}{\partial H^2} \quad (1)$$

In this equation,  $M$  is the magnetization density and  $F$  the magnetic Helmholtz free energy defined by the statistical mechanical rule:

$$e^{-F/k_B T} = \sum_n e^{E_n(H)/k_B T} \quad (2)$$

where  $E_n$  are the field dependent energies of the excited states of the system. If  $\chi > 0$ , the system is said to be paramagnetic, while if  $\chi < 0$  the system is diamagnetic.

Ferromagnetism is the special case where the material creates a magnetic field without any external field needed. This phenomenon is the basis of all the usual permanent magnets. As all the other forms of magnetism, it is an inherently quantum effect.

Several elements are needed to explain ferromagnetism. First let us consider a free atom. In its filled shells, electrons of opposite spin pair up, generating no net magnetic moment. On the other hand, partially filled shells obey Hund's rule, which states that the total spin must be maximal (filling first with similar spins). Therefore unfilled shells are a necessary condition for ferromagnetism. Another smaller contribution to the total magnetic moment of the atom comes from the orbital moment.

In a solid, neighboring spins tend to pair up to minimize the kinetic energy while respecting the Pauli principle. However, the total energy is a competition between the kinetic energy, and the Coulomb interaction. In some cases, having some electrons on higher energy levels (and with the same spin) minimizes the Coulomb interaction by forcing them further apart. This is the so-called exchange interaction, and it is a very short range (inter-atomic scale) high energy interaction. Thermal fluctuations can compensate it, and the temperature at which this occurs, called the Curie temperature, depends on the material. Iron's is 1043 K, cobalt's is 1400 K, and nickel's is 627 K, making this interaction's energy around 0.1 eV.

### 1 - 1.2 *Long-range interactions in ferromagnets*

As we saw, the exchange interaction is short-ranged, on the scale of a few atoms only. But other types of interactions exist, such as the dipole interactions, or the Ruderman-Kittel-Kasuya-Yosida (RKKY) interaction. Those are long, and mid-range respectively.

The dipole interaction (resulting from the dipole field created by the individual moments. This tends to anti-align the moments. We go into more details in the next section.

The RKKY interaction is responsible for the coupling between different magnetic layers (either in contact, or separated by a thin non-magnetic spacer). Depending on

the spacing between those layers, the coupling can be either ferromagnetic (magnetizations tend to align) or antiferromagnetic (magnetizations tend to be opposite)[18, 19, 20].

### I - 1.3 *Magnetic domains and domain walls*

In macroscopic samples, the exchange interaction doesn't hold over long distances, so the dipole interaction becomes the main effect. Consequently, although locally spins stay aligned, over longer distances domains with different orientations will appear and because of the dipole interaction, they will tend to cancel each other. A strong enough magnetic field could however reorient all the spins along the same direction. But as soon as the external magnetic field is switched off, domains will reform.

Actual domains are made of spins pointing mostly in the same direction. The transition from a domain to the next occurs over a few to a hundred nanometers. This transition zone is called a domain wall, and can be displaced as a result of an external magnetic field, or a current. However, they are prone to get pinned by defects, impurities etc.

There are two types of domain walls, depending on how the magnetization goes from one orientation to the other. If the axis of rotation is within the plane of the wall, it is called a Bloch wall, while if it goes out of plane, it is called a Néel wall, after the discoverer of each type of wall.

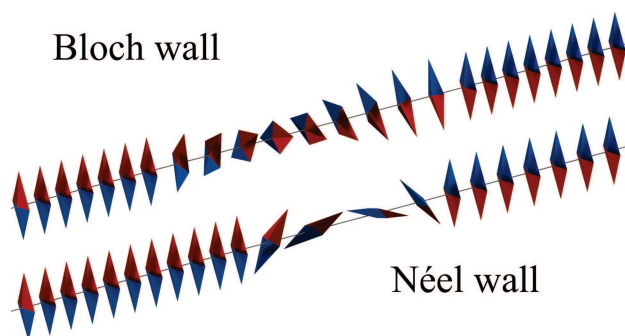


Figure 1.: The two types of domain walls, the Bloch wall with the rotation axis in the plane of the, and the Néel wall with the rotation axis out-of-plane.

The underlying crystal structure and the geometry are two sources of magnetic anisotropy. This means that in most cases, the magnetization will have a favored (easy) axis or plane. In particular, magnetization in thin films usually lies in the

film's plane. Anisotropy is the most important criterion of selection between each type of domain wall.

## I - 2 MAGNETIC DYNAMICS

At the mesoscopic scale (longer than the atomic scale, but smaller than the exchange length of around 3 nm), an effective description of the dynamics of the magnetization is given by the Landau-Lifshitz-Gilbert equation. In the following sections, we introduce the equation in its full form, then give a description of its constituent terms, and finally give a few examples of application.

### I - 2.1 Landau-Lifshitz-Gilbert equation

In magnetic systems, the magnetization possesses its own dynamics, in response to an external magnetic field or as a result of electron transport (through the spin-transfer torque). The (generalized) Landau-Lifshitz-Gilbert equation describes the evolution of the magnetization unit vector  $\mathbf{m}$  in response to a magnetic field and an applied torque. This equation has many different forms, one of which:

$$\dot{\mathbf{m}} = \mathbf{m} \times \left[ -\gamma_0 \mathbf{H}_{eff} + \alpha \dot{\mathbf{m}} + \frac{\gamma_0}{M_s L} \tau (\mathbf{m}' \times \mathbf{m} - \beta_\tau \mathbf{m}') \right] \quad (3)$$

The first term describes the precession of the magnetization around the local effective field  $\mathbf{H}_{eff}$ , which is the local field actually felt by the magnetization. We will go into more details about this effective field after the overall description of the equation.

The second term is the phenomenological Gilbert damping, a material-specific constant. It makes a precessing magnetization relax over time to align it with its precession axis.

The two last terms are the in-plane (*resp.* out-of-plane) components of the spin-transfer torque. Those are out-of-equilibrium effects, resulting from the application of a spin-polarized current<sup>1</sup>.  $\gamma_0$  is the gyromagnetic ratio,  $M_s$  is the saturation magnetization density,  $L$  the thickness of the magnetized layer (transverse to the current direction) and  $\mathbf{m}'$  is the axis of the magnetization of the reference fixed layer. The study of the spin-transfer torque is one of the main object of this thesis, we will

---

<sup>1</sup> this polarization is usually the result of spin filtering by a ferromagnetic layer of an unpolarized current, but other sources are possible

therefore present it in more details in Chapter III. And although those terms are out-of-equilibrium effects, the characteristic times of transport phenomena (the Fermi velocity is about  $10^6$  m/s, over typical lengths of a hundred nanometers, giving typical times in the picosecond range) are much faster than typical magnetic dynamics (generally in the range of the nanosecond[21]) This equation states that the in-plane torque can either balance out, or increase the damping, whereas the (smaller in amplitude) out-of-plane torque has a destabilizing effect, particularly important when describing domain wall motion. Descriptions of domain wall motion have only included the in-plane torque for a long time (as reported in Ref[15] for example), and predicted a critical torque (and therefore current density) for starting the motion 2 orders of magnitude stronger than what experiments suggested. We go into more details about that in Section III - 5.

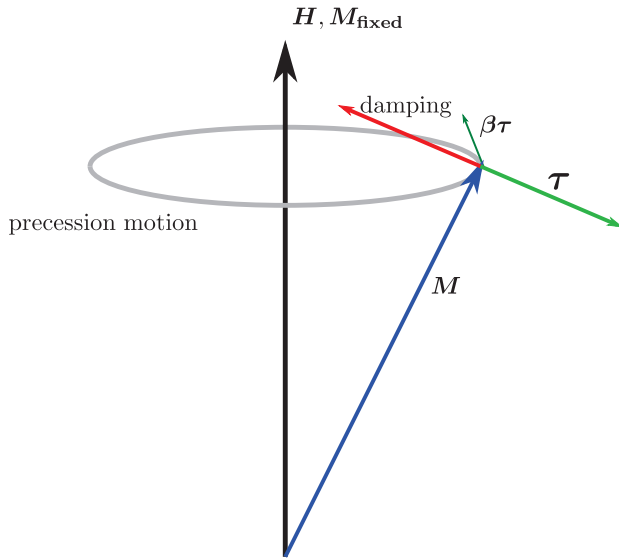


Figure 2.: Graphical representation of the terms in the LLG equation. The magnetization precesses around the effective field or the magnetization of a fixed layer, the damping brings the magnetization back towards the axis of precession. The sign of the torques depend on the current. Particularly the in-plane torque  $\tau$  can either oppose the damping, or increase it.

### I - 2.2 Effective field

Since it can be made up of several contributions, we give here a review of the most important ones. Some of them may be sometimes dropped for simplicity, therefore the composition of the effective field has to be specified for each calculation.

$$\mathbf{H}_{eff} = \mathbf{H}_{ext} + \mathbf{H}_K + \mathbf{H}_{exch} + \mathbf{H}_d \quad (4)$$

In this decomposition,  $\mathbf{H}_{ext}$  is the external applied field.  $\mathbf{H}_K$  is the field created by the anisotropy (effect of the crystal lattice). In the case of uniaxial anisotropy along the  $z$  axis:

$$\mathbf{H}_K = -KVm_z\mathbf{e}_z / M_s \quad (5)$$

with  $K$  the anisotropy constant of the material,  $V$  the volume of the sample.  $\mathbf{H}_{exch}$  is the exchange field and results from the interaction of neighboring spins on each other,

$$\mathbf{H}_{exch} = \frac{2A}{\mu_0 M_s} \nabla^2 \mathbf{m} \quad (6)$$

with  $A$  the exchange interaction constant of the material.  $\mathbf{H}_d$  is the demagnetizing (or dipolar) field, the effect of the field created by the magnetization on itself. This field can be solved as an electrostatic problem. To understand that, let us start from the Maxwell equations:

$$\nabla \times \mathbf{B} = \mu_0 \mathbf{j} \quad (7)$$

$$\nabla \cdot \mathbf{B} = 0 \quad (8)$$

Taking into account the magnetization can be done by considering small current loops acting like dipoles, on top of the applied current:  $\mathbf{j} = \mathbf{j}_M + \mathbf{j}_{app}$ . Additionally,  $\mathbf{j}_M$  must have zero divergence (since it does not contribute to the total current). Since  $\nabla \cdot \mathbf{j}_M = 0$ , there is a vector field  $\mathbf{M}$  such as  $\mathbf{j}_M = \nabla \times \mathbf{M}$ . By using the definition  $\mu_0 \mathbf{H}_d = \mathbf{M} - \mu_0 \mathbf{M}$ , we can rewrite Eq. (7) and Eq. (8) in terms of  $\mathbf{H}$ . We also set the applied current to zero (by linearity, then can be added later):

$$\nabla \times \mathbf{H}_d = 0 \quad (9)$$

$$\nabla \cdot \mathbf{H}_d = -\nabla \cdot \mathbf{M} \quad (10)$$

Because  $\mathbf{H}$  has zero curl, there is a scalar field  $\phi$  such as  $\nabla \phi = \mathbf{H}_d$ . Finally, we get an equation:

$$\nabla^2 \phi = -\nabla \cdot \mathbf{M} \quad (11)$$

This corresponds to an electrostatic problem, which are a very well known class of problems, and easily solved.

### I - 2.3 *Levels of description*

The magnetization dynamics can be studied at two different levels: one can either perform a full numerical simulation, trying to compute the local magnetization everywhere in the device. This is the most accurate, but also the most demanding in terms of computational time and power. On the other hand, one can solve the equation assuming a constant magnetization all over the device. Since the magnetization behaves in that case as if it was a giant unique spin, this approximation is called the macrospin approximation. Using it has the strong advantage that it can usually be solved by hand (*cf.* Section I - 2.6). Of course, both approaches can be combined, to improve performance. Some areas (for example those corresponding to hard magnets subject to a strong anisotropy) can be kept at the macrospin description, while other areas (like free layers of soft magnets) will need a full analysis.

### I - 2.4 *Applications*

One important use of the LLG equation was to describe domain wall motion under the application of a current. If a strong enough current is applied to a domain wall, under the effect of the spin-transfer torque, it will move along the direction of the current. This concept is currently investigated to create magnetic memories where the information is stored in the position of a train of domain walls. The most promising design is the so-called race-track memory [22].

Another system under investigation is the spin-torque oscillator. When the torque compensates the damping, a steady-state precessional motion can occur. Such a system can be used as a GHz frequency generator or detector. We go into more details in Section I - 2.7

### I - 2.5 *Magnetization reversal*

Although the hope is that this will change soon thanks to the use of magnetic memories based on the spin-transfer torque, information storage in magnetic devices has relied so far on the use of external magnetic fields (at least for writing). Because of the spatial extension of the field, downscaling is difficult. However, it has been an easy way of orienting the magnetization of a ferromagnetic material. We give here a short description of this phenomenon both for historical completeness, and because it introduces a few important concepts in magnetism.

We saw that the within a domain, individual dipoles in a ferromagnet tend to align spontaneously in the same direction while on a larger scale, the dipole interaction tend to align them in the opposite direction, hence forming various domains. When a strong enough external field is applied, those domains align with it, and most of them will stay in this direction indefinitely even when the field is switched off. The material has become magnetized. If the field is then reduced from its maximum value, because of the coercivity of the ferromagnet, the dependence of the magnetization with the field will be different. The influence of the state of the magnetization on its dependence with the applied field leads to what is called an hysteresis loop, see Fig. 3.

The magnetization attained when an increase in the field does not increase the value of the magnetization anymore is called the saturation magnetization. The value of the remaining magnetization when the field is switched off is called the remanent magnetization. And finally, the value of the field needed to cancel the magnetization is called the coercive field. However, all those values exist for a positive and negative direction. Therefore, depending on the state the ferromagnet was before switching, one of two equilibrium positions can be achieved.

### I - 2.6 *Current-induced magnetization reversal*

Historically, to switch the direction a magnetization, the only way was to apply a magnetic field to it. As we saw, this magnetic field had to be greater than the saturation magnetization of the layer to be switched, but less than that of the other layers, therefore inducing the need to pin the fixed layers in some way.

With the advent and the understanding of the spin-transfer torque, it became possible to switch a given layer by flowing a polarized current through it. Obtaining a polarized current can be done by placing another magnetic layer before the layer to switch. All this will be explained in greater details in Chapter III. Examples of practical experiments using current-induced reversal (*a.k.a.* spin injection) as well as a model for the calculation of the torque can be found for example here[23, 24].

Within the macrospin approximation, it is even possible to evaluate how much torque (and therefore how much current) is needed to switch a layer using the LLG equation. Let us consider a magnetized layer of length  $L$ , magnetization density  $M_s$ , and with an uniaxial anisotropy field  $B_u$ . We neglect the Zeeman field.

Let us introduce the (spherical) local magnetization basis (LMB)  $(\mathbf{m}, \mathbf{e}_1, \mathbf{e}_2)$ , with  $\mathbf{m}$  doing an angle  $\theta$  with the reference axis  $\mathbf{m}' = \mathbf{e}_z$  (aligned with the anisotropy axis, in this instance).  $\mathbf{e}_1$  is the orthogonal vector in the  $(\mathbf{e}_z, \mathbf{m})$  plane, and  $\mathbf{e}_2 = \mathbf{m} \times \mathbf{e}_1$ .

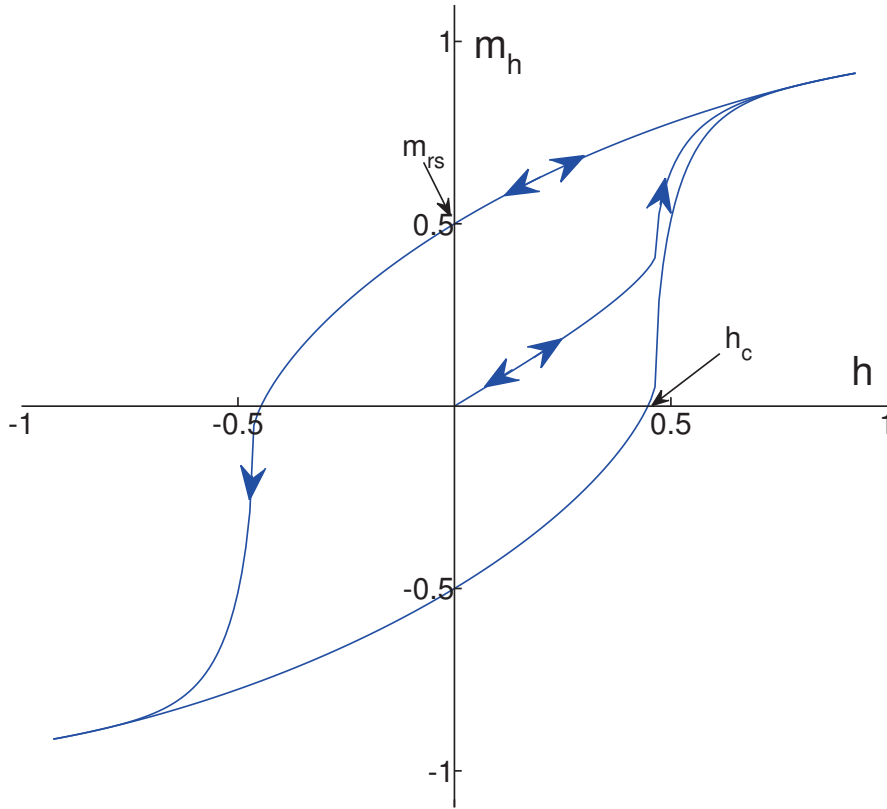


Figure 3.: Hysteresis loop in magnetic switching. Reading start at the origin, and follows the arrows. The points indicated on the plot are the remanent magnetization  $m_{rs}$  and the coercive field  $h_c$ . Not indicated on this plot is the saturation magnetization, which would be the asymptotic value reached for very high fields. Retrieved from <http://commons.wikimedia.org/wiki/File:StonerWohlfarthMainLoop.svg#mediaviewer/File:StonerWohlfarthMainLoop.svg>

The second angle of these spherical coordinates will be noted  $\varphi$ . In this basis, we have the identity:

$$\dot{\mathbf{m}} = \dot{\theta}\mathbf{e}_1 + \dot{\varphi}\sin\theta\mathbf{e}_2 \quad (12)$$

We wrote the time derivative with a dot. The LLG equation reads:

$$\dot{\mathbf{m}} = \mathbf{m} \times \left[ -\gamma_0 B_u \cos\theta \mathbf{e}_z + \alpha \dot{\mathbf{m}} + \frac{J\gamma_0 \hbar}{eM_s L} \eta(\cos\theta) \sin\theta \mathbf{e}_2 \right] \quad (13)$$

We replaced the torque  $\tau$  with an expression (see Ref[25, 26] for instance) involving the current density  $J$ :

$$\tau = \frac{\hbar}{e} J \eta(\mathbf{m} \cdot \mathbf{e}_z) \quad (14)$$

The term  $\eta(\mathbf{m} \cdot \mathbf{e}_z)$  is a shape factor for the torque. It has the following form, with  $0 \leq q < 1$ :

$$\eta(\mathbf{m} \cdot \mathbf{e}_z) = \frac{a}{1 + q\mathbf{m} \cdot \mathbf{e}_z} \quad (15)$$

We now expand Eq. (13) onto the LMB, and obtain the following two equations:

$$\dot{\theta} = -\alpha\dot{\varphi} \sin \theta - \frac{J\gamma_0\hbar}{eM_sL} \eta(\cos \theta) \sin \theta \quad (16)$$

$$\dot{\varphi} \sin \theta = \alpha\dot{\theta} + \gamma_0 B_u \sin \theta \cos \theta \quad (17)$$

We then eliminate the angle  $\varphi$  and by substituting  $u = \cos \theta$  we obtain the closed equation:

$$\dot{u} = \frac{1 - u^2}{1 + \alpha^2} \left[ \alpha\gamma_0 B_u u + \frac{J\gamma_0\hbar}{eM_sL} \eta(u) \right] \quad (18)$$

We obtain out of this that a criterion to destabilize a parallel (antiparallel) configuration is:

$$\left. \frac{\partial \tau}{\partial \theta} \right|_{\theta=0/\pi} = \pm \alpha B_u M_s L = \frac{\hbar}{e} J \eta(\theta = 0/\pi) \quad (19)$$

Obtaining the critical current density out of this expression depends on the actual form of the torque, which can be obtained either by simulations, or by using expression Eq. (15) or another one obtained through another model.

### 1 - 2.7 Spin-Torque Oscillator

Let us consider a  $F_{\text{fixed}}|N|F_{\text{free}}$  trilayer, on which we apply a magnetic field strong enough to tilt the magnetization of the free layer by an angle  $\theta$  with the  $z$  axis, but weak enough not to affect the fixed layer. As seen on Fig. 2, if tuned carefully, the torque on the free layer can exactly compensate the damping. This means that in such a device, the free magnetization would display a steady-state precession around the fixed magnetization. Such a device is called a Spin-Torque Oscillator (STO), and is a good candidate for nano- or micro-scale microwave sources [27, 28, 29]

# II

---

## THE GIANT MAGNETO-RESISTANCE

---

The Giant Magneto-Resistance (GMR) is an effect of paramount importance in spintronics. It is the first discovered effect, and the very origin of the field, and is still one of its most important features. In the last twenty years, it has impacted the way we measure magnetic fields by providing cheap and small magnetic detectors. In particular, it strongly impacted the data storage industry. Around 1990, the first magnetoresistive drives appeared, and 1995 the first ones using GMR. Since then, the areal density of hard drives increased by a factor 10 every 5 or 6 years, a much higher rate as before.

Magnetoresistance is the fact that the resistance of a piece of ferromagnetic metal depends on the orientation of an applied magnetic field. The reason behind that dependence actually depends on the system. Mathematically, it is written as:

$$\delta R_H = \frac{R(0) - R(H)}{R(0)} \quad (20)$$

Other forms appear in the literature, for example involving resistivities rather than resistance, or by normalizing by  $R(H)$  rather than  $R(0)$ . Therefore, numbers should be carefully examined to know what the result is really about.

We start our review of the giant magnetoresistance by giving an historical overview of its origin until its award as a Nobel Prize. We then introduce in details the Valet-Fert theory, which a simple and effective theory giving an accurate description of the effect. We use this theory in a toy device to obtain an expression for its magnetization-dependent resistance. As a conclusion, we give an overview of modern devices and materials.

## II - 1 HISTORY OF A NOBEL PRIZE

The first report of magnetoresistance is by William Thompson (Lord Kelvin) in 1851. He discovered that a piece of iron subjected to a magnetic field exhibited a maximum resistance if the current flowed parallel to the magnetic field, and minimum if it was perpendicular. The same experiment in nickel confirmed the same result, only with a higher amplitude. However, the highest value for the magnetoresistance he ever obtained was of the order of 5%. This type of magnetoresistance is called Anisotropic Magnetoresistance, and is due to the spin-orbit interaction inside the ferromagnet.

In 1988, the groups of Albert Fert[7] in Université Paris-Sud, France and Peter Grünberg[8] in Forschungszentrum Jülich, Germany, independently found that the resistance of iron/chromium multilayers depended on the orientation of the applied magnetic field. Owing to the very large GMR value (almost 50%) obtained by Fert's group, we will describe their experiment.

They created a stack of about 30 bcc Fe(001)/Cr(001) bilayers, of varying thickness. The Fe magnetization was lying in-plane, with an antiferromagnetic coupling between the Fe layers if the Cr layer is thinner than 30 Å. Keeping the system at liquid helium temperature (4.2K), applying a magnetic field, and flowing a current through the layers, they obtained various results. Firstly, regardless of this orientation, they observed that the resistance was higher at zero field, and that above a given value of the field  $H_S$ , the resistance did not change anymore. Secondly, the value of  $H_S$  depends on the orientation of the field. It is higher when applied perpendicular to the plane of growth, because it needs to overcome the shape anisotropy of the layers, on top of the antiferromagnetic coupling.

These results opened the way to the study of more devices, and created a whole new field, called spintronics (shorter form of spin electronics). Because the implications for the electronics industry were tremendous, a lot of money was invested into this new field. The result was that in less than ten years, IBM released a GMR-based hard drive, outperforming the AMR-based used at the time[30]. This is the fastest any technology was brought from the lab to the market.

## II - 2 THE VALET-FERT THEORY

In the original experiment of Fert and Grünberg, the current was flowing parallel to the plane of growth. This geometry, the easiest to grow, is called the Current In-

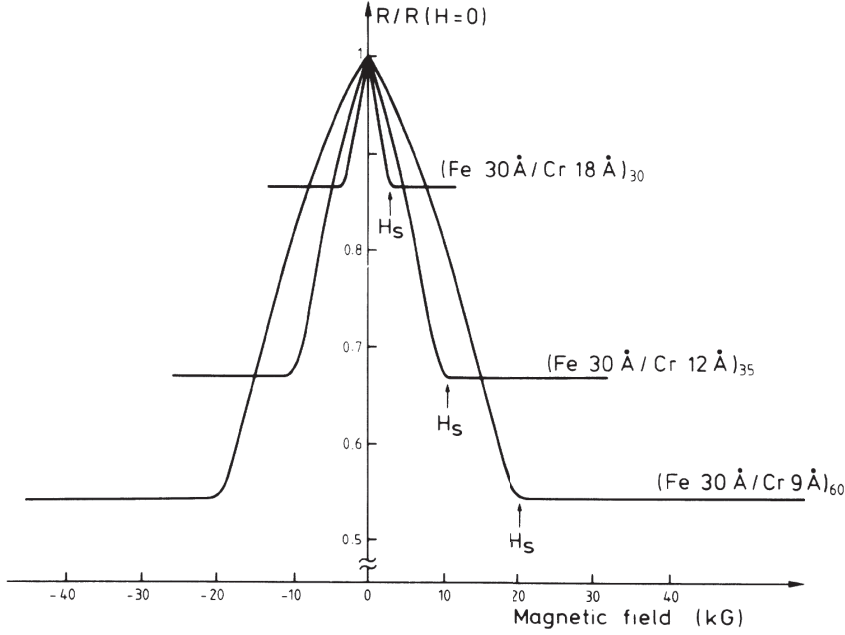


Figure 4.: Ratio  $R(H)/R(H=0)$  for three superlattices at 4.2K. The current and field are both along the [110] axis (in-plane). Taken from Ref[7]

Plane (CIP) geometry. The GMR in this geometry is of ballistic origin, and relies mostly on the electrons (spin-dependent) mean free paths.

However, another geometry arose in 1991[31], where the current was perpendicular to the growth plane. Although not as easy to manufacture as the CIP geometry, the physics behind the GMR in this geometry is simpler to explain, thanks to a two-current model, and a (very simple) equivalent electrical circuit. This model is summarized into a set of diffusion equations: the Valet-Fert (VF) equations[1].

Based on the linearized Boltzmann equation, these equations relate through a two-current model the local spin current  $J_\sigma$  (with sigma representing the majority  $\uparrow$  or minority  $\downarrow$  spin specie) to the spin-resolved electrochemical potential  $\mu_\sigma$ . These equations, which are only applicable in the case of collinear magnetizations and in the CPP geometry read:

$$e\rho_\sigma J_\sigma = -\partial_z \mu_\sigma \quad (21)$$

$$4\rho_* e \partial_z J_\sigma = \frac{\mu_\sigma - \mu_{-\sigma}}{\ell_{sf}^2} \quad (22)$$

The first equation is simply a generalization of Ohm's law taking spin into account, with  $\rho_\sigma$  the resistivity of a given spin specie. The second equation, on the

other hand, gives the (non-)conservation of the spin current, with a spin relaxation length (also called spin-flip length)  $\ell_{sf}$  giving the depth up to which a current retains its polarization. In particular, a polarized current injected into a normal metal will become completely unpolarized after a few  $\ell_{sf}$ .

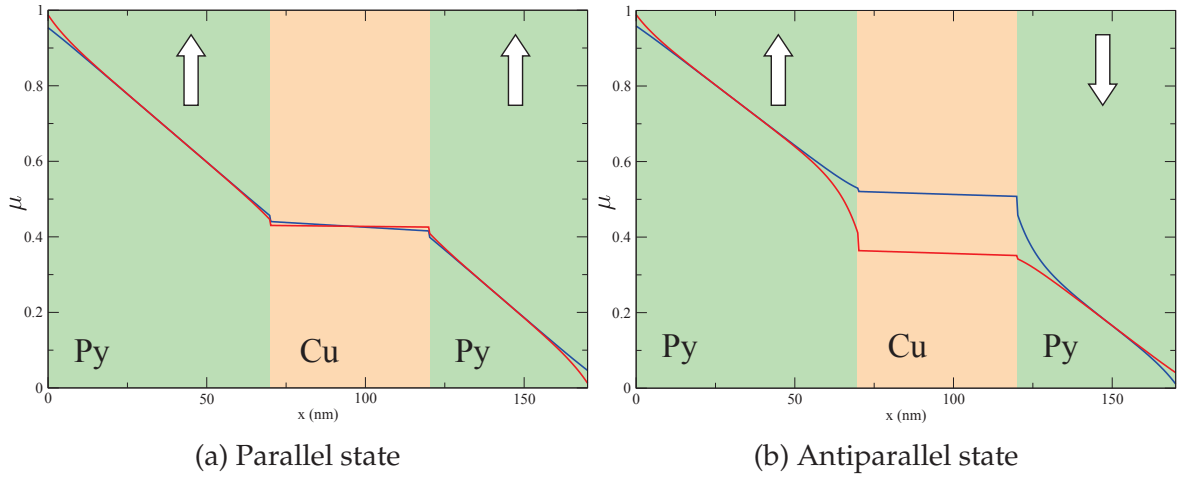


Figure 5.: Graph of the spin-resolved potentials (red for majority, blue for minority) in a Py|Cu|Py trilayer. The difference between the majority and minority potentials is known as the spin accumulation, visible mostly at interfaces.

### II - 3 FIRST EXAMPLE: GMR OF A MINIMAL SPIN-VALVE

We first give here an extremely simple picture of the calculation of the GMR in the minimal spin-valve Fig. 7, within the Valet-Fert framework, when spin-flip is not accounted for. In this case, the spin-valve reduces to the equivalent two-current circuit given in Fig. 6: Thanks to the absence of spin-flip, this model simply assumes that each spin channel can be considered as a parallel branch of a circuit. Each channel therefore has a well defined resistance, made up of the resistance of the relevant channel of each of the two layers in consideration. As the size of the boxes suggest, the majority channel in the parallel state is much less resistive than the the minority channel. However, in the antiparallel state, both channel have a similar resistance.

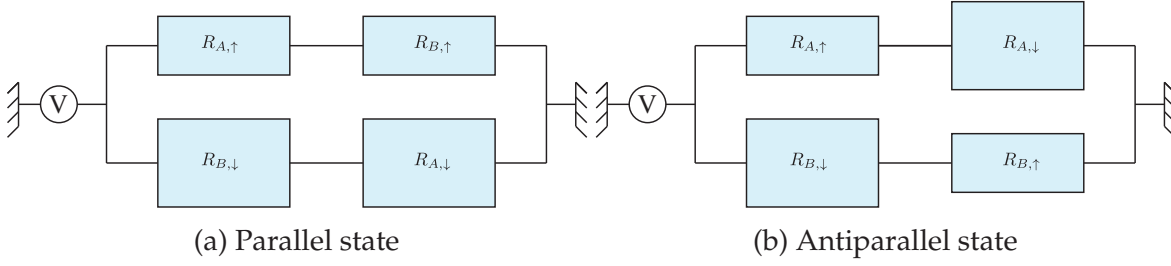


Figure 6.: Two current model for a spin-valve without spin-flip. The size of the boxes are proportional to the magnitude of the resistance of the spin channel.

This is the easiest visualization of the origin of GMR. In terms of equations, Kirchhoff's laws simply give us:

$$R_P = \frac{(R_{A,\uparrow} + R_{B,\uparrow})(R_{A,\downarrow} + R_{B,\downarrow})}{R_{A,\uparrow} + R_{B,\uparrow} + R_{A,\downarrow} + R_{B,\downarrow}} \quad (23)$$

$$R_{AP} = \frac{(R_{A,\uparrow} + R_{B,\downarrow})(R_{A,\uparrow} + R_{B,\downarrow})}{R_{A,\uparrow} + R_{B,\uparrow} + R_{A,\downarrow} + R_{B,\downarrow}} \quad (24)$$

This leads to the following expression for the GMR:

$$\delta R = \frac{R_{AP} - R_P}{R_P} = \frac{(R_{A,\downarrow} - R_{A,\uparrow})(R_{B,\downarrow} - R_{B,\uparrow})}{(R_{A,\uparrow} + R_{B,\uparrow})(R_{A,\downarrow} + R_{B,\downarrow})} \quad (25)$$

If we write  $R_{X,\uparrow(\downarrow)} = R_X^* \mp \Delta R_X$  where  $X$  stands for  $A$  or  $B$ , this expression becomes:

$$\delta R = \frac{\Delta R_A \Delta R_B}{(R_A^* + R_B^*)^2 - (\Delta R_A + \Delta R_B)^2} \quad (26)$$

This expression makes obvious that increasing the GMR means increasing the asymmetry between the majority and minority channel, while keeping the overall resistance as low as possible. Let us now take a look at a derivation including spin-flip.

We now show a derivation in the Valet-Fert framework, to compute the GMR in a spin-valve in the presence of spin-flip. This example, chosen for its pedagogical purpose, is a slightly more general form of the one presented in Ref[1]. Let us consider a system made of two ferromagnets brought together. We assume the material to be

the same, while their magnetization can have a different orientation. Because of this, the notations for the spin species may be confusing. To make this matter as clear as possible, we introduce two sets of indices for the spin:  $\pm$  correspond to the sign of the projection onto the  $z$ -axis, while  $\uparrow$  ( $\downarrow$ ) describe the majority and minority spins. These notations are consistent with those of Eq. (21) and Eq. (22). For the calculation we are about to present, we will consider a case similar to the Fe|Cr|Fe trilayer originally measured, that is majority spins are antiparallel to the magnetization ( $\uparrow = -$ ,  $\downarrow = +$ ). This distinction is of utmost importance when dealing with a system in the antiparallel state, as we shall see momentarily. The system is naturally divided in a

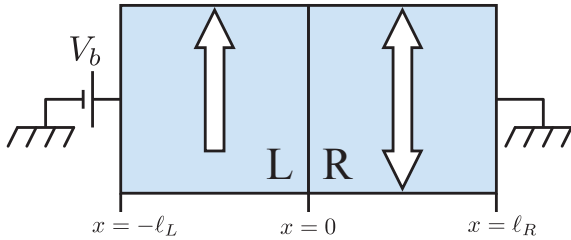


Figure 7.: Toy device for the calculation of GMR within the Valet-Fert framework. The left magnetization is fixed in the up position, while the right one can be pointing either up or down.

left (L) and a right (R) part. We assume the left magnetization to be along the positive  $z$ -axis, and take this as our reference axis. The right part however can be either in the parallel ( $P \equiv$  positive  $z$ -axis), or antiparallel ( $AP \equiv$  negative  $z$ -axis). Contrary to Ref[1], we do not assume that the materials are semi-infinite, nor that they have the same length. We will however recover those results in a final step, to prove that our derivation is more general than the one presented in the seminal article. The reason behind the choice of another system is threefold. First, although formally correct, the original derivation assumes a current flowing in an infinitely long resistive system, which we did not find pedagogically satisfying. Second, to define the GMR in an infinite system, the ratio should be defined on equivalent resistivities, rather than resistances.

II - 4.1 *Some useful notations*

We introduce new notations for the potential, namely  $\mu_c$  which is the usual electrochemical potential,  $\Delta\mu$  the spin accumulation (the antisymmetric part of the spin-resolved potential) and  $\bar{\mu}$  the symmetric part of the spin-resolved potential:

$$\mu_{\pm} = \bar{\mu} \pm \Delta\mu \quad (27)$$

$$\mu_c = 2\rho_* \left( \frac{\mu_+}{\rho_+} + \frac{\mu_-}{\rho_-} \right) \quad (28)$$

Because these equations depend on the spin-dependent resistivity, they also depend on the magnetic orientation. We have the following decomposition:

$$\rho_{\uparrow(\downarrow)} = 2\rho_*(1 \pm \beta) \quad (29)$$

We introduced  $\beta$ , the spin-asymmetry of the material, defined as  $\beta = (\rho_{\downarrow} - \rho_{\uparrow}) / (\rho_{\downarrow} + \rho_{\uparrow})$ .

There are two sets of boundary conditions. At the edges of the sample, we have:

$$\mu_c(-\ell_L) = eV_b \quad (30)$$

$$\mu_c(+\ell_R) = 0 \quad (31)$$

$$\Delta\mu(-\ell_L) = 0 \quad (32)$$

$$\Delta\mu(+\ell_R) = 0 \quad (33)$$

And at the interface, we have:

$$J_{\pm}(0^-) = J_{\pm}(0^+) \quad (34)$$

$$\mu_{\pm}(0^-) - \mu_{\pm}(0^+) = r_{\pm} J_{\pm}(0) \quad (35)$$

Where  $r_{\pm}$  is a spin-dependent interface resistance. It has the same structure as the bulk resistivity  $r_{\pm} = 2r_*(1 \pm \gamma)$ , where  $\gamma$  is the interface spin-asymmetry. However, since this interface behaves essentially as a zero thickness bulk material, it does not bring any new physics. For the sake of simplicity, we assume that  $r_* = 0$ , making the spin-resolved potential continuous at the interface.

II - 4.2 *Derivation example: the spin accumulation and spin currents in the antiparallel state of spin-valve*

We assume that the system is in its antiparallel state. With the relation between majority/minority and the projection introduced before, we have:

$$\rho_{\pm}^L = 2\rho_*(1 \pm \beta) \quad (36)$$

$$\rho_{\pm}^R = 2\rho_*(1 \mp \beta) \quad (37)$$

With those definitions, we obtain for the spin-resolved potentials:

$$\mu_{\pm}^L = \frac{1 - \beta^2}{2} \mu_c + \beta \Delta\mu \pm \Delta\mu \quad (38)$$

$$\mu_{\pm}^R = \frac{1 - \beta^2}{2} \mu_c - \beta \Delta\mu \pm \Delta\mu \quad (39)$$

Eq. (21) and Eq. (22) give for each side:

$$\partial_z^2 \Delta\mu = \frac{1}{\ell_{sf}^2} \Delta\mu \quad (40)$$

$$\partial_z^2 \mu_c = 0 \quad (41)$$

Solving those equations gives:

$$\Delta\mu = A_i e^{z/\ell_{sf}} + B_i e^{-z/\ell_{sf}} \quad (42)$$

$$\mu_c = C_i z + D_i \quad (43)$$

With  $i$  indicating the  $L$  or  $R$  side.

From Eq. (34), we find that  $J = J_+ + J_-$  is not only continuous, but also constant through the whole system. This implies that  $C_L = C_R = C$ , with the relation  $C = 2e\rho_*J$ . However,  $D_L \neq D_R$ . Similarly, one of the consequence of Eq. (35) is that  $\Delta\mu(0^-) = \Delta\mu(0^+)$ , that is the spin-accumulation is continuous at the interface. Finally, we obtain from those interface conditions:

$$A_L + B_L = A_R + B_R \quad (44)$$

$$A_L - B_L - A_R + B_R = \beta C \ell_{sf} \quad (45)$$

We obtain also from the boundary conditions:

$$A_L \varepsilon_L^{-1} + B_L \varepsilon_L = 0 \quad (46)$$

$$A_R \varepsilon_R + B_R \varepsilon_R^{-1} = 0 \quad (47)$$

with  $\varepsilon_{L/R} = e^{\ell_{L/R}/\ell_{sf}}$ .

A few steps of algebra give finally the following results:

$$\Delta\mu^L = \frac{1 - \varepsilon_R^{-2}}{\varepsilon_L^2 - \varepsilon_R^{-2}} \beta e \rho_* \ell_{sf} J \left( \varepsilon_L^2 e^{z/\ell_{sf}} - e^{-z/\ell_{sf}} \right) \quad (48)$$

$$\Delta\mu^R = \frac{1 - \varepsilon_L^2}{\varepsilon_L^2 - \varepsilon_R^{-2}} \beta e \rho_* \ell_{sf} J \left( \varepsilon_R^{-2} e^{z/\ell_{sf}} - e^{-z/\ell_{sf}} \right) \quad (49)$$

$$J_{\pm}^L = \frac{1 \mp \beta}{2} J \left( 1 \pm \frac{\beta}{1 \mp \beta} \frac{1 - \varepsilon_R^{-2}}{\varepsilon_L^2 - \varepsilon_R^{-2}} \left[ \varepsilon_L^2 e^{z/\ell_{sf}} + e^{-z/\ell_{sf}} \right] \right) \quad (50)$$

$$J_{\pm}^R = \frac{1 \pm \beta}{2} J \left( 1 \pm \frac{\beta}{1 \pm \beta} \frac{1 - \varepsilon_L^2}{\varepsilon_L^2 - \varepsilon_R^{-2}} \left[ \varepsilon_R^{-2} e^{z/\ell_{sf}} + e^{-z/\ell_{sf}} \right] \right) \quad (51)$$

$$J = \frac{\varepsilon_L^2 - \varepsilon_R^{-2}}{2(1 - \varepsilon_R^{-2})(1 - \varepsilon_L^2)\beta\ell_{sf} - (\varepsilon_L^2 - \varepsilon_R^{-2})(1 - \beta^2)(\ell_L + \ell_R)} \frac{1 - \beta^2}{2\rho_*} V_b \quad (52)$$

$$\mu_c^L = \frac{2(1 - \varepsilon_R^{-2})(1 - \varepsilon_L^2)\beta\ell_{sf} - (1 - \beta^2)(\varepsilon_L^2 - \varepsilon_L^{-2})(z + \ell_R)}{2(1 - \varepsilon_R^{-2})(1 - \varepsilon_L^2)\beta\ell_{sf} - (1 - \beta^2)(\varepsilon_L^2 - \varepsilon_L^{-2})(\ell_L + \ell_R)} eV_b \quad (53)$$

$$\mu_c^R = \frac{(1 - \beta^2)(\varepsilon_L^2 - \varepsilon_L^{-2})(z - \ell_R)}{2(1 - \varepsilon_R^{-2})(1 - \varepsilon_L^2)\beta\ell_{sf} - (1 - \beta^2)(\varepsilon_L^2 - \varepsilon_L^{-2})(\ell_L + \ell_R)} eV_b \quad (54)$$

To recover the results in Ref[1], we take  $\ell_L = \ell_R \rightarrow \infty$ , and we suppose that  $J$  is the applied current in the system, without evaluating the (infinite) potential needed for it. We obtain:

$$\Delta\mu^L = \beta e \rho_* \ell_{sf} J e^{z/\ell_{sf}} \quad (55)$$

$$\Delta\mu^R = \beta e \rho_* \ell_{sf} J e^{-z/\ell_{sf}} \quad (56)$$

$$J_{\pm}^L = \frac{1 \mp \beta}{2} J \left( 1 \pm \frac{\beta}{1 \mp \beta} e^{z/\ell_{sf}} \right) \quad (57)$$

$$J_{\pm}^R = \frac{1 \pm \beta}{2} J \left( 1 \pm \frac{\beta}{1 \pm \beta} e^{-z/\ell_{sf}} \right) \quad (58)$$

## II - 5 MODERN GMR DEVICES

Modern devices are usually based on the spin-valve design. The basic concept of a spin-valve consists in two ferromagnetic layers sandwiching a normal layer. Al-

tough we deal exclusively in this thesis with all-metallic spin-valves, it is worth noting that actually, replacing the normal layer by a thin oxide layer through which the electron can tunnel gives even better results. Such a device is called a tunnel junction, and is intensively studied[32, 33].

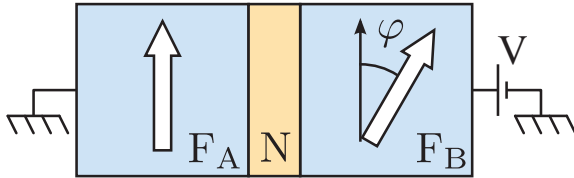


Figure 8.: Sketch of the working principle of a spin-valve

In spin-valves, care is taken to be as close as the macrospin limit as possible, in order to consider each layer to have “a” magnetization direction. By various means (anisotropy, antiferromagnetic coupling with another magnetic layer, pinning, high coercive field, etc...), one of the ferromagnetic layer is made to have its magnetization fixed. By this, we mean that a much higher magnetic field is needed to change the direction of this layer (called the fixed layer) than the other (the free layer).

Permalloy (an alloy of 80% Ni, 20% Fe, usually abbreviated Py) is the material of choice for the free layer. It is an alloy of readily available metals in any lab, and has the property to have both a strong magnetic susceptibility, as well as low coercive field. It also has a strong spin asymmetry (reported values up to 0.76[34]).

Spin-valves are the simplest devices exhibit GMR, and are well-described by the Valet-Fert theory. The GMR is taken in this case between the parallel and antiparallel configurations for the magnetizations. Switching one of the magnetizations (that of the free layer) is usually done by applied an appropriate magnetic field. However, another route for switching exists. Using the concept of spin-transfer torque (that will be introduced in Chapter III), it is possible to switch the free layer by subjecting it to a polarized current. Such a current can be easily achieved in a spin valve, by using the fixed layer as a polarizer. Therefore, applying a voltage to a spin-valve and let the current flow is one way of switching from a magnetic configuration to another.

The current density needed to switch a layer has been decreased over the years thanks to cleaner samples, better choice of materials, and so on. The current reference value[35, 36, 37] for the current density is  $10^7 \text{ A} \cdot \text{cm}^{-2}$ .

The highest GMR ratio reported are about 220% for CIP-GMR[38].

Metal	$\ell_{sf}$ [nm]
Ag	30
Al	500
Au	30
Co	60
CoFe	12
Cr	6
Cu	500
Fe	60
Ni	21
Pt	14
Py (NiFe)	5.5
Ru	14
Ta	1.8

Table 1.: Values of the spin-flip length for usual magnetic and non-magnetic metals. Values can vary quite a lot, depending on the measurement technique and the temperature. These values are the one used in our simulations. More details can be found in Ref[39]

## II - 6 SPIN-ORBIT COUPLING AND SPIN-FLIP

The spin-orbit interaction, or spin-orbit coupling is an effect occurring when the spin of an electron interacts with its motion, for example due to the magnetic field created by a nucleus. A number of theories explain particular cases, such as the Rashba effect, or the Dresselhaus effect. As a general rule of thumb, spin-orbit effects are more prominent in heavy atoms, such as gold, platinum.

From a spintronics point of view, the spin-orbit interaction is the main source of spin relaxation, and the origin of the finite spin-flip length (*a.k.a.* spin-diffusion length). This length  $\ell_{sf}$ , introduced in the Valet-Fert theory, corresponds to a mean free path of the orientation of a spin. It can be noted that because of the loss of translation symmetry, edges and interfaces can induce some more spin-orbit coupling, leading to even more spin-flip.

Spin-flip is also one of the ingredients necessary for the existence of the out-of-plane spin-transfer torque (which again will be introduced in Chapter III)[40]. This specific component is of paramount importance to explain in any detail the motion of domain walls subjected to an electrical current.



# III

---

## SPIN-TRANSFER TORQUE

---

As we saw in the previous section, the Valet-Fert formalism describes well systems in a collinear state (either parallel or antiparallel). In particular, it is sufficient to compute (within the correct set of approximation) the value of the GMR. However, this theory fails entirely to deal with non-collinear systems.

In collinear systems, we saw that the magnetization influences the spin polarization of the current, giving rise to the GMR. The opposite is also true, and the influence of the electron's spin over the surrounding magnetization is what we call the spin-transfer torque. It occurs whenever spin sources or sinks are present in the system, therefore yielding a non-conservation of the spin current.

DEFINITION:

**The spin-transfer torque (STT) is the non-conserved part of the spin current that is given to (or taken from) the magnetization.**

In part 1, we will give a slightly more in-depth overview of the torque, and how it impacted the community. In part 2 we will see how it came to be discovered. In part 3 we will consider a toy model to illustrate that it is a fundamental effect with very few assumptions.

### III - 1 OVERVIEW AND CONSEQUENCES IN SPINTRONICS

In collinear systems, the only source of non-conservation are spin-flip processes. And because they originate from the spin-orbit interaction, the lost spin is not given to the magnetization, but to the lattice. However, in non-collinear systems, spin currents are filtered when reaching a magnetic layer. If the magnetization and the current polarization are not collinear, the transverse part is absorbed by the layer as

a torque. In turn, if enough momentum is deposited onto the layer, it exerts an influence on the magnetization by modifying its direction. In multilayers, this means switching the magnetization between a parallel and antiparallel state, or start a sustained precessional motion. In domain walls, STT can start a motion of the position of the wall. In that case, the critical current density is more difficult to evaluate, because the wall may be pinned by a defect in the lattice. The shape and nature of this defect being extremely hard to include into any model, one has to perform very fine numerical simulations to take it into account. A more common route is to get rid (as much as possible) of the influence of this defect by heating the wall locally. This extra amount of energy helps overcoming the Arrhenius-like potential barrier, and put the wall into motion.

At first, the facts that STT vanishes in collinear states (no transverse part in the spin current) and that it can switch magnetization between parallel and antiparallel states seem impossible to reconcile. To start switching the magnetization, the torque needs to be non-zero. What makes it all possible are thermal fluctuations. What we consider as the magnetization axis is always an average position. Therefore, if the torque is strong enough at angles close to its zero values, and if the fluctuations are strong enough, switching can occur. This leads to the conclusion that higher temperatures help decreasing the critical current for switching. Additionally, higher temperatures reduce the saturation magnetization, leaving fewer spins to be switched, and therefore reducing the total momentum that needs to be transferred.

### III - 2 HISTORY OF SPIN-TRANSFER TORQUE

The question of non-longitudinal magnetic systems actually came up a long time before the Valet-Fert theory, with the prediction in the late 1970s by Berger[41] that spin torques should be able to move domain walls. However, because of the lack of maturity in the fabrication of nanoscale devices at the time, and of the very high current densities required, the concept of spin transfer remained largely ignored for another twenty years.

In an article[42] in 1989 where he calculated the interlayer exchange coupling of two ferromagnets separated by an insulating tunnel barrier, Slonczewski looked at two cases which would later lead the way to a systematic study of spin transfer torque. He first estimated the spin current flowing between two ferromagnetic electrodes, with non-collinear magnetization (which is the source of the interlayer exchange coupling). Then, he made the same calculation while applying a bias voltage on the junction.

Then, Berger and Slonczewski published independently, and roughly at the same time, an article[2, 3] predicting that it should be possible to switch the magnetization of a layer in a multilayer nanopillar, at reasonable current densities. More precisely, Slonczewski showed that two types of magnetic excitations were possible, depending on the applied field, and the device design. The first, a static excitation, is simply switching from one magnetic configuration to another (for instance antiparallel to parallel). The second is a dynamical state, where one magnetization precesses steadily, see Section I - 2.7. STT was first experimentally observed around 2000 [43, 44, 45]

The main limiting factor against the excitation of either mode is the critical current density. Advancing lithographic techniques and better material choices have made it possible to reduce it, to the state-of-the-art values obtained nowadays. Values around  $10^7 \text{ A}\cdot\text{m}^{-2}$  are reported for metallic multilayers[35, 36, 37], and can go down by two orders of magnitude when dealing with tunnel junctions[46].

### III - 3 TORQUE AND SPIN FILTERING

The effect known as spin filtering is the fact that, due to different transmissions and reflections for different spin orientation, a ferromagnet will allow more majority spins to be transmitted, and more minority spins to be reflected.

#### III - 3.1 *Spin filtering of an unpolarized current*

An unpolarized charge current obtains a polarization if it encounters a ferromagnet on its path. If we consider a ideal ferromagnet ( $t_{\uparrow} = 1, t_{\downarrow} = 0, r_{\uparrow} = 0, r_{\downarrow} = 1$ ), it will separate the spins in the unpolarized current, allowing the majority to pass through, and reflecting the minority.

Fig. 9 gives an idea of how the transmitted current becomes polarized. However, for simplicity, only half of the effect is shown here. Indeed, only the transmitted part is shown polarized. It is important to note that the once unpolarized current will become polarized because of the reflected minority spins.

A real ferromagnet will differ from an ideal one simply by not letting all the majority spins through, and reflecting some. Similarly, some minority spins may be transmitted instead of being reflected.

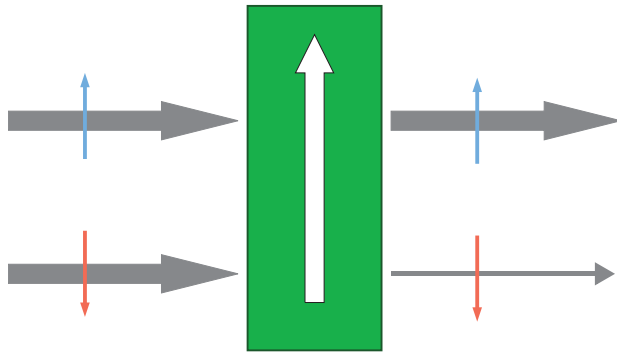


Figure 9.: A simple picture illustrating how a unpolarized current (as many up and down spins) becomes polarized after going through a ferromagnet.

### III - 3.2 Spin filtering of a polarized current

Now, assuming that a polarized current impacts a (still ideal for simplicity) ferromagnetic layer, with a magnetization that is not collinear to the polarization of the current, we know that a torque is created, see Fig. 10.

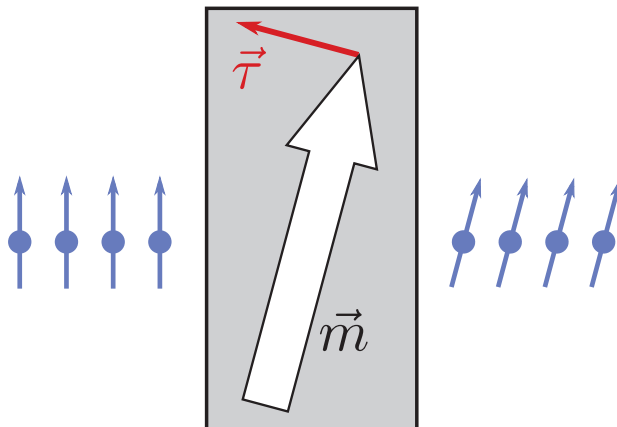


Figure 10.: Drawing of filtering on a polarized current, and the resulting torque. The current comes from the left, becomes polarized by transmission through the magnet, and leaves some momentum as spin transfer torque.

Because spin currents do not arise naturally, one needs some of creating them. The usual way to produce them is by using a second ferromagnetic layer to polarize the incoming current, also thanks to the spin filtering effect. However, because of the presence of a second ferromagnetic layer, multiple reflections and transmission take place. And because the reflected spins have a strong component opposite to the incoming ones, the net effect is to reduce the value of the torque one would find by simply considering the case in Fig. 10.

Fig. 11 displays the effect the presence of a second layer has in the two cases corresponding of the two possible direction of the current. Let us consider the case

when the (unpolarized) current comes from the left. The transmitted part is polarized along  $m_A$  (the magnetization of layer A), and the reflected part along  $-m_A$ . This transmitted part is then filtered by layer B, and separated into a transmitted part polarized along  $m_B$ , and reflected along  $-m_B$ . The process iterates, by alternating orientation. And although, the value of the torque is reduced, its orientation remains the same as the leading order (first transmission/reflection).

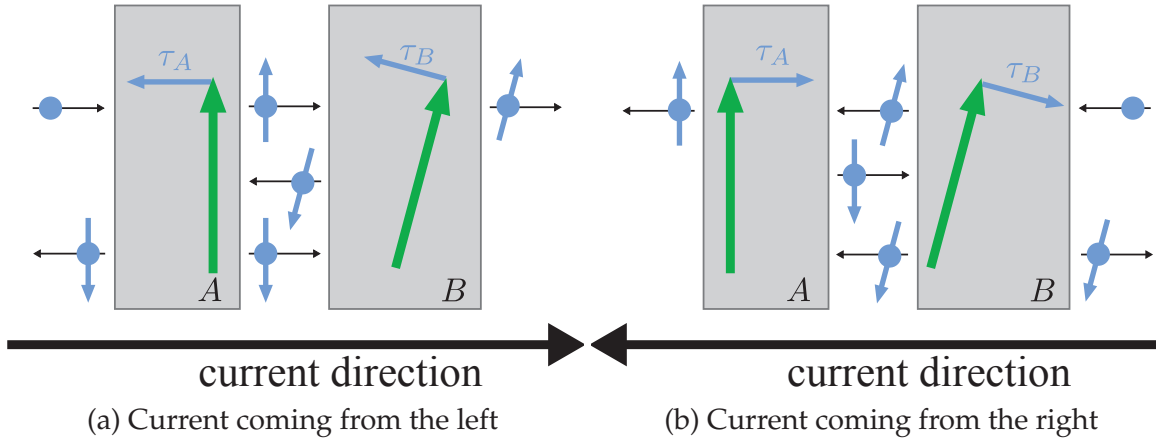


Figure 11.: Drawing of how a current becomes polarized after passing through and being reflected multiple times between two non-collinearly magnetized ferromagnetic layers. Transmitted currents are on the same line, while reflected are on the line directly below. Reading starts from the origin of the current. Resulting torques are displayed on each layer.

Let us now examine how spin filtering works with a very simple quantum model.

### III - 4 ILLUSTRATION WITH A TOY MODEL

Let us first set up some notation conventions. Bold symbols correspond to vectors in spin space, and arrowed symbols correspond to vectors in real space. Let us now consider a magnetic layer, with its magnetization pointing to the  $z$ -axis. Let us now consider an incoming electron ( $\vec{k} = k\vec{e}_x$ ), with its spin making an angle  $\theta$  with the  $z$ -axis, in the  $(x, z)$  plane. We describe the magnetic layer in the scattering formalism with its transmission (resp. reflexion) spin-dependent coefficients  $t_\uparrow, t_\downarrow$  (resp.  $r_\uparrow, r_\downarrow$ ). By doing so, we are free of any model to describe the ferromagnetic layer, and we

simply assume that there is a spin-dependence of the properties of the layer. The wave function describing this incoming electron is:

$$\Psi_{in} = \frac{e^{ikx}}{\sqrt{\Omega}} \left( \cos \frac{\theta}{2} |\uparrow\rangle + \sin \frac{\theta}{2} |\downarrow\rangle \right) \quad (59)$$

This form may be found in any book of basic quantum mechanics, in the chapter dealing with spin-1/2 systems. It is obtained for instance by applying the rotation properties to the  $|\uparrow\rangle$  state.  $\Omega$  is a normalization factor.

The transmitted and reflected parts are, respectively:

$$\Psi_t = \frac{e^{ikx}}{\sqrt{\Omega}} \left( t_{\uparrow} \cos \frac{\theta}{2} |\uparrow\rangle + t_{\downarrow} \sin \frac{\theta}{2} |\downarrow\rangle \right) \quad (60)$$

$$\Psi_r = \frac{e^{-ikx}}{\sqrt{\Omega}} \left( r_{\uparrow} \cos \frac{\theta}{2} |\uparrow\rangle + r_{\downarrow} \sin \frac{\theta}{2} |\downarrow\rangle \right) \quad (61)$$

If we write  $\boldsymbol{\sigma} = (\sigma_x, \sigma_y, \sigma_z)$  the vector of the three Pauli matrices, and  $m$  the mass of an electron, the spin current density operator is given by:

$$\vec{\mathbf{J}} = \frac{\hbar^2}{2m} \text{Im} \left[ \Psi \boldsymbol{\sigma} \vec{\nabla} \Psi^* \right] \quad (62)$$

This leads to the following expressions for the various spin currents:

$$\mathbf{J}_{in} = \frac{\hbar^2 k}{2m\Omega} [\sin \theta \mathbf{e}_x + \cos \theta \mathbf{e}_z] \quad (63)$$

$$\mathbf{J}_t = \frac{\hbar^2 k}{2m\Omega} \left[ \text{Re}(T_{\text{mx}}) \sin \theta \mathbf{e}_x + \text{Im}(T_{\text{mx}}) \sin \theta \mathbf{e}_y + (|t_{\uparrow}|^2 \cos^2 \theta - |t_{\downarrow}|^2 \sin^2 \theta) \mathbf{e}_z \right] \quad (64)$$

$$\mathbf{J}_r = -\frac{\hbar^2 k}{2m\Omega} \left[ \text{Re}(R_{\text{mx}}) \sin \theta \mathbf{e}_x + \text{Im}(R_{\text{mx}}) \sin \theta \mathbf{e}_y + (|r_{\uparrow}|^2 \cos^2 \theta - |r_{\downarrow}|^2 \sin^2 \theta) \mathbf{e}_z \right] \quad (65)$$

We introduced  $T_{\text{mx}} = t_{\uparrow} t_{\downarrow}^*$  and  $R_{\text{mx}} = r_{\uparrow} r_{\downarrow}^*$ . By definition, the torque is the difference of spin current on either side of the magnet. We note  $\boldsymbol{\tau}$  the torque areal density, and we have  $\boldsymbol{\tau} = \mathbf{J}_{in} + \mathbf{J}_r - \mathbf{J}_t$ . By using  $|t_{\uparrow}|^2 + |r_{\uparrow}|^2 = 1$  and  $|t_{\downarrow}|^2 + |r_{\downarrow}|^2 = 1$ , we obtain:

$$\boldsymbol{\tau} = \frac{\hbar^2 k}{2m\Omega} \sin \theta \left[ (1 - \text{Re}(T_{\text{mx}} + R_{\text{mx}})) \mathbf{e}_x - \text{Im}(T_{\text{mx}} + R_{\text{mx}}) \mathbf{e}_y \right] \ddot{\theta} \quad (66)$$

We recover some important results from this expression. The torque vanishes for  $\theta = 0$  and  $\theta = \pi$  (collinear configurations), but also if  $t_{\uparrow} = t_{\downarrow}$  and  $r_{\uparrow} = r_{\downarrow}$  (no spin

filtering). However, provided we are not in one of those cases, we can see that the spin current is not conserved. The spin-transfer torque is a intrinsic consequence of spin-filtering, regardless of the detailed properties of the material. Worth noting, the torque does not have any component on the magnetization (here  $z$  axis). It is therefore entirely orthogonal (transverse) to the magnetization. Although, nothing prevents it to have components on both transverse axes  $x$  and  $y$ , the imaginary part of the coefficients was assumed to be small, and people focused on the in-plane ( $x$  in our case) torque, with good results. We will see in the next section that discrepancies arose, and that accounting of the out-of-plane torque solved them.

### III - 5 IN-PLANE AND OUT-OF-PLANE TORQUES

Other than dealing with multilayers, the results of Slonczewski and Berger opened the possibility of influencing domain walls (more often than not in nanowires). However, although the micromagnetic simulations indeed showed that it was possible, the predicted threshold current needed for starting the displacement was much higher than what was experimentally measured.

The out-of-plane component was found[15, 47] to play an important role in domain wall motion, by destabilizing the wall, and thus reducing its threshold current. From a theoretical point of view, the solution consisted of including the out-of-plane torque in the LLG equation.

Originally, the in-plane torque was introduced as a term collinear to the damping. Depending on the sign of the torque, it could either balance it out, or increase it further. The out-of-plane was then introduced thanks to a single additional parameter  $\beta_\tau = -\tau_2/\tau_1$ , where  $\tau_1$  is the in-plane torque, and  $\tau_2$  is out-of-plane. The minus sign is to make it a positive value in most cases. In the end, this  $\beta_\tau$  is merely a scaling factor for the torque, allowing simpler notations. It is also consistent with the first additional term in the LLG equation, namely the Gilbert term, proportional to the Gilbert damping coefficient  $\alpha$ <sup>1</sup>.

### III - 6 ANGULAR DEPENDENCE OF THE TORQUE

According to Eq. (66), the simple picture of the Slonczewski torque gives a sinusoidal dependence of the torque with the angle that the polarization of the spin current

<sup>1</sup> Please note that the subscript  $\tau$  is not generally used in the literature, but it allows us to make a clear distinction between the out-of-plane torque factor, and the spin asymmetry of a material, see Section II - 2.

does with the magnetization of the magnetic layer. Although The derivation leading to this result gives the main contribution, it neglects one major aspect of any device. We assumed the existence of a spin-polarized current impacting a magnetic layer. In any device, such a spin current is created by placing a second (polarizing) magnetic layer before the one we want to act upon thanks to STT. And the presence of this first layer may change everything, because of the multiple reflections between the layers. In some extreme cases, those additional contributions may lead to a completely different angular dependence, where the torque vanishes for an intermediate angle  $0 < \theta_* < \pi$ . When this occurs, the torque is said to be “wavy”.

Such a wavy torque may lead to a steady-state precession, if the damping does not compensate. Depending on the sign of the current, this angle becomes a stable or unstable equilibrium position for the magnetization. Such a behavior has been reported and studied[48, 49, 50, 51, 17], because of the possibilities it offers to create spin-torque oscillators without the need of an external magnetic field.

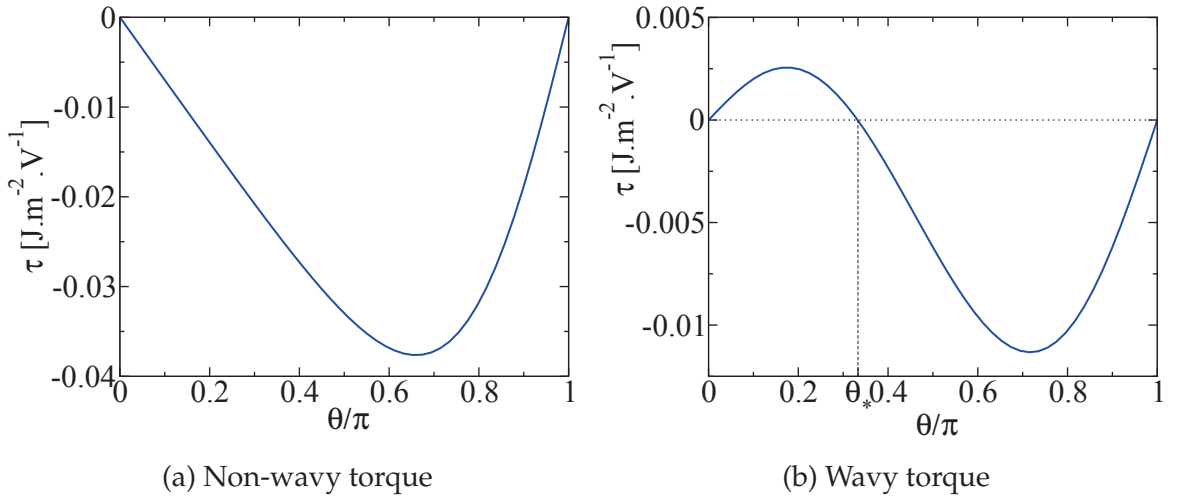


Figure 12.: Example of the angular dependence of the torque (measured on the second magnetic layer) in two difference stacks of the type  $\text{Cu}_{10}|\text{F}_{10}|\text{Cu}_{10}|\text{Py}_{10}|\text{Cu}_{10}$ , where F stands for Py (left plot) or Ni (right plot). The indices correspond to the thickness of the layer in nm. On the left plot, one can see the regular angular dependence of the torque with the angle  $\theta$ . However, on the right plot, this dependence is quite different, with the presence of an angle  $\theta_*$  where the torque goes to zero. It is then qualified as wavy, and  $\theta_*$  is the waviness angle.

In Ref[17], Waintal *et al.* presented a geometric criterion to determine whether the torque exerted on a magnetic layer is wavy or not. The system under consideration is a  $N|F_A|N|F_B|N$  multilayer (N is a normal metal, F is a ferromagnet). This criterion however works under some assumptions. First, mixing coefficients (describing transverse behavior, see Section V - 3.2) need to be small, which is the case in metallic systems. Second, the system must be thin enough so that spin-flip scattering can be neglected. The consequences of the first condition is that the torque is orthogonal to the magnetization of the relevant layer, while the second ensures that the spin currents on the outer normal layers are collinear to the adjacent magnetization.

The construction works by drawing the spin currents, which are collinear to their respective magnetization. Then, by applying the definition of the torque, we get the following expressions:

$$\vec{\tau}_{tot} = \vec{J}_A - \vec{J}_B \quad (67)$$

$$\vec{\tau}_A = \vec{J}_A - \vec{J}_N \quad (68)$$

$$\vec{\tau}_B = \vec{J}_N - \vec{J}_B \quad (69)$$

In those expressions,  $\vec{\tau}_{tot}$  is the total torque deposited on both magnetic layers,  $\vec{\tau}_A$  (resp.  $\vec{\tau}_B$ ) is the torque on layer A (resp. B), and  $\vec{J}_A, \vec{J}_B, \vec{J}_N$  are the spin currents in the normal layer respectively before layer A, after layer B, and between them. From those definitions, we get that  $\vec{\tau}_{tot} = \vec{\tau}_A + \vec{\tau}_B$ . Consequently, the total torque is found by drawing the vector going from the tip of  $\vec{J}_B$  to the tip of  $\vec{J}_A$ . As for the individual torque, they are found by drawing the orthogonal line to each spin current, and finding their intersection. Fig. 13 shows this construction.

In Fig. 13,  $\|\vec{J}_B\| > \|\vec{J}_A\|$ . The consequence of this is that  $\vec{\tau}_B$  can change its sign when  $\theta$  changes. Stated in another way, this also means that there is an angle  $\theta_*$  for which  $\vec{\tau}_B = 0$ . To the contrary, if  $\|\vec{J}_B\| < \|\vec{J}_A\|$ , it is obvious that the torque on layer B will never go to zero.

To obtain stronger spin currents on layer B, an obvious condition is to have very different materials making up each layer. As we shall prove mathematically in Section X - 2, the main parameter to consider is the spin asymmetry of the material. Within the same set of approximations, Ref[17] report a result that we obtained with a slightly different derivation (see Eq. (306)):

$$\cos \theta_* = \frac{\beta_A r_B + 1}{\beta_B r_B} \quad (70)$$

Where  $r_A$  and  $r_B$  are the equivalent resistance (per unit area) of the relevant magnetic layer, the neighboring outer normal layer, as well as the interface.  $\beta_A$  and  $\beta_B$

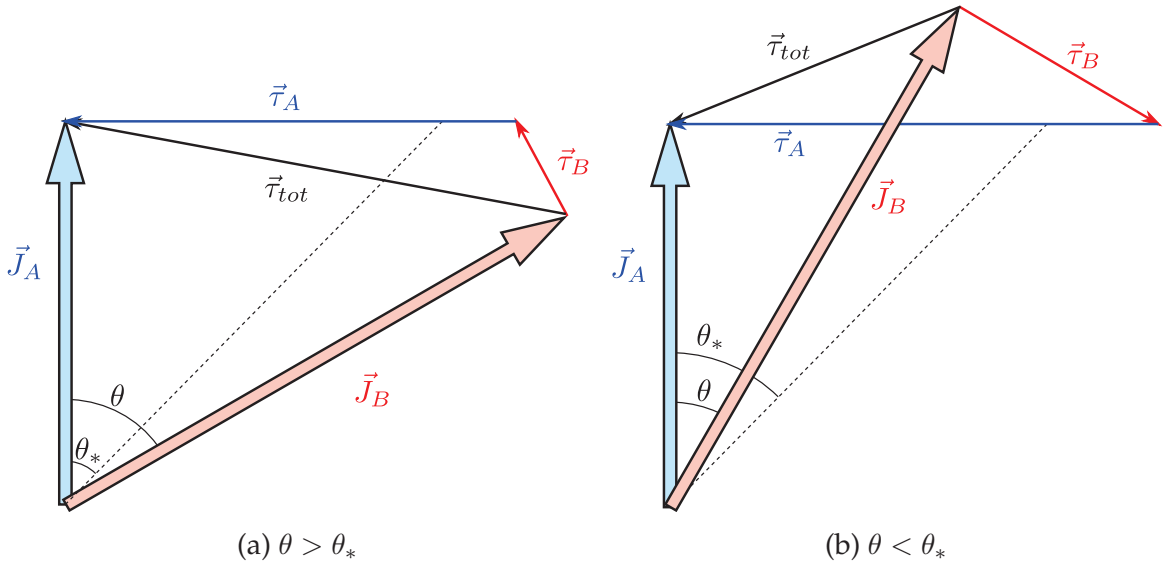


Figure 13.: Geometric construction for waviness. The current  $\vec{J}_A$  and  $\vec{J}_B$  are represented by the thick arrows, the torques by the thin ones. The torque is always orthogonal to the related current (within the relevant set of approximations, see text). The waviness angle  $\theta_*$  is the angle for which  $\vec{\tau}_B$  goes to zero.

are the equivalent spin asymmetry of the same group. The link between those quantities and the material parameters of the constituents will be introduced formally in Section VI - 5. Their consequence is simply that to obtain a wavy structure, layer B must be as polarized and as resistive as possible, while layer A must be weakly polarized, and have a lower resistivity. Of course, these conditions have to be balanced with the need to have a low critical current density. For instance, a thicker layer B means a higher resistance, which is beneficial to waviness. However a thicker magnetic layer means a higher total spin, and therefore more momentum needed for switching, which in the end translates to a higher critical current density.

We introduced in this section all the concepts and tools necessary to understand the physics of the spin-transfer torque that will be discussed in our results.

# IV

---

## THERMOELECTRICITY

---

In this section we will introduce some effects related to heat transport. In particular, we will describe the relevant thermoelectric effects for our consequent work. Namely, we introduce the Seebeck and Peltier effects, which have been known for over a century. Then, we will give their extension for ferromagnets, where the spin of the electron has an influence. This leads the way to the spin-dependent Seebeck and Peltier effects, discovered much more recently[4].

### IV - 1 SEEBECK AND PELTIER EFFECT

We first give an historical overview and description of the phenomena, then give a description of their main application, and finally give a simple derivation of the expression of the thermoelectric coefficients in the Landauer-Büttiker formalism, as well as their consequences.

After reviewing the history of those effects, we give a short description of the working principle of the main application of thermoelectricity as of yet, thermocouples. Then, we present the hopes for the future of thermoelectric effects in terms of energy production/gathering, and its main criterion, the figure of merit  $ZT$ .

#### IV - 1.1 *History of discovery*

The Seebeck effect describes the conversion of a temperature difference across a conductor into electricity. In 1821, the German-Estonian physicist Thomas Johann Seebeck found that a loop consisting of two different materials, soldered together to create two junctions, exerted an influence over a compass needle when one of the junctions was heated. He thought that the difference of temperature induced a magnetization in the metals, and called this effect thermomagnetism. However, two years before, Hans Christian Ørsted showed that an electrical current in a loop cre-

ates a magnetic field. Much to Seebeck's displeasure, he offered an explanation of Seebeck's discovery in terms of electrical currents. This interpretation, that we now know to be true, was rapidly accepted by the community, and was more aptly named the "thermoelectric effect". The formula for the voltage  $\Delta V$  created by a temperature  $T_0 + \Delta T$  across one metal  $X$ , where  $T_0$  is the room temperature is given by:

$$\Delta V_X = \int_{T_0}^{T_0 + \Delta T} S_X(T) dT \quad (71)$$

The voltage across a junction between two materials  $A$  and  $B$  is:

$$\Delta V = \Delta V_A - \Delta V_B = \int_{T_0}^{T_0 + \Delta T} (S_A(T) - S_B(T)) dT \quad (72)$$

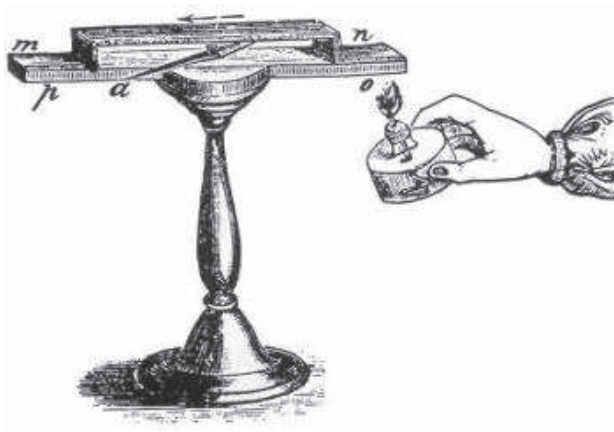


Figure 14.: Experimental setup used by Seebeck. Two different metals are soldered, creating two junctions. One of the junctions is heated while the other one stays at a lower temperature. The needle in the middle of the loop will align in response to the magnetic field induced by the current flowing in the loop. Retrieved from <http://www.ling.fju.edu.tw/hearing/historical%20review1821.htm>

The converse effect was discovered a few years later, in 1834, when Jean Charles Athanase Peltier found out that flowing a current would heat or cool a thermoelectric junction. In 1838, Heinrich Friedrich Emil Lenz showed that heat would be given or removed depending on the sign of the current. The law giving the heat flux per second is:

$$\dot{Q} = (\Pi_A - \Pi_B) I_{AB} \quad (73)$$

with  $\Pi_A$  ( $\Pi_B$ ), the Peltier coefficients, and  $I_{AB}$  the current across the junction from  $A$  to  $B$ .

#### IV - 1.2 Thermocouples

Nowadays, the Seebeck effect is used to create thermocouples. These devices allow for the inexpensive measurement of temperature differences. Another advantage is that it does not need any external source of energy. However, the accuracy is limited, and precision beyond the  $^{\circ}\text{C}$  is difficult to achieve[52].

A thermocouple works by creating a junction between two wires of dissimilar conductors and applying heat to it. The other end of the wire is kept at room temperature, and the voltage measured between the two ends of the wires gives the temperature difference, knowing the Seebeck coefficients of the pair of materials.

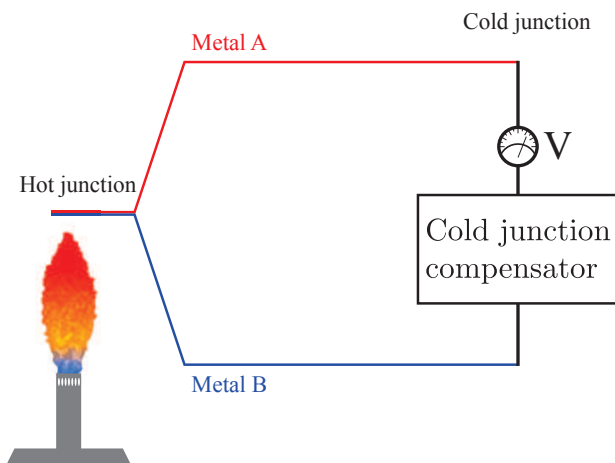


Figure 15.: Working principle of a thermocouple, with its cold junction compensator. Two different metals are connected and heated on one side. On the other side, kept at room temperature, a voltage proportional to the temperature difference builds up. The cold junction compensator allows for the conversion from voltage to temperature, taking into account the influence of the room temperature.

In practice, the Seebeck coefficients vary with temperature, and are tabulated at  $0^{\circ}\text{C}$ . Therefore, in order to make the conversion from voltage to temperature difference, a map between the current room temperature and the tabulated coefficients needs to be provided. An integrated circuit called a cold junction compensator provides a voltage corresponding to the thermocouple voltage between  $0^{\circ}\text{C}$  and the room temperature. Using this additional voltage, the temperature difference can be

extracted. However, because this method matches the actual behavior of the thermocouple to a tabulated curve, an error is introduced in the resulting temperature measurement.

The simplicity of the device, as well as the large range of operating temperatures (from  $-270^{\circ}\text{C}$  up to almost  $2000^{\circ}\text{C}$ , depending on the materials[53]) still make thermocouple popular ways of measuring temperature in science, industry, but also for home and office thermostats and security devices.

#### IV - 1.3 Microscopic origin

In this section, we aim at providing a simple model to explain the origin of the thermo effects, and an expression of the coefficients in terms of microscopic quantities.

Let us consider a piece of scattering material  $S$  connected to two reservoirs at thermal equilibrium. Each reservoir has a given temperature  $\theta = k_B T$  and electrochemical potential  $\mu$ .

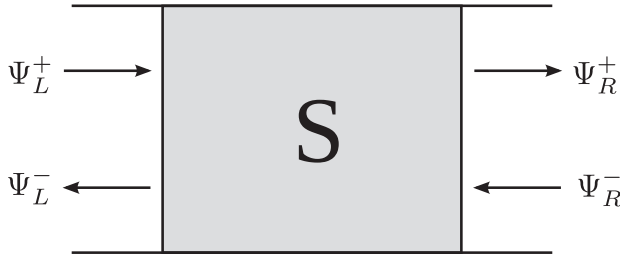


Figure 16.: Cartoon of the scatterer  $S$  with the two reservoirs (grayed) and their respective potential and temperature.

We use the Landauer formalism to describe the quasi-one dimensional transport through the scatterer. We are interested in the electrical current  $I$  and the heat current  $I_Q$ .

An incoming electron at energy  $E$  contributes an amount  $dI_{inc}$  to the current. For a unidimensional conductor, this current is:

$$dI_{inc} = ev_F \frac{dn}{dE} \delta E \quad (74)$$

$n$  is the density of state per unit length, therefore  $\frac{dn}{dE} \delta E$  is the number of states per unit length, at energy  $E$ .

$$\frac{dn}{dE} = \frac{dn}{dk} \frac{dk}{dE} \quad (75)$$

We use the relation  $\frac{dE}{dk} = \frac{1}{\hbar}v_F$ , and periodic boundary conditions to evaluate  $\frac{dn}{dk}$ .

$$e^{ik_nL} = 1 \Rightarrow k_n = \frac{2\pi n}{L}, n \in \mathbb{N} \quad (76)$$

(negative  $n$  give electrons propagating in the other direction). This gives  $\frac{dn}{dk} = \frac{1}{2\pi}$ . It is worth noticing that in (quasi-)1D systems, the energy does not depend on the channel. Finally, we obtain:

$$dI_{inc} = \frac{e}{h}dE \quad (77)$$

Similarly, one state gives a contribution  $dI_E = \frac{1}{h}E\delta E$  to the energy current.

To get the total current we need the probability to find an electron at the energy  $E$ , given by the Fermi-Dirac function  $f(\mu, \theta, E) = 1/(1 + \exp[-(E - \mu)/\theta])$ . Finally, the total transmission of the scatterer is given by the contribution of each of its channels through  $\mathbb{T}(E) = \text{Tr}(t^\dagger t)$ , where  $t$  is its transmission matrix.

The transport through  $S$  is given, in the Landauer formalism, by:

$$I = \frac{2e}{h} \int \mathbb{T}(E) \left[ f(\mu_1, \theta_1, E) - f(\mu_2, \theta_2, E) \right] dE \quad (78)$$

$$I_E = \frac{2}{h} \int E \mathbb{T}(E) \left[ f(\mu_1, \theta_1, E) - f(\mu_2, \theta_2, E) \right] dE \quad (79)$$

with  $I$ , the electrical current and  $I_E$  the energy current through  $S$ . In order to get the heat current, one has to use the thermodynamics identity  $dE = TdS + \mu dn$ . This means that the heat current is the part of the energy current that is not proportional to the electrochemical potential. Let us use the following change of variables:

$$\theta = (\theta_1 + \theta_2)/2 \quad (80)$$

$$\delta\theta = \theta_1 - \theta_2 \quad (81)$$

$$\mu = (\mu_1 + \mu_2)/2 \quad (82)$$

$$\delta\mu = \mu_1 - \mu_2 \quad (83)$$

Assuming low enough temperatures, we also use the Sommerfeld expansion, given by:

$$f(\mu_i, \theta_i, E) = \Theta(\mu_i - E) - \frac{\pi^2}{6}\theta_i^2\delta'(E - \mu_i) \quad (84)$$

In the limit of the linear response, we evaluate the contribution of a difference in either potential or temperature on the two currents  $I$  and  $I_E$ .

A)  $\mu_1 = \mu_2$ ,  $\theta_1 > \theta_2$

By simply replacing 84 in 78, we get:

$$I = -\frac{\pi^2 2e}{6 h} \int \mathbb{T}(E)(\theta_1^2 - \theta_2^2) \delta'(E - \mu) dE \quad (85)$$

This gives after using the definition of the  $\delta'$  distribution:

$$I = \frac{2e \pi^2}{h 3} \frac{\partial \mathbb{T}}{\partial E}(\mu) \theta \delta \theta \quad (86)$$

This means that a temperature gradient can give rise to a current if and only if the transmission depends on energy. As for the energy current:

$$I_E = -\frac{\pi^2 2}{6 h} \int E \mathbb{T}(E)(\theta_1^2 - \theta_2^2) \delta'(E - \mu) dE \quad (87)$$

$$= \frac{2 \pi^2}{h 3} \left( \underbrace{\mu \frac{\partial \mathbb{T}}{\partial E}(\mu)}_{\propto \mu dn} + \mathbb{T}(\mu) \right) \theta \delta \theta \quad (88)$$

From this expression, we finally extract the heat current, using the criterion mentioned at the beginning of this section:

$$I_Q = \frac{2 \pi^2}{h 3} \mathbb{T}(\mu) \theta \delta \theta \quad (89)$$

B)  $\mu_1 > \mu_2$ ,  $\theta_1 = \theta_2$

The same derivation as before, keeping only the lowest order of the Sommerfeld expansion, gives as well the expressions for the current and energy current:

$$I = \frac{2e}{h} \mathbb{T}(\mu) \delta \mu \quad (90)$$

$$\begin{aligned} I_E &= \frac{2}{h} \mu \mathbb{T}(\mu) \delta \mu + \frac{2 \pi^2}{h 6} \theta^2 \left[ \frac{\partial}{\partial E} (E \mathbb{T}) \right]_{\mu_2}^{\mu_1} \\ &= \frac{2}{h} \left( \mathbb{T}(\mu) + \frac{\pi^2}{6} \frac{\partial^2 \mathbb{T}}{\partial E^2}(\mu) \right) \mu \delta \mu + \frac{2 \pi^2}{h 3} \theta^2 \frac{\partial \mathbb{T}}{\partial E}(\mu) \delta \mu \end{aligned} \quad (91)$$

Once again ignoring terms proportional to  $\mu$ , we obtain:

$$I_Q = \frac{2 \pi^2}{h 3} \theta^2 \frac{\partial \mathbb{T}}{\partial E}(\mu) \delta \mu \quad (92)$$

Finally, we can summarize the thermoelectric transport with:

$$\begin{pmatrix} I \\ I_Q \end{pmatrix} = \frac{2}{h} \begin{pmatrix} e\mathbb{T}(\mu) & e\frac{\pi^2}{3}\theta\frac{\partial\mathbb{T}}{\partial E}(\mu) \\ \frac{\pi^2}{3}\theta^2\frac{\partial\mathbb{T}}{\partial E}(\mu) & \frac{\pi^2}{3}\theta\mathbb{T}(\mu) \end{pmatrix} \begin{pmatrix} \delta\mu \\ \delta\theta \end{pmatrix} \quad (93)$$

Of course, we recover the well known result  $G = \frac{2}{h}e^2\mathbb{T}$ . Because the conductance depends on the length of the sample, we prefer expressing Eq. (93) in terms of local current densities and conductivities. Simply noting that  $G = \sigma\Sigma/L$ , where  $\Sigma$  is the cross section and  $L$  is the length of the sample. We take the limit of small  $L$  and easily relate the current densities to the local voltage and temperature gradients:

$$\begin{pmatrix} J \\ J_Q \end{pmatrix} = - \begin{pmatrix} \sigma & \sigma S \\ \sigma\Pi & \kappa \end{pmatrix} \begin{pmatrix} \partial V \\ \partial T \end{pmatrix} \quad (94)$$

With this formulation, we obtain the microscopic expression of the macroscopic thermoelectric coefficients:

$$S = \frac{\pi^2}{3} \frac{k_B^2}{e} T \frac{\partial \ln \sigma}{\partial E} \quad (95)$$

$$\Pi = ST \quad (96)$$

$$\kappa = \frac{\pi^2}{3} \left( \frac{k_B}{e} \right)^2 \sigma T \quad (97)$$

Eq.(95) is the microscopic definition of the Seebeck coefficient, Eq.(96) illustrates one of the Onsager reciprocal relations between the Seebeck and Peltier effects, and finally Eq.(97) is known as Wiedemann-Franz' law. It is worth noting that during the derivation, we assumed that heat was transported by electrons only, which is the limit of validity of Wiedemann-Franz' law. A more complete description of heat transport would need to include the contribution of phonons, magnons, *etc.* In particular, this description is not enough to describe the spin Seebeck effect [54, 55, 56]. Similarly, some thermoelectric effects like the Nernst effect require a special treatment, because of the influence of an external magnetic field.

Finally, we give in Table 2 a list of the Seebeck coefficient for various materials:

material	$S$ [ $\mu\text{V} \cdot \text{K}^{-1}$ ]	$s$ [ $k_B/e$ ]
Ag	1.4	0.0163
Al	-1.7	-0.0197
Au	1.6	0.0186
Bi	-69.3	-0.804
Cd	3.3	0.0383
Co	-22	-0.232
Cu	1.9	0.022
Fe	13.7	0.159
Hg	-5.7	-0.0661
K	-15.1	-0.175
Mg	-1.3	-0.0151
Mo	6.3	0.0731
Na	-7.8	-0.0905
Ni	-22.1	-0.256
Ni <sub>80</sub> Fe <sub>20</sub> (Permalloy)	-18	-0.232
Ni <sub>43</sub> Cu <sub>56.5</sub> Mn <sub>0.5</sub> (Copel)	-39.3	-0.456
Ni <sub>45</sub> Cu <sub>55</sub> (Constantan)	-39.3	-0.456
Ni <sub>80</sub> Cr <sub>20</sub> (Nichrome)	16.7	0.193
Ni <sub>90</sub> Cr <sub>10</sub> (Chromel)	22.7	0.263
Ni <sub>95</sub> Mg <sub>2</sub> Al <sub>2</sub> Si <sub>1</sub> (Alumel)	-18.6	-0.216
Pb	-1.3	-0.0151
Pd	-10.2	-0.118
Pt	-5.7	-0.0661
Sb	41.7	0.484
Sn	-1.5	-0.0174
W	2.3	0.0267
Zn	1.8	0.209

Table 2.: Values of the Seebeck coefficients for a variety of metals and common thermoelectric alloys. The coefficients are given both in SI units and in reduced form, in values of  $k_B/e = 8.617 \cdot 10^{-5} \mu\text{V} \cdot \text{K}^{-1}$ , and at room temperature. Values are taken from [57], except for the values for Co and Ni<sub>80</sub>Fe<sub>20</sub>, which are taken from [58]

IV - 1.4 *Figure of merit ZT*

A review on thermoelectricity would not be complete without at least a word on the much discussed figure of merit  $ZT$ . Thermoelectric effects are under of lot of investigation for their potential to harness energy out of heat waste. For example, only 30%<sup>[59]</sup> of the energy created by fuel combustion in a car engine is actually put to use (vehicle mobility and accessories). Thermal solar energy is another path where thermoelectrics would be of use. With this in mind, it seems highly relevant for people to investigate new materials and systems to put all these sources of heat to use.

We all know that thermoelectric systems have been so far highly inefficient to produce energy. But what does this mean ? What makes a thermoelectric material a good or bad candidate for energy production ? An ideal thermoelectric material has the following properties:

- a high Seebeck coefficient, to convert heat into as much electricity as possible
- a high electrical conductivity, so that the electricity produced by the Seebeck effect is not lost directly into the material
- a poor thermal conductivity, to maintain for as long as possible the temperature difference fueling the electricity production

When estimating the efficiency of a thermoelectric system<sup>[60]</sup>, a ratio  $Z$  naturally arises as a scaling parameter. Since this ratio as the dimension of the inverse of a temperature, it is more convenient to use the dimensionless product  $ZT$  as reference, or figure of merit, to describe the quality of the thermoelectric system. This number has the following expression:

$$ZT = \frac{\sigma S^2 T}{\kappa} = \frac{\sigma S \Pi}{\kappa} \quad (98)$$

The maximum efficiency of this system is a function of  $ZT$ , and of the temperatures of the hot ( $T_H$ ) and of the cold ( $T_C$ ) sides. It has the following expression:

$$\eta_{max} = \frac{\sqrt{1 + ZT} - 1}{\sqrt{1 + ZT} + \frac{T_C}{T_H}} \eta_C \quad (99)$$

with  $\eta_C = (T_H - T_C)/T_H$  the Carnot efficiency. There is no theoretical limit to  $ZT$ , and the higher its value, the closer to the Carnot efficiency the system is. The highest

THERMOELECTRICITY

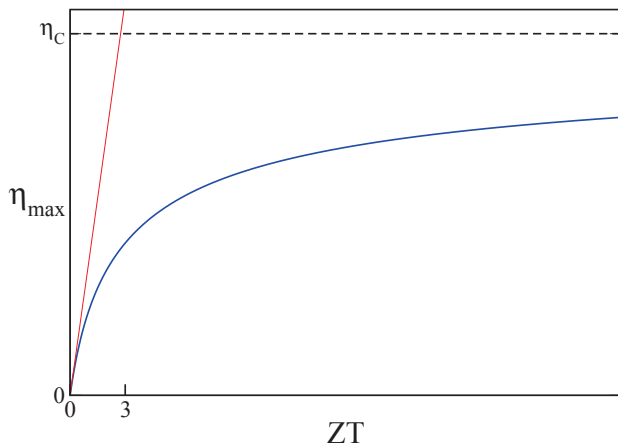


Figure 17.: Thermoelectric efficiency as a function of  $ZT$ . The function eventually saturates at the Carnot efficiency  $\eta_C$ . It is linear for small values of  $ZT$ , as indicated by the tangent at the origin (in red).

value reported to day is 2.6[61] at 923 K along the  $b$  direction of a SnSe single crystal. Values of  $ZT > 3$  are necessary to consider using thermoelectricity as a mean to gather energy.

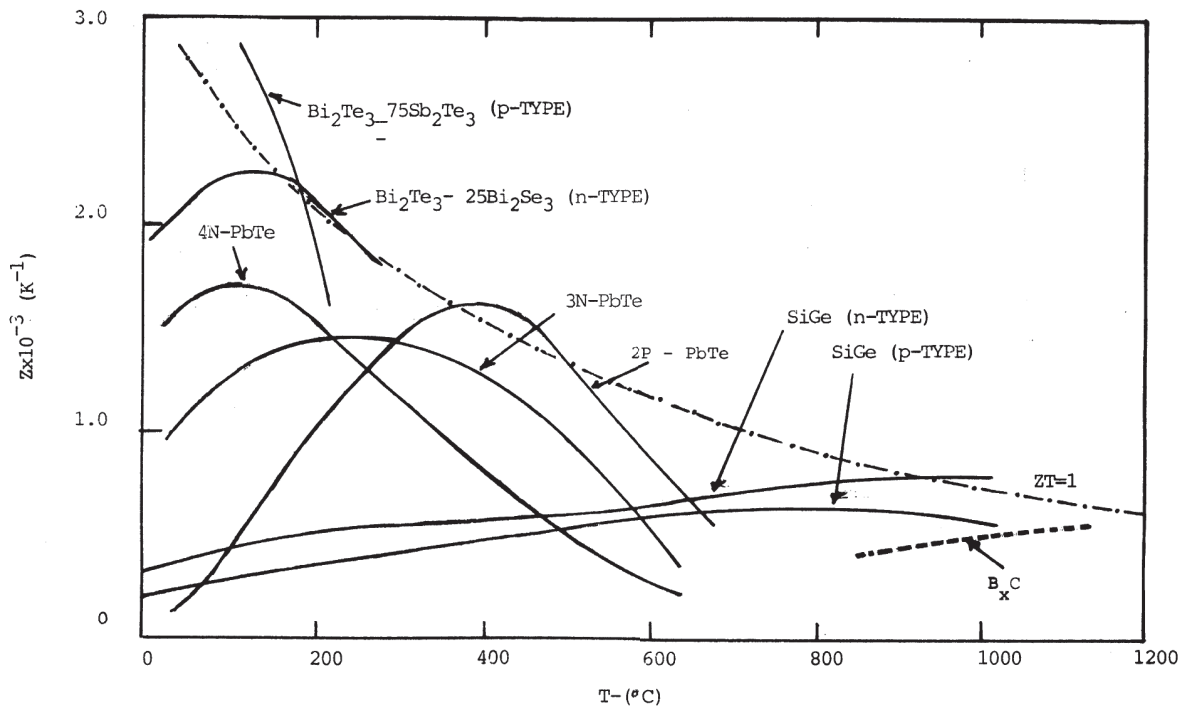


Figure 18.: Values of  $Z$  against  $T$  for common thermoelectric materials, taken from [60]. The dashed line corresponds to  $ZT = 1$ .

## IV - 2 SPIN-DEPENDENT SEEBECK EFFECT

We introduce here the building block of most of the present work, namely spin-dependent thermoelectric effects. Where the Seebeck effect is the voltage resulting from a temperature gradient, the spin-dependent Seebeck effect induces spin accumulation from the same input.

We start by giving an historical overview of the concept and its origin. We then present an experimental setup designed to measure the value of the new coefficients. We finish by giving an outlook as well as some state-of-the-art results that are yet to be published.

IV - 2.1 *Justification of the theory*

Although the name of spin-dependent Seebeck (and Peltier) effect is recent[5, 6], the basic concept was published almost twenty years earlier[4]. Although the idea was not formulated in the current simpler form, Johnson and Silsbee already explained in 1987 there that an temperature gradient can induce a magnetization current. Gravier *et al.* showed in 2006, using an extended version of the two-currents model (simply called the “three-currents model”, to emphasize the analogy) that a temperature gradient can induce a spin current<sup>1</sup>. Let us now present an informal, but intuitive way of introducing these concepts.

In the simple two-currents model used to describe the longitudinal spintronics effects, one uses the fact that the electrical conductivity (and resistivity) of a ferromagnetic metal depends on the spin species. Therefore, the quantities  $\sigma_{\uparrow}$  and  $\sigma_{\downarrow}$  are introduced, and everything works as if the two spin channels were separate, or as if two different materials in parallel were used (this holds as long as spin-flip processes are ignored).

The microscopic definition of the electrical conductivity given by Eq. (93) indicates that, through the transmission coefficient of the scatterer, the conductivity depends on the density of states of the material. Since in ferromagnets this density of states depends on spin, each spin species has its own conductivity.

The same equation indicates that the thermoelectric coefficients should also depend on spin. However, while the conductivity depends on the density of states that matters, the thermoelectric coefficients depend on its energy derivative, see Fig. 20

---

<sup>1</sup> Of course both articles also mention the converse effect, where a certain potential related to the magnetization can create a heat current.

for example. Assuming a similar conductivity matrix as Eq. (94), we include the spin dependence, and obtain:

$$\begin{pmatrix} J_{\uparrow} \\ J_{\downarrow} \\ J_Q \end{pmatrix} = \begin{pmatrix} \sigma_{\uparrow} & 0 & \sigma_{\uparrow} S_{\uparrow} \\ 0 & \sigma_{\downarrow} & \sigma_{\downarrow} S_{\downarrow} \\ \sigma_{\uparrow} \Pi_{\uparrow} & \sigma_{\downarrow} \Pi_{\downarrow} & \kappa \end{pmatrix} \begin{pmatrix} \partial\mu_{\uparrow}/e \\ \partial\mu_{\downarrow}/e \\ -\partial T \end{pmatrix} \quad (100)$$

Let us first clarify an important point. The exact same arguments we used to justify the existence of a spin-dependence of the thermoelectric coefficients should point at a spin-dependence of the thermal conductivity, and at the same time, at the existence of one temperature per spin channel, the same way the chemical potential depends on the spin. Some experiments[62] do indicate the presence of a spin-dependent temperature, though in the conditions we consider (in particular the fact that we describe diffusive systems), there is enough spin-conserving scattering like electron-electron interaction, or electron-phonon interaction to provide thermalization, and therefore consider only one temperature[63, 64, 62]. Very low temperatures and very clean samples are needed to observe the effect of spin temperatures, and measurements only show corrections to the main effect (10% of the applied temperature gradient in Ref[62]).

The derivation in the previous section gave back one of the Onsager relations, namely  $\Pi = ST_{av}$ . The same result can be obtained by using the methodology described by Onsager. Moreover, the exact same calculation, but taking spin into account, gives us the spin-dependent equivalent  $\Pi_{\uparrow} = S_{\uparrow} T_{av}$  and  $\Pi_{\downarrow} = S_{\downarrow} T_{av}$ . Therefore, from now on, we will abandon the notation involving the Peltier coefficients, and focus solely on the Seebeck coefficients, keeping in mind how closely they are related.

We introduce now some notations and writing conventions. First, we separate the spin-dependent Seebeck coefficients into a spin-independent part  $S$ , and a purely spin-related part  $\Delta S$ , as:

$$S_{\uparrow\downarrow} = S_* \pm \Delta S \quad (101)$$

We also introduce so-called dimensionless Seebeck numbers  $s$  and  $\Delta s$ , so that:

$$S = s \frac{k_B}{e} \quad (102)$$

$$\Delta S = \Delta s \frac{k_B}{e} \quad (103)$$

One important thing to note is that  $S$  is not what is measured in a standard Seebeck experiment. This can be clearly seen in Eq. (100). Let us assume that a temperature gradient is applied on a piece of ferromagnetic material. The charge current therefore is:

$$J_c = J_{\uparrow} + J_{\downarrow} = -(\sigma_{\uparrow}S_{\uparrow} + \sigma_{\downarrow}S_{\downarrow})\partial T \quad (104)$$

we also know, from Eq. (94) that:

$$J_c = -\sigma S_c \partial T \quad (105)$$

Here we noted  $S_c$  the total “charge” Seebeck coefficient, to emphasize that it is not the spin-independent part of  $S_{\uparrow}$  and  $S_{\downarrow}$ . By identification, we find that:

$$S_c = \frac{\sigma_{\uparrow}S_{\uparrow} + \sigma_{\downarrow}S_{\downarrow}}{\sigma_{\uparrow} + \sigma_{\downarrow}} \quad (106)$$

#### IV - 2.2 Experimental demonstration

Recently, some values for the spin-dependent Seebeck coefficients have been measured in metals. A group at Delft University prepared a device allowing them to extract the value of the spin-dependent Seebeck coefficient of a ferromagnet[58].

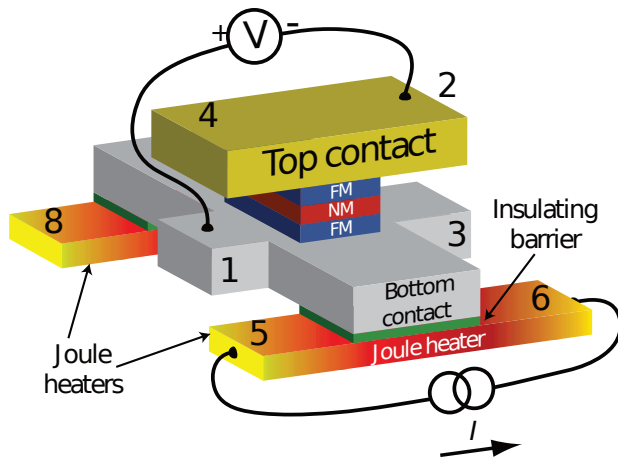


Figure 19.: Sketch of the device used by van Wees *et al.* to measure the spin-dependent Seebeck coefficient, as published in Ref[58]

This twofold experiment is performed in a lock-in setup, where they inject a low frequency (17 Hz) AC current  $I$ , and record the first and second harmonic of the measured voltage on each of the probes.

First, they perform a four-probes resistance measurement of the spin-valve as a function of the applied magnetic field. This gives them a measure of the polarization  $\beta$  of the ferromagnet.

Next, they perform a thermal spin injection measurement, where they flow a current in the heating lines (noted “Joule heaters” on Fig. 19). Since heat comes from Joule heating, it is proportional to  $I^2$ . The Seebeck signal is therefore contained in the second harmonic of the signal.

To extract the value of the spin-dependent thermoelectric coefficients, one needs to know the temperature gradient over the sample. Since it is not possible to probe it directly, van Wees *et al.* relied on a numerical simulation to estimate it. Knowing the material parameters from measurement, or from the literature, they used a finite elements model, with the spin polarization of the Seebeck coefficient as the only fitting parameter, to extract its value from their measurements. They found a value of  $\Delta S = -4.5\mu\text{V} \cdot \text{K}^{-1}$  for permalloy, and  $\Delta S = -1.68\mu\text{V} \cdot \text{K}^{-1}$  for cobalt.

#### IV - 2.3 Outlook

Because the Seebeck coefficients depend on the energy derivative of the transmission, it can have either sign, see Table 2. Furthermore, since the spin-dependent Seebeck coefficients depend on the derivative of the transmission of the relevant spin species, at least mathematically, nothing prevents  $S_{\uparrow}$  and  $S_{\downarrow}$  to be of opposite signs. Nickel is a very good candidate for such property thanks to the peak in the density of states of the minority electrons at the Fermi level, see Fig. 20. However, no measurement or numerical prediction has been made so far for this material.

Some results came to our knowledge during the writing of this thesis, regarding a material exhibiting several properties of utmost interest. The group of Kimura *et al.* [66] measured the spin-dependent properties of the Heusler alloy  $\text{Co}_{45}\text{Fe}_{52}\text{Al}_3$  and found two very interesting and original features. Their measurements indicate that their material has  $S_{\uparrow} = -35\mu\text{V} \cdot \text{K}^{-1}$  and  $S_{\downarrow} = 36\mu\text{V} \cdot \text{K}^{-1}$ . This gives an example material of the property we expect in nickel, the opposite signs for the majority and minority Seebeck coefficient. What is also striking in those values is their amplitude. Published values in metals so far indicated low values for  $\Delta s$  (0.044 for Py, 0.02 for Co). This material has a reported value higher than 0.4. This is a factor of ten higher than whatever else measured before. This is very reassuring for the future of spin caloritronics, and in all-metallic systems in particular.

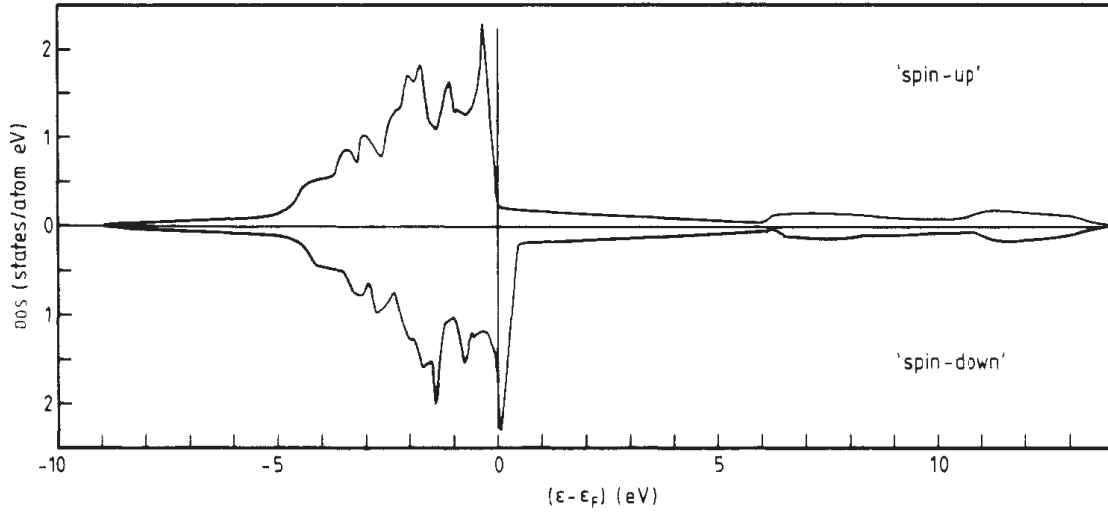


Figure 20.: Spin-split density of states for Nickel, as published in [65]. The vertical line at the zero abscissa corresponds to the Fermi level.

#### IV - 2.4 Spin Seebeck effect: a clash of vocabulary

Finally, it would be useful to clarify an important point of vocabulary that has, and still leads to many confusions. What has been presented so far was the so-called spin-dependent Seebeck effect. The term magnetoSeebeck effect can also be found in the literature[67]. Another effect with an unfortunately close name has been reported, the spin Seebeck effect.

This effect, is the observation of an electromotive force in a paramagnetic contact to a ferromagnetic material (either conductive[55, 68], insulating[56], or (ferromagnetic) semi-conducting[69]), in the presence of a temperature gradient. Two geometries exist, called transverse and longitudinal. The direction of the respective vectors differ depending on geometry, as can be seen on Fig. 21

As Fig. 21 suggests, the electromotive force is a result of the inverse spin Hall effect, where the trajectories of spins up and down are bent in opposite directions, thanks to the spin-orbit interaction. This indicates that a heavy metal as paramagnet is preferable if one wants to measure a strong signal.

The reason of the creation of the spin current, in the first place, is currently thought to be a thermal imbalance between the magnon temperature and the electron/phonon temperature. For a more detailed review beyond the scope of this thesis, one can read Ref[67] and included references.

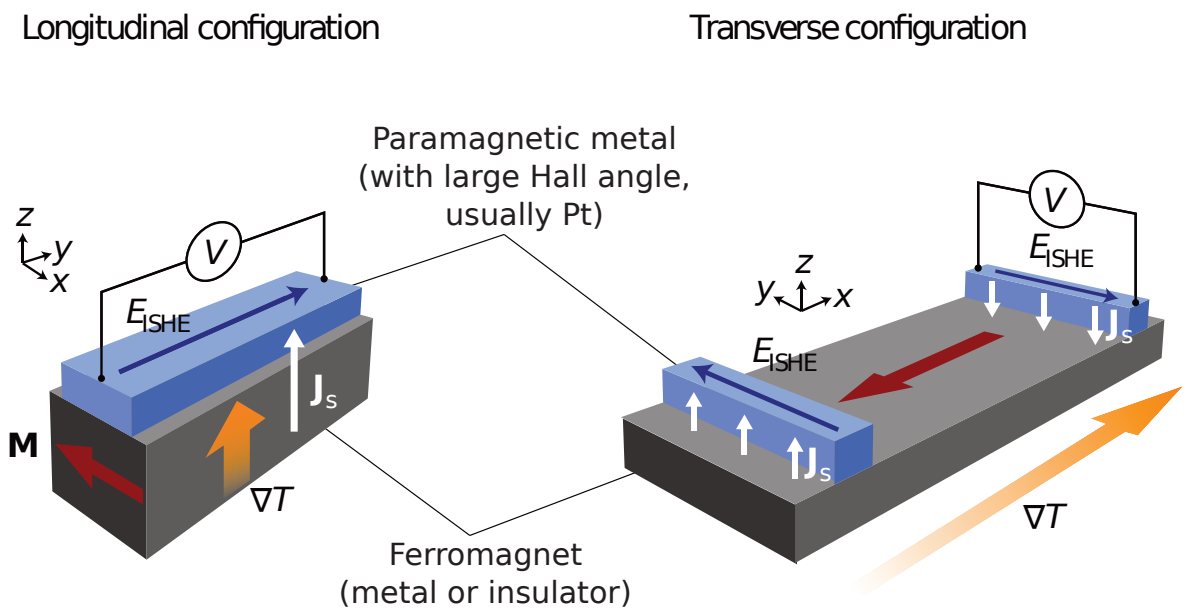


Figure 21.: Spin Seebeck geometries and orientation of the various vectors. Picture adapted from [67].  $J_S$  is the spin current,  $E_{ISHE}$  the inverse spin Hall effect electromotive force,  $M$  the magnetization.

## Part B

### DESCRIPTION OF OUR SEMI-CLASSICAL THEORY



### Summary of Part B

The first and main result of this thesis is the completion of a theory describing electron transport in ferromagnetic systems. More specifically, we focused on the the transport of charge, spin and heat by the electrons, in a diffusive regime. The story of our theory is summarized in Fig. 22.

Our theory, the Continuous Random Matrix Theory (CRMT) is a semi-classical description of electron transport in solid-state devices, originally based on the Landauer-Büttiker scattering formalism. A coherent quantum system is described by a scattering matrix  $S$ , made of the the probability amplitudes of transmission and reflection of an electron in each channel.

Assuming a system with many channels and applying a random matrix theory on this  $S$  matrix allowed us to get a semi-classical description, while retaining some quantum features, such as the spin of the electron and the Sharvin resistance (the resistance arising at the leads). At this point, a system is described by a  $8 \times 8$   $\hat{S}$  scattering matrix where the elements describe the probability of an electron to be transmitted or reflected in a given spin state.

By dividing a system into slices, each described by a  $\hat{S}$  matrix, we proved the equivalence of our theory with the generalized Circuit Theory[10]. Then, by making those slices small, we obtained a continuous theory. Using an appropriate scheme to describe rotations in spin space and a change of variables, it was possible to transform our matrix equations into a set of drift-diffusion differential equations. These equations, so far derived for a 1D conductor, were then extended to properly describe systems of any dimensionality.

Finally, we extend those equations further by adding the effect of a temperature gradient through heat transport, thermoelectric effects, and the more recent spin-dependent thermoelectric effects.

In the end, we obtain a set of six equations. Three of them are conservation (or continuity) equations for the charge, spin and heat currents. In particular, spin currents are not conserved due to spin-flip scattering (spin given to the lattice) and spin filtering (spin given to the surrounding magnetization). The other three equations relate those currents to the charge and spin-resolved potential as well to the temperature in an Ohm-like (or Fourier-like) fashion. The charge and heat variables are scalar, while the spin current and potential are vectors in spin space.

## THERMOELECTRICITY

### Résumé de la Partie B

Le premier, mais aussi le plus important des résultats de cette thèse est la complétion d'une théorie décrivant le transport électronique dans les systèmes ferromagnétiques. Plus spécifiquement, nous nous sommes concentrés sur le transport de la charge, du spin et de la chaleur par les électrons dans le régime diffusif. L'histoire de notre théorie est résumée dans la Fig. 22.

Notre théorie, la Continuous Random Matrix Theory (CRMT) est une description semi-classique du transport électronique dans les systèmes de matière condensée, basée sur le formalisme de Landauer-Büttiker. Un système quantique cohérent est décrit par une matrice de scattering  $S$ , composée des amplitudes de probabilité de transmission et de réflexion d'un électron dans chaque canal.

Dans le cas d'un système avec de nombreux canaux, et en appliquant une théorie de matrices aléatoires sur la matrice  $S$ , nous obtenons une description semi-classique tout en conservant certaines propriétés quantiques, comme le spin et la résistance de Sharvin (la résistance entre les réservoirs et le reste du système). A ce niveau, un système est décrit par une matrice de scattering  $\hat{S}$  de dimension  $8 \times 8$  dont les éléments décrivent les probabilités d'un électrons d'être transmis ou réfléchis dans un état de spin donné.

En découpant un systèmes en tranches, chacune décrite par une matrice  $\hat{S}$ , nous avons prouvé l'équivalence de notre théorie avec la circuit theory généralisée[10]. Ensuite, en prenant la limite infinitésimale de la taille des tranches, nous obtenons une théorie continue. En utilisant une technique adaptée pour décrire les rotations dans l'espace des spins, et en utilisant un changement de variables, il a été possible de transformer nos équations matricielles en une série d'équations différentielles de diffusion. Ces équations, jusque là dérivée dans le cas d'un système 1D, ont ensuite été étendues pour décrire convenablement des systèmes de n'importe quelle dimension.

Enfin, nous étendons encore plus loin ces équations en y ajoutant l'effet d'un gradient de température à travers le transport de chaleur, les effets thermoélectriques, et les effets thermoélectriques récemment découverts.

Au final, nous obtenons un ensemble de six équations. Trois d'entre elles sont des équations de conservation (ou de continuité) pour les courants de charge, de spin et de chaleur. En particulier, les courants de spin ne sont pas conservés à cause de l'effet de spin-flip scattering (relaxation des spins en faveur du réseau) et du filtrage de spin (le spin est donné à l'aimantation ambiante). Les trois autres équations relient ces courant aux potentiels de charge et de spin, ainsi qu'à la température, le tout selon un processus rappelant la loi d'Ohm (ou de Fourier). Les variables liées à la charge et à la chaleur sont scalaires, alors que les courants et potentiels de spin sont des vecteurs dans l'espace des spins.



---

## THE STATE OF THE THEORY BEFORE THIS THESIS

---

### V - 1 ORIGIN OF THE THEORY

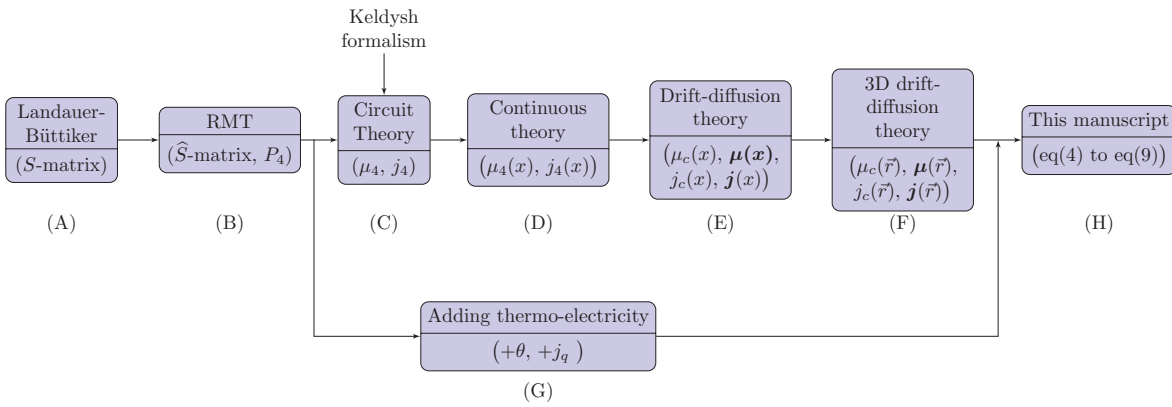


Figure 22.: Evolution and origin of the Continuous Random Matrix Theory, up to the state presented in this manuscript, the Generalized Drift-Diffusion Theory. A box corresponds to a milestone in the evolution of CRMT. Each box represents a theory in its own right, and contains its name, as well as its main variables. See text for details on each box, labeled (A)-(H)

The history of the Continuous Random Matrix Theory (CRMT)[70, 17] has known many milestones, each one corresponding to a full-fledged theory of its own. We sum up those theories in Fig. 22, each box corresponding to a given theory. In the following summary, we indicate the correspondence with Fig. 22 by giving the name of the relevant box.

The theory presented in this manuscript originates from the (fully quantum) Landauer-Büttiker formalism, where the modes going out of a scatterer are linked to the incoming ones through a scattering matrix  $S$  (**box A**). Each spin direction and

each channel is individually described, and quantum effects such as weak localization and universal conductance fluctuations are perfectly taken into account. The validity of this theory also extends further than the field of spintronics, since it can be used to describe involving superconductivity, quantum dots and so on[71].

By applying a form of the Random Matrix Theory (**box B**), one obtains a semi-classical framework linking the incoming and outgoing spin states instead of the wave function of each channel. The dimension of the variables are therefore reduced from  $N_{\text{ch}}$  to 4 (one for the charge, three for each spin direction). This link is made through a  $8 \times 8 \hat{S}$  matrix. Where a coefficient in the Landauer-Büttiker described the transmission or reflexion probability amplitude from a channel to another, a coefficient in this  $\hat{S}$  matrix only considers the incoming and outgoing spin state. Those assumptions make some of the coefficients (corresponding to quantum coherences) negligible.

By dividing the scatterer into smaller parts, each described by a  $\hat{S}$  matrix, and by operating a very simple change of variables, one can prove the equivalence of our theory to the successful (generalized) Circuit Theory [10] (**box C**). As indicated in Fig. 22, the Circuit Theory was originally derived from the Keldysh formalism. This is in this step that the concepts of currents and potentials arise.

The natural next step was to make those slices small, consider the continuous limit, and obtain (matrix) differential equations (**box D**). By matching those differential equations to the Valet-Fert theory, it was possible to parametrize the  $\hat{S}$  matrix with known and tabulated for the most part (the only exception being the mixing parameters, describing the behavior of a spin transverse to the magnetization).

This thesis started at this point, and the next step was to expand the matrix equations into a set of differential equations linking observables (charge and spin currents and potentials), for any magnetic texture (**box E**). This was made possible by choosing the right matrix basis and applying to them the rotation properties in spin space.

So far, the equations had been derived for a 1D system. The next natural step was to expand the equations to three-dimensional systems, and obtain the set of equations describing the 3D drift-diffusion theory that was presented in Ref[72] (**box F**).

Since our theory describes electron transport in metallic systems, and since electrons are the main carriers of heat in a metal, it was only natural to extend the theory to include heat transport, as well as thermoelectric effects (**box G**). The recent discovery of spin-dependent thermoelectric effects gave an even stronger incentive, and allowed us to model experiments relying on the spin-dependent Seebeck or Peltier

effects. The end result, and also the latest state of the theory, is the set of equations presented in Ref[73] (**box H**), describing the drift-diffusion transport of charge, spin and heat in three-dimensional metallic systems.

The following chapters focus on each theory and give its most important features. The first chapter focuses on the state of the theory before the work presented in this thesis, while the second chapter is the work, and probably the most important result of this thesis. Each section corresponds to a single theory, and is introduced with a version of Fig. 22 where the relevant theory is highlighted. This can be seen as a roadmap for the reader to know exactly where we stand.

V - 2 SCATTERING FORMALISM

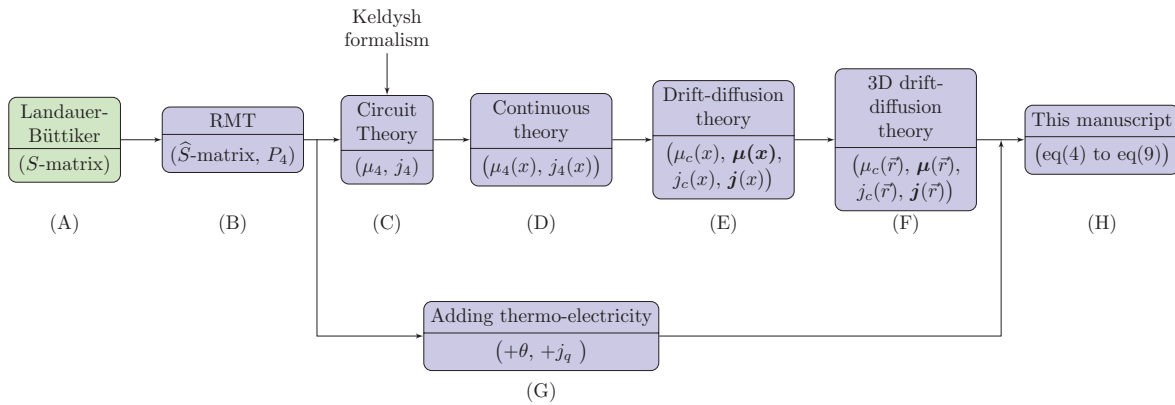


Figure 23.: First step in the history of CRMT: the scattering theory

In this section, we present Theory A in Fig. 23: the Landauer-Büttiker formalism, or scattering formalism. CRMT is based on that theory, and is originally expressed through a (fully quantum) scattering matrix  $S$ [70] for a coherent system.

V - 2.1 Description of the formalism

Considering a 1D system made of a scattering region connected to two leads, we assume that the solutions  $\Psi_n^\pm = \psi_n(y)e^{\pm ik_n x}$  to the Schrödinger equation are known outside of the scattering region. The wave function  $\Psi(x, y)$  on each side of the scat-

terer can therefore be expressed as a linear combination of those solutions. In particular, we separate the two contributions (going left and going right) and write:

$$\Psi_{L/R}^{\pm}(x, y) = \sum_n a_{n,L/R}^{\pm} \psi_n(y) e^{\pm i k_n x} \quad (107)$$

If we write  $\Psi_{L/R}^{\pm}$  the vector of the expansion coefficients  $a_{n,L/R}^{\pm}$ , then  $\Psi_L^{\pm}$  and  $\Psi_R^{\pm}$  are related through  $S$ , see Fig. 24. We give an expression for  $S$  in terms of two reflexion ( $r$  and  $r'$ ) and two transmission ( $t$  and  $t'$ ) submatrices and show how it bridges the wave functions:

$$\begin{pmatrix} \Psi_L^- \\ \Psi_R^+ \end{pmatrix} = \underbrace{\begin{pmatrix} r' & t \\ t' & r \end{pmatrix}}_S \begin{pmatrix} \Psi_L^+ \\ \Psi_R^- \end{pmatrix} \quad (108)$$

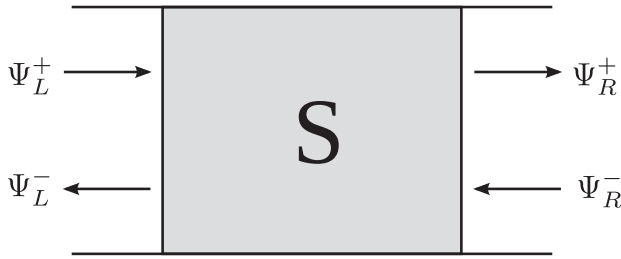


Figure 24.: Sketch of the wave functions on each side of the scatterer  $S$

## V - 2.2 Addition law for two scatterers in series

When two such conductors are in series, an electron can either be directly transmitted, or be subject to multiple reflexions. For the transmission and reflexion, one obtains the geometric series:

$$t_{AB} = t_B t_A + t_B (r_A r'_B) t_A + t_B (r_A r'_B)^2 t_A + \dots \quad (109)$$

$$r_{AB} = r_B + t_B r_A t'_B + t_B (r_A r'_B) r_A t'_B + t_B (r_A r'_B)^2 r_A t'_B + \dots \quad (110)$$

The sum of these series gives the equivalent transmission and reflexion of the system  $\{A+B\}$ :

$$t_{AB} = t_B \frac{1}{1 - r_A r'_B} t_A \quad (111)$$

$$r_{AB} = r_B + t_B \frac{1}{1 - r_A r'_B} r_A t'_B \quad (112)$$

If its transmission is  $t$ , the conductance of a system is given by:

$$g = \frac{e^2}{h} \mathbb{T} = \frac{e^2}{h} \text{Tr} [tt^\dagger] \quad (113)$$

This trace corresponds to the sum over all the eigenvalues of  $tt^\dagger$ , which is the probability transmission matrix. The quantity  $\mathbb{T}$  is the sum over the probabilities of being transmitted from one side of the system to the other. The similar quantity<sup>1</sup>  $\mathbb{R} = \text{Tr} [rr^\dagger]$  exists for reflexions.

### V - 2.3 Semi-classical limit

Now, applying this formula to the system  $\{A+B\}$ , we are going to prove that under some conditions the addition law on transmission and reflexion amplitudes holds for probabilities. To prove that, we assume that the successive reflexions mix the channels together. This means that an electron coming from one channel will exist the system in another, ergodically. To make the calculation easier, we will take the case of only one spinless channel (scalar case). If we assume that the length of the scattering region is long ( $kL \gg 1$ ), we can consider that it picks up a random phase. If we write  $z = e^{i\varphi}$  this phase factor, we have:

$$t_{AB} = t_B \frac{1}{1 - |r_{Ar'_B}|z} t_A \quad (114)$$

The conductance of the system, averaged over this random phase, is given by:

$$\langle g_{AB} \rangle = \frac{e^2}{h} \langle \mathbb{T}_{AB} \rangle \quad (115)$$

The value of  $\langle \mathbb{T}_{AB} \rangle$  is then evaluated using an average over  $\varphi$  on the unit circle  $\mathcal{C}$ . Using  $dz = izd\varphi$ , we get:

$$\langle \mathbb{T}_{AB} \rangle = \frac{1}{2i\pi} \oint_{\mathcal{C}} |t_B|^2 \frac{1}{(1 - |r_{Ar'_B}|z)(1 - |r_{Ar'_B}|z^*)} |t_A|^2 dz/z \quad (116)$$

$$= \frac{1}{2i\pi} \oint_{\mathcal{C}} |t_B|^2 \frac{1}{(1 - |r_{Ar'_B}|z)(z - |r_{Ar'_B}|)} |t_A|^2 dz \quad (117)$$

This integral can be evaluated using the residue theorem. In this case, this reduces to the residue of the main fraction evaluated at  $|r_{Ar'_B}|$ , the only pole inside the unit circle. Fig. 25 gives a sketch of the positions of the poles. Finally, we obtain the

<sup>1</sup> Not to be confused with  $\mathbb{R}$ , the set of real numbers, of course.

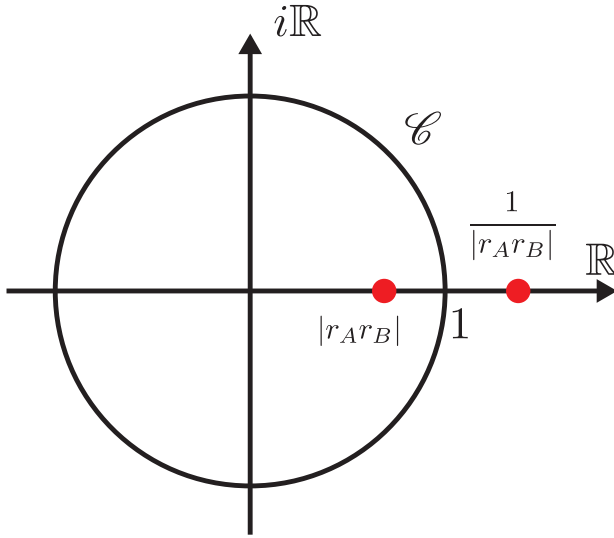


Figure 25.: Position of the poles of the transmission probability  $\mathbb{T}_{AB}$ . The pole inside the unit circle  $\mathcal{C}$  is the only one relevant to the residue theorem.

important result:

$$\langle \mathbb{T}_{AB} \rangle = \mathbb{T}_B \frac{1}{1 - \mathbb{R}_A \mathbb{R}'_B} \mathbb{T}_A \quad (118)$$

We obtain the exact same addition law as Eq. (111), except we are dealing with probabilities instead of amplitudes. This means that within the semi-classical limit, transport can be described by a scattering-like formalism at the probability level of description (and therefore getting rid of most of the purely quantum degrees of freedom)

It can be proven by using the Random Matrix Theory, that this result holds for multiple channels, and when including spins. The next section gives a review of those results, in the more general case.

### V - 3 RANDOM MATRIX APPROACH

If one includes the spin and multiple channels, the transmission and reflexion matrices have a dimension of  $4N_{ch} \times 4N_{ch}$ . By applying an extension of the Random Matrix Theory (RMT) introduced in Ref[70], one can account for the mixing of the channels and the loss of the coherence of the system, as we did in the previous section by introducing a random phase and averaging over it.

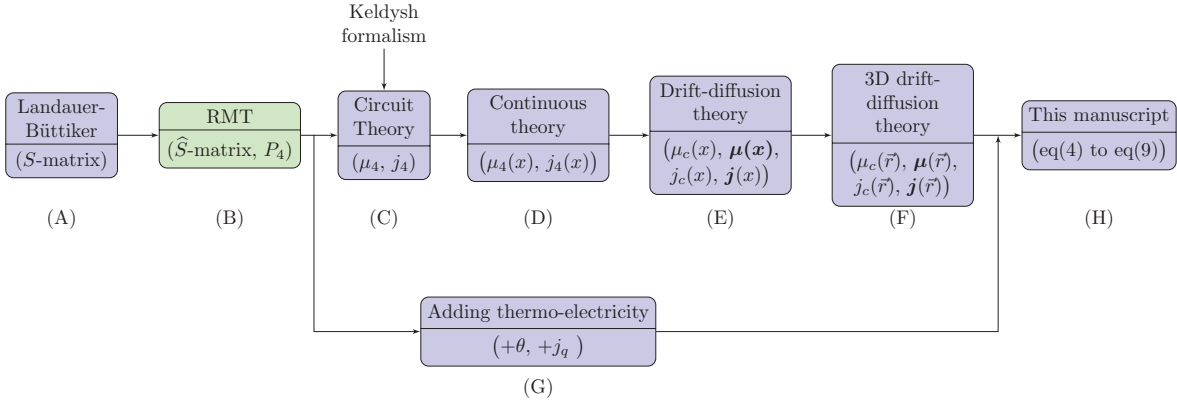


Figure 26.: Second step in the history of CRMT: the use of the random matrix theory on the scattering matrix.

### V - 3.1 Definition of the “hat” matrices

The result of this use of the RMT gives a theory with a structure very similar to the scattering formalism. A conductor is described by  $4 \times 4$  matrices (marked with a hat) describing reflexion and transmission:

$$\hat{S} = \begin{pmatrix} \hat{r}' & \hat{t} \\ \hat{t}' & \hat{r} \end{pmatrix} \quad (119)$$

where each submatrix is defined from the  $4N_{ch} \times 4N_{ch}$  matrices of the scattering theory by:

$$\hat{t}_{\sigma\eta, \sigma'\eta'} = \frac{1}{N_{ch}} \text{Tr}_{N_{ch}} [t_{\sigma\sigma'} t_{\eta\eta'}^\dagger] = \frac{1}{N_{ch}} \text{Tr}_{N_{ch}} \begin{pmatrix} t_{\uparrow\uparrow}^\dagger t_{\uparrow\uparrow} & t_{\uparrow\uparrow}^\dagger t_{\uparrow\downarrow} & t_{\uparrow\downarrow}^\dagger t_{\uparrow\uparrow} & t_{\uparrow\downarrow}^\dagger t_{\uparrow\downarrow} \\ t_{\uparrow\uparrow}^\dagger t_{\downarrow\uparrow} & t_{\uparrow\uparrow}^\dagger t_{\downarrow\downarrow} & t_{\uparrow\downarrow}^\dagger t_{\downarrow\uparrow} & t_{\uparrow\downarrow}^\dagger t_{\downarrow\downarrow} \\ t_{\downarrow\uparrow}^\dagger t_{\uparrow\uparrow} & t_{\downarrow\uparrow}^\dagger t_{\uparrow\downarrow} & t_{\downarrow\downarrow}^\dagger t_{\uparrow\uparrow} & t_{\downarrow\downarrow}^\dagger t_{\uparrow\downarrow} \\ t_{\downarrow\uparrow}^\dagger t_{\downarrow\uparrow} & t_{\downarrow\uparrow}^\dagger t_{\downarrow\downarrow} & t_{\downarrow\downarrow}^\dagger t_{\downarrow\uparrow} & t_{\downarrow\downarrow}^\dagger t_{\downarrow\downarrow} \end{pmatrix} \quad (120)$$

with similar definitions for  $\hat{t}'$ ,  $\hat{r}$  and  $\hat{r}'$ .

In this description, the coefficients in the matrices are highly inequivalent in terms of their amplitude. The most important ones are the probabilities  $T_{\sigma\eta} = \hat{t}_{\sigma\eta, \sigma\eta}$ . Then come the (complex) mixing coefficients on the diagonal  $T_{\text{mx}} = \hat{t}_{\sigma\sigma, -\sigma-\sigma}$ , describing the behavior of a spin transverse to the magnetization. The other coefficients involve coherence between spin-flip and non-spin-flip processes and can be disregarded altogether in the systems we consider. Finally, the matrices have the following struc-

ture in the local magnetic basis (the basis where the projection axis is parallel to  $\mathbf{m}$ ), given here for  $\hat{t}$ :

$$\hat{t} = \begin{pmatrix} T_{\uparrow\uparrow} & 0 & 0 & T_{\uparrow\downarrow} \\ 0 & T_{\text{mx}} & 0 & 0 \\ 0 & 0 & T_{\text{mx}}^* & 0 \\ T_{\downarrow\uparrow} & 0 & 0 & T_{\downarrow\downarrow} \end{pmatrix} \quad (121)$$

$T_{\sigma\eta}$  is the probability for an incoming spin  $\sigma$  electron to be transmitted (reflected, in the case of the reflexion matrices) as a spin  $\eta$  electron. As for the  $T_{\text{mx}}$  and  $R_{\text{mx}}$  coefficients, the next section is dedicated to their meaning and origin.

### v - 3.2 Mixing coefficients

Let us consider a spin-polarized conductor (with polarization along the  $z$  axis) with a transmission coefficient  $t_\sigma = |t|e^{i\vec{k}_\sigma \cdot \vec{u}}$  ( $\sigma = \uparrow$  or  $\downarrow$ ). We write  $\vec{k}_\sigma = (k_\perp^\sigma, k_\parallel^\sigma)$ , where  $k_\perp$  is the component in the direction of propagation (in our case, orthogonal to the magnetization) and  $k_\parallel$  the component collinear to the magnetization. We limit ourselves to only two dimensions only to simplify the notations. In the general case,  $k_\parallel$  should have two components. We also decompose  $\vec{u}$  in the same basis, and write  $\vec{u} = (x, y)$ .

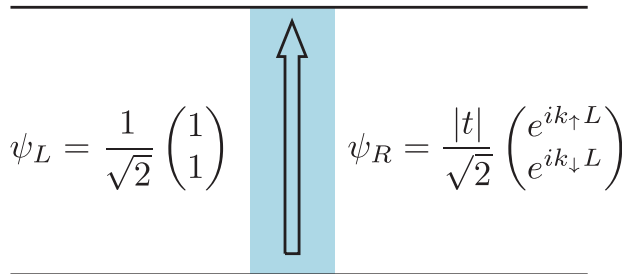


Figure 27.: Drawing of an incoming transverse spin on a polarized layer. The incoming electron (from the left) is polarized along the  $x$  axis. To the right, it is transmitted and its polarization is modified, according the the length of the path it had in the layer.

Now let us consider an electron polarized along the  $x$  axis. Its spinor wave function is:

$$\psi_L = \frac{1}{\sqrt{2}} \begin{pmatrix} 1 \\ 1 \end{pmatrix} \quad (122)$$

After going through the conductor, the electron feels the influence of the polarized layer, according to the length of its path inside it.

$$\psi_R = \frac{|t|}{\sqrt{2}} \begin{pmatrix} e^{i\vec{k}_\uparrow \cdot \vec{u}} \\ e^{i\vec{k}_\downarrow \cdot \vec{u}} \end{pmatrix} \quad (123)$$

The spin density is given (on the right side) by:

$$\vec{\eta} = \psi_R^\dagger \vec{\sigma} \psi_R = |t|^2 \begin{pmatrix} \cos \left[ (k_\perp^\uparrow - k_\perp^\downarrow)x + (k_\parallel^\uparrow - k_\parallel^\downarrow)y \right] \\ \sin \left[ (k_\perp^\uparrow - k_\perp^\downarrow)x + (k_\parallel^\uparrow - k_\parallel^\downarrow)y \right] \\ 0 \end{pmatrix} \quad (124)$$

The spin density oscillates with respect to  $x$ , the distance of penetration. We note the typical length of oscillation (precession)  $\ell_L$ . The second component in the argument indicates that the amount of precession depends on the direction of incidence of the electron into the ferromagnet. This means that two electrons with different incidences will lose their coherence the deeper they propagate. At a given depth  $x$ , the average over the directions of incidence will result in an exponentially decaying spin density: the transverse component of the spin current is absorbed by the surrounding magnetization. We note the typical length of absorption  $\ell_\perp$ .

Using the definition of  $T_{\text{mx}}$ , we get:

$$T_{\text{mx}} = \langle t_\uparrow t_\downarrow^* \rangle = \left\langle e^{i(\vec{k}_\uparrow - \vec{k}_\downarrow) \cdot \vec{u}} \right\rangle \approx e^{-\frac{x}{\ell_\perp} + i\frac{x}{\ell_L}} \quad (125)$$

where the average is made over all the incident angles. One of the results of this thesis is providing a measuring scheme of those two length, see Section VII

### V - 3.3 Properties of the $\hat{S}$ matrix

Most of the quantum effects (like universal conductance fluctuations, weak localization, etc) disappear in this description. This semi-classical description only keeps the spin, the Sharvin resistance, and mixing transmission and reflexion for transverse spins.

In this description, the conductance is given by  $g = [T_{\uparrow\uparrow} + T_{\uparrow\downarrow} + T_{\downarrow\uparrow} + T_{\downarrow\downarrow}] / \mathcal{R}_{\text{Sh}}$ , where  $\mathcal{R}_{\text{Sh}}$  is the Sharvin resistance, defined as  $\mathcal{R}_{\text{Sh}} = h / (e^2 N_{\text{ch}})$ . It is the (quantum) resistance of a perfectly transparent scatterer, arising at the leads.

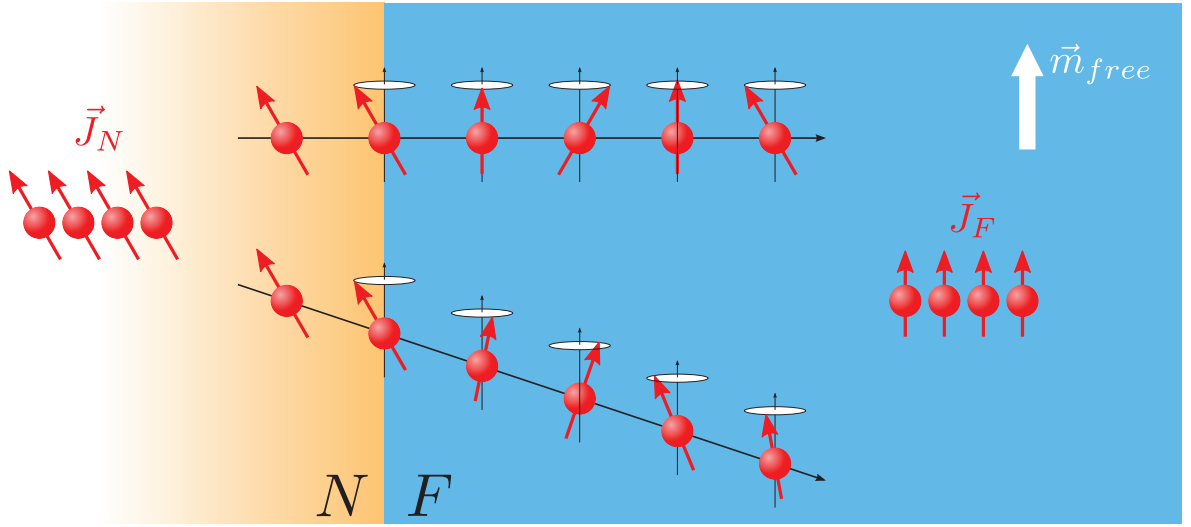


Figure 28.: Origin of the finite spin penetration length. A polarized current arrives from the left with its polarization making a non-zero angle with the magnetization of the free magnetic layer. Upon arriving to the magnetic layer, the individual spins start precessing. Due to their different incident directions, at a given distance from the interface, each spin will have traveled a different length and therefore precessed a different angle. The superposition of the spins will therefore quickly lose its coherence, averaging to the local magnetization direction. The distance over which the coherence is lost is our transverse spin penetration length  $\ell_{\perp}$ .

Ref[70] gave the important result that once again, the same addition law still holds.

$$\hat{t}_{AB} = \hat{t}_B \frac{1}{1 - \hat{r}_A \hat{r}'_B} \hat{t}_A \quad (126)$$

$$\hat{r}_{AB} = \hat{r}_B + \hat{t}_B \frac{1}{1 - \hat{r}_A \hat{r}'_B} \hat{r}_A \hat{t}'_B \quad (127)$$

In the spinless case, this can be recast to give the addition law for resistances. It reads:

$$\mathcal{R}_{AB} = \mathcal{R}_A + \mathcal{R}_B - \mathcal{R}_{Sh} \quad (128)$$

One can understand Eq. (128) as the usual addition law for resistances, but applied on the intrinsic resistance defined as  $\mathcal{R}_{intr} = \mathcal{R} - \mathcal{R}_{Sh}$ , as one can see by rewriting Eq. (128):

$$\mathcal{R}_{AB} - \mathcal{R}_{Sh} = \mathcal{R}_A - \mathcal{R}_{Sh} + \mathcal{R}_B - \mathcal{R}_{Sh} \quad (129)$$

In the scattering theory, the variables exchanged between two scatterers were the incoming and outgoing wave function coefficients. After going through the RMT transformation, only length 4 vectors remain, storing the charge and spin degrees of freedom. Those vectors, written  $P_4^{in}$  and  $P_4^{out}$  on each side of the conductor are related through the  $\hat{S}$  matrix as:

$$\begin{pmatrix} P_{4,L}^{out} \\ P_{4,R}^{out} \end{pmatrix} = \begin{pmatrix} \hat{r}' & \hat{t} \\ \hat{t}' & \hat{r} \end{pmatrix} \begin{pmatrix} P_{4,L}^{in} \\ P_{4,R}^{in} \end{pmatrix} \quad (130)$$

Again, in the spinless case, this equation is equivalent to a master equation. The algorithm of our solver is based on this fact and despite the presence of the spin (and in particular transverse spins, resulting in the presence of complex numbers in the matrix), it has always shown the convergence properties expected from a master equation<sup>2</sup>

The basis for these vectors, the same as for the  $\hat{t}$  and  $\hat{r}$  matrices, corresponds to the  $\uparrow$ , mx, mx\* and  $\downarrow$  projections. As before, the mixing mx coefficients are complex numbers.

The next section is an interlude in the chronological scheme we followed so far, and introduces how to change the basis of a  $\hat{S}$  matrix. The practical application for this is combining  $\hat{S}$  matrices describing ferromagnetic materials with different magnetization orientation.

## V - 4 ROTATIONS OF $\hat{S}$ MATRICES

We saw that it is possible to add several  $\hat{S}$  matrices together to describe for example several layers of the same or different materials. However all the results presented so far assumed that the matrices we written in the basis aligned with the magnetization. New and interesting effects arise when dealing with non-collinear magnetizations. Therefore, we present here the way to apply rotations to  $\hat{S}$  matrices, in order to be able to deal with arbitrary magnetization direction.

<sup>2</sup> This is true as long as the coefficients in the matrix correspond to a material with properties respecting the physics.

## V - 4.1 Rotations in spin space

Let us first define the rotation transforming a vector  $\mathbf{a}$  into a vector  $\mathbf{b}$ . This rotation can be characterized by an angle  $\varphi$  and the winding axis, noted  $\mathbf{n} = \frac{\mathbf{a} \times \mathbf{b}}{\|\mathbf{a} \times \mathbf{b}\|}$ .

Noting  $\boldsymbol{\sigma}$  the Pauli vector  $\boldsymbol{\sigma} = (\sigma_x, \sigma_y, \sigma_z)$ , we define the following rotation matrix:

$$R = \exp\left(-i\frac{\varphi}{2}\boldsymbol{\sigma} \cdot \mathbf{n}\right) \quad (131)$$

We have then the following identity, defining the rotation of the Pauli basis:

$$R(\mathbf{a} \cdot \boldsymbol{\sigma})R^{-1} = \mathbf{b} \cdot \boldsymbol{\sigma} \quad (132)$$

In particular, for  $\mathbf{a} = \mathbf{e}_z$  and  $\mathbf{b} = \mathbf{m}$  (what will be the magnetization unit vector) it gives:  $R\sigma_zR^{-1} = \mathbf{m} \cdot \boldsymbol{\sigma}$ . This defines the rotation of the magnetization from the reference axis  $z$  to any direction given by  $\mathbf{m}$ .

Let us then introduce the matrix  $\hat{R} = R \otimes R^*$ , where  $\otimes$  is the Kronecker product. As we can see from Eq. (120), the submatrices of  $\hat{S}$  have the structure of a Kronecker product, which is the reason why  $\hat{R}$  is the correct rotation matrix to transform them from the local magnetization basis to a global basis. For any scattering submatrix like  $\hat{t}(\mathbf{e}_z)$  written for a magnetization along the  $z$ -axis:

ROTATION OF A SCATTERING SUBMATRIX:

$$\hat{t}(\mathbf{m}) = \hat{R}\hat{t}(\mathbf{e}_z)\hat{R}^{-1} \quad (133)$$

## V - 5 EQUIVALENCE OF CRMT WITH THE CIRCUIT THEORY

In this section, we go back to following the history of CRMT. Inspired by the generalized Circuit Theory[10] (and in order to prove its equivalence with this theory), the concepts of nodes and links were introduced, and lead the way to the description of three-dimensional systems. The idea is to discretize the system into small parts connected to each other. The connexion between two nodes is made through a link, where the material information is stored (as a  $\hat{S}$  matrix). Allowing the possibility to have multiple links connected to a given node is the cornerstone of the description of multidimensional systems.

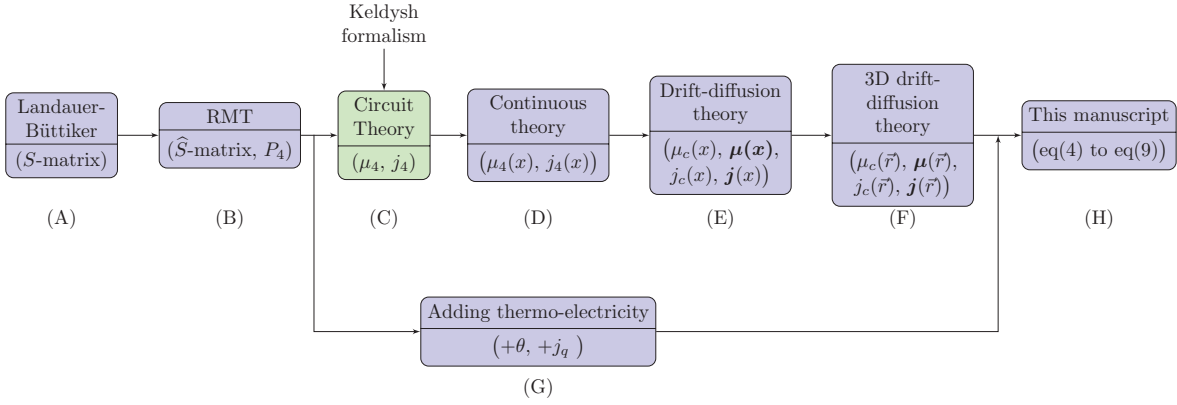


Figure 29.: Third step in the history of CRMT: its equivalence to the circuit theory, proven to a simple change of variables.

Let us apply these concepts to a 1D conductor, divided into  $N$  parts (we assume them to be of same length, so that the  $\hat{S}$  matrix is always the same, in order to simplify the notations in the derivation). We will start from a formulation using the CRMT concepts, and by using a change of variable show that it is equivalent to a 1D circuit theory problem. Since we consider a 1D problem, we can index the nodes from 1 to  $N$ .

There are two (matrix) equations to consider:

- The node equation, ensuring current conservation and potential isotropy (we will delve deeper into that later)
- The link equation, encoding the material properties

Because we deal with a 1D system, the node equation simply boils down to

$$P_{4,R}^+[i] = P_{4,L}^+[i+1] \quad (134)$$

$$P_{4,R}^-[i] = P_{4,L}^-[i+1] \quad (135)$$

where the index of the node is specified into the square brackets, to emphasize the discrete nature of this system. We then use the following change of variables, intended to make the bridge between CRMT and the Generalized Circuit Theory:

$$\mu_4 = \frac{1}{2} [P_{4,L}^- + P_{4,L}^+] \quad (136)$$

$$j_4 = \frac{1}{2} [P_{4,L}^+ - P_{4,L}^-] \quad (137)$$

As the notations suggest, they correspond to potentials and currents[9], as we shall see. Before going further, we will make the simple assumption from this point on that the material is symmetric, in the sens that its reflexion and transmission properties do not depend on the direction ( $\hat{t} = \hat{t}'$  and  $\hat{r} = \hat{r}'$ ). For bulk metallic metals, this assumption is of course always respected. A few lines of algebra allow us to rewrite the link equation using that change of variable:

$$2(\mu_4[i] - \mu_4[i+1]) = (\mathbb{1} + \hat{r} - \hat{t})(\mu_4[i] - \mu_4[i+1] + j_4[i] + j_4[i+1]) \quad (138)$$

$$2(j_4[i+1] - j_4[i]) = (\hat{r} + \hat{t} - \mathbb{1})(\mu_4[i] + \mu_4[i+1] + j_4[i] - j_4[i+1]) \quad (139)$$

Eq. (138) is reminiscent of a (discreet) Ohm law, while Eq. (139) is a conservation equation. To see that more clearly, let us take the case of a normal metal. This is equivalent to say that Eq. (138) and Eq. (139) become scalar, with the additional property that  $\hat{t} + \hat{r} = 1$ . Because they are not needed anymore, we drop the subscript 4 in this derivation. Eq. (139) obviously become:

$$j[i] = j[i+1] \quad (140)$$

And similarly Eq. (138) becomes, taking the previous equation into account:

$$\mu[i] - \mu[i+1] = 2 \left(1 - \frac{1}{\mathbb{T}}\right) j[i] \quad (141)$$

where  $\mathbb{T} = T_{\uparrow\uparrow} + T_{\uparrow\downarrow} + T_{\downarrow\uparrow} + T_{\downarrow\downarrow}$ . Setting  $j = e\mathcal{R}_{\text{Sh}}J/2^3$  where  $J$  is the actual (still discreet) current density in  $\text{A} \cdot \text{m}^{-2}$ , and  $\mu = eV$ , we obtain by using  $\mathcal{R} = \mathcal{R}_{\text{Sh}}/\mathbb{T}$ :

$$V[i] - V[i+1] = (\mathcal{R} - \mathcal{R}_{\text{Sh}}) J[i] \quad (142)$$

which is exactly a discreet Ohm's law taking the Sharvin resistance into account.

### v - 5.1 Interface equations

Eq. (138) and Eq. (139) have been obtained by assuming  $\hat{t} = \hat{t}'$  and  $\hat{r} = \hat{r}'$ . Their form has also been chosen with the idea of going to the continuous limit. We now backtrack a little bit to obtain more general equations to describe any interface. Let us first rewrite Eq. (130) in the case of a normal-ferromagnetic interface:

$$\begin{pmatrix} P_F^- \\ P_N^+ \end{pmatrix} = \begin{pmatrix} \hat{r}_F & \hat{t}_N \\ \hat{t}_F & \hat{r}_N \end{pmatrix} \begin{pmatrix} P_F^+ \\ P_N^- \end{pmatrix} \quad (143)$$

<sup>3</sup> The factor 2 difference with Eq. (190) comes from the fact that  $\mathbb{T}$  can be seen as containing both  $\uparrow$  and  $\downarrow$  spin channels.

$N$  (resp.  $F$ ) indicate the normal (resp. ferromagnetic) side of the interface. Using the usual change of variable  $j = (P^+ - P^-)/2$  and  $\mu = (P^+ + P^-)/2$  we obtain a set of two equations of the form:

$$\begin{pmatrix} j_N \\ j_F \end{pmatrix} = \begin{pmatrix} c_{NN} & c_{NF} \\ -c_{FN} & -c_{FF} \end{pmatrix} \begin{pmatrix} \mu_N \\ \mu_F \end{pmatrix} \quad (144)$$

We give the expression for the coefficients  $c_{ij}$ , obtained by applying the change of variables on Eq. (143) and isolating the currents:

$$c_{NN} = \left[ \mathbb{1} + \hat{r}_N - \hat{t}_F (\mathbb{1} + \hat{r}_F)^{-1} \hat{t}_N \right]^{-1} \left[ \hat{r}_N - \mathbb{1} - \hat{t}_F (\mathbb{1} + \hat{r}_F)^{-1} \hat{t}_N \right] \quad (145)$$

$$c_{NF} = \left[ \mathbb{1} + \hat{r}_N - \hat{t}_F (\mathbb{1} + \hat{r}_F)^{-1} \hat{t}_N \right]^{-1} 2\hat{t}_F (1 + \hat{r}_F)^{-1} \quad (146)$$

$$c_{FN} = \left[ \mathbb{1} + \hat{r}_F - \hat{t}_N (\mathbb{1} + \hat{r}_N)^{-1} \hat{t}_F \right]^{-1} 2\hat{t}_N (1 + \hat{r}_N)^{-1} \quad (147)$$

$$c_{FF} = \left[ \mathbb{1} + \hat{r}_F - \hat{t}_N (\mathbb{1} + \hat{r}_N)^{-1} \hat{t}_F \right]^{-1} \left[ \hat{r}_F - \mathbb{1} - \hat{t}_N (\mathbb{1} + \hat{r}_N)^{-1} \hat{t}_F \right] \quad (148)$$

We take the same structure for  $\hat{t}$  and  $\hat{r}$  as in Eq. (121), to the exception that we neglect any spin-flip. This assumption has the consequence that  $R_{\sigma\sigma} = \mathbb{1} - T_{\sigma\sigma}$ . For the sake of readability, we will drop one of the two spin indices, since they will always be the same. We also assume that the only source of ‘‘asymmetry’’ of the interface comes from the mixing coefficients. The transmission and reflexion matrices therefore are:

$$\hat{t}_a = \begin{pmatrix} T_\uparrow & 0 & 0 & 0 \\ 0 & T_{\text{mx}}^a & 0 & 0 \\ 0 & 0 & T_{\text{mx}}^{*,a} & 0 \\ 0 & 0 & 0 & T_\downarrow \end{pmatrix} \quad (149)$$

$$\hat{r}_a = \begin{pmatrix} 1 - T_\uparrow & 0 & 0 & 0 \\ 0 & R_{\text{mx}}^a & 0 & 0 \\ 0 & 0 & R_{\text{mx}}^{*,a} & 0 \\ 0 & 0 & 0 & 1 - T_\downarrow \end{pmatrix} \quad (150)$$

$$(151)$$

where  $a = N$  or  $F$ . This gives first for the longitudinal part ( $\sigma = \uparrow$  or  $\downarrow$ ) of the current:

$$j_{N,\sigma} = j_{F,\sigma} = \frac{1}{4} \frac{T_\sigma}{1 - T_\sigma} (\mu_{F,\sigma} - \mu_{N,\sigma}) \quad (152)$$

One has to be careful here because the notations may be misleading. We take the convention that the charge current is  $j_c = j_\uparrow + j_\downarrow$  (the total current is the sum of the current of each spin specie). However, our convention is that  $\mu_c = (\mu_\uparrow + \mu_\downarrow)/2$ . This prevents any factor in the final equations. But it also means that  $\mu_\uparrow$  is twice the first component of  $\mu_4$ . This accounts for the factor 1/4 instead of 1/2 in Eq. (152). For the transverse part, we obtain:

$$j_{N,\text{mx}} = -\eta_{\text{mx}}^N \mu_{\text{mx},N} + \sigma_{\text{mx}}^N (\mu_{\text{mx},F} - \mu_{\text{mx},N}) \quad (153)$$

$$j_{F,\text{mx}} = \eta_{\text{mx}}^F \mu_{\text{mx},F} + \sigma_{\text{mx}}^F (\mu_{\text{mx},F} - \mu_{\text{mx},N}) \quad (154)$$

$$(155)$$

with  $\eta_{\text{mx}}^{N/F}$  and  $\sigma_{\text{mx}}^{N/F}$ :

$$\sigma_{\text{mx}}^{N/F} = \frac{2T_{\text{mx}}^{N/F}}{(1 + R_{\text{mx}}^F)(1 + R_{\text{mx}}^N) - T_{\text{mx}}^N T_{\text{mx}}^F} \quad (156)$$

$$\eta_{\text{mx}}^{N/F} = \frac{(1 + R_{\text{mx}}^{F/N})(1 - R_{\text{mx}}^{N/F}) + (T_{\text{mx}}^{F/N} - 2)T_{\text{mx}}^{N/F}}{(1 + R_{\text{mx}}^F)(1 + R_{\text{mx}}^N) - T_{\text{mx}}^N T_{\text{mx}}^F} \quad (157)$$

These equations are valid for any material (bulk or interface) as long as spin-flip can be neglected.

We now continue the derivation of the bulk equations. When all the steps are introduced, we will apply them to interfaces. Next section will go to the limit where  $L$  is very small, and show that this result still holds when including the spin.

## V - 6 FROM DISCREET TO CONTINUOUS

In the previous section, the slices were of arbitrary length  $L$ . We now go to the limit where  $L = dx$ , an infinitely small quantity. Since the links correspond now to thin slices, we assume that, their  $\hat{S}$ -matrix can be written using the following parametrization[17]:

$$\hat{r} = \Lambda_r dx \quad (158)$$

$$\hat{t} = \mathbb{1} - \Lambda_t dx \quad (159)$$

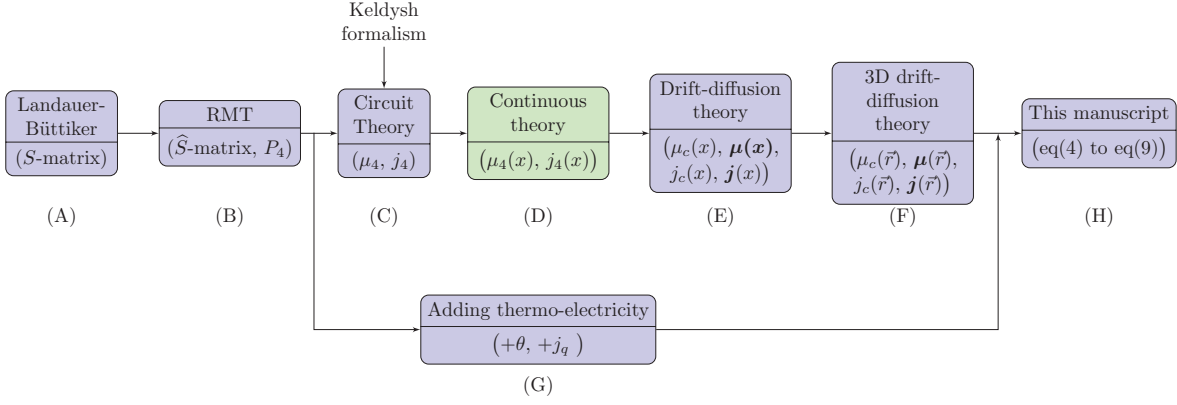


Figure 30.: Fourth step in the history of CRMT: taking the circuit theory to the continuous limit by setting  $L = dx$ .

Substituting those expression into Eq. (138) and Eq. (139), we obtain:

$$2\left(j_4(x+dx) - j_4(x)\right) = (\Lambda_r - \Lambda_t) dx \left(\mu_4(x) + \mu_4(x+dx) + j_4(x) - j_4(x+dx)\right) \quad (160)$$

$$2\left(\mu_4(x) - \mu_4(x+dx)\right) = (\Lambda_r + \Lambda_t) dx \left(\mu_4(x) - \mu_4(x+dx) + j_4(x) + j_4(x+dx)\right) \quad (161)$$

Developing the variables to the first order in  $dx$ , we obtain continuous differential equations in  $\mu_4$  and  $j_4$ :

$$-\frac{d\mu_4}{dx}(x) = 2\Lambda_\Omega j_4(x) \quad (162)$$

$$-\frac{dj_4}{dx}(x) = 2\Lambda_\Xi \mu_4(x) \quad (163)$$

Eq. (163) and Eq. (162) express now clearly the current conservation and the Ohm-like behavior announced in the previous section. We used the change of parametrization  $\Lambda_t = \Lambda_\Omega + \Lambda_\Xi$  and  $\Lambda_r = \Lambda_\Omega - \Lambda_\Xi$ .

In order to fit the Valet-Fert theory, we assume the following form for those matrices:

$$\Lambda_{\Omega} = \begin{pmatrix} \Gamma_{\uparrow} & 0 & 0 & 0 \\ 0 & \Gamma_{\text{mx}}^{\text{eff}} & 0 & 0 \\ 0 & 0 & \Gamma_{\text{mx}}^{\text{eff}*} & 0 \\ 0 & 0 & 0 & \Gamma_{\downarrow} \end{pmatrix} \quad (164)$$

$$\Lambda_{\Xi} = \begin{pmatrix} \Gamma_{\text{sf}} & 0 & 0 & -\Gamma_{\text{sf}} \\ 0 & \Gamma_{\tau} & 0 & 0 \\ 0 & 0 & \Gamma_{\tau}^* & 0 \\ -\Gamma_{\text{sf}} & 0 & 0 & \Gamma_{\text{sf}} \end{pmatrix} \quad (165)$$

This form for the  $\Lambda$  matrices was already introduced in Ref[17]. However, some minor changes were introduced since then, in order for the same matrices to describe both ferromagnetic and normal metals (simply setting the purely ferromagnetic components to zero in the latter case). The various coefficients depend on the characteristic lengths of the material. Namely,  $\ell_{\uparrow(\downarrow)} = 1/\Gamma_{\uparrow(\downarrow)}$  is the mean free path for the majority and minority electrons. We prefer to rewrite it using, in the Valet-Fert fashion, the average mean free path  $\ell_*$  and  $\beta$ , the spin asymmetry of the material. This gives  $\Gamma_{\uparrow(\downarrow)} = (1 \mp \beta)/2\ell_*$ .

$\Gamma_{\text{mx}}^{\text{eff}} = \Gamma_{\text{mx}}/2 + (\Gamma_{\uparrow} + \Gamma_{\downarrow})/2$  describes the behavior of the spins transverse to the local magnetization. The first part  $\Gamma_{\text{mx}}$  is of ballistic origin and depends on two characteristic lengths:  $\Gamma_{\text{mx}} = 1/\ell_{\perp} - i/\ell_L$ .  $\ell_{\perp}$ , the transverse spin penetration length describes of deep a transverse spin can penetrate into a ferromagnet before losing its spin to the magnetization. See Section V - 3.2 for more information.  $\ell_L$ , the Larmor precession length, describes how much the same transverse spin will precess around the axis of the local magnetization. The second part of  $\Gamma_{\text{mx}}^{\text{eff}}$  describes the spin-independent transport of the electrons. In particular, this makes the transport through a normal metal independent on the chosen matrix basis.

$\Gamma_{\text{sf}} = \ell_*/4\ell_{\text{sf}}^2$  describes spin-flip processes, and depends on the spin diffusion length  $\ell_{\text{sf}}$ .

Finally,  $\Gamma_{\tau} = \Gamma_{\text{mx}}/2 + 2\Gamma_{\text{sf}}$  describes the non-conserved part of the transverse spins, including the fact that transverse spins feel as much spin-flip as collinear ones. Again, this makes the case of the normal metal independent of the basis of representation.

# VI

## THE STATE OF THE THEORY AFTER THIS THESIS

### VI - 1 RECOVERING CLASSICAL VARIABLES AND OBTAINING DRIFT-DIFFUSION EQUATIONS

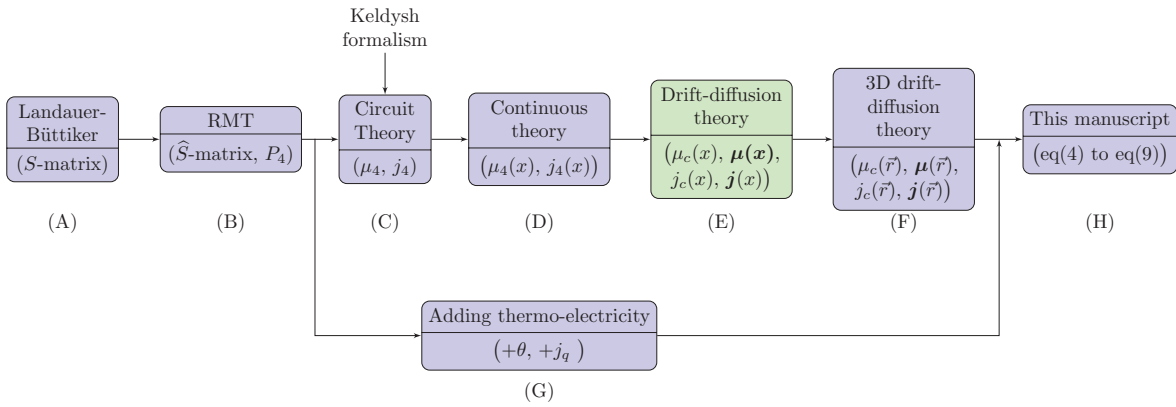


Figure 31.: Fifth step in the history of CRMT: going from matrix equations to differential equations

In this section, we show how to go from the  $\mu_4$  and  $j_4$  vectors to the classical variables  $\mu_c$  and  $\boldsymbol{\mu}$ , the charge and spin potentials (called spin accumulation in collinear configurations), as well as  $j_c$  and  $\boldsymbol{j}$  the charge and spin currents. To do so, we first present one basis of matrices adapted to our problem, and then explain how to apply rotations in spin space.

#### VI - 1.1 Matrix basis

We first define a set of  $4 \times 4$  matrices as follows:

$$I_{ij} = \sigma_i \otimes \sigma_j^* \quad (166)$$

with  $\sigma_0$  being the identity and the  $\sigma_i$  being the Pauli matrices.

We introduce now a basis for the 4-vectors used in our theory:

$$\Sigma_c = \begin{pmatrix} 1 \\ 0 \\ 0 \\ 1 \end{pmatrix} \quad \Sigma_1 = \begin{pmatrix} 0 \\ 1 \\ 1 \\ 0 \end{pmatrix} \quad \Sigma_2 = \begin{pmatrix} 0 \\ -i \\ i \\ 0 \end{pmatrix} \quad \Sigma_3 = \begin{pmatrix} 1 \\ 0 \\ 0 \\ -1 \end{pmatrix} \quad (167)$$

Any 4-vectors can be written on this basis, using the following convention:

$$\mathbf{p}_4 = p_c \Sigma_c + \mathbf{p} \cdot \boldsymbol{\Sigma} = p_c \Sigma_c + \sum_{i=1}^3 p_i \Sigma_i \quad (168)$$

The index  $c$  represents the charge part, the bold symbol the 3-dimensional spin part. The bridge between the 4-vectors and observable quantities is entirely contained in that equation. This projection may seem trivial, but understanding it was the key element to unlock the transition to the drift-diffusion theory.

By recalling the following identity of the Pauli matrices:

$$\sigma_i \sigma_j = \delta_{ij} \sigma_0 + i \sum_k \varepsilon_{ijk} \sigma_k \quad (169)$$

where  $\varepsilon_{ijk}$  is the Levi-Civita symbol, we can now straightforwardly obtain the next identities:

for  $i, j, k \in \llbracket 1, 3 \rrbracket$

$$I_{i0} \Sigma_c = I_{0i} \Sigma_c = \Sigma_i \quad (170)$$

$$I_{ij} \Sigma_c = \delta_{ij} \Sigma_c + i \sum_{l=1}^3 \varepsilon_{ijl} \Sigma_l \quad (171)$$

$$I_{0i} \Sigma_k = \delta_{ki} \Sigma_c + i \sum_{l=1}^3 \varepsilon_{kil} \Sigma_l \quad (172)$$

$$I_{i0} \Sigma_k = \delta_{ki} \Sigma_c - i \sum_{l=1}^3 \varepsilon_{kil} \Sigma_l \quad (173)$$

$$I_{ij} \Sigma_k = \delta_{ik} \Sigma_j + \delta_{jk} \Sigma_i - \delta_{ij} \Sigma_k + i \varepsilon_{ikj} \Sigma_c \quad (174)$$

The matrices  $I_{03}$  and  $I_{30}$  in particular play an important role, however only through their sum and difference. In order to simplify the notation, we therefore introduce the matrices  $I_{\parallel} = (I_{30} + I_{03})/2$ ,  $I_L = (I_{30} - I_{03})/2$  and  $I_{\perp} = (I_{00} - I_{33})/2$ . We also introduce the rotation-invariant  $I_2 = \sum_i I_{ii}/2$ . Their expression are:

$$I_{\parallel} = \begin{pmatrix} 1 & 0 & 0 & 0 \\ 0 & 0 & 0 & 0 \\ 0 & 0 & 0 & 0 \\ 0 & 0 & 0 & -1 \end{pmatrix} \quad (175)$$

$$I_L = \begin{pmatrix} 0 & 0 & 0 & 0 \\ 0 & 1 & 0 & 0 \\ 0 & 0 & -1 & 0 \\ 0 & 0 & 0 & 0 \end{pmatrix} \quad (177)$$

$$I_{\perp} = \begin{pmatrix} 0 & 0 & 0 & 0 \\ 0 & 1 & 0 & 0 \\ 0 & 0 & 1 & 0 \\ 0 & 0 & 0 & 0 \end{pmatrix} \quad (176)$$

$$I_2 = \begin{pmatrix} 1 & 0 & 0 & 1 \\ 0 & 0 & 0 & 0 \\ 0 & 0 & 0 & 0 \\ 1 & 0 & 0 & 1 \end{pmatrix} \quad (178)$$

The next section describes the effect of rotations on those matrices, in order to obtain relations for any orientation of the magnetization.

### VI - 1.2 *Rotation properties*

We now provide a few identities by applying the rotation introduced in Section V - 4.1 to the basis matrices we just introduced. First, we give the identities for the rotation-invariant matrices:

$$[\widehat{R}I_{00}\widehat{R}^{-1}] = I_{00} \quad (179)$$

$$[\widehat{R}I_2\widehat{R}^{-1}] = I_2 \quad (180)$$

As for the non rotation-invariant ones, their effect is best seen on a generic 4-vector  $\mathbf{p}_4$ :

$$[\widehat{R}I_{\parallel}\widehat{R}^{-1}]\mathbf{p}_4 = p_c \mathbf{m} \cdot \boldsymbol{\Sigma} + (\mathbf{m} \cdot \mathbf{p}) \Sigma_c \quad (181)$$

$$[\widehat{R}I_L\widehat{R}^{-1}]\mathbf{p}_4 = i (\mathbf{m} \times \mathbf{p}) \cdot \boldsymbol{\Sigma} \quad (182)$$

$$\begin{aligned} [\widehat{R}I_{\perp}\widehat{R}^{-1}]\mathbf{p}_4 &= \mathbf{p}_{\perp} \cdot \boldsymbol{\Sigma} \\ &= [(\mathbf{m} \times \mathbf{p}) \times \mathbf{m}] \cdot \boldsymbol{\Sigma} \end{aligned} \quad (183)$$

### VI - 1.3 *1D continuous equations*

Let us finally write Eq. (163) and Eq. (162) as a linear combination of the matrices introduced in Section VI - 1.1:

$$\Lambda_{\Omega} = \frac{\Gamma_{\uparrow} + \Gamma_{\downarrow}}{2} I_{00} + \frac{\Gamma_{\uparrow} - \Gamma_{\downarrow}}{2} I_{\parallel} + \frac{1}{2} \text{Re}(\Gamma_{\text{mx}}) I_{\perp} + \frac{i}{2} \text{Im}(\Gamma_{\text{mx}}) I_L \quad (184)$$

$$\Lambda_{\Xi} = \Gamma_{\text{sf}} (2I_1 - I_2) + \frac{1}{2} \text{Re}(\Gamma_{\text{mx}}) I_{\perp} + \frac{i}{2} \text{Im}(\Gamma_{\text{mx}}) I_L \quad (185)$$

The last step is now to apply a generic rotation to this equation, so that we can write it for any magnetization direction  $\mathbf{m}$ .

Finally, using Eq. (184) and Eq. (185) in Eq. (163) and Eq. (162), and applying the rotation properties we just derived gives us a set of equations, the main result of box (E) in Fig. 22, as well as the foundation of Ref[72]:

$$-\ell_* \frac{d\mu_c}{dx} = j_c - \beta \mathbf{j} \cdot \mathbf{m} \quad (186)$$

$$-\ell_* \frac{d\boldsymbol{\mu}}{dx} = \mathbf{j} - \beta j_c \mathbf{m} + \frac{\ell_*}{\ell_{\perp}} (\mathbf{m} \times \mathbf{j}) \times \mathbf{m} - \frac{\ell_*}{\ell_L} (\mathbf{m} \times \mathbf{j}) \quad (187)$$

$$\frac{dj_{\alpha}^c}{dx} = 0 \quad (188)$$

$$\frac{d\mathbf{j}}{dx} = -\frac{\ell_*}{\ell_{sf}^2} \boldsymbol{\mu} - \frac{1}{\ell_{\perp}} (\mathbf{m} \times \boldsymbol{\mu}) \times \mathbf{m} + \frac{1}{\ell_L} (\mathbf{m} \times \boldsymbol{\mu}) \quad (189)$$

Now is a good time to make the link between the variables  $j_c, \mathbf{j}, \mu_c, \boldsymbol{\mu}$  and the usual observables. With  $J_c, \mathbf{J}$  the charge and (vector) spin current density in units of  $\text{A} \cdot \text{m}^{-2}$  and  $\text{J} \cdot \text{m}^{-2}$  respectively:

$$J_c = \frac{4}{e\mathcal{R}_{\text{Sh}}} j_c \quad (190)$$

$$\mathbf{J} = \frac{2\hbar}{e^2\mathcal{R}_{\text{Sh}}} \mathbf{j} \quad (191)$$

Of course  $\mu_c = eV$  where  $V$  is the local potential.

## VI - 2 FROM 1D TO 3D

Going from the 1D equations from the 3D can be done easily by formally replacing the derivatives by a gradient in the Ohm-like equations Eq. (186) and Eq. (187) (or simply  $\partial_{\alpha}$ , since each component is independent of the others), and by a divergence in the conservation equations Eq. (188) and Eq. (189).

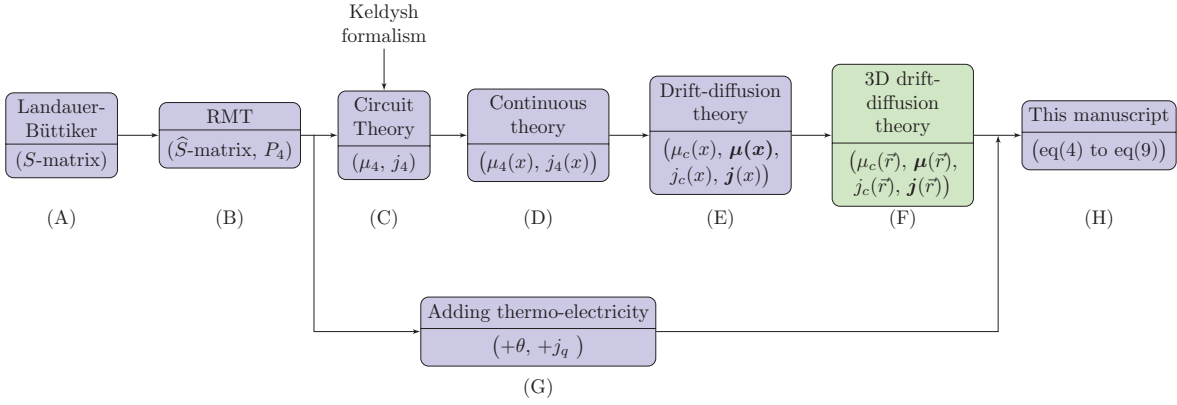


Figure 32.: Sixth step in the history of CRMT: expanding the derivation to work for a three-dimensional lattice of nodes and links.

Keeping that result in mind, we now give some clues about how to derive the 3D equations. In the unidimensional system considered so far, the probabilities were transmitted from one link (corresponding to a given  $S$  matrix) to the other. When taking into account several dimensions, the need of a so-called node arises. The probability vectors coming out of the links arrive at a node, and are dispatched back, according to the node equation. In 1D, this node equation simply states that what comes into the node gets out without any change. When more dimensions are involved, the node equation enforces two facts. First, the local current conservation, second the isotropy of the potential. Fig. 33 gives a 2D view of how a node (circle) is connected to other nodes through links (squares). The subscripts *in* and *out* describe whether the probability is coming in or going out of the link. + and – indicate the direction of propagation, with respect to the indicated axis.

In order to express the node equation easily, we introduce as before the following change of variables between  $P$ -vectors and currents and potentials:

$$j_L^\alpha = \frac{1}{2} (P_{out}^{\alpha+} - P_{in}^{\alpha-}) \quad (192)$$

$$j_R^\alpha = \frac{1}{2} (P_{in}^{\alpha+} - P_{out}^{\alpha-}) \quad (193)$$

The subscripts  $L$  and  $R$  indicate the side of the node at which the current is evaluated. Current conservation reads:

$$\sum_{\alpha \in \{x,y,z\}} j_L^\alpha - j_R^\alpha = 0 \quad (194)$$

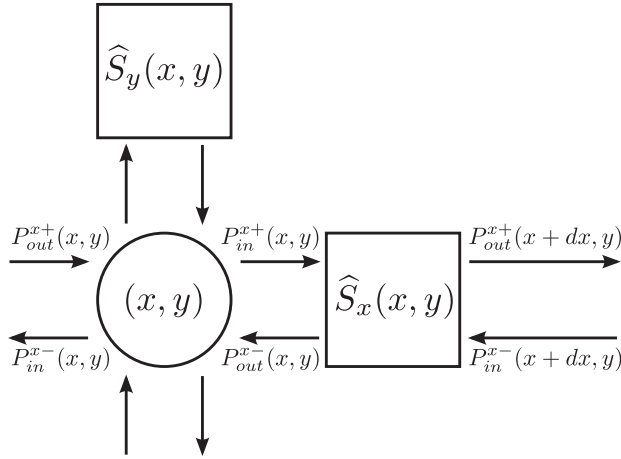


Figure 33.: Sketch of the nodes (circle) and links (boxes) in CRMT3D (in 2D for readability).

The potential is given by, for any  $\alpha$ :

$$\begin{aligned} \mu &= \frac{1}{2} (P_{in}^{\alpha+} + P_{out}^{\alpha-}) \\ &= \frac{1}{2} (P_{in}^{\alpha-} + P_{out}^{\alpha+}) \end{aligned} \quad (195)$$

This notation emphasizes the fact that the potential must be isotropic at a node. It does not depend on alpha, nor does it depend on which side of the node is used. By rewriting Eq. (194) and Eq. (195) in terms of the  $P$  vectors, we obtain the node equation in three dimensions:

$$\begin{pmatrix} P_{in}^{x-} \\ P_{in}^{x+} \\ P_{in}^{y-} \\ P_{in}^{y+} \\ P_{in}^{z-} \\ P_{in}^{z+} \end{pmatrix} = \mathcal{N} \begin{pmatrix} P_{out}^{x-} \\ P_{out}^{x+} \\ P_{out}^{y-} \\ P_{out}^{y+} \\ P_{out}^{z-} \\ P_{out}^{z+} \end{pmatrix}, \quad \text{with } \mathcal{N} = \begin{pmatrix} 1 & 1 & 1 \\ 1 & 1 & 1 \\ 1 & 1 & 1 \end{pmatrix} \otimes \left[ \frac{1}{3} \begin{pmatrix} \mathbb{1} & \mathbb{1} \\ \mathbb{1} & \mathbb{1} \end{pmatrix} - \begin{pmatrix} 0 & \mathbb{1} \\ \mathbb{1} & 0 \end{pmatrix} \right] \quad (196)$$

The  $3 \times 3$  matrix full of ones corresponds to each dimension (for a 2D system, it would only be  $2 \times 2$ , and in 1D, it would just be the scalar 1), and the effect they have on each other. This effect is modeled by the term after the Kronecker product  $\otimes$ . This matrix is of size  $(2 \times 4) \times (2 \times 4)$ , where the  $(2 \times 4)$  emphasizes it is twice the size of the  $P$  vectors (four components: charge + three spin directions)<sup>1</sup>. The factor

<sup>1</sup> To which one must add one component for heat, when including the thermoelectric effects described in Section VI - 3

1/3 is actually  $1/d$ , where  $d$  is the dimension. It comes from the sum in the current conservation equation.

This equation is important, in particular for the software we developed, which is based directly on this equation, and the link equation. However, because of the work we already did on the theory, it is easier to use Eq. (194) and Eq. (195) to obtain our 3D equations.

As we did before, we consider the links to be small slices of material, and use a first order expansion to obtain continuous equations. However, the 3D equivalent of Eq. (160) and Eq. (161) involve terms of the form  $j_R^\alpha(\alpha) - j_L^\alpha(\alpha)$ . They can be removed by summing the equation over  $\alpha$ , and using the current conservation equation. To keep the same notations, the definition of the  $\Lambda$  matrices must be slightly altered to compensate for the additional dimensions. Using the definition for  $\Lambda_\Omega$  and  $\Lambda_\Xi$  introduced in Section V - 6, we get for any dimension  $d$ :

$$\Lambda_t^d = \Lambda_\Omega + \frac{1}{d}\Lambda_\Xi \quad (197)$$

$$\Lambda_r^d = \Lambda_\Omega - \frac{1}{d}\Lambda_\Xi \quad (198)$$

Current conservation finally reads in its continuous form:

$$\sum_{\alpha \in \{x,y,z\}} \partial_\alpha j_\alpha(\alpha) = \Lambda_\Xi \mu(\alpha) \quad (199)$$

Finally, applying the rotation properties on this new set of equations gives us the 3D partial differential equations, corresponding to box (f) in Fig. 22:

$$-\ell_* \partial_\alpha \mu_c = j_\alpha^c - \beta \mathbf{j}_\alpha \cdot \mathbf{m} \quad (200)$$

$$\begin{aligned} -\ell_* \partial_\alpha \boldsymbol{\mu} &= \mathbf{j}_\alpha - \beta j_\alpha^c \mathbf{m} \\ &+ \frac{\ell_*}{\ell_\perp} (\mathbf{m} \times \mathbf{j}_\alpha) \times \mathbf{m} - \frac{\ell_*}{\ell_L} (\mathbf{m} \times \mathbf{j}_\alpha) \end{aligned} \quad (201)$$

$$\sum_\alpha \partial_\alpha j_\alpha^c = 0 \quad (202)$$

$$\sum_\alpha \partial_\alpha \mathbf{j}_\alpha = -\frac{\ell_*}{\ell_{sf}^2} \boldsymbol{\mu} - \frac{1}{\ell_\perp} (\mathbf{m} \times \boldsymbol{\mu}) \times \mathbf{m} + \frac{1}{\ell_L} (\mathbf{m} \times \boldsymbol{\mu}) \quad (203)$$

The derivation thus far has completely ignored the influence of temperature. This both reflects the history of the theory, as well as answers a need for clarity. To include

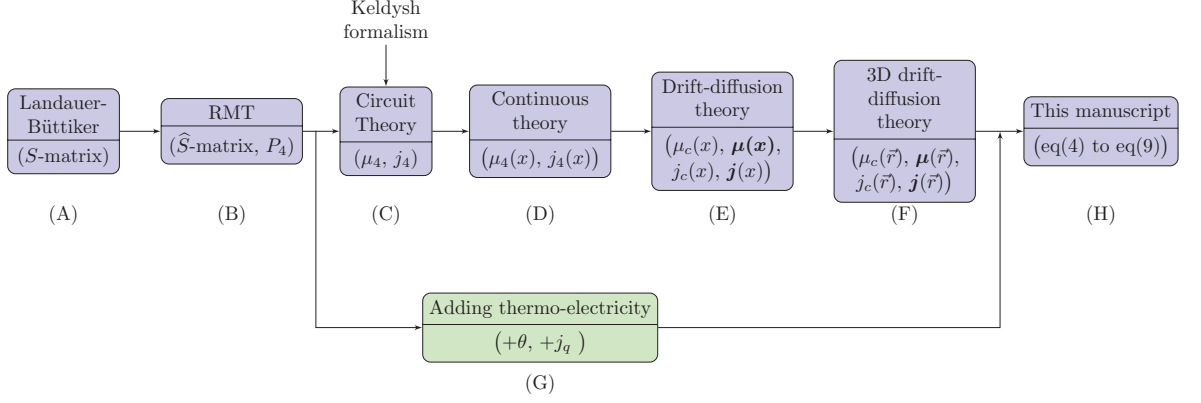


Figure 34.: Seventh and final step in the history of CRMT: including thermoelectric effects.

thermoelectric effects, we simply extend the matrices and  $P$ -vectors to be of rank 5 instead of 4, and follow the same path we used to obtain Eq. (200) to Eq. (203).

We give to the new matrices the form:

$$\widetilde{\Lambda}_{\Omega} = \begin{pmatrix} \widetilde{\Gamma}_{\uparrow} & 0 & 0 & \widetilde{\Gamma}_{\uparrow\downarrow} & \Gamma_{S,\uparrow} \\ 0 & \Gamma_{\text{mx}}^{\text{eff}} & 0 & 0 & 0 \\ 0 & 0 & \Gamma_{\text{mx}}^{\text{eff}*} & 0 & 0 \\ \widetilde{\Gamma}_{\uparrow\downarrow} & 0 & 0 & \widetilde{\Gamma}_{\downarrow} & \Gamma_{S,\downarrow} \\ \Gamma_{\Pi,\uparrow} & 0 & 0 & \Gamma_{\Pi,\downarrow} & \Gamma_H \end{pmatrix} \quad (204)$$

$$\widetilde{\Lambda}_{\Xi} = \begin{pmatrix} \Gamma_{\text{sf}} & 0 & 0 & -\Gamma_{\text{sf}} & 0 \\ 0 & \Gamma_{\tau} & 0 & 0 & 0 \\ 0 & 0 & \Gamma_{\tau}^* & 0 & 0 \\ -\Gamma_{\text{sf}} & 0 & 0 & \Gamma_{\text{sf}} & 0 \\ 0 & 0 & 0 & 0 & 0 \end{pmatrix} \quad (205)$$

We assume that the thermoelectric effects do not affect current conservation, and that of course the heat current is conserved. We also assume that the behavior of transverse spins is not affected by temperature gradients. We also extend naturally the variables  $\mu_4$  and  $j_4$  to  $\mu_5$  and  $j_5$ , so that the first four rows are unchanged, and the last corresponds to the temperature  $\theta = k_B T$  (last row of  $\mu_5$ ) and the heat current  $j_q$  in units of energy. The conversion to the heat current  $Q$  in SI units, is made through:

$$Q = \frac{4k_B T_{av}}{e^2 \mathcal{R}_{\text{Sh}}} j_q \quad (206)$$

We assume that the new coefficients keep reflecting the diffusive transport of heat by the electrons. We showed in Section IV that this includes heat diffusion, as well as the Seebeck et Peltier effects. Although we did not prove it, we assume this also includes the spin-dependent thermoelectric effects. Because we assume that the thermoelectric effects only affect the spin components longitudinal to the magnetization, we will disregard the transverse effects to simplify the notations.

Ohm's law for each of the majority and minority spins can be extended to include the Seebeck effect. The contribution is the product of the Seebeck coefficient and the conductivity (each for the relevant spin species) times the temperature gradient. On the other hand, the heat current is the sum of the two Peltier contributions (for majority and minority spins) and of the heat diffusion (Fourier's law).

This is summarized into the following matrix equation found, for example, in Ref[67, 74]:

$$\begin{pmatrix} J_{\uparrow} \\ J_{\downarrow} \\ J_Q \end{pmatrix} = \begin{pmatrix} \sigma_{\uparrow} & 0 & \sigma_{\uparrow}S_{\downarrow} \\ 0 & \sigma_{\downarrow} & \sigma_{\downarrow}S_{\downarrow} \\ \sigma_{\uparrow}S_{\uparrow}T_{av} & \sigma_{\downarrow}S_{\downarrow}T_{av} & \kappa \end{pmatrix} \begin{pmatrix} \partial_{\alpha}\mu_{\uparrow}/e \\ \partial_{\alpha}\mu_{\downarrow}/e \\ -\partial_{\alpha}T \end{pmatrix} \quad (207)$$

We set the additional coefficients in  $\Lambda_{\Omega}$  so that they match the previous thermoelectric diffusion equations. We first convert this equation to use the variables in units of energy using Eq. (190), Eq. (191) and Eq. (206). Then, we invert the system, so that we express potential and temperature gradients as functions of the currents, in order to identify it with the non-transverse coefficients in:

$$\partial_{\alpha}\mu_5 = \widetilde{\Lambda}_{\Omega}j_5 \quad (208)$$

This identification yields:

$$\widetilde{\Gamma}_{\uparrow(\downarrow)} = \frac{1 \mp \beta}{2\ell_*} + \frac{\Gamma_H}{2}(s \pm \Delta s)^2 \quad (209)$$

$$\widetilde{\Gamma}_{\uparrow\downarrow} = \frac{\Gamma_H}{2}(s^2 - \Delta s^2) \quad (210)$$

$$\Gamma_{S,\uparrow(\downarrow)} = -\Gamma_H(s \pm \Delta s) \quad (211)$$

$$\Gamma_{\Pi,\uparrow(\downarrow)} = -\frac{\Gamma_H}{2}(s \pm \Delta s) \quad (212)$$

$$\Gamma_H = \frac{1}{2\ell_H} \quad (213)$$

The tilded coefficients have a common property, they depend on the square of the  $s$  and  $\Delta s$  coefficients. This comes from the inversion of Eq. (207). For most metals however, these values are fairly small, and can be neglected. In that limit, they reduce to their expression in the purely electrical limit:

$$\tilde{\Gamma}_{\uparrow(\downarrow)} = \Gamma_{\uparrow(\downarrow)} \quad (214)$$

$$\tilde{\Gamma}_{\uparrow\downarrow} = 0 \quad (215)$$

We also obtain the expression of  $\ell_H = \frac{\ell_*}{1-\beta^2} (\mathcal{L} - [s^2 + 2\beta s \Delta s + \Delta s^2])$ . Note that all the terms inside the square brackets would also disappear in the limit of small values of  $s$  and  $\Delta s$ .  $\ell_H$  is essentially the determinant of the matrix in Eq. (207).

Finally, we extend our matrix basis, and we give their rotation properties. First, we define  $\tilde{I}_{ij}$ , our new set of matrices. The first four rows and column is the matrix  $I_{ij}$  previously defined, while the remaining entries are set to zero. We add to that collection the following matrices:

$$I_H = \begin{pmatrix} 0 & 0 & 0 & 0 & 0 \\ 0 & 0 & 0 & 0 & 0 \\ 0 & 0 & 0 & 0 & 0 \\ 0 & 0 & 0 & 0 & 0 \\ 0 & 0 & 0 & 0 & 1 \end{pmatrix} \quad (216)$$

$$I_S^\pm = \begin{pmatrix} 0 & 0 & 0 & 0 & 1 \\ 0 & 0 & 0 & 0 & 0 \\ 0 & 0 & 0 & 0 & 0 \\ 0 & 0 & 0 & 0 & \pm 1 \\ 0 & 0 & 0 & 0 & 0 \end{pmatrix} \quad (217)$$

$$I_\Pi^\pm = \begin{pmatrix} 0 & 0 & 0 & 0 & 0 \\ 0 & 0 & 0 & 0 & 0 \\ 0 & 0 & 0 & 0 & 0 \\ 0 & 0 & 0 & 0 & 0 \\ 1 & 0 & 0 & \pm 1 & 0 \end{pmatrix} \quad (218)$$

Finally, we also extend our rotation matrices:

$$\tilde{R} = \begin{pmatrix} \hat{R} & 0 \\ 0 & 1 \end{pmatrix} \quad (219)$$

Its block-diagonal form ensures that  $\tilde{R}^{-1}$  has the same structure. Eq. (179) to Eq. (183) remain valid in their rank 5 form, and we add to the list of rotation properties some rotation-invariant ones (related to the heat and charge transport only):

$$\left[ \tilde{R}I_H \tilde{R}^{-1} \right] \mathbf{p}_5 = p_H \Sigma_H \quad (220)$$

$$\left[ \tilde{R}I_S^+ \tilde{R}^{-1} \right] \mathbf{p}_5 = p_H \Sigma_c \quad (221)$$

$$\left[ \tilde{R}I_{\Pi}^+ \tilde{R}^{-1} \right] \mathbf{p}_5 = 2p_c \Sigma_H \quad (222)$$

and some that depend on rotations (they encode the spin-dependent part)

$$\left[ \tilde{R}I_S^- \tilde{R}^{-1} \right] \mathbf{p}_4 = p_H \mathbf{m} \cdot \Sigma \quad (223)$$

$$\left[ \tilde{R}I_{\Pi}^- \tilde{R}^{-1} \right] \mathbf{p}_4 = 2\mathbf{p} \cdot \mathbf{m} \cdot \Sigma_H \quad (224)$$

With those last ingredients, we have presented all that is needed to derive the final set of differential equations describing charge, spin and heat transport in the bulk of three-dimensional metallic systems:

$$-\ell_* \partial_\alpha \mu_c = j_\alpha^c - \beta \mathbf{j}_\alpha \cdot \mathbf{m} + \frac{\ell_*}{\ell_H} s (s j_\alpha^c + \Delta s \mathbf{j}_\alpha \cdot \mathbf{m}) - \frac{\ell_*}{\ell_H} s j_\alpha^q \quad (225)$$

$$\begin{aligned} -\ell_* \partial_\alpha \boldsymbol{\mu} = & \mathbf{j}_\alpha - \beta j_\alpha^c \mathbf{m} + \frac{\ell_*}{\ell_H} \Delta s (s j_\alpha^c \mathbf{m} + \Delta s \mathbf{j}_\alpha) - \frac{\ell_*}{\ell_H} \Delta s j_\alpha^q \mathbf{m} \\ & + \frac{\ell_*}{\ell_\perp} (\mathbf{m} \times \mathbf{j}_\alpha) \times \mathbf{m} - \frac{\ell_*}{\ell_L} (\mathbf{m} \times \mathbf{j}_\alpha) \end{aligned} \quad (226)$$

$$-\ell_H \partial_\alpha \theta = -s j_\alpha^c - \Delta s \mathbf{j}_\alpha \cdot \mathbf{m} + j_\alpha^q \quad (227)$$

$$\sum_\alpha \partial_\alpha j_\alpha^c = 0 \quad (228)$$

$$\sum_\alpha \partial_\alpha j_\alpha^q = 0 \quad (229)$$

$$\sum_\alpha \partial_\alpha \mathbf{j}_\alpha = -\frac{\ell_*}{\ell_{sf}^2} \boldsymbol{\mu} - \frac{1}{\ell_\perp} (\mathbf{m} \times \boldsymbol{\mu}) \times \mathbf{m} + \frac{1}{\ell_L} (\mathbf{m} \times \boldsymbol{\mu}) \quad (230)$$

This set of equation is the current and final state of the theory derived during this thesis

## VI - 4 3D THERMOELECTRIC INTERFACE EQUATIONS AND BOUNDARY CONDITIONS AT THE RESERVOIRS

A set of equations describing the properties of a bulk material cannot be complete without two more elements: equations describing the interface between two materials, and equations describing the interaction of the system with the outside world, in other world boundary conditions. We present them here in their latest form, for three-dimensional systems, and including effects from the temperature.

## VI - 4.1 Interfaces

In Section V - 5.1 we gave a first expression for the matching conditions at a  $F|N$  interface. Applying the techniques introduced for the bulk equations, we go one step further on those interface equations. First, let us place ourselves in the case where temperature is taken into account. Because the thermoelectric properties of interfaces are very poorly known, we will neglect them altogether. If the need arises one day, the derivation presented here can be easily extended to incorporate them.

If we write  $T_H$  the transmission coefficient for the heat in  $\hat{t}$ , we get:

$$j_\sigma = \frac{1}{4} \frac{T_\sigma}{1 - T_\sigma} (\mu_{F,\sigma} - \mu_{N,\sigma}) \quad (231)$$

$$j_q = \frac{1}{2} \frac{T_H}{1 - T_H} (\theta_F - \theta_N) \quad (232)$$

In the Valet-Fert theory, interfaces are parametrized by a surface resistance  $r_b^*$  and a spin asymmetry  $\gamma$ . We introduce the parameter  $g_* = \mathcal{R}_{\text{Sh}}/4r_b^*(1 - \gamma^2)$ ,  $n_\alpha$  the component in the  $\alpha$  direction of the normal pointing from the normal to the ferromagnetic side and  $\varepsilon_N = -\varepsilon_F = 1$ . We set the value of  $T_{\uparrow/\downarrow}$  so that it matches the Valet-Fert condition:

$$T_{\uparrow/\downarrow} = \frac{\mathcal{R}_{\text{Sh}}}{\mathcal{R}_{\text{Sh}} + 2r_b^*(1 \mp \gamma)} \quad (233)$$

Using the notation  $\Delta\mu = \mu_F - \mu_N$  and  $\Delta\theta = \theta_F - \theta_N$  we give the final form of the interface equations:

$$\sum_{\alpha} n_{\alpha} j_{\alpha}^c = g_* [\Delta\mu_c + \gamma \Delta\boldsymbol{\mu} \cdot \mathbf{m}] \quad (234)$$

$$\begin{aligned} \sum_{\alpha} n_{\alpha} j_{\alpha}^a = g_* & \left[ \mathbf{m} \cdot \Delta\boldsymbol{\mu} + \gamma \Delta\mu_c \right] \mathbf{m} \\ & + \operatorname{Re}(\sigma_{\text{mx}}^a) (\mathbf{m} \times \Delta\boldsymbol{\mu}) \times \mathbf{m} - \operatorname{Im}(\sigma_{\text{mx}}^a) \mathbf{m} \times \Delta\boldsymbol{\mu} \\ & + \varepsilon_a \left[ \operatorname{Re}(\eta_{\text{mx}}^a) (\mathbf{m} \times \boldsymbol{\mu}^a) \times \mathbf{m} - \operatorname{Im}(\eta_{\text{mx}}^a) \mathbf{m} \times \boldsymbol{\mu}^a \right] \end{aligned} \quad (235)$$

$$\sum_{\alpha} n_{\alpha} j_{\alpha}^q = \mathcal{L} g_* \Delta\theta \quad (236)$$

To obtain the last equation, we rewrote Wiedemann-Franz law in terms of  $g_*$ , and derived an expression for  $T_H$ :

$$T_H = \frac{\mathcal{L} \mathcal{R}_{\text{Sh}}}{\mathcal{L} \mathcal{R}_{\text{Sh}} + 2r_b^* (1 + \gamma^2)} \quad (237)$$

Let us finally discuss our design choice. The interframedace described here, as we said, is between a normal and a ferromagnetic material. It can of course describe an interface between two normal materials, by setting the mixing coefficients to zero, and by lifting the spin dependence of the coefficients. However, as presented here, it cannot describe an interface between two ferromagnets with non-collinear magnetizations. This case should be rare anyway, except in oversimplified models. Indeed, very few real devices involve neighboring ferromagnetic layers, because of the difficulty to stay in the macrospin limit in that case. This is the reason why spacer layers are usually placed between the two ferromagnets\*

#### VI - 4.2 Boundary conditions at the reservoirs

In order to include the Sharvin resistance properly, the conditions at the reservoirs are not as simple as imposing directly a value to the potential and temperature.

Assuming the applied voltage  $V_b$  and temperature  $\Delta T$ , and using the normal  $n_{\alpha}$ , pointing towards the system, they read:

$$\sum_{\alpha} n_{\alpha} j_{\alpha}^c + \mu_c = eV_b \quad (238)$$

$$\sum_{\alpha} n_{\alpha} \mathbf{j}_{\alpha} + \boldsymbol{\mu} = 0 \quad (239)$$

$$\sum_{\alpha} n_{\alpha} j_{\alpha}^q + \theta = k_B \Delta T \quad (240)$$

The next and final section of this chapter introduces addition laws for material properties, a very good tool to describe efficiently the complex stacks of materials in actual devices.

## VI - 5 EFFECTIVE PARAMETERS

This last section is actually a journey back to the basics of our theory. We started by introducing the addition law for  $S$  and  $\hat{S}$  matrices. We finish by giving the same kind of addition laws directly for the material parameters.

In real systems, the layers of interest (namely the fixed and free magnetic layers) are surrounded by many other layers, aiming at introducing magnetization pinning, (anti-)ferromagnetic coupling, spin-flip, and so on. However, from a transport point of view, these layers do not introduce any new feature. For a high level, qualitative description of the system, disregarding them is not a problem, and is the simplest solution. But as soon as a quantitative description is needed, the only solution seems to be numerical simulation. We present here an intermediate solution, which also gives the possibility of engineering the material parameters to suit the needs of the experiment by choosing the correct materials.

Let us consider a number of layers of various materials in series. Those materials can be normal or magnetic, up to the condition that the magnetization orientations must all be the same. This stack of layers (and their respective interfaces) can be considered a single material, with equivalent parameters. To give a simple expression, we assume a few things:

- we neglect spin-flip
- we ignore the transverse penetration length
- because thermoelectric coefficients are usually small, we keep them only at the lowest order

Material  $i$  in the stack is described by the following set of parameters:  $\{r_i, \beta_i, \mathcal{L}_i, s_i, \Delta s_i\}$ . They describe its reduced surface resistance, spin asymmetry, reduced Lorenz number ( $\mathcal{L} = \pi^2/3$  by default), Seebeck number and spin-dependent Seebeck number.

parameter	Bulk material	Interface
$r$	$2\rho_*L/\mathcal{R}_{\text{Sh}}$	$2r_b^*/\mathcal{R}_{\text{Sh}}$
$\beta$	$\beta$	$\gamma$
$s$	$\frac{e}{k_B}S$	0
$\Delta s$	$\frac{e}{k_B}\Delta S$	0

Table 3.: Reduced parameters used in the effective parameters formula, with their expression depending on whether they correspond to bulk or interface materials.

Table 3 describes the expression of the reduced parameters whether they are for bulk or interface. In the case of bulk,  $L$  is the thickness of the layer. Since  $\mathcal{L}$  does not intrinsically depend on the type of material, it is not displayed in the table. With those notations, the corresponding effective material is described by the set of parameters  $\{\bar{r}, \bar{\beta}, \bar{\mathcal{L}}, \bar{s}, \bar{\Delta s}\}$ , with:

$$\bar{r} = \sum_i r_i \quad (241)$$

$$\bar{r}\bar{\beta} = \sum_i r_i\beta_i \quad (242)$$

$$\bar{r}(1 - \bar{\beta}^2)/\bar{\mathcal{L}} = \sum_i r_i(1 - \beta_i^2)/\mathcal{L}_i \quad (243)$$

$$\bar{r}(1 - \bar{\beta}^2)\bar{s}/\bar{\mathcal{L}} = \sum_i r_i(1 - \beta_i^2)s_i/\mathcal{L}_i \quad (244)$$

$$\bar{r}(1 - \bar{\beta}^2)\bar{\Delta s}/\bar{\mathcal{L}} = \sum_i r_i(1 - \beta_i^2)\Delta s_i/\mathcal{L}_i \quad (245)$$

With those expression, one can either reduce the number of layers in an analytical (or numerical) description while keeping the real properties of the ensemble. Another consequence of these equations is that one can also engineer new values for the parameters with a limited number of different materials, by adjusting their re-

spective thicknesses, choosing the proper normal spacers to benefit from interface properties of interest, or reducing a parameter to the benefit of another.

For instance, we saw with Eq. (70) that for a spin-valve's torque to display a wavy behavior, having one layer much strongly polarized than the other is beneficial. The ideal case would be to have for the fixed layer a ferromagnetic material with almost  $\beta = 0$ . We can construct such a material by using for example a layer of 2.9 nm of Co, followed by a layer of 1 nm of Ru. Using Eq. (242), Table 8 and Table 9, we find that  $\beta_{\text{Co}_{2.9}|\text{Ru}_1} = 0.00006$ .

Those equations also underline the importance of the interface parameters, especially considering the small thicknesses of nowadays bulk layers (a few nanometers usually).

Part C

APPLICATIONS TO TRANSVERSE SPIN CURRENTS  
IN VARIOUS MAGNETIC LANDSCAPES



### Summary of Part C

Our theory extends the well-known Valet-Fert theory by properly accounting for the Sharvin resistance, and more importantly by describing non-collinear systems (that is systems where the magnetizations are not all along the same axis). In particular, in our bulk equations the transverse behavior depends on two characteristic lengths: the transverse penetration length  $\ell_{\perp}$  and the Larmor precession length  $\ell_L$ . Although those lengths have never, at the time when this thesis was written, been measured, some *ab initio* calculations hinted at very short lengths, a few nanometers. We extracted from the *ab initio* literature possible values for these lengths, and proposed a device aiming at measuring them experimentally.

Going to another class of devices, we investigated transport in magnetic domain walls. Our focus went to long ( $> 20$  nm) walls, since they have the property that the spin accumulation follows the magnetization orientation adiabatically. We investigated there the out-of-plane component of the spin-transfer torque, which is poorly known. We found and proved that in such walls this component of the torque is related to the in-plane component through the aforementioned transverse transport properties. This means we can relate a micromagnetic concept to the transport through the system.

Finally, we pushed our theory to its limits by considering the presence of a magnetic insulator in a non-local spin-valve, and investigated how it reflected transverse spins. This study was motivated by experiments by van Wees *et al.*, and tried to account qualitatively for some of their results and in one occurrence explain their lack thereof. We propose a simple model describing the interface, with simple parameters, and show that the various limits of this model explain their findings. Our 3D simulation also gave indications on how to obtain a stronger measured signal by optimizing the geometry of the device.

### Résumé de la Partie C

Notre théorie étend la célèbre théorie de Valet-Fert en incluant proprement la résistance de Sharvin, et plu simportant encore, en permettant de décrire des systèmes non-collinéaires (c'est à dire des systèmes où les aimantations ne pointent pas toutes le long du même axe). En particulier, dans nos équations décrivant les matériaux massifs, le comportement transverse dépend de deux longueurs caractéristiques : la longueur de pénétratio transverse  $\ell_{\perp}$  et la longueur de précession de Larmor  $\ell_L$ . Bien que ces longueurs n'aient jamais, à l'heure d'écriture de cette thèse, été mesurées, certains calculs *ab initio* tendent à indiquer qu'elles sont très courtes, de l'ordre de quelques nanomètres. Nous avons extrait de ces calculs des valeurs possibles pour ces longueurs, and proposons un système servant à les mesurer de manière expérimentale.

Concernant une autre classe de systèmes, we avons étudié le transport dans les murs de domaines magnétiques. Nous nous sommes concentrés sur les murs longs ( $> 20$  nm), car ils ont la capacité de laisser l'accumulation de spin suivre l'aimantation de manière adiabatique. Nous y avons étudié la composante hors-plan du torque de transfert de spin, qui est très mal connue. Nous avons trouvé et prouvé que dans de tels murs cette composante du torque est relié à sa composante dans le plan à travers les propriétés de transport transverse mentionnées précédemment. Cela signifie que nous avons la possibilité de relier un concept micromagnétique au transport dans le système.

Enfin, nous avons poussé notre théorie dans ses limites en considérant la présence d'un isolant magnétique dans une valve de spin non-locale, et étudié comment les spins transverses étaient réfléchis. Cette étude a été motivée par des expériences de van Wees *et al.*, et a essayé de comprendre de manière qualitative certains de résultats, et dans un cas, leur absence. Nous proposons un modèle simple décrivant l'interface, avec des paramètres simples, et montrons que les différentes limites du modèle expliquent leurs résultats. Notre simulation 3D a aussi indiqué comment obtenir un signal mesuré plus important en optimisant la géométrie du système.

# VII

---

## TRANSVERSE PENETRATION AND PRECESSION

---

Most of the original work in this thesis is related, in some way or another, with the behavior of spins transverse to the surrounding magnetization. In this chapter we focus only on the results involving solely voltage biases. Results based on the presence of temperature gradients are treated in Part D.

Most of the work about spin currents arriving on a magnetic layer with non-collinear magnetization and current polarization assumed the transverse part of the spin current was absorbed at the interface with the ferromagnet. Although some of it is indeed absorbed at the interface, in most cases some is transmitted, and absorbed by the bulk material. The assumption held as long as the layers were thick enough, but the shrinking dimensions of nowadays devices makes it necessary to address this question more precisely. We found that the characteristic thickness of absorption is usually of the order of the nanometer. However, some materials (Ni for instance) display a much lower absorption rate, along certain crystalline directions. This means that the typical layer thicknesses are not enough to fully absorb transverse spins. One consequence is that the deposited momentum by a spin current is actually less than what the interface absorption assumption suggests. Therefore, a magnetic layer could be more difficult to switch than anticipated.

Magnetic domain walls are a prime example of the need to investigate the behavior of the spins transverse to the local magnetization in bulk materials. In micromagnetism, the dynamics of domain walls can be properly discussed only when taking the spin-transfer torque into account, and furthermore by considering its in-plane as well as its out-of plane component. The latter is responsible for critical current densities lower than what was expected when taking only the in-plane component into account. Describing properly the torque (and its out-of-plane component in particular) is therefore critical to predict accurately domain wall dynamics. And since the out-of-plane component plays such an important role, the rate of absorption of transverse spins is important, but their rate of precession around the local magneti-

zation becomes utterly important too, since it is directly related to how much of the torque will point out-of-plane.

Finally, more and more experiments and devices are based on magnetic insulators. Understanding the behavior of spins transverse to the insulator's magnetization is also important to ensure the device works as intended. How much of the spin current is absorbed? For the reflected part, how much was its polarization altered by the reflexion? Those are typical questions that needs answers to take experimental devices to industrial prototypes.

In this part, we start focusing on the absorption and precession properties of bulk ferromagnets. We extract their value from *ab initio* calculation, and explain how a modified spin-valve can help measure them. Then we show a study of the spin-transfer torque in domain walls, and give an expression of the ratio of its out-of-plane to in-plane component (the so-called  $\beta$  factor in micromagnetism) in the case of long walls. Finally, we give the result of a cooperation with van Wees' group in Gröningen University, where we studied the reflexion of spins transverse to the magnetization of an insulator layer.

## VII - 1 PENETRATION AND PRECESSION OF SPINS TRANSVERSE TO THE MAGNETIZATION

The transverse part of our equations for bulk materials is parametrized with only two lengths, but unlike the other parameters, they are not readily available in the literature. We show however that they can be extracted from *ab initio* calculations that are in the literature, and then give the example of a device that can be used to measure those lengths.

### VII - 1.1 *Ab initio calculations*

The quantities  $\ell_{\perp}$  and  $\ell_L$ , appearing in the transverse part of the transport equations Eq. (226) and Eq. (230), are very poorly known as of now. The only hint we have about their value is the fact that the interface approximation, stating that all the transverse behavior happens only at interfaces, works very well for many systems. This must mean that those lengths are short. Their ballistic origin also gives the mean free path as an upper bound.

Although no direct measurement of the mixing conductance exists, there are however some *ab initio* calculations, typically in N|F|N trilayers. We are interested in particular in graphs of the mixing conductance (or transmission) *vs.* the thickness

of the ferromagnetic layer. The mixing transmission  $T_{\text{mx}}$  is a complex number (encoding the two transverse directions in its real and imaginary part), and up to tiny corrections due to the multiple reflexions at the interfaces, the mixing transmission for a N|F|N trilayer, with a ferromagnetic layer of thickness  $d$  is given by:

$$T_{\text{mx}} = [T_{\text{mx}}^{\text{int}}]^2 \exp\left(-\frac{d}{\ell_{\perp}} + i\frac{d}{\ell_L}\right) \quad (246)$$

Knowing this, we expect the graphs of the mixing conductance to show dampened oscillations, with pseudo-period of  $\ell_L$  and dampening constant  $\ell_{\perp}$ .

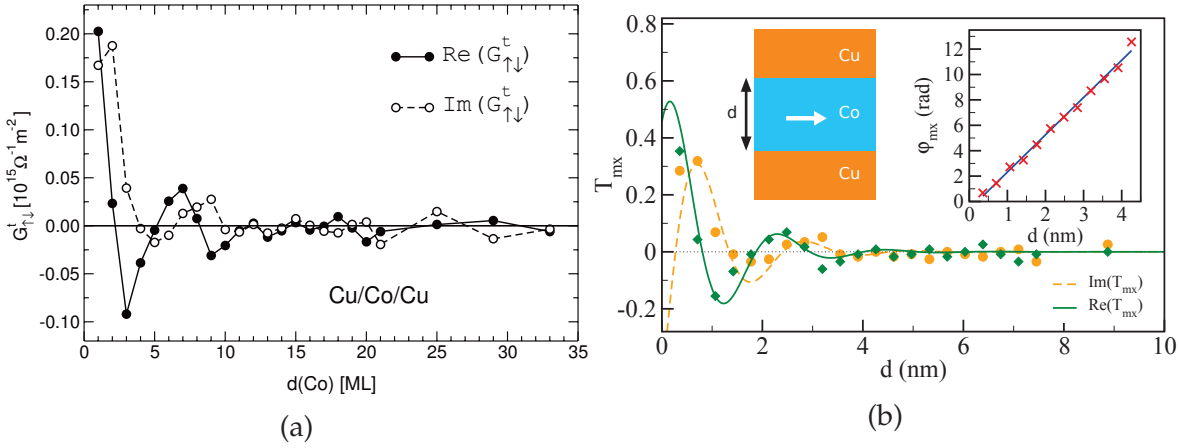


Figure 35.: (a) *ab initio* calculation of the mixing conductance of a Cu|Co|Cu trilayer, for fcc Co in the (111) direction. (b) Fit of Fig. 35a using Eq. (246). The x-axis has been converted into nanometers instead of monolayers, while the y-axis has been converted to a transmission instead of a conductance. The lattice constant used for conversion is  $a = 3.549 \text{ \AA}$ . The left inset is a sketch of the simulated system, with length  $d$  indicated. The right inset is a plot of the phase of  $G_{\text{mx}}$  and its linear fit with respect to  $d$ . Data and relevant information are taken from [11].

Fig. 35a is a typical graph of an *ab initio* calculation of the mixing conductance of a N|F|N trilayer. With such data, we fit Eq. (246), and extract the two lengths of interest  $\ell_L$  and  $\ell_{\perp}$ , as well as the mixing transmission for the interface (when the transmission and not the conductance is plotted). This fit is displayed in Fig. 35b. Information about interface properties are to be taken with caution, since they depend heavily on how clean, how smooth and how sharp the interface actually is.

Since  $\ell_L$  and  $\ell_{\perp}$  are intrinsically ballistic effects, they depend, among other things, on the crystalline direction under consideration. This can lead to huge differences,

depending on the material, as can be seen on Table 4. The case of nickel is interesting to more than one account. It is the reported material with the longer transverse penetration length  $\ell_{\perp}$ , but also the one exhibiting the biggest dependence on crystallinity. We will see in the next chapter that this deep penetration of transverse spins is beneficial towards having a stronger out-of-plane torque in domain-walls (which in turn helps reducing the critical current needed to start their motion).

Material	Reference	$\ell_L$ (nm)	$\ell_{\perp}$ (nm)	Interface	$T_{\text{mx}}^{\text{int}}$
Co(110)	[14]	$0.2 \pm 0.05$	$3 \pm 0.1$	CuCo	/
Co(111)	[14]	$0.2 \pm 0.05$	$4 \pm 0.1$	CuCo	/
Co(111)	[11]	0.34	$0.75 \pm 0.02$	CuCo	0.28-0.55i
Co(111)	[12]	0.37	$0.95 \pm 0.05$	CuCo	/
Fe(001)	[11]	0.30	$1.2 \pm 0.05$	AuFe	0.57-0.18i
Ni(100)	[13]	0.64	$10 \pm 0.1$	CuNi	/
Ni(111)	[12]	0.72	$4.6 \pm 0.1$	CuNi	/
Py(100)	[13]	1.42	$0.9 \pm 0.05$	CuPy	/
Py(111)	[12]	0.7	$1 \pm 0.1$	CuPy	/

Table 4.: Values of  $\ell_L$  and  $\ell_{\perp}$  for various materials, and various crystalline directions, extracted from *ab initio* calculations found in the literature.

## VII - 1.2 Measurement setup

Here we present a simple experimental setup allowing the measurement of those two lengths. It is a CPP-GMR measurement in a multilayer with a structure of the type  $N|P_{\parallel}|N|X_{\perp}|N|A_{\parallel}|N$ , as presented in the inset of Fig. 36. In essence, it is a regular spin-valve where we inserted a third magnetic layer in the middle, with its magnetization orthogonal to the two other ones. N represents normal spacers, P the first ferromagnetic layer, acting as a polarizer, X the (ferromagnetic) study layer, and A the last ferromagnetic layer, acting as the analyzer. The subscript indicate that the magnetization of the polarizer and analyzer must be along the same axis, while the study layer (which transverse properties we want to investigate) should have a magnetization along an orthogonal axis. Depending on the nature of the study layer, this can be implemented in two ways.

- if the study layer has a strong perpendicular anisotropy, take advantage of it, and use analyzer and polarizer with planar anisotropy

- if the study layer has a weak or no perpendicular anisotropy, make its magnetization lie in the plane of growth, and use materials with perpendicular anisotropy for the polarizer and analyzer

Bulk materials with perpendicular anisotropy are rare, and rather exotic. However, as reported in Ref[75], a multilayer of  $(\text{Cu}_{0.4}|\text{Ni}_{0.8})_{\times 3}$  displays perpendicular anisotropy, and is made up of materials readily available and used by any laboratory able to create CPP-GMR devices. We used this configuration in the simulation displayed in Fig. 36, as is suggested on the sketch in inset.

To understand the signal of the CPP-GMR obtained in this configuration, let us assume that the ferromagnetic materials are perfectly polarized, and consider an electron coming into that device. The polarizer imposes its direction onto the spin of this electron, which then enters the X layer. There, feeling an orthogonal local field (due to the magnetization), it starts precessing, until it reaches the analyzer layer. If the X layer has a thickness  $d = (2k + 1)\pi\ell_L/2$  ( $k$  an integer), the spin has made a quarter of a rotation, and the spin is orthogonal to the magnetization of the analyzer layer. Therefore, the conductance of the system is zero (assuming a transverse spin is not transmitted). If  $d = k\pi\ell_L$ , the spin will be fully transmitted, as it is collinear to the magnetization of the analyzer. The resulting conductance will be either minimum or maximum depending on the parity of  $k$  and the state (parallel or antiparallel) of the device. We summarize this in Table 5:

	Parallel	Antiparallel
$k$ even	max	min
$k$ odd	min	max

Table 5.: Conductance value for the transverse lengths measurement, with a study layer of thickness  $d = k\pi\ell_L$ , and for the parallel or antiparallel state of the device.

Additionally, on top of that oscillating pattern, one has to take into account that less and less spins go all the way through, the thicker the study layer is. Finally, the CPP-GMR in this geometry has the following form:

$$\text{GMR}(d) = A \cos\left(\frac{d}{\ell_L} - \delta\right) e^{-d/\ell_{\perp}} \quad (247)$$

where  $A$  is some amplitude constant, and  $\delta$  is a dephasing, depending on the phase of the  $T_{\text{mx}}$  of the interfaces, among other things. Both are material dependent<sup>1</sup>.

<sup>1</sup> They may even be sample dependent, since the randomness of the interfaces may affect their value

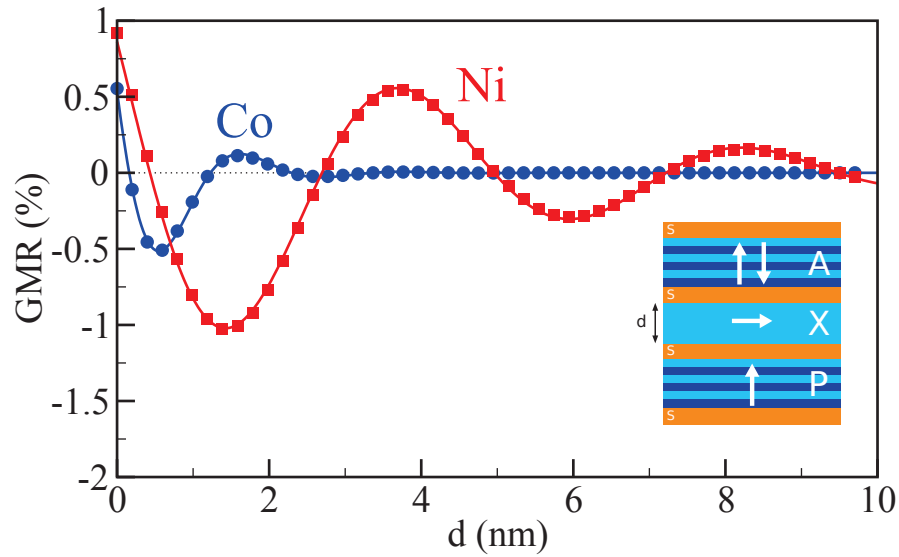


Figure 36.: GMR signal for a spin-valve with transverse layer versus the thickness  $d$  (nm) of this layer. Squares (circles) correspond to the simulation data for Ni(100) (Co (111)), while the lines correspond to a numerical fit with Eq. (247). The inset is a sketch of the device, with the multilayer  $(\text{Cu}_{0.4}|\text{Ni}_{0.8})_{\times 3}$  as polarizer and analyzer.

As the plot in Fig. 36 shows, the simulation and the theoretical formula agree perfectly. Although the GMR signal is weaker than usual values, it stays of the order of a percent, which should be enough to extract relevant data, in clean enough samples. It is our hope that such a simple device can be used to measure values of the spin transverse lengths, and first confirm the *ab initio* predictions, and second provide a corpus of values useful to predict the transverse behavior of devices.

# VIII

---

## TORQUES IN A DOMAIN WALL

---

As introduced in Section III - 5, there are two components to the torque. And although the in-plane torque is much stronger and has received most of the research effort, the presence of the out-of-plane is needed to explain with any accuracy experiments of domain wall motion.

### VIII - 1 IN-PLANE AND OUT-OF-PLANE TORQUES

We now present a model to derive an expression for  $\beta_\tau$ , introduced in Section III - 5 in a domain wall. As a reminder,  $\beta_\tau = -\tau_2/\tau_1$ , where  $\tau_1$  is the in-plane torque, and  $\tau_2$  is out-of-plane.

This derivation will hold two parts. The first will assume very little about the magnetic texture, only that the magnetization is not constant, and that only the angle between  $\mathbf{m}$  and  $\mathbf{e}_z$  varies. The results from this first part can be applied to any system. The second part will introduce some assumptions so as to give an analytical expression for  $\beta_\tau$ .

We start from Eq. (200) to Eq. (203), in a 1D piece of bulk material. We use the local magnetization basis  $(\mathbf{m}, \mathbf{e}_1, \mathbf{e}_2)$  introduced in Section I - 2.6. If  $\mathbf{m}$  varies continuously and smoothly in space (which we assume to be the case in domain walls),  $\mathbf{e}_1 = \partial_x \mathbf{m} / |\partial_x \mathbf{m}|$ . From this definition, it comes that  $\mathbf{e}_2 = \mathbf{m} \times \mathbf{e}_1$ . Expanding the spin vectors in that basis, we get  $\boldsymbol{\mu} = \mu_{\parallel} \mathbf{m} + \mu_1 \mathbf{e}_1 + \mu_2 \mathbf{e}_2$  (and similarly for  $\mathbf{j}$ ).

We assume that only the angle  $\theta$  between  $\mathbf{m}$  and  $\mathbf{e}_z$  varies with space. That assumption makes  $\mathbf{e}_2$  constant. This is not a restriction, since in domain walls the magnetization changes by varying only one angle (in our calculation we take the

case of a Néel wall). We give the projections of Eq. (201) and Eq. (203) onto  $e_1$  and  $e_2$ :

$$-\ell_* (\dot{\theta}\mu_{\parallel} + \partial_x \mu_1) = j_1 + \frac{\ell_*}{\ell_{\perp}} j_1 + \frac{\ell_*}{\ell_L} j_2 \quad (248)$$

$$-\ell_* \partial_x \mu_2 = j_2 + \frac{\ell_*}{\ell_{\perp}} j_2 - \frac{\ell_*}{\ell_L} j_1 \quad (249)$$

$$\partial_x j_1 = -\dot{\theta} j_{\parallel} - \frac{\ell_*}{\ell_{sf}^2} \mu_1 - \frac{1}{\ell_{\perp}} \mu_1 - \frac{1}{\ell_L} \mu_2 \quad (250)$$

$$\partial_x j_2 = -\frac{\ell_*}{\ell_{sf}^2} \mu_2 + \frac{1}{\ell_{\perp}} \mu_2 - \frac{1}{\ell_L} \mu_1 \quad (251)$$

with  $\dot{\theta} = \partial_x \theta$

We now introduce a new quantity  $\tilde{\mu} = \mu_1 + i\mu_2$ . Taking the derivative of the first two equations, and inserting the last two, we obtain:

$$\partial_{xx} \tilde{\mu} + \partial_x (\dot{\theta} \mu_{\parallel}) = \left( \frac{1}{\ell_*} + \frac{1}{\ell_{\perp}} - \frac{i}{\ell_L} \right) \left[ \left( \frac{\ell_*}{\ell_{sf}^2} + \frac{1}{\ell_{\perp}} - \frac{i}{\ell_L} \right) \tilde{\mu} + \dot{\theta} j_{\parallel} \right] \quad (252)$$

This is the most general equation for the transverse part of the spin-resolve potential. It clearly shows how the collinear part of the transport affects the transverse part. However, this form is not easy to interpret because of the complex interdependence. In the next section, we will restrict ourselves to the case of long domain walls, and use that assumption to simplify this equation.

## VIII - 2 $\beta_{\tau}$ , A BRIDGE BETWEEN TRANSPORT AND MICROMAGNETISM

In the case of long domain walls (the so-called adiabatic limit), the spin accumulation  $\mu_{\parallel}$  follows the magnetization adiabatically[76].

Since  $\partial_x \approx 1/\ell_W$ , with  $\ell_W$  the length of the wall. Therefore, we keep only the lowest order  $\mathcal{O}(x/\ell_W)$  in the derivatives with respect to  $x$ , Eq. (252) becomes:

$$\left( \frac{\ell_*}{\ell_{sf}^2} + \frac{1}{\ell_{\perp}} - \frac{i}{\ell_L} \right) \tilde{\mu} = -\dot{\theta} j_{\parallel} \quad (253)$$

As previously stated, the torque is the non-conserved part of the spin current that is given to the magnetization. In our framework, this translates to: the non-

conserved part of the spin current not due to spin-flip (this part being given to the lattice). With that definition in a bulk material, according to Eq. (203), the torque is:

$$\boldsymbol{\tau} = \frac{2\hbar}{e^2\mathcal{R}_{\text{Sh}}} \left( \frac{1}{\ell_\perp} (\mathbf{m} \times \boldsymbol{\mu}) \times \mathbf{m} - \frac{1}{\ell_L} (\mathbf{m} \times \boldsymbol{\mu}) \right) \quad (254)$$

Recalling the definition of  $\beta_\tau = -\tau_2/\tau_1$ , we easily obtain from Eq. (253) that:

$$\beta_\tau = \frac{\ell_L \ell_*}{\ell_{sf}^2} \left[ 1 + \frac{\ell_* \ell_L^2}{\ell_\perp \ell_{sf}^2} + \left( \frac{\ell_L}{\ell_\perp} \right)^2 \right]^{-1} \quad (255)$$

The first to note about this equation is that it relates  $\beta_\tau$ , which is essentially a micromagnetic quantity, to  $\ell_*$ ,  $\ell_{sf}$ ,  $\ell_L$  and  $\ell_\perp$ , which are related to transport. This equation therefore creates a bridge between the two communities, and brings together notions that were before completely separate.

The assumption behind Eq. (255) that the domain wall is long and that the direction of the magnetization changes smoothly over space allows for that simple expression in terms of transport characteristic lengths. In order to investigate the strength of this assumption, we performed a series of simulations for varying wall thicknesses, from very short (1 nm) to very long walls (100 nm), and from various materials. We also investigated the influence of  $\ell_L$  on the value of  $\beta_\tau$  for various wall thicknesses. These investigations are reported in Fig. 37. For the purpose of the simulation, we used a domain wall shape given by [9]  $\tan[\theta(x)/2] = \exp(x/l_w)$ , and took the value of  $\beta_\tau$  at the middle of the wall. For long walls, this should not make any difference, as the absence of space dependence in Eq. (255) indicates.

More specifically, the numerical simulation was performed using the slightly different formula:

$$\theta(x) = 2 \arctan(\exp((x - l_{sys}/2)/l_w)) \quad (256)$$

The original formula assumes an infinite system, which is of course not possible in any numerical simulation. Therefore, we have a system of length  $l_{sys} \gg l_w$ , where  $l_w$  is the characteristic length of the wall. In practice,  $l_{sys} = 10 \times l_w$  worked fairly well. A factor of 10 means that at the edges of the system, the angle is less than  $0.05\pi$  away from  $\pm\pi$ . A factor 20 would give a difference of  $0.00003\pi$ . However, a twice as long system means twice as much computing time. We found that  $l_{sys} = 10 \times l_w$  gave the best accuracy, while keeping computing time reasonable.

As both plots in Fig. 37 show, Eq. (255) works fairly well for domain walls longer than 10 nm. However, strong deviations are expected for shorter walls.

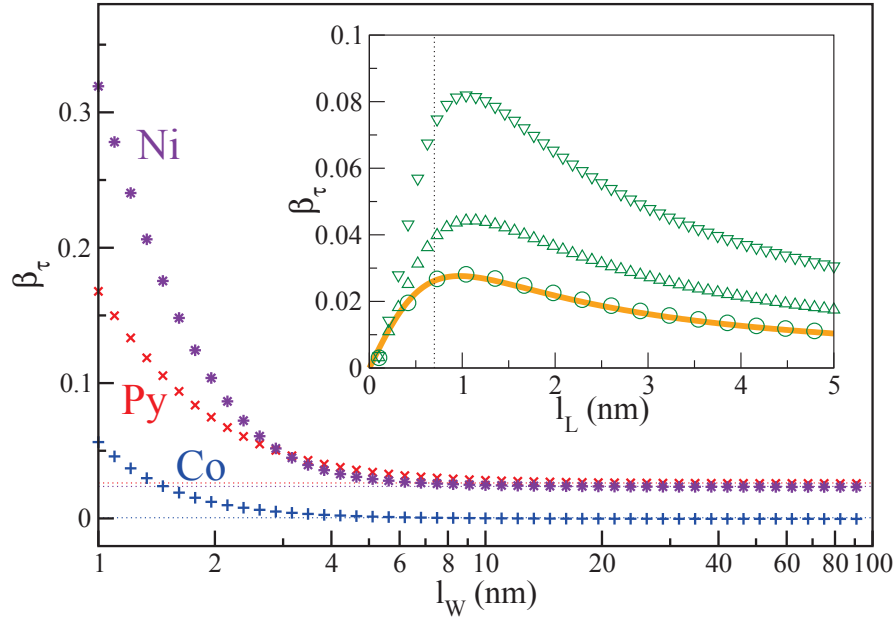


Figure 37.:  $\beta_\tau$  ratio in domain walls vs wall thickness  $l_w$ , for Ni (\*), Py ( $\times$ ), and Co (+). The horizontal dotted colored line indicates the adiabatic limit given by Eq. (255). Inset:  $\beta_\tau$  vs  $l_L$  in Py, for various wall thicknesses:  $l_w = 2$  nm ( $\nabla$ ),  $l_w = 4$  nm ( $\triangle$ ), and  $l_w = 20$  nm ( $\circ$ ). The full line is the adiabatic asymptotic value ( $l_w \rightarrow \infty$ ). The vertical dotted line corresponds to the expected value of  $l_L = 0.7$  for Py.

Two limits of Eq. (255) are of interest. In the case of weak spin-flip (*i.e.* long  $l_{sf}$ ),  $\beta_\tau \approx l_L l_* / l_{sf}^2$ , up to a prefactor of order unity. Zhang and Li [77] obtained a similar expression, with  $\beta_\tau \approx l_L / l_{sf}$ . In the case of very strong spin-flip (*i.e.* short  $l_{sf}$ ),  $\beta_\tau \approx l_\perp / l_L$ . We summarize in Table 6 the values of the adiabatic limit of  $\beta_\tau$ . This table uses the values in Table 4 for  $l_L$  and  $l_\perp$ .

The values of  $\beta_\tau$  in Table 6 are easily explained with the two limits given above. Co and Fe are on the “weak spin-flip” side, and are average conductors (and therefore do not have a high value for  $l_*$ ), hence their poor  $\beta_\tau$ . On the other hand, Ni and Py are on the “strong spin-flip” side. Their lower conductivity and, in the case of Ni, the high spin transverse penetration also helps.

Finally, we expect that very thin walls of materials with strong spin-orbit coupling will give values of  $\beta_\tau$  close to unity.

Material	$l_*$ (nm)	$l_{sf}$ (nm)	$l_L$ (nm)	$l_\perp$ (nm)	$\beta_\tau$
Co(110)			0.2	3	$3.687 \times 10^{-4}$
Co(111)	6.67	60	0.2	4	$3.694 \times 10^{-4}$
Co(111)			0.34	0.75	$5.2 \times 10^{-4}$
Co(111)			0.37	0.95	$5.9 \times 10^{-4}$
Fe(001)			6.25	60	0.3
Ni(100)	14.88	21	0.64	10	$2.1 \times 10^{-2}$
Ni(111)			0.72	4.6	$2.4 \times 10^{-2}$
Py(100)	1.72	5.5	1.42	0.9	$2.2 \times 10^{-2}$
Py(111)			0.7	1	$2.6 \times 10^{-2}$

Table 6.: Values of  $\beta_\tau$ , for the same materials, and using the same references as in Table 4.



# IX

---

## SPIN-VALVE ON YIG

---

In Section VII, we studied the effect of the mixing transmission, both at interfaces and in bulk materials. In this section we set our interest on the mixing properties of interfaces. In particular, we consider interfaces between a normal metal, and a magnetic insulator. The Yttrium-Iron Garnet (YIG) is one example of such magnetic insulators, and probably the most used in recent experiments.

Although our theory aims at describing metals, insulators can be dealt with as boundary conditions. This is the approach we took in this case. In particular, we assumed the insulator to be entirely modeled by its interface with the other materials. With another magnetic material, it is taken entirely reflective. With the normal metal (copper in our simulations), the interface is taken reflective for up and down spins (to ensure current conservation), but only partly reflective for transverse spins. This allows the YIG to act as a sink for transverse spins, which is its expected behavior. It is worth noting that some of the physics is lost, such as the effect of magnons, which are entirely ignored.

To summarize, this study, inspired by a collaboration with van Wees *et al.*, aims at probing the mixing reflection coefficient  $R_{\text{mx}}$  of a Cu/YIG interface. The experiment (and the simulated device) consists in a non-local spin-valve deposited on top of a YIG substrate. The valve itself is made of Cu, and has two Py electrodes. We first present the experimental results obtained at Groningen University. Then we go into more details into the exact physical model we used to match their experiments. Finally, we give the results of our simulations. This collaboration resulted in a joint publication[16]

### IX - 1 EXPERIMENTAL MEASUREMENTS AND RESULTS

The results obtained at Groningen University were obtained on a series of devices all based on the same geometry. It consists of a non-local spin-valve on a YIG substrate.

On this device, they measured the non-local magnetoresistance (to which we will often refer as the signal), under various magnetic field orientations and intensities.

### IX - 1.1 *Description of the system*

The device created by van Wees *et al.* is made of a substrate of YIG, on top of which two ferromagnetic Py electrodes are grown. On top of these, a cross of Cu is deposited, so that it bridges the two electrodes, and also provides two normal electrodes, giving a total of four contacts, see Fig. 38a. In order to probe the mixing reflection of the YIG/Cu interface, the YIG magnetization is set to be along the z-axis, while that of Py lie in-plane, along the x-axis. Although this magnetic setup is the one which will be held as reference, we will present some results using magnetic sweeps, where this setup will not be preserved. Fig. 38b and Fig. 38c give a view of how the system looks like from the numerical end.

### IX - 1.2 *Non-local spin-valves*

A regular spin-valve, is a two-terminal device where the charge current and the spin current flow along the same path. This class of device is essentially 1D (the cross section is not relevant to the physics). Non-local spin-valves on the other hand are at least 2D systems. They have at least four terminals, and are usually made up of a bar of a normal metal, with two orthogonal bars on top of it, made of a magnetic metal, see Fig. 39. A current is made to flow between one normal end and one ferromagnetic bar (F1), while measuring the voltage between the other ferromagnetic electrode (F2) and the other end of the normal bar. The diffusion of spins, coming from F1 towards F2, creates a spin accumulation and therefore a voltage. The fact that only pure spin currents (no charge current) arrive at F2 has two consequences. The first is that the (non-local) resistance is lower, and the second is that the absence of charge current removes a lot of the noise from the measurement. Overall, this configuration allows for a much better signal-to-noise ratio, and is therefore preferred to accurately measure a magnetoresistance, especially when the goal is to extract material parameters.

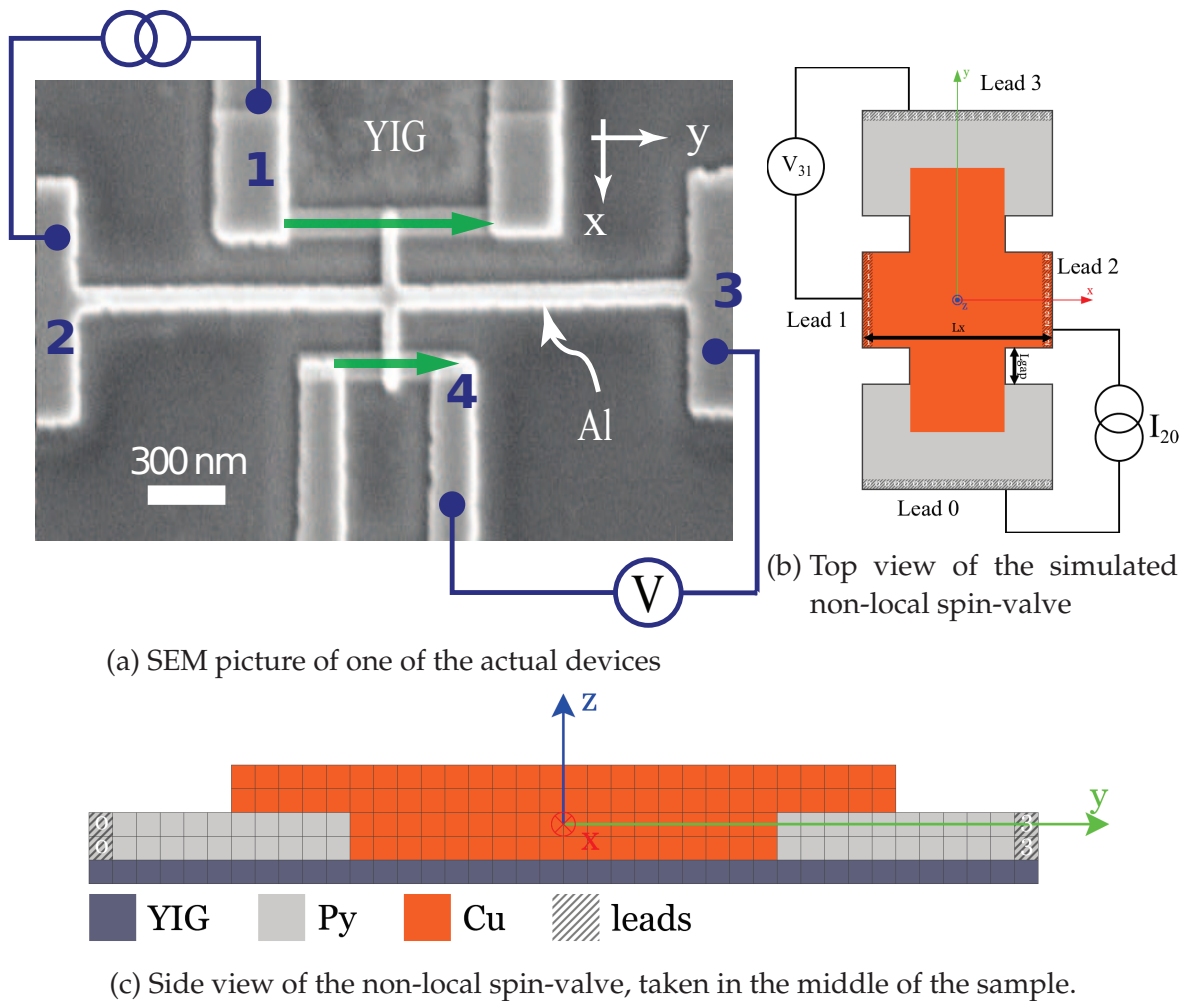


Figure 38.: (a) SEM picture of the measured device. The distance between the Py electrodes is 500 nm (green arrows show magnetization orientation). Note that although they used Al where we simulated Cu for the normal metal, this will not change the physics of the results. (b) Top and (c) side views of the simulated device

### IX - 1.3 Experimental measurements

In the actual device, the measured signal was the non-local magnetoresistance ( $GMR = (V_{31}(\uparrow\uparrow) - V_{31}(\uparrow\downarrow)) / V_{31}(\uparrow\uparrow)$ , with  $V_{31}$  as on Fig. 38b, and  $\uparrow\uparrow$  and  $\uparrow\downarrow$  indicating the parallel and antiparallel states of the Py electrodes.). To that end, a current is injected between one normal lead and the fixed ferromagnetic lead, while the voltage

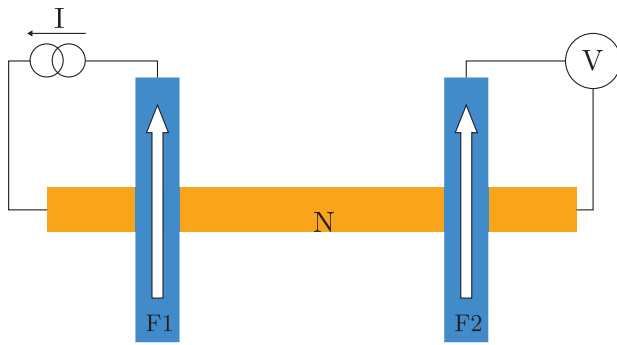


Figure 39.: Sketch of a generic non-local spin valve. It usually consists in four terminals. The current flows between one ferromagnetic electrode (usually the fixed one) and one of the normal leads. The voltage is measured between the other end of the normal bar and the other ferromagnetic electrode.

between the two other leads is measured. A magnetic sweep is performed, to switch the magnetization of the second ferromagnetic lead from the parallel to antiparallel configuration, and vice versa. The graph of the voltage vs field in such a measurement displays a plateau on top of a flat dependence, corresponding of the switching of each ferromagnetic lead. In that description, we assume that the magnetization of the YIG is pinned enough not to change in the range of fields used to switch the magnetization in the leads. The measurement is performed in a lock-in setup to maximize accuracy.

This signal is measured for various values of the applied magnetic field. Depending on the orientation of the field, this means that the sweep will switch the orientation of the free Py electrode, or change the orientation of the YIG magnetization. This leads to four configurations: the Py magnetizations being parallel and antiparallel, with the YIG collinear or orthogonal with respect to the Py magnetization orientation.

In Table 7, we summarized the measurements performed on various sample geometries, in a first batch of measurements. Unfortunately, on sample II the orientation of the YIG magnetization has no influence. The fact that the same geometry deposited on a SiO<sub>2</sub> substrate (sample III) yields a much higher GMR suggests that the YIG|Cu interface is of bad quality. This feature was at the origin of the dirty interface model we present.

Nevertheless, later measurements with better interfaces gave encouraging results. In Fig. 41 we display those results, which are very similar to our simulations. They were adapted from a preliminary draft of an article yet to be submitted.

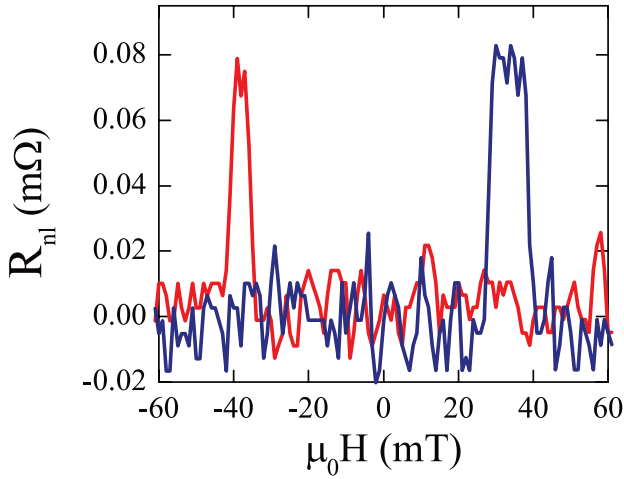


Figure 40.: Typical signature of the non-local resistance, subjected to a magnetic field sweep. A background resistance of 117 mΩ has been subtracted. The two different levels correspond to the parallel/antiparallel configuration for the Py electrodes (the orientation of the YIG magnetization does not vary)

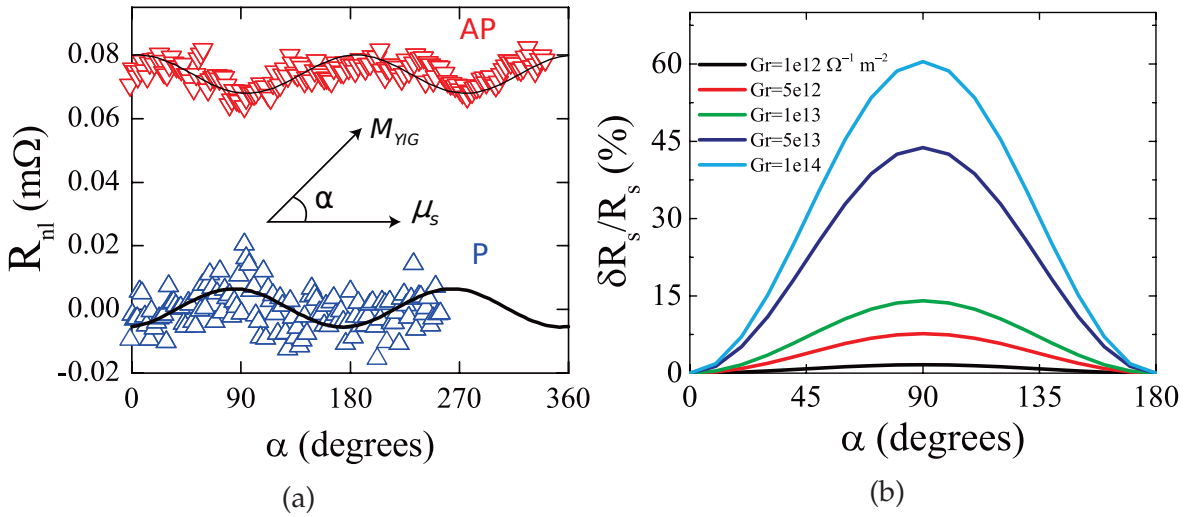


Figure 41.: (a) Measurement of the dependence of the non-local resistance with the YIG magnetization orientation. It clearly displays the  $\cos(2\alpha)$  dependence obtained in our simulations. The solid line is a simulation of the non-local resistance made for a mixing conductance of  $10^{13}\Omega^{-1} \cdot \text{m}^{-2}$ . (b) Dependence of the non-local resistance difference versus the YIG magnetization orientation.  $R_s = \Delta R_{31}$  in our notations, and  $\delta R_s = \Delta R_{31}(\alpha=0) - \Delta R_{31}(\alpha=90^\circ)$

Fig. 41a and Fig. 41b are clearly in agreement with our simulations (see Section IX - 3). The only point to be taken into account is that the angle  $\alpha$  used by van Wees'

Sample	$R_P(m\Omega)$	$R_{AP}(m\Omega)$	$\Delta R(m\Omega)$
I with $L_{\text{gap}}=50\text{nm}$	118.7	120.5	1.8
II with $L_{\text{gap}}=100\text{nm}$	148.4	148.8	0.4
II with $L_{\text{gap}}=200\text{nm}$	121.2	121.4	0.2
III with $L_{\text{gap}}=200\text{nm}$ on $\text{SiO}_2$	105.3	106	0.7
II with $L_{\text{gap}}=200\text{nm}$ and YIG orthogonal to Py	121.2	121.4	0.2

Table 7.: Measured values of the non-local resistance with the Py magnetization parallel (subscript P) and antiparallel (subscript AP), on various devices. The last line is the only one where the YIG magnetization is orthogonal to the Py magnetization.

group is the complementary angle to our  $\theta_{YIG}$ . They therefore see a peak in the non-local GMR at  $\alpha=90^\circ$ , where we have it at  $\theta_{YIG}=0$ . The result displayed in Fig. 41b is simply another way of plotting Fig. 44. One simply has to keep in mind that the higher  $R_{\text{mx}}$ , the lower  $G_r$  in Fig. 41b, because  $G_r$  is the real part of the mixing conductance, which is proportional to the mixing transmission, and not reflection.

## IX - 2 PHYSICAL MODEL

The model we use (in terms of transmission and reflection matrices within the CRMT framework) consists in several distinct parts. First, we want to probe the Cu/YIG interface. To avoid any other contribution, we therefore used a perfect lossless reflective interface between Py and YIG.

As for the relevant interface, we first assumed it to be perfectly reflective for longitudinal spins (no spin-flip), and with a reflection coefficient  $R_{\text{mx}}$  for the transverse part. Because the comparison with measurements showed that our simulation gave overly optimistic results, we devised an effective “dirty” interface by adding in series what would be a bulk layer of resistive material, with some spin-flip. We present those steps in the following sections.

IX - 2.1 *Perfect interface model*

As stated above, in this simplistic model, we only assume that transverse spins are affected by some process, summarized in a reflection coefficient  $R_{\text{mx}}$ .

$$\hat{r} = \begin{pmatrix} 1 & 0 & 0 & 0 \\ 0 & R_{\text{mx}} & 0 & 0 \\ 0 & 0 & R_{\text{mx}}^* & 0 \\ 0 & 0 & 0 & 1 \end{pmatrix} \quad (257)$$

No spin-flip occurs, which makes the interpretation of the results extremely easy. The one important trend is that the lower the value  $R_{\text{mx}}$ , the more spins transverse to the YIG are absorbed, and the less they reach the second electrode, meaning less GMR signal. On the other end,  $R_{\text{mx}}$  close to unity means that almost no absorption takes place, giving the maximum possible GMR signal.

IX - 2.2 *Dirty interface model*

Because the results in the clean interface model were so different, we assumed that the interface between YIG and Cu was not as clean as hoped. An interface has two main ways of being “dirty”. The first is when the limit between the materials are well defined, but rough. This leads to some additional specular reflections behaving like a resistive layer before the interface. The second type of interface is when the limit between the two materials is badly defined, where intermixing occurs. We will use the term alloying in that case. If one of the two materials is made up of heavy elements, chances are that some spin-flip will occur because of the additional spin-orbit coupling induced by the impurities.

We assume that any real interface is a combination of the two mentioned before, and we model it by placing an effective bulk layer in series before the interface. This layer is parametrized by a reflection coefficient  $R$  (independent of the spin), measuring the roughness of the interface, and a spin-flip reflection coefficient  $R_{\text{sf}}$  measuring its degree of alloying between the YIG layer and the copper layer. Using the law of addition of two scattering matrices in series (see Eq. (126) and Eq. (127)), we find:

$$\hat{r} = \begin{pmatrix} 1 - R_{\text{sf}}^{\text{eff}}/2 & 0 & 0 & R_{\text{sf}}^{\text{eff}}/2 \\ 0 & R_{\text{mx}}^{\text{eff}} & 0 & 0 \\ 0 & 0 & R_{\text{mx}}^{\text{eff}*} & 0 \\ R_{\text{sf}}^{\text{eff}}/2 & 0 & 0 & 1 - R_{\text{sf}}^{\text{eff}}/2 \end{pmatrix} \quad (258)$$

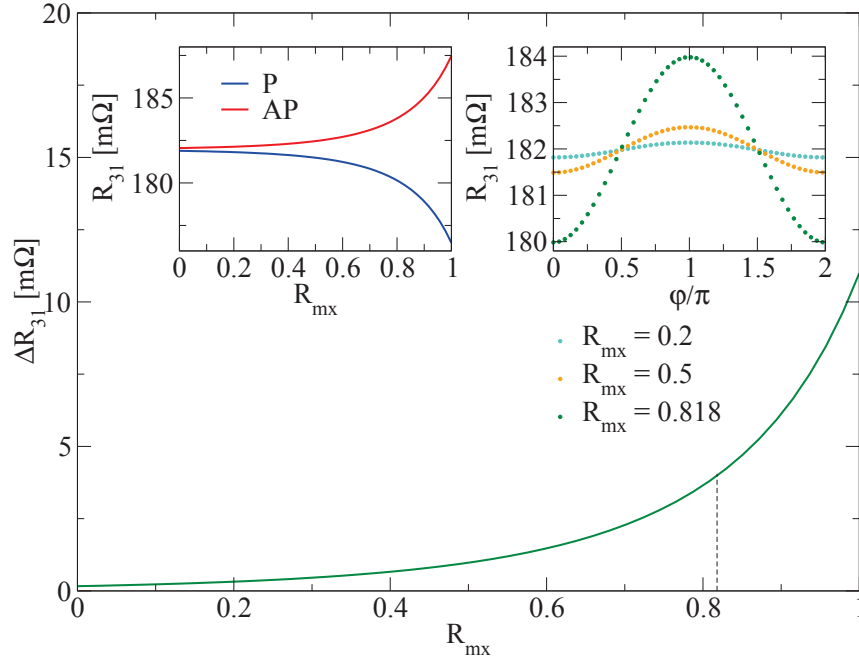


Figure 42.: Non-local GMR signal in the YIG system vs  $R_{\text{mx}}$ . In the main plot, the indicated value  $R_{\text{mx}} = 0.818$  corresponds to the measured value. Top left inset: value of the resistance in the parallel (blue) and antiparallel (red) configuration versus  $R_{\text{mx}}$ . Top right inset: angular dependence of the the resistance for several values of  $R_{\text{mx}}$ .

with:

$$R_{\text{sf}}^{\text{eff}} = 2R_{\text{sf}} + \frac{R_{\text{sf}}^2}{R - R_{\text{sf}} - 1} \quad (259)$$

$$R_{\text{mx}}^{\text{eff}} = R - R_{\text{sf}} + \frac{1 - R^2}{1 - (R - R_{\text{sf}})R_{\text{mx}}} R_{\text{mx}} \quad (260)$$

To respect the physics, the coefficients are limited in range, relative to each other.  $R$  can be anywhere in the  $[0, 1]$  range. However, the condition  $0 < R_{\text{sf}} < R$  is important, since there cannot be more spin-flipping scattering events than the total scattering events. Finally,  $R_{\text{mx}}$  can also be anywhere in the  $[0, 1]$  range.

An interface with  $R = 0$  would have no roughness, and therefore allow all the spins to “see” the YIG. On the other hand,  $R = 1$  means that all the spins are reflected before feeling any influence from the YIG.  $R_{\text{sf}} = 0$  means that no spin-flip occurs, and therefore all the spins are conserved (until the next process takes place).

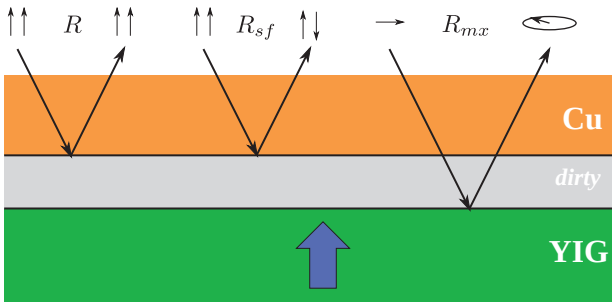


Figure 43.: The three processes occurring at a YIG interface.  $R$  describes spin-conserving reflections,  $R_{sf}$  reflections without spin memory. For transverse spins (with respect to the YIG magnetization),  $R_{mx}$  describes the proportion that are reflected, the rest being simply absorbed.

$R_{sf} = R$  corresponds to a completely “alloyed” interface, where all the scattering events destroy the spin memory. Finally,  $R_{mx}$  simply describes the proportion of the incoming transverse spins that are reflected, the rest being absorbed by the magnetization of the YIG. Its imaginary part (not investigated here) would describe how much a transverse would precess.

### IX - 3 SIMULATIONS AND NUMERICAL RESULTS

Since most of the material parameters are very difficult to measure independently, the one used in our simulations probably differ quite a lot from reality. The lengths and thicknesses may also be different from the measured samples. However, the orders of magnitude are well respected. This means that the results presented here do not aim at estimating  $R_{mx}$  from the experimental results, but rather show the dependence of the signal with the various parameters, may they be geometrical, or material-related.

#### IX - 3.1 Case of a perfect interface

Let us not consider any spin-flip or roughness at the Cu|YIG interface. In that case, all the spin along the YIG magnetization are reflected, and the fraction  $|R_{mx}|$  of the transverse spins are reflected, the rest being absorbed. In that limit, we obtained Fig. 42 and Fig. 44. We used the suggested value  $R_{mx} = 0.818$  (computed from the mixing conductance provided with the experiments results) as a reference. The main result is that the higher  $R_{mx}$ , the stronger the non-local resistance difference  $\Delta R_{31}$  is

in the case where the YIG magnetization is orthogonal to the Py (the transverse spins are absorbed by the magnetization of the YIG). However the lower  $R_{\text{mx}}$ , the stronger the dependence of  $\Delta R_{31}$  is with respect of the orientation of the YIG. Indeed, in the extreme case where all the spins are reflected, the orientation becomes irrelevant.

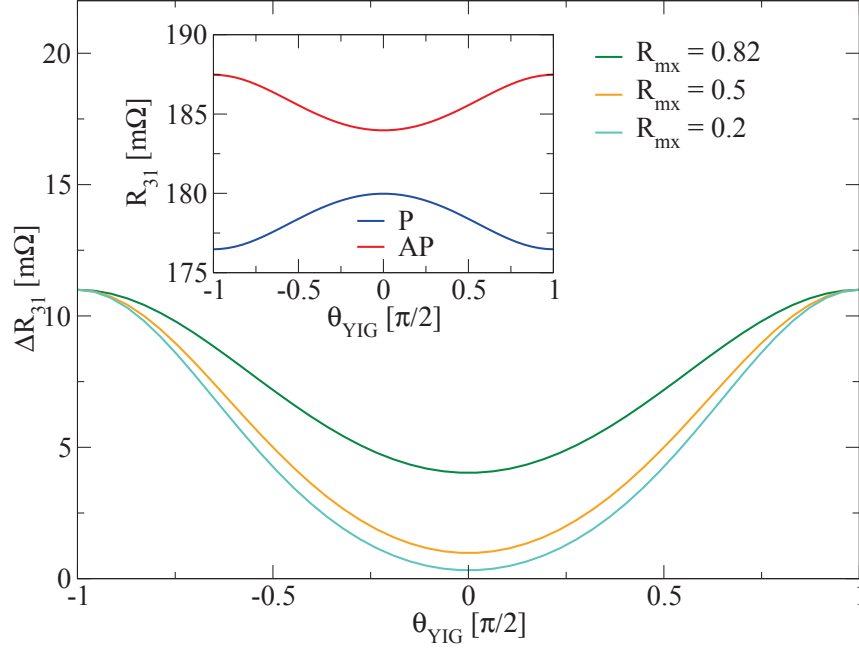


Figure 44.: Main plot: dependence of the difference of the non-local resistance between the P and AP configuration, vs the angle of the YIG magnetization with respect to the pinned-layer Py magnetization axis, for different values of  $R_{\text{mx}}$ . Inset: Dependence of the P and AP component vs the YIG magnetization angle.  $\theta_{\text{YIG}} = 0$  corresponds to the YIG being orthogonal to the Py, and  $\theta_{\text{YIG}} = \pm\pi/2$  is when it lies in plane.

Fig. 42 shows that the stronger  $R_{\text{mx}}$  is, the more the resistance of the system depends on the orientation of the magnetizations of the Py layers with respect to each other. The figure shows that the dependence of this resistance with  $R_{\text{mx}}$  between the parallel and antiparallel configurations of the Py layers is symmetric around their average.

Fig. 44 shows that a higher value of  $R_{\text{mx}}$  means a lower signal  $\Delta R_{31}(\theta=\frac{\pi}{2}) - \Delta R_{31}(\theta=0)$ , where  $\theta$  is the angle of the YIG magnetization with the growth axis. As stated before, a higher  $R_{\text{mx}}$  means less electrons depending on the YIG magnetiza-

tion orientation. An important point to note is that  $R_{\text{mx}}$  was taken real in this study. The influence of an imaginary part was not investigated, and may prove relevant. This figure also shows that the graph of the resistance in the parallel and antiparallel (for the Py electrodes) cases are symmetric with respect to their average. This means that the experiment can be carried out only in one of those configurations, and still display signs of the influence of the YIG. However looking at the difference has the advantage of providing a cleaner experimental signal.

### IX - 3.2 Dirty interface

The lack of signal related to the YIG interface lead us to introduce the model for a dirty interface. For the study, we could have looked at the effect of the effective parameters, but we think that, although the model has no microscopic reality, the non-effective parameters are a better measure of the "dirtiness" of the interface (both its roughness and the amount of alloying between the copper and the YIG layers).

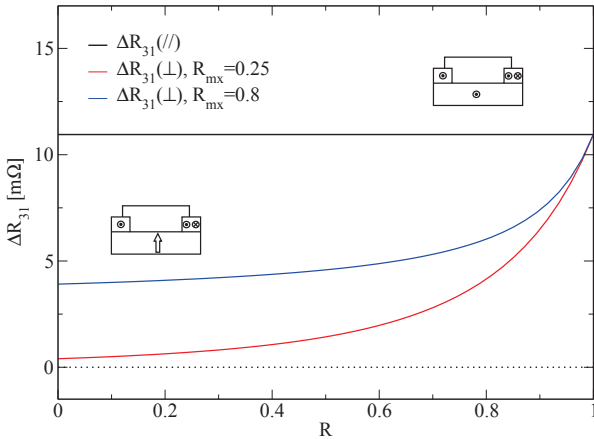


Figure 45.:  $\Delta R_{31}$  vs  $R$  for the collinear case (black line) and for the orthogonal case (red:  $R_{\text{mx}} = 0.25$ , blue:  $R_{\text{mx}} = 0.8$ ).

In Fig. 45, only one line is displayed for the parallel case (YIG and Py magnetization collinear), because in that case no transverse spin arrive at the YIG interface. They are all reflected back into the sample, which also explains why  $R$  has no effect. However, if some spin-flip scattering occurs, the signal will decrease, as we can see in Fig. 46 (symbols).

In the orthogonal case, since we saw that  $R_{\text{mx}}^{\text{eff}} = R + \frac{(1-R)^2}{1-RR_{\text{mx}}}R_{\text{mx}}$ , we notice that the mixing reflection is clamped at least at  $R$ . This explains the saturation for

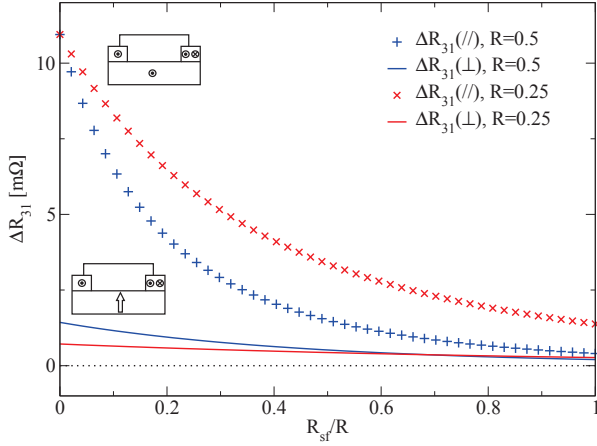


Figure 46.:  $\Delta R_{31}$  vs  $R_{sf}/R$  for  $R = 0.25$  (red curves) and  $R = 0.5$  (blue curves). Since  $R_{sf} < R$ , we use the normalized parameter  $R_{sf}/R$  to have the same scale. The symbols correspond to the collinear case, while the full lines correspond to the YIG and the Py layers having orthogonal magnetizations.

small values of  $R_{mx}$ , and the fact that the higher the value of  $R$ , the more the behavior resembles that of the collinear case (no effect of the mixing). In the extreme case where  $R = 1$ , the interface reflects back everything, and no mixing can be felt. If some spin-flip is added, the signal is killed (all the more so  $R$  is high). In order to respect the condition  $R_{sf} < R$ , we used a normalized coefficient  $R_{sf}/R$  to have all the curves on the same scale. In the most extreme case  $R = R_{sf} = 1$  (not displayed here), we computed a value  $\Delta R_{31} = 0.16$ . Of course, the signal has been tremendously reduced compared to when there is no spin-flip. The non-zero value can be understood by the fact that the copper layer short-circuits some of the current, and some of the spins never reach the interface, regardless of its quality.

The trend displayed in Fig. 46 is enough to explain why no signal due to  $R_{mx}$  was observed in sample II, and why the value of the GMR is so low compared to our simulations. An alloyed interface would result in a lot of spin-flip, and high resistivity, reducing the value of the GMR, and screening the sample for the YIG. Also, some of the bulk and interface parameters might be over or underestimated, leading to our optimistic results.

#### IX - 4 EFFECTS OF THE GEOMETRY

The shape of the sample will have a strong influence on the results. We analyzed the effect of two lengths: the gap length, between the copper and the permalloy pads (see Fig. 38b), and the thickness of copper. We find that  $\Delta R_{31}$  decays exponentially

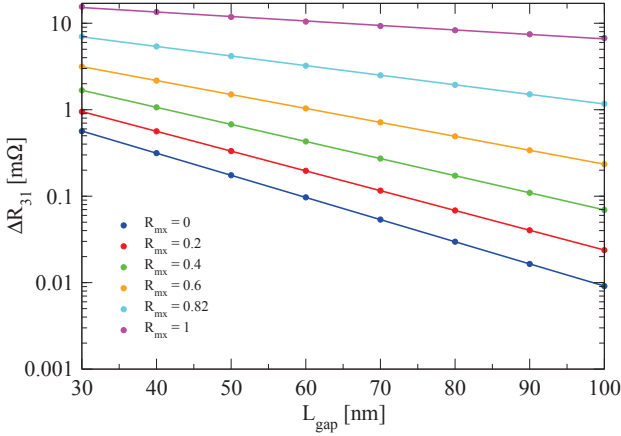


Figure 47.:  $\Delta R_{31}$  vs  $L_{\text{gap}}$  (as indicated on Fig. 38b) for various values of  $R_{\text{mx}}$ .

with  $L_{\text{gap}}$ . The typical length of decay depends on the value of  $R_{\text{mx}}$ , and thus on the quality of the interface. We write this dependence as:

$$\Delta R_{31} = \Delta R_0 e^{-L_{\text{gap}}/\lambda_{\text{mx}}} \quad (261)$$

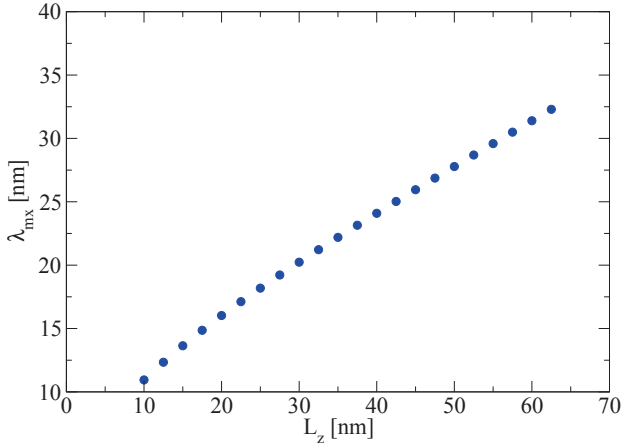


Figure 48.:  $\lambda_{\text{mx}}$  vs the Cu thickness

The thickness of the copper will impact the values of  $\Delta R_0$  and  $\lambda_{\text{mx}}$ . Because copper has a much lower resistivity than permalloy, it will have a short-circuiting effect. Therefore, the thicker the copper, the smaller a fraction of the current will be affected by the Cu|YIG interface, and the longer  $\lambda_{\text{mx}}$  will be.

$\Delta R_0$  has a less trivial dependence. There are two regimes, depending on if the copper is thicker than the permalloy pads or not. If not, the dependence is roughly

linear. If the Cu is thicker than the Py, there will be an overlap, and it will again act as a short-circuit. A longer overlap means again a stronger short-circuiting effect (not shown on the graphs).

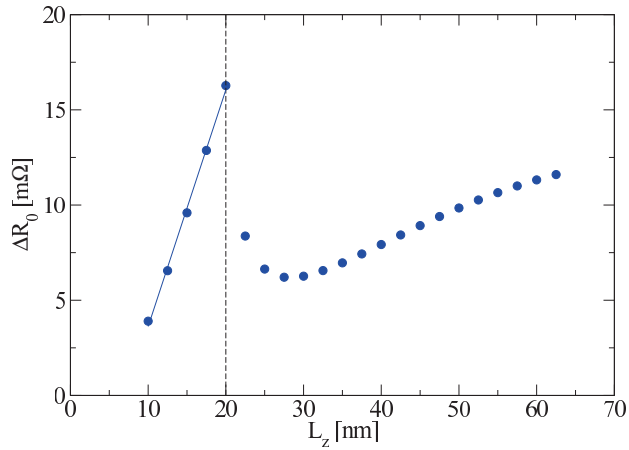


Figure 49.:  $\Delta R_0$  vs the Cu thickness. The full line is a linear regression of the points below  $L_z = 20\text{nm}$ . This value corresponds to the copper and the permalloy pads being at the same height.

Part D

APPLICATIONS TO SPIN CALORITRONICS



**Summary of Part D**

Because we wanted to study if it was possible to induce spin-transfer torque through the thermoelectric effects, we extended our theory to include those effects. In particular, we introduced the recently discovered spin-dependent thermoelectric effects, relevant in ferromagnets. We studied the impact these effects have on the spin-transfer torque in a spin-valve subjected both to a temperature gradient and to a voltage bias. We consider in particular two main cases: the electrically closed or open circuits. We found that whether the electrical current was allowed (closed circuit) or not (open circuit) changes quite a lot the behavior of the torque. The main result is that it is much easier to design a system where the torque is wavy (see Section III - 6) in the open circuit configuration.

We also prove that thermoelectric switching of a magnetic layer is indeed possible, and give a study of the material parameters necessary to generate that switching, as well as an estimate of how much of a temperature difference is needed.

We then show that the out-of-plane (non-adiabatic) component of the torque (see Eq. (255)) remains unchanged whether the torque is induced by a voltage or a temperature gradient.

Finally, we show the result of simulations compared to experimental results on a spin-dependent Seebeck measurement performed by van Wees' group in Groningen university.

**Résumé de la Partie D**

Afin d'étudier la possibilité de générer un torque par transfert de spin grâce aux effets thermoélectriques, nous avons étendu notre théorie afin d'y inclure ces effets. Nous avons en particulier introduit les effets thermoélectriques dépendant du spin, récemment découverts, et nécessaires dans le cas des métaux ferromagnétiques. Nous avons étudié l'impact de ces effets sur le torque par transfert de spin dans une valve de spin soumise à une tension ainsi qu'à un gradient de température. Nous avons considéré en particulier deux cas : un circuit électriquement fermé ou ouvert. Nous avons trouvé que le fait de laisser circuler le courant électrique (circuit fermé) ou pas (circuit ouvert) changeait le comportement du torque. Notre résultat principal est qu'il est beaucoup plus facile de créer un système où le torque est wavy (voir Section III - 6) en circuit ouvert.

Nous avons aussi prouvé qu'inverser thermoélectriquement l'aimantation d'une couche magnétique est bien possible, et nous donnons une étude des paramètres matériaux nécessaires à cette inversion, ainsi qu'une estimation de la différence de température nécessaire.

Nous montrons ensuite que la composante hors-plan du torque (le torque non-adiabatique, voir Eq. (255)) reste inchangée, que le torque résulte d'une tension ou d'un gradient de température.

Enfin, nous montrons nos résultats de simulations comparées aux résultats expérimentaux de mesure du coefficient de Seebeck dépendant du spin obtenus par le groupe de van Wees à l'université de Groningen.



---

## SPIN-TRANSFER TORQUE IN A SPIN-VALVE SUBJECTED TO A TEMPERATURE GRADIENT

---

Our everyday technology dissipates a lot of heat, may it come from the Joule effect, mechanical friction, or any other source. So far, in almost all cases, this heat is nothing but wasted. The thermoelectric effects have been the focus of the hope to convert that waste into something useful. As far as producing reusable energy goes, the materials are not ready yet. Another, more medium term option exists though. Heat could be used to power directly small devices. Including the conversion from heat to electricity directly into the device helps reducing the conversion cost (since as of yet, the thermoelectric materials are rather inefficient), and the hope is that nanoscale devices could be powered even by today's thermoelectric materials under reasonable temperature gradients (a few to a few tens of Kelvin).

Spintronics devices usually rely on the possibility to change its magnetic configuration, either by switching the magnetization of a magnetic layer, or by inducing some dynamical property such as a steady-state precession. The only ingredient needed to power those effects is the presence of a polarized current. The usual way of creating this polarized current is by placing a polarizing magnetic layer before the one to be switched and by applying a voltage to the stack. However any source of polarized current would work as well. In this part of the manuscript, we consider applying a temperature gradient to spin-valves. That way, two sources of polarized current are created at the same time. The strongest one (usually) is the normal Seebeck effect inducing a charge current that gets polarized by the polarizing layer. The result is very similar to applying an equivalent voltage. The second source, usually weaker, is due to the spin-dependent Seebeck effect creating directly a spin-polarized current.

In the following sections, we first describe the system and how it behaves in open and closed-circuit conditions, by performing numerical simulations. Then, we derive an expression of the torque when both a voltage and a temperature gradient are

applied. We use this derivation as well as simulations to discuss the wavy nature of the angular dependence of the torque, and how strong the temperature gradient needs to be to initiate switching.

We also present a study proving that in-plane and out-of-plane components of the spin-transfer torque have the same ratio, regardless of the driving force (voltage or temperature gradient). More generally speaking, this means that the behavior of transverse spins is not influenced by the presence of temperature gradients.

Finally, we present a comparison between experimental measurements of the polarization of the thermoelectric coefficients and numerical simulation we performed. This served as validation of their results, and maybe provides improvements on the device design, especially concerning how heat is brought to the system.

For our simulations, we take the material parameters obtained by various GMR experiments (see Table 8 and Table 9). As for the thermoelectric coefficients (especially their spin-dependent part), we took the values reported by van Wees *et al.* in Ref[58].

## X - 1 DESCRIPTION OF THE SYSTEM AND ITS CONFIGURATIONS

A spin-valve is the most common system in spintronics, and can be used by applying a voltage to it, but also by being subjected to a thermal gradient. The Seebeck effect will induce a current and the same effects (namely the spin-transfer torque) will arise as in the voltage case.

A spin-valve can be placed in two possible electrical configurations: in closed or open circuit. In closed circuit, the electrical current is allowed to flow freely in the system. On the other hand, in open circuit, the electrical current is prevented from flowing (although the heat current does). However, although the charge current is zero, pure spin currents may exist in the system. The spin-dependent Seebeck effect is a prime example of source of such pure spin currents. This is the reason why we will refer to this configuration as the “pure” configuration, and note it on plots and sketches by the letter P. As for the closed circuit condition, the spin currents are the superposition of these pure spin currents and a voltage-like component, resulting from the conventional Seebeck effect creating a charge current that gets polarized by the various magnetic layers. The presence of these two components led us to call it the “mixed” configuration, that is noted M on the plots and sketches. Finally, when simply applying a voltage, we call it the voltage configuration, and mark it with a V. Those configurations are summarized in Fig. 50.

Thanks to the linearity of our equations, the open-circuit condition  $j_c = 0$  is strictly equivalent to an applied voltage canceling the current. Since our boundary conditions are expressed through the applied voltages and temperatures, we chose the latter description. We will see in the next section that this current-canceling voltage arises naturally from the equations.

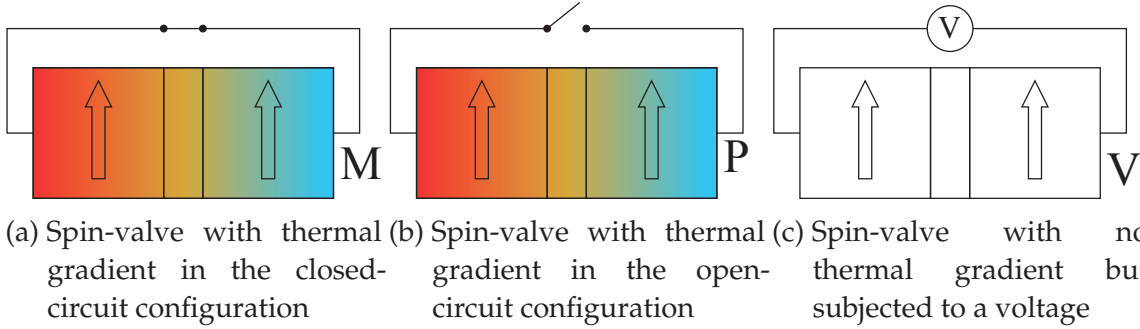


Figure 50.: The three configurations of a spin-valve subjected to a temperature gradient and/or a voltage. The hot side is colored red, the cold side blue. The letters M, P and V correspond to the mixed, pure and voltage case, see text. The spin-valves are all presented in their parallel configuration.

X - 2 DERIVATION OF AN EXPRESSION FOR THE TORQUE

We now derive the expression of the torque on the rightmost layer in the spin-valve  $F_A|N|F_B(\varphi)$  presented in Fig. 50 ( $\varphi$  is the angle the magnetization of layer B does with that of layer A). A voltage and a temperature gradient are applied on the left lead. We make the following simplifying assumptions:

- i - we consider a 1D system: the spin-valve has no variation along the  $y$  and  $z$  axes.
- ii - spin-flip scattering is neglected
- iii - transverse spins are absorbed directly at the ferro-normal interface
- iv - the thermoelectric coefficients  $s$  and  $\Delta s$  are only considered at first order
- v - the normal spacer and the interfaces are taken perfectly transparent without loss of generality (their properties are absorbed by the effective material A and B, see Section VI - 5)

We note that in the numerics presented in the text, condition (ii) and (iv) are relaxed which only leads to small corrections to the results.

Within this set of approximations, Eq. (225) to Eq. (230) become for each material:

$$-\ell_* \frac{d\mu_c}{dx} = j^c - \beta j_{\parallel} - \frac{1 - \beta^2}{\mathcal{L}} s j^q \quad (262)$$

$$-\ell_* \frac{d\mu_{\parallel}}{dx} = j_{\parallel} - \beta j^c - \frac{1 - \beta^2}{\mathcal{L}} \Delta s j^q \quad (263)$$

$$-\ell_* \frac{d\theta}{dx} = -\frac{1 - \beta^2}{\mathcal{L}} (s j^c + \Delta s j_{\parallel} - j^q) \quad (264)$$

and the conservation equations are:

$$\frac{dj^c}{dx} = 0 \quad (265)$$

$$\frac{dj^q}{dx} = 0 \quad (266)$$

$$\frac{dj_{\parallel}}{dx} = 0 \quad (267)$$

with  $j_{\parallel} = \mathbf{j} \cdot \mathbf{m}$ ,  $\mu_{\parallel} = \boldsymbol{\mu} \cdot \mathbf{m}$ .

The conservation equations imply that  $j^c$  and  $j^q$  are constant, and the absence of spin-flip makes  $j_{\parallel}$  piecewise constant. As a consequence,  $\theta$  and  $\mu_{\parallel}$  are piecewise linear.

Once we have the effective Ohm law for the two materials - in the basis parallel to their respective magnetization - we need to combine the two materials together. This is done using Eq. (234) assuming vanishing mixing reflection (or equivalently a mixing conductance equal to the Sharvin conductance). We introduce  $\boldsymbol{\mu} = (\mu_x, 0, \mu_z)$  and  $\mathbf{j} = (j_x, 0, j_z)$  the spin-resolved potential and spin current in the normal layer, and  $\boldsymbol{\mu}_A$  (resp.  $\boldsymbol{\mu}_B$ ) the value of the spin-resolved potential in the relevant magnetic layer, infinitely close to the interface. The equation relating the two magnets reads,

$$\boldsymbol{\mu} \cdot \mathbf{m}_A = \boldsymbol{\mu}_A \cdot \mathbf{m}_A \quad (268)$$

$$\boldsymbol{\mu} \cdot \mathbf{m}_B = \boldsymbol{\mu}_B \cdot \mathbf{m}_B \quad (269)$$

$$\mathbf{j} \cdot \mathbf{m}_A = \mathbf{j}_A \cdot \mathbf{m}_A \quad (270)$$

$$\mathbf{j} \cdot \mathbf{m}_B = \mathbf{j}_B \cdot \mathbf{m}_B \quad (271)$$

for the longitudinal part and,

$$-\left[\mathbf{j} - (\mathbf{j} \cdot \mathbf{m}_A) \mathbf{m}_A\right] = \left[\boldsymbol{\mu} - (\boldsymbol{\mu} \cdot \mathbf{m}_A) \mathbf{m}_A\right] \quad (272)$$

$$\left[\mathbf{j} - (\mathbf{j} \cdot \mathbf{m}_B) \mathbf{m}_B\right] = \left[\boldsymbol{\mu} - (\boldsymbol{\mu} \cdot \mathbf{m}_B) \mathbf{m}_B\right] \quad (273)$$

for the transverse part. Explicitly, they give:

$$\mu_z = \boldsymbol{\mu}_A \cdot \mathbf{m}_A \quad (274)$$

$$\mu_x \sin \varphi + \mu_z \cos \varphi = \boldsymbol{\mu}_B \cdot \mathbf{m}_B \quad (275)$$

$$j_z = \mathbf{j}_A \cdot \mathbf{m}_A \quad (276)$$

$$j_x \sin \varphi + j_z \cos \varphi = \mathbf{j}_B \cdot \mathbf{m}_B \quad (277)$$

$$j_x = -\mu_x \quad (278)$$

$$j_x \cos \varphi - j_z \sin \varphi = \mu_x \cos \varphi - \mu_z \sin \varphi \quad (279)$$

Which translates eventually by eliminating  $j_x$ ,  $\mu_x$ ,  $j_z$  and  $\mu_z$  to:

$$(\boldsymbol{\mu}_A - \mathbf{j}_A) \cdot \mathbf{m}_A = \cos \varphi (\boldsymbol{\mu}_B - \mathbf{j}_B) \cdot \mathbf{m}_B \quad (280)$$

$$(\boldsymbol{\mu}_B + \mathbf{j}_B) \cdot \mathbf{m}_B = \cos \varphi (\boldsymbol{\mu}_A + \mathbf{j}_A) \cdot \mathbf{m}_A \quad (281)$$

The last set of equations that we need are the boundary conditions at the reservoirs. They read:

$$j^c + \mu_c^L = eV_b \quad (282)$$

$$j^c - \mu_c^R = 0 \quad (283)$$

$$j_{\parallel A} + \mu_{\parallel}^L = 0 \quad (284)$$

$$j_{\parallel B} - \mu_{\parallel}^R = 0 \quad (285)$$

$$j^q + \theta^L = k_B \Delta T \quad (286)$$

$$j^q - \theta^R = 0 \quad (287)$$

with  $\mu_c^{L/R}$ ,  $\mu_{\parallel}^{L/R}$ ,  $\theta^{L/R}$  the value of the potential, spin-resolved potential and temperature infinitely close to the left (L) and right (R) reservoir.

Finally, after some algebra, and using the notations introduced in Section VI - 5 for the effective parameters, we can obtain the expressions of the currents and potentials given by equations Eqs.(288) to (295):

$$j^c = FG [GYeV_b + Sk_B\Delta T] \quad (288)$$

$$j^q = FG [SeV_b + Kk_B\Delta T] \quad (289)$$

$$j_{\parallel A} = F\gamma_A [GYeV_b + Sk_B\Delta T] + FK\delta_A k_B\Delta T \quad (290)$$

$$j_{\parallel B} = F\gamma_B [GYeV_b + Sk_B\Delta T] + FK\delta_B k_B\Delta T \quad (291)$$

$$\begin{aligned} \mu_c = & 2r_B F \left( \left[ \left(1 + \frac{1}{2r_B}\right)G - \beta_B\gamma_B \right] [GYeV_b + Sk_B\Delta T] \right. \\ & \left. - \frac{1 - \beta_B^2}{\mathcal{L}_B} [s_B G + \Delta s_B \gamma_B] Kk_B\Delta T \right) \end{aligned} \quad (292)$$

$$\begin{aligned} \mu_{\parallel A} = & F \left[ \beta_A \left(1 + \frac{1}{r_B}\right) - \beta_B \cos \varphi - \gamma_A \right] [GYeV_b + Sk_B\Delta T] \\ & + F \left[ \frac{1 - \beta_A^2}{\mathcal{L}_A} \Delta s_A \left(1 + \frac{1}{r_B}\right) - \frac{1 - \beta_B^2}{\mathcal{L}_B} \Delta s_B \cos \varphi - \delta_A \right] Kk_B\Delta T \end{aligned} \quad (293)$$

$$\begin{aligned} \mu_{\parallel B} = & -F \left[ \beta_B \left(1 + \frac{1}{r_A}\right) - \beta_A \cos \varphi - \gamma_B \right] [GYeV_b + Sk_B\Delta T] \\ & - F \left[ \frac{1 - \beta_B^2}{\mathcal{L}_B} \Delta s_B \left(1 + \frac{1}{r_A}\right) - \frac{1 - \beta_A^2}{\mathcal{L}_A} \Delta s_A \cos \varphi - \delta_B \right] Kk_B\Delta T \end{aligned} \quad (294)$$

$$\theta = 2r_B F \left[ \left( \frac{1 - \beta_B^2}{\mathcal{L}_B} + \frac{1}{2r_B} \right) (SeV_b + Kk_B\Delta T) - \frac{1 - \beta_B^2}{\mathcal{L}_B} Y (s_B G + \Delta s_B \gamma_B) eV_b \right] \quad (295)$$

with the following notations:

$$G = \frac{1}{2} \left( \sin^2 \varphi + \frac{1}{r_A} + \frac{1}{r_B} + \frac{1}{r_A r_B} \right) \quad (296)$$

$$Y = \left( \frac{1 - \beta_B^2}{\mathcal{L}_B} + \frac{1}{2r_B} \right) \frac{1}{2r_A} + \left( \frac{1 - \beta_A^2}{\mathcal{L}_A} + \frac{1}{2r_A} \right) \frac{1}{2r_B} \quad (297)$$

$$\gamma_i = \left( \frac{1}{2} \sin^2 \varphi + \frac{1}{2r_j} \right) \beta_i + \frac{1}{2r_i} \beta_j \cos \varphi \quad (298)$$

$$\delta_i = \left( \frac{1}{2} \sin^2 \varphi + \frac{1}{2r_j} \right) \frac{1 - \beta_i^2}{\mathcal{L}_i} \Delta s_i + \frac{1}{2r_i} \frac{1 - \beta_j^2}{\mathcal{L}_j} \Delta s_j \cos \varphi \quad (299)$$

with  $(i, j) = (A, B)$  or  $(B, A)$

$$K = \frac{1}{2} \left( \frac{1}{r_A} + \frac{1}{r_B} + \frac{1}{r_{A^T B}} \right) G - \frac{r_B \beta_B \gamma_B + r_A \beta_A \gamma_A}{2r_A r_B} \quad (300)$$

$$S = \frac{1}{2r_A} \left( \frac{1 - \beta_B^2}{\mathcal{L}_B} s_B G + \frac{1 - \beta_B^2}{\mathcal{L}_B} \Delta s_B \gamma_B \right) + \frac{1}{2r_B} \left( \frac{1 - \beta_A^2}{\mathcal{L}_A} s_A G + \frac{1 - \beta_A^2}{\mathcal{L}_A} \Delta s_A \gamma_A \right) \quad (301)$$

$$F = \frac{1}{2r_A} \frac{1}{2r_B} \frac{1}{KGY} \quad (302)$$

The torque on layer B is defined in the local magnetization basis by:

$$\boldsymbol{\tau} = \mathbf{J}_N - \mathbf{J}_B = \frac{2\hbar}{e^2 \mathcal{R}_{\text{Sh}}} (j_x \mathbf{e}_x + j_z \mathbf{e}_z - \mathbf{j}_{\parallel B}) = \frac{2\hbar}{e^2 \mathcal{R}_{\text{Sh}}} \tau \mathbf{e}_1 \quad (303)$$

We remind that  $\mathbf{e}_1$  is the in-plane normal vector orthogonal to the magnetization of  $F_B$ . We obtain:

$$\begin{aligned} \tau &= -\frac{1}{2} \sin \varphi (\mu_{\parallel A} + j_{\parallel A}) \\ &= -\frac{F}{2} \sin \varphi \left\{ \left[ \beta_A \left( 1 + \frac{1}{r_B} \right) - \beta_B \cos \varphi \right] (GY e V_b + S k_B \Delta T) \right. \\ &\quad \left. + \left[ \frac{\Delta s_A}{\mathcal{L}_A} (1 - \beta_A^2) \left( 1 + \frac{1}{r_B} \right) - \frac{\Delta s_B}{\mathcal{L}_B} (1 - \beta_B^2) \cos \varphi \right] K k_B \Delta T \right\} \end{aligned} \quad (304)$$

To justify the approximation that spin-flip and the second-order thermoelectric coefficients can be neglected, we performed a simulation including them and compared to the analytical solution Eq.(304). The spin-valve under consideration is  $\text{Cu}_{20}|\text{Co}_5|\text{Cu}_2|\text{Py}_5(\varphi)|\text{Cu}_{10}$  (indices are the thicknesses of the layers in nm), and a sketch of this stack is provided in Fig. 51, along with the simulated and analytical value of the torque:

We recover the usual feature that the spin-transfer torque is stronger in the antiparallel configuration than in the parallel configuration. As stated before, the mixed (closed-circuit) configuration strongly resembles the voltage case. This is rather obvious in Fig. 51:  $\tau_V$  and  $\tau_M$  have a very close angular dependence and seem almost to differ by a scaling factor.  $\tau_P$  however has a very different shape, hinting at its different origin. An important point is to note that this is not a general truth, but merely a trend. As Fig. 52 indicates,  $\tau_V$  and  $\tau_M$  may also have very different behaviors. What should be remembered is that  $\tau_M$  is somewhat intermediate between  $\tau_V$

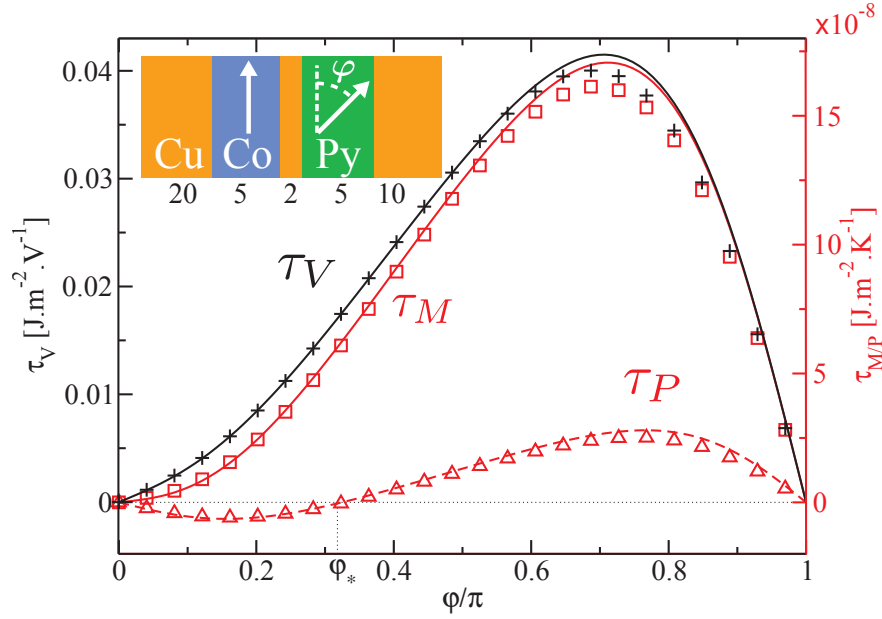


Figure 51.: Spin-transfer torque obtained when applying a voltage ( $\tau_V$ , bottom curve), a temperature gradient ( $\tau_M$ , top full curve), and a temperature gradient in the open-circuit configuration ( $\tau_P$ , top dashed curve), versus the magnetization angle  $\varphi$  of the Py layer with respect to that of the Co layer. Symbols represent the simulations including spin-flip scattering, while lines correspond to the analytical calculation Eq. (304). Here  $L_{Co} = L_{Py} = 5$  nm. Inset: sketch of the spin valve.

and  $\tau_P$ . How close it is to them strongly depends on the materials and system in play.

Although the coefficients  $G$ ,  $Y$ ,  $S$  and  $K$  may depend on  $\varphi$ , they have the property that their sign does not depend on this angle. We can therefore extract from Eq. (304) an expression of the waviness angle, for any applied temperature gradient and/or voltage:

$$\cos \varphi_* = \frac{\beta_A \left(1 + \frac{1}{r_B}\right) (GYeV_b + Sk_B\Delta T) + \frac{\Delta s_A}{\mathcal{L}_A} (1 - \beta_A^2) \left(1 + \frac{1}{r_B}\right) Kk_B\Delta T}{\beta_B (GYeV_b + Sk_B\Delta T) + \frac{\Delta s_B}{\mathcal{L}_B} (1 - \beta_B^2) Kk_B\Delta T} \quad (305)$$

With Eq. (305), we can recover a result presented in [17]: a criterion of waviness for a voltage-induced torque. Setting  $\Delta T$  to zero, we obtain:

$$\cos \theta_* = \frac{\beta_A r_B + 1}{\beta_B r_B} \quad (306)$$

This means that for the voltage-induced torque to be wavy, the layer must have a stronger spin-polarization than the fixed layer. A high resistance also helps, but there is a trade-off with the critical current: a thicker layer means more magnetic dipoles to switch, and therefore a higher critical current density.

We summarize this formula by saying that for a torque to be wavy, the spin-valve must be very asymmetric. We will see in the next section that this statement holds when applying a temperature gradient, although the exact meaning differs quite a bit.

### X - 3 WAVINESS OF THE THERMALLY-INDUCED TORQUE

As the introduction suggests, the configuration of the spin-valve (open or closed circuit) has an impact on its behavior. This is especially true when dealing with the waviness state of the spin-valve. Eq. (288) provides the open-circuit condition:  $GYeV_b + Sk_B\Delta T = 0$ . This gives for the pure (open-circuit) and mixed (closed-circuit) configurations the following waviness condition:

$$\cos \varphi_*^M = \frac{\beta_A S + \frac{\Delta s_A}{\mathcal{L}_A} (1 - \beta_A^2) K}{\beta_B S + \frac{\Delta s_B}{\mathcal{L}_B} (1 - \beta_B^2) K} \frac{r_B + 1}{r_B} \quad (307)$$

$$\cos \varphi_*^P = \frac{1 - \beta_A^2}{1 - \beta_B^2} \frac{\mathcal{L}_B \Delta s_A}{\mathcal{L}_A \Delta s_B} \frac{r_B + 1}{r_B} \quad (308)$$

Although Eq. (307) does not provide a closed equation for  $\cos \varphi_*$ , it is however enough to determine the waviness state. Indeed, even if the value of  $\varphi_*$  can only be found by solving a third degree polynomial equation in  $\cos \varphi_*$ , it is relatively straightforward to evaluate if the absolute value of the right-hand side of Eq. (307) is greater or lesser than 1.

Eq. (308) on the other hand provides a direct expression for  $\cos \varphi_*$ . We can see that a wavy torque can be obtained again by having very different material (an asymmetric valve). Where in the case of voltage-induced torque the quantity that

needed to be asymmetric was the polarization  $\beta$ , here we are interested in the quantity  $(1 - \beta^2)\Delta s/\mathcal{L}$ . Therefore, the free layer should have a stronger spin-dependent Seebeck coefficient than the fixed layer, but a smaller polarization. The part about the reduced Lorenz number  $\mathcal{L}_B/\mathcal{L}_A$  is essentially irrelevant, because it stays usually close to unity, in the Wiedemann-Franz limit.

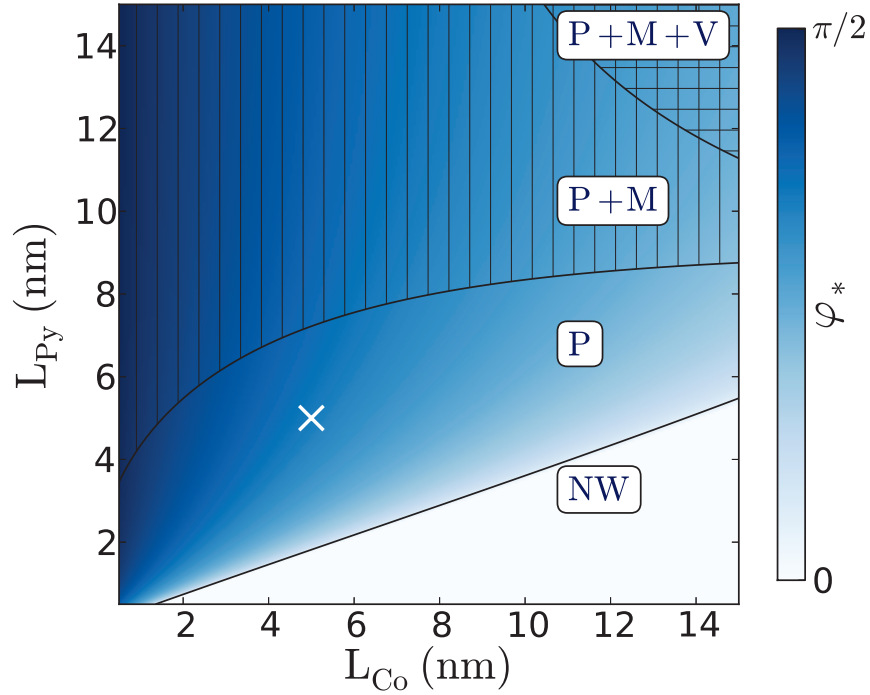


Figure 52.: Left: Waviness angle  $\varphi_*$  of the pure thermal torque  $\tau_P$  as a function of  $L_{Co}$  and  $L_{Py}$ . The white cross indicates value  $L_{Co} = L_{Py} = 5$  nm corresponding to Fig. 51. The presence of a letter V, M or P in a given region means that the angular dependence of the corresponding torkance  $\tau_V$ ,  $\tau_M$  or  $\tau_P$  is wavy. NW indicates the region where none of them are wavy.

The spin-valve can be engineered to give either a wavy or a non-wavy behavior for the torque on the free layer. The choice of materials of course is of major importance, but the geometry itself plays an important role, even for a 1D system. We illustrate this point in Fig. 52 by providing a “waviness phase diagram”<sup>1</sup>, as a function of the thicknesses  $L_{Co}$  and  $L_{Py}$  of the ferromagnetic layers in the stack

<sup>1</sup> By that, we simply want to indicate the domain of waviness for some couple of parameters, such as here the thicknesses of the ferromagnetic layers.

$\text{Cu}_{40}|\text{Co}_{L_{\text{Co}}}| \text{Cu}_2|\text{Py}_{L_{\text{Py}}}(\varphi)|\text{Cu}_{10}$ . We remind it gives in particular, for  $L_{\text{Py}} = L_{\text{Co}} = 5$  nm the results presented in Fig. 51.

The results in Fig. 52 and Eq. (306) may seem at first to contradict each other. The analytical result states that for the voltage-induced torque to be wavy, a lower polarization on layer A is preferable. Therefore, a thinner cobalt layer should be beneficial (because the copper layer in front of it will make the group less polarized). Our phase diagram shows however that a thicker cobalt layer gives a more wavy torque. The reason behind this is a rather common mistake when dealing with our effective parameters. The  $\text{Co}|\text{Cu}$  interface has a strong polarization  $\gamma = 0.77$ , whereas cobalt has a polarization of  $\beta = 0.46$ . Increasing the cobalt thickness therefore lowers the overall polarization of the group  $\text{Cu} + \text{Cu}|\text{Co} + \text{Co}$ .

As observed before, the waviness of the pure configuration is much easier to achieve, and also reaches much higher values. In the limit of very thin cobalt layers, the pure waviness angle reaches almost  $\pi/2$ , whereas in the same range, the voltage-induced waviness angle is five times lower.

Although this study presents the influence of the geometry on the waviness state, it does not provide a study of the influence of the parameters on the state of waviness, neither does it indicate how strong the temperature gradient must be to start switching.

Next section is dedicated to address those points, and more generally give clues to answer the questions: is thermal switching possible? and is a thermally-driven STO without external magnetic field possible?

#### X - 4 CRITICAL TEMPERATURE FOR SWITCHING

We saw in Section I - 2.6 the link between the critical current density and the slope of the torque at  $\varphi = 0$ , and  $\varphi = \pi$ . We remind the result we obtained, linking the torque slope to the magnetic parameters and to the critical current:

$$\left. \frac{\partial \tau}{\partial \theta} \right|_{\theta=0/\pi} = \pm \alpha B_u M_s L = \frac{\hbar}{e} J \eta (\theta = 0/\pi) \quad (309)$$

Writing  $\tau = \tau_P \Delta T$  and  $\tau = \tau_M \Delta T$  the link between the torque and the applied temperature difference, we get an expression for the critical temperature difference, that is the temperature needed to start switching the free layer using a thermal torque, in the pure or mixed case.

$$\Delta T_{P/M} = \frac{\alpha B_u M_s L}{\partial \tau_{P/M} / \partial \varphi} \approx \frac{L}{\partial \tau_{P/M} / \partial \varphi} \times 1.67 \text{ kJ} \cdot \text{m}^{-3} \text{rad}^{-1} \quad (310)$$

To obtain the estimate we give as the last part of this equation, we used the results from Ref[37]. They report the rather standard critical current density of  $J_{crit} = 10^7 \text{ A} \cdot \text{cm}^{-2}$  for a  $\text{Py}_{24}|\text{Cu}_6|\text{Py}_6(\varphi)$ . Simulating this spin-valve gives us a critical torque of the order of  $10^{-5} \text{ J} \cdot \text{m}^{-2} \cdot \text{rad}^{-1}$ . We take that value as a reference to evaluate how strong the temperature difference must be to start switching the free layer.

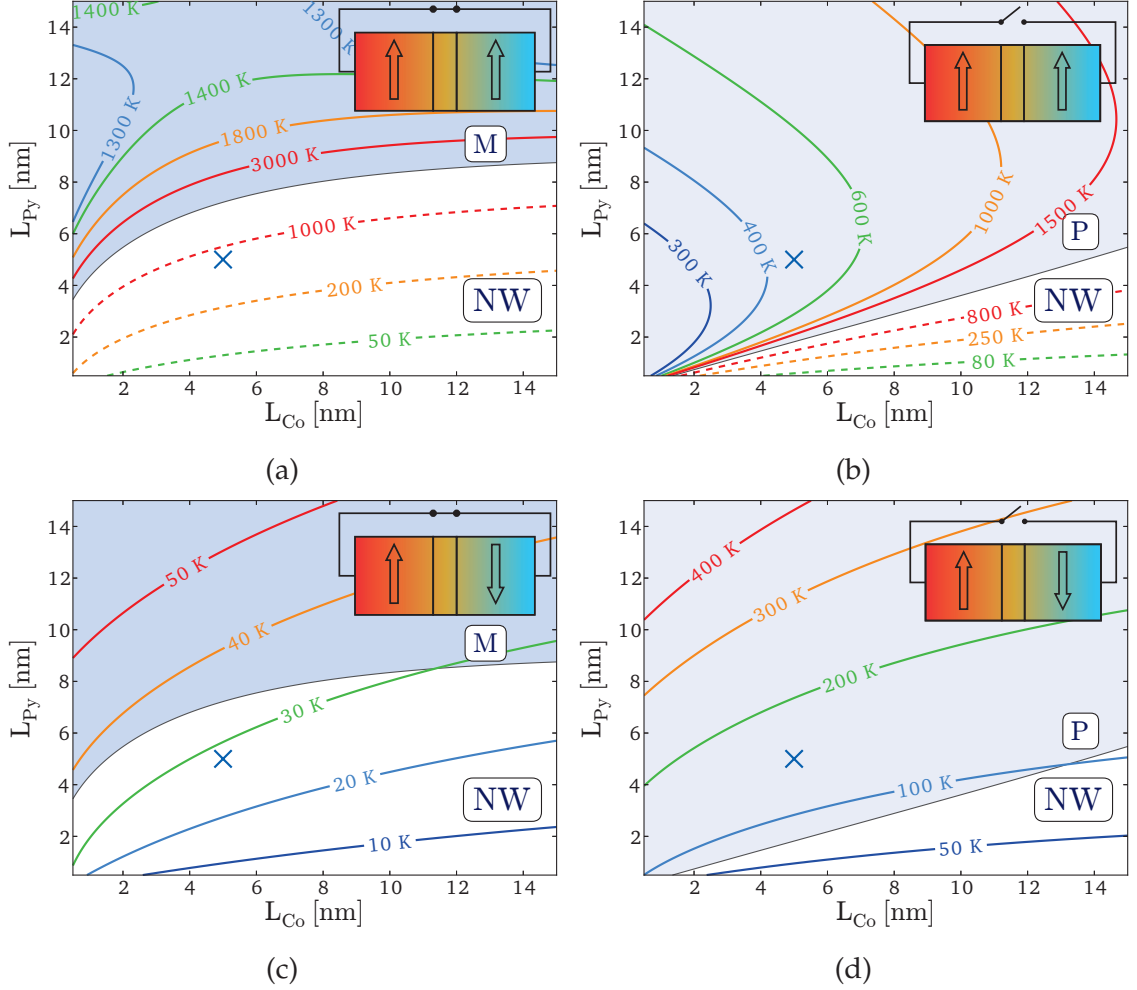


Figure 53.: Dependence of  $\Delta T_P$  (left column) and  $\Delta T_M$  (right column) in a  $\text{Cu}_{20}|\text{Co}_{L_{Co}}|\text{Cu}_2|\text{Py}_{L_{Py}}(\varphi)|\text{Cu}_{10}$  stack as a function of the layer thicknesses  $L_{Co}$  and  $L_{Py}$  in the parallel ((a) and (b)) and antiparallel ((c) and (d)) configurations. The blue cross indicates  $L_{Co} = L_{Py} = 5 \text{ nm}$ , cf Fig. 51. The background displays the waviness domains of Fig. 52.

Using that knowledge, we draw again Fig. 52, including the lines corresponding to

some values for the critical temperature in the pure and mixed configuration, for a parallel and an antiparallel configuration.

We took for the material parameters  $s_{Co} = -0.25$ ,  $s_{Py} = -0.21$ ,  $\Delta s_{Co} = -0.02$  and  $\Delta s_{Co} = -0.044$ . Those are small values, which explain the high values for the critical temperature gradient. In Fig. 54, we push the study further away by setting  $s_{Py} = 1.3$  and letting the values of  $\Delta s_{Py}$  go as high as 0.5. Doing so makes sense in our effective parameters approach, provided that we can find a material with a strong enough  $\Delta s$ . Although this goes beyond the scope of this thesis, materials such as semi-conductors, topological insulators or tunnel barriers can provide spin-dependent Seebeck coefficients that high. A recent discovery by the group of Kimura[66] even indicate that a CoFeAl alloy has a  $\Delta s \approx 0.4$ . It is worth noting that the shape of the iso- $\Delta T_{M/P}$  depends only weakly on the material parameters. The values however do depend a lot on those parameters, and in particular on the spin-dependent Seebeck coefficient, as Fig. 54 indicates.

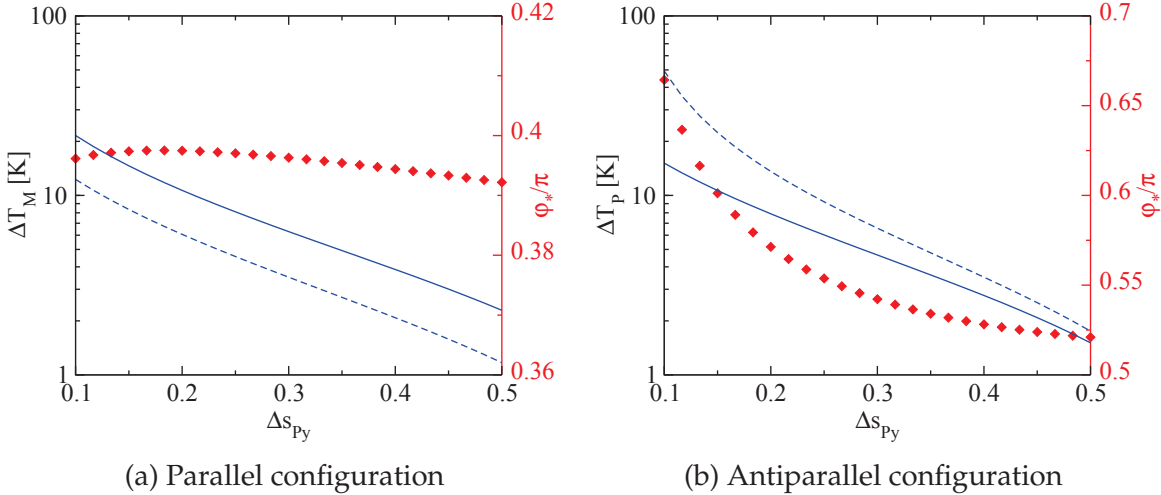


Figure 54.: Dependence on  $\Delta s_B$  of the critical temperature. The full (dashed) line corresponds to the parallel (antiparallel) configuration for  $L_{Co} = 50$  nm,  $L_{Py} = 2$  nm and  $s_{Py} = 1.3$ . Red symbols indicate the value of the waveness angle (right scale)

We see that although wavy stacks are more difficult to switch, the advent of novel materials makes it viable, with temperature differences of only a few degrees. Additionally, thanks to our parameter engineering, it is easy to create a fixed layer with a spin-dependent Seebeck coefficient close to zero, making the whole stack extremely wavy, of course in the open-circuit case, but in the closed-circuit case too.

This means that using those highly Seebeck-polarized materials, thermally-driven, magnetic field-free STOs are possible to create.

Another point we can emphasize is that since higher temperature decrease the saturation magnetization, and since the trend is to decrease the critical current density, our estimate for the critical torque is rather conservative, making our results all the more promising.

# XI

---

## $\beta_\tau$ IN A DOMAIN WALL SUBJECTED TO A TEMPERATURE GRADIENT

---

In Section III - 5, we investigated the out-of-plane torque in a long domain wall. We found an expression for the out-of-plane to in-plane torque ratio  $\beta_\tau$  involving the transport lengths, in particular  $\ell_L$  and  $\ell_\perp$ . We also presented numerical simulations of the value of  $\beta_\tau$  for domain walls not in the adiabatic limit.

For the sake of completeness, we investigate the same problem, in the case of thermally induced torque. The main and only result is quite simple: the origin of the torque does not affect how much of it is in-plane or out-of-plane.

### XI - 1 LONG WALLS: THE ADIABATIC LIMIT

To prove this, let us use the same derivation as in Section III - 5, using the same notations (except that to avoid confusion, since  $\theta$  is reserved for the temperature, we write the angle  $(\mathbf{m}, \mathbf{e}_z) = \varphi$ ). Using the local magnetization basis  $(\mathbf{m}, \mathbf{e}_1, \mathbf{e}_2)$ , projecting Eq. (225) to Eq. (227) onto it, and re-introducing  $\tilde{\mu} = \mu_1 + i\mu_2$ , we obtain:

$$\partial_{xx}\tilde{\mu} + \partial_x(\mu_\parallel\dot{\varphi}) = \left(\frac{1}{\ell_*} + \frac{\ell_*}{\ell_H}\Delta s^2 + \frac{1}{\ell_\perp} - \frac{i}{\ell_L}\right) \times \left[\left(\frac{\ell_*}{\ell_{sf}^2} + \frac{1}{\ell_\perp} - \frac{i}{\ell_L}\right)\tilde{\mu} + j_\parallel\dot{\varphi}\right] \quad (311)$$

As before, in the adiabatic limit, the left hand side of this equation is negligible, and what remains is:

$$\left(\frac{\ell_*}{\ell_{sf}^2} + \frac{1}{\ell_\perp} - \frac{i}{\ell_L}\right)\tilde{\mu} = -j_\parallel\dot{\varphi} \quad (312)$$

This equation is exactly the one obtained in the voltage-induced case, see Eq. (253). This makes sense because in our equations, the thermoelectric coefficients have no

influence on the transverse behavior. As a reminder, we obtain the following the expression:

$$\beta_\tau = \frac{\ell_L \ell_*}{\ell_{sf}^2} \left[ 1 + \frac{\ell_* \ell_L^2}{\ell_\perp \ell_{sf}^2} + \left( \frac{\ell_L}{\ell_\perp} \right)^2 \right] \quad (313)$$

Next, we show that this result is not a consequence of the adiabaticity of the wall, but a more general feature.

## XI - 2 SHORT WALLS

We performed a series of simulations in order to show that  $\beta_\tau$  is never influenced by the fact that the torque is induced by a voltage or a temperature gradient. First,

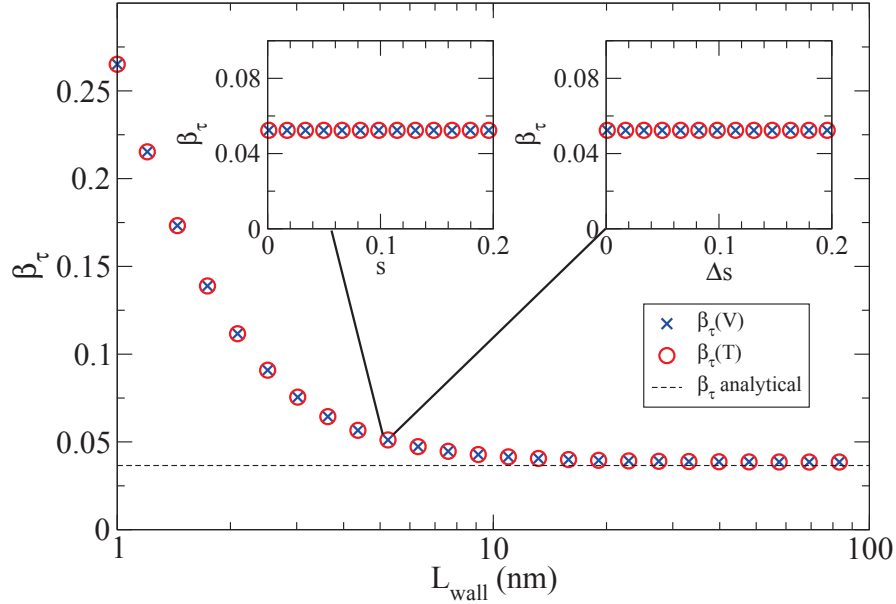


Figure 55.: Value of  $\beta_\tau$  when applying a voltage (blue crosses) or a temperature difference (red circles) to a Py domain wall of length  $L_{\text{wall}}$ . The dashed line is the theoretical value in the adiabatic limit. Insets: dependence of  $\beta_\tau$  with  $s$  (top left) and  $\Delta s$  (top right)

we go to shorter walls to rule out the effect of the adiabaticity. Then we vary the thermoelectric parameters to prove that this result is not due to a specific set of parameters, or the small values they have in metals. By linearity, proving this result

in the voltage case and a closed-circuit configuration is enough to prove it also for an open-circuit configuration. Fig. 55 summarizes these findings.

We think this short study is enough to prove the lack of influence of the driving force (voltage or temperature) of the torque in our model on the out-of-plane torque.



# XIII

---

## COMPARING SIMULATIONS TO SPIN-DEPENDENT SEEBECK MEASUREMENTS

---

Although the last part of this thesis was dedicated to applications of the spin caloritronics, one of its main ingredients (namely the polarization of the Seebeck coefficient) is poorly known, at the time of this thesis. A series of experiments by van Wees *et al.* is dedicated to measuring this coefficient, and has provided at least an estimate of its values for Py and Co.

We present first in this chapter their experimental setup. We then show the simulation we performed in order to confirm their results. It is worth noting that an exact match between their experiment and our simulation is impossible, because of the great number of material parameters that may not be exactly the same (especially those of the interfaces). The order of magnitude however is found to be very consistent, and our simulations also show that their measurement apparatus is viable, albeit subject to improvements.

### XII - 1 DESCRIPTION OF THE EXPERIMENT

Ref [78] presents an experimental setup to measure the value of the polarization of the Seebeck coefficient. The device they use is sketched in Fig. 57. It consists in a F|N|F spin-valve, where  $F$  is either Co or Py. A gold strip sits on top of it, with contacts at each end. The spin-valve sits on a piece of Pt, with three contacts. The central contact is used to measure the voltage across the spin-valve, and the two others are used for the thermoelectric part of the experiment. One is connected to a so-called heat line, through a layer of aluminum oxide. The heat line is a strip of platinum through which a low frequency ac current flows to generate heat thanks to the Joule effect. The oxide prevents the current from going into the electrical part of the device. The last contact is a thermocouple used to estimate the temperature in the system.

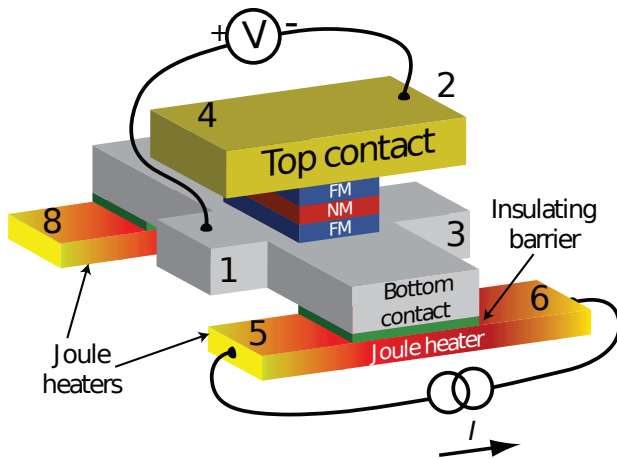


Figure 56.: Device used to measure the spin polarization of the Seebeck coefficient, as presented in Ref [78].

Their experiment consists in a GMR measurement performed in electrical open-circuit. A low frequency AC current is used in the heat line as the source of heat in the system. The heat line is separated from the rest of the system by a layer of  $\text{Al}_2\text{O}_3$ , to ensure that this current does not enter the device. The spin valve area is therefore under a gradient of temperature. The thermoelectric effects (spin-dependent and conventional) will convert this temperature difference into a voltage, and a GMR can be measured. The measurement is performed in a locked-in setup, and the second harmonics is extracted. Indeed, this second harmonics is the one proportional to the square of the current, and therefore to the Joule effect in the heat line, and the input temperature.

This signal is then fitted to match simulations they performed. By estimating the temperature difference on the spin-valve area only, they manage to link the value of the GMR to the value of the polarization of the Seebeck coefficient in the ferromagnet. Because of how this experiment is performed, our simulations can only stay at the semi-quantitative level, at best. To be actually quantitative, we would need all the material parameters involved, including those of the various interfaces. Since the latter in particular were not provided (nor measured), a strong uncertainty remains on the actual values of  $\Delta s$ . Nevertheless, this study gives a proof of concept, and a confirmation that their results are related to the spin-dependent thermoelectric effects, as they claimed.

XII - 2 SIMULATIONS AND COMPARISON

Fig. 57 displays two views of the simulated version of vanWees' device. It is made up of two leads used to measure the GMR in the central stack, and a lead used only to inject heat into the system. This last lead is electrically insulated from the rest of the system by a layer of  $\text{Al}_2\text{O}_3$ . Simulation-wise, this material is electrically insulating, thermally transparent. Since this material is non-physical, its thickness is therefore irrelevant, and is always one layer, regardless of the discretization step.

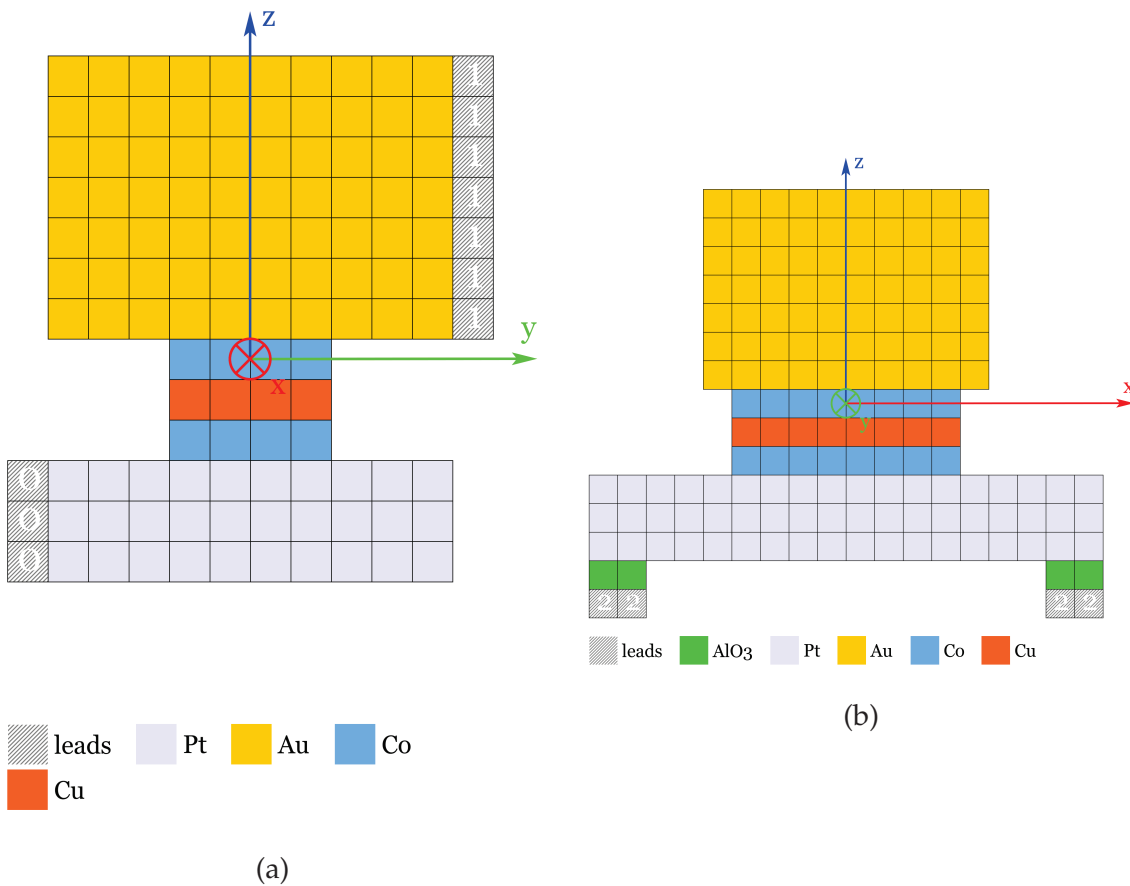


Figure 57.: Simulated version of the spin-dependent Seebeck measurement device. Each cell is 20 nm wide. (a) is a side view, while (b) is a front view (or rather a central cut) of the device.

First, we look at the temperature profile in the device. It becomes quickly apparent that it could be improved, too much heat being lost in lead 0 (see on Fig. 57a). Since

we want most of the gradient to occur on the spin-valve region, centering the heater may be beneficial.

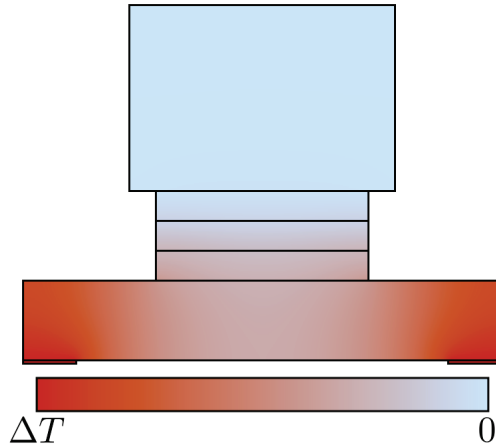


Figure 58.: Temperature profile in the spin-dependent Seebeck measurement (central cut, front view). Hot regions are red, cold ones are blue.

Now, in order to compare the measurements to the simulations, we extract the magnetoresistance  $\Delta R = R_{AP} - R_P$ , where AP stands for antiparallel and P for parallel, the magnetic configuration of the spin-valve.  $\Delta R$  is not strictly speaking a resistance, since it is the voltage drop over the device (between lead 0 and 1) by applied Kelvin (on lead 2). We then perform a series of simulations and plot  $\Delta R$  for varying values of  $\Delta S$  for the ferromagnet. Those plots are given in Fig. 59, with values reported by van Wees' group. The fact that Fig. 59a matches so well is probably a stroke of luck. Although we tried to match their material coefficients as best as we could, all of them were not reported. Also, some variation about the geometry is to be expected between our simulation and their actual device. The first message to be taken out of this simulation is that this device does provide a signal that is proportional to the spin-dependent part of the Seebeck coefficient, but extracting it directly is not possible, without relying on some kind of numerical model to estimate the temperature gradient over either the spin-valve area (as they did), or the entire device (as we did). The second message is that the current technique is not as precise as a direct measurement of a coefficient, but gives a good estimate of the order of magnitude of the coefficient.

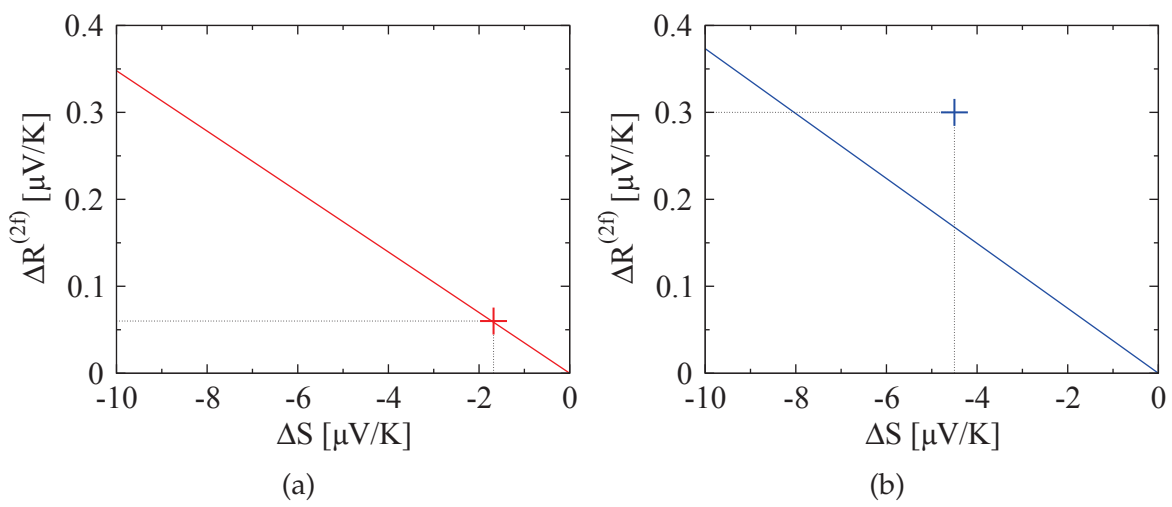


Figure 59.: Signal  $\Delta R$  vs spin-dependent Seebeck coefficient of the ferromagnet. (a) is for Co, (b) for Py. The cross is the value reported by van Wees' group in Ref [78]



Part E

ALGORITHM AND NUMERICS



**Summary of Part E**

Very soon during the process of deriving our theory, we understood its potential as a simulation tool using a rather original paradigm. The usual approach to solve the diffusion equation is by using a finite elements (or difference) approach, and discretizing the partial differential equations. The knowledge acquired during the derivation of our theory allowed us to implement an equivalent scheme where the diffusion equation is a consequence, and not a starting point.

We describe here the two parts of our software. CRMT1D deals only with 1D systems, and 1D devices can be built extremely fast (up to a logarithmic dependence with the total length of the system). CRMT3D on the other hand is designed to handle up to three-dimensional geometries of any shape. The geometry is discretized on a cubic lattice (as in Section VI - 2) acting as the nodes of our theory. The link equation, based on the  $\hat{S}$  matrix, connects each of this node, or cell. This results in an iterative solver, applying the equations on each cell/links set, and repeating it until convergence is reached.

After describing how the software operates, we give the work flow through a few detailed examples. We aim at proving in particular how user-friendly our simulation tool is.

We conclude by giving some convergence graphs, as well as simulation execution times with respect to the discretization step.

**Résumé de la Partie E**

Très tôt durant le processus de dérivation de notre théorie, son potentiel en tant qu'outil de simulation basé sur un paradigme novateur a été très clair. L'approche classique est de résoudre l'équation de diffusion en utilisant l'approche des éléments (ou différences) finies, et en discrétisant les équations différentielles partielles. La compréhension acquise durant notre dérivation nous a permis d'implémenter un algorithme équivalent où l'équation de diffusion est une conséquence et non plus un point de départ.

Nous décrivons ici les deux parties de notre logiciel. CRMT1D s'occupe exclusivement des systèmes 1D, et ces systèmes 1D peuvent être construits extrêmement rapidement (jusqu'à une dépendance logarithmique en la longueur totale du système). CRMT3D à l'inverse a été conçu pour gérer des géométries quelconques, jusqu'à trois dimensions. La géométrie est discrétisée selon un réseau cubique (comme dans Section VI - 2), correspondant aux noeuds dans notre théorie. L'équation de lien, reposant sur la matrice  $\hat{S}$ , connecte chacun de ces noeuds, ou cellules. Le résultat est un solveur itératif, appliquant les équations sur chaque ensemble cellule/liens, et recommençant jusqu'à convergence.

Après avoir décrit comment notre logiciel fonctionne, nous donnons les différentes étapes d'une simulation à travers quelques exemples détaillés. Nous essayons en particulier de prouver à quel point notre logiciel est intuitif et facile d'utilisation.

Nous finissons par donner quelques graphes de convergence, ainsi que des temps d'exécution en fonction du niveau de discrétisation.

# XIII

---

## ALGORITHM

---

One of the main results of this thesis is a numerical implementation of CRMT3D, allowing for reliable and fast simulations of charge, spin and heat transport in metallic devices. This package is written in Python, to use its readability and ease to write, while some parts are written in C++ to benefit from the speed of that language. The bridge between the two is custom made through the use of the Python/C API. No external automated wrapper has been used.

In the first section, we make the transition between the mathematical formulation and the computer side. Then we give an overview of the framework (through an object-oriented presentation). Finally, we go into more details and focus on the parts of the code that received some heavy optimizations.

### XIII - 1 DESCRIPTION OF THE BASE ALGORITHM

The CRMT code is based on equations Eq. (130), as well as Eq. (194) and Eq. (195) (for the probability conservation). They form respectively the link and node equation, that will be solved for each cell (and each direction, for the links).

The solver goes through all the cells and applies the node equation, and the link equations for each direction. These equation couple the outgoing (with respect to a link) probabilities with the incoming probabilities. In matrix form, those equations read:

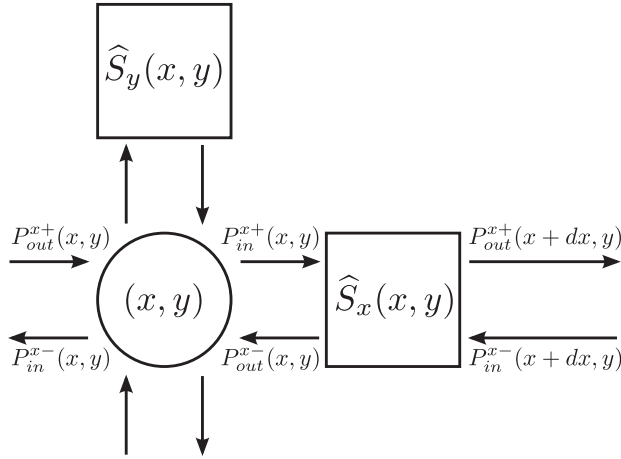


Figure 60.: Sketch of the nodes (circle) and links (boxes) in CRMT3D (in 2D for readability).

$$\begin{pmatrix} P_{out}^{\alpha-} \\ P_{out}^{\alpha+} \end{pmatrix} = \begin{pmatrix} \hat{r}' & \hat{t} \\ \hat{t}' & \hat{r} \end{pmatrix} \begin{pmatrix} P_{in}^{\alpha+} \\ P_{in}^{\alpha-} \end{pmatrix} \quad (314)$$

$$\begin{pmatrix} P_{in}^{x-} \\ P_{in}^{x+} \\ P_{in}^{y-} \\ P_{in}^{y+} \\ P_{in}^{z-} \\ P_{in}^{z+} \end{pmatrix} = \mathcal{N} \begin{pmatrix} P_{out}^{x-} \\ P_{out}^{x+} \\ P_{out}^{y-} \\ P_{out}^{y+} \\ P_{out}^{z-} \\ P_{out}^{z+} \end{pmatrix}, \quad \text{with } \mathcal{N} = \frac{1}{d} \underbrace{\begin{pmatrix} 1 & \dots & 1 \\ \vdots & & \vdots \\ 1 & \dots & 1 \end{pmatrix}}_{2d} \otimes \mathbb{1} - \underbrace{\begin{pmatrix} 1 & \dots & 1 \\ \vdots & & \vdots \\ 1 & \dots & 1 \end{pmatrix}}_d \otimes \begin{pmatrix} 0 & \mathbb{1} \\ \mathbb{1} & 0 \end{pmatrix} \quad (315)$$

In Eq. (315),  $d$  stands for the number of dimensions of the system. The dimension of  $\mathbb{1}$  is the same as the  $P$  vectors (4 elements for charge and spin, and possibly one for the heat if it is taken into account in the simulation).

Most of the programming work went into building the system. Once this is done, solving it is extremely straightforward, since it consists only in applying repeatedly the same two equations. Of course, knowing that, those operations had to be optimized to apply them as fast as possible. For example, in the first version of the solver, a profiling tool indicated that one complex multiplication took 16 CPU cycles, where it should have taken only one (or two, depending on the CPU technology) in the best case scenario. A simple rewriting using only float multiplications made it possible to improve this value to less than 4 cycles, on average (measured on a processor where it can be 2 cycles at best). Similarly, because  $\mathcal{N}$  is made of real numbers only, it was possible to drop one float multiplication and one addition. It may not seem much,

but over thousands and thousands of application of the same function, it adds up to make the whole solver quite efficient.

### XIII - 2 ARCHITECTURE OF THE FRAMEWORK

CRMT consists of four subpackages for computation, and two visualization subpackages.

We start briefly with the latter because they do not contain any physics, and we will not give any details about them. All the illustrations present in this thesis (unless specified) have been made thanks to either one of those subpackages. The first one is designed to produce 2D pictures of a slice of the geometry (ideal to represent 2D, or quasi-2D geometries). It also allows the display of any numerical field within the geometry. It is based on the Cairo drawing library.

The second subpackage, written in C++ and OpenGL, gives a dynamic 3D view of the geometry, ideal to visualize it under any angle. An extension to view scalar and vector fields in 3D is currently under development.

The four remaining packages, containing the simulation tools, are the following:

- CRMT
- CRMT1D
- CRMT3D
- Tools

#### XIII - 2.1 *Package CRMT*

The package CRMT contains two modules `S_builder` and `VFdatabase`.

`S_builder` contains a class `Smat`, corresponding to  $\hat{S}$ -matrices, as well as all the functions necessary to fill the coefficients of the matrices with the correct value, depending on the input material.

`VFdatabase` contains the Valet-Fert parameters of a variety of materials, and their interfaces. It also permits the creation of custom materials.

#### XIII - 2.2 *Package CRMT1D*

Because the node equation becomes extremely simple in the 1D case, simply adding in series the scattering matrices is enough to describe a 1D system. Taking advan-

tage of that, the `CRMT1D` package gives a much more efficient way of simulating devices. In particular, it contains two classes, the `Pillar` class describing multilayers, and the `DomainWall` class representing domain walls. Each of this class is a subclass of the `Device` class, grouping the common functions and attributes needed to compute currents, torques, etc... anywhere in the device.

Building a `Pillar` takes a time in  $\mathcal{O}(\ln(L))$ , where  $L$  is the total length of the system, while a `DomainWall` takes  $\mathcal{O}(L)$ . The building step of a `Device` is the longest, and many operations can be done without the need of rebuilding it completely (for instance varying the angle of a free layer in a `Pillar`)

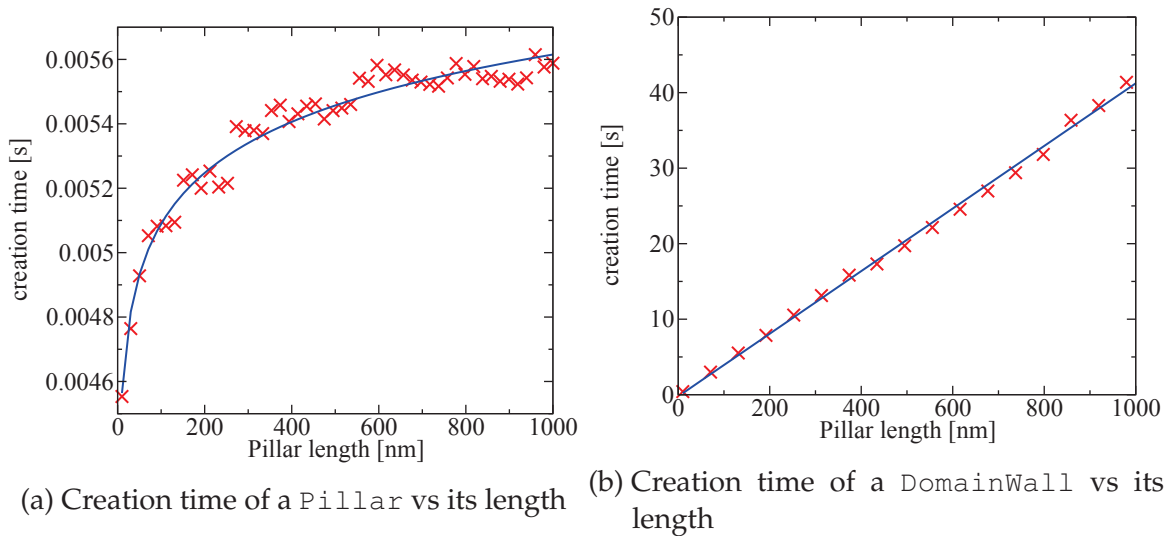


Figure 61.: Creation time (in seconds) of the `CRMT1D` systems versus length of the system. Those plots exhibit clearly the logarithmic (for the `Pillar`) and linear (for the `DomainWall`). The measurement method is discussed in the text.

Fig. 61 shows clearly the estimated building time dependence with the length, for the two types of systems. However, it also shows that building a `DomainWall` required much longer.

To measure the execution time, we used the `timeit` module in Python, which allows running a certain portion of code a great number of times, and returns how much time the total operation took. For each length, the same `Pillar` was built 1000 times, while a `DomainWall` build was repeated only 100 times (due to its longer building time, this measurement was less prone to variations due to background programs).

To understand why creating a `DomainWall` takes so long, one must understand how it is built. The whole length of the system is first divided into  $N$  sections. Those sections are where the currents and potentials will be measured, and are a first coarse level of discretization. However, there is a finer level of discretization, which is the one used to build the system. Each section is further divided into small slices (here they are  $10^{-2}$  nm long) of constant magnetization. The matrix of the slices are finally added together to create the matrix of the section. Building the slice takes a logarithmic time with respect to its length (it is the same code used in the `Pillar`). Therefore the thinner the slice, the less we benefit from this logarithmic time. A step of  $10^{-2}$  nm is probably an overkill for most purposes, but a too coarse step would disrupt the continuity of the magnetization and lead to wrong results. As always, one has to find the point where the level of description and the computation time are both satisfying.

### XIII - 2.3 Package *CRMT3D*

Although this package is perfectly able to describe 1D systems, its performances are not comparable with what `CRMT1D` provides. However, it provides the capability to create and deal with 2D and 3D structures, regardless of their shape (They do not need to be rectangular, they can have holes, etc...). The `geometry` module provides a `Geometry` class, which is basically an optimized `numpy.ndarray`. A `Geometry` is made to contain instances of `Atom`, which are basic containers for a material name and rotation angles if the material is magnetic. Because many cells will contain the exact same `Atom`, the memory is optimized by internally storing an index to an `Atom` instance. Since most devices (the only notable exception being devices with magnetic texture) contain very few different materials and angles, it is usually possible to store the information in 8 bits cells (up to 255 different materials, plus the `NONE_INDEX` to store empty cells). The `geometry` package also contains an `Atom` subclass called `Lead`, that contains a purely transparent material, and should be used as leads for the system.

When the `Geometry` is created, it is fed into the `System` class from the `finalized_system` package. This class will transform the `Geometry` into something that can be parsed into a solver. This is where the  $\hat{S}$ -matrices for each link is computed, and the variables of the problem, the `Pin` and `Pout` are initialized. In this class, the  $(x, y, z)$  coordinates of a cell is translated into a single integer  $u$ . The order by which the coordinates are read can be specified by the user to improve the performance of the solver. This translation is used to ensure that the solver does as

few checks as possible. In particular, empty cells (where no equation needs to be applied) do not have an equivalent  $u$  value, and are therefore ignored naturally by the solver.

Finally, the `System` can be parsed to one of the solvers present in the `solver` package. Our software comes with two solvers. The first applies the node equation, then the link equation to each cell, always in the same order and starts over until convergence is reached. We refer to it as the direct solver.

The second, improved, solver can be understood as the direct solver applied twice, first in the normal order, and a second time in the reverse order. These two operations are then iterated until convergence. This ensures for example that in simple geometries (namely bars) the input information from a lead is transmitted to the other lead in only one iteration, but also that some information comes back in the same iteration. Applying the equations always in the same direction makes the first backward information to come back in  $\mathcal{O}(L/dl)$  steps, where  $L$  is the length between the two leads, and  $dl$  the discretization step. We refer to this second solver as the sweeping solver.

The sweeping solver is the default behavior of the software (because of its improved performance in almost every case), and is used by simply calling the function `solve`, although the direct solver can be achieved by providing another option to this function. The number of iteration may be specified to this function, but the default behavior is to automatically detect convergence by summing the incoming and outgoing charge (and heat, when applicable) currents over the leads. When the solver has reached convergence, this sum should be close to zero, up to some numerical error. A relative error can be specified to the function, and the value of  $10^{-6}$  is usually more than enough. Lower values drastically improve the convergence time, but lowers the precision. Also, a parameter `N` indicates how many iterations are applied before checking for convergence. Checking every step is of course detrimental to the performance.

The last module in this package is the `observables` module, containing the `Observables` class. It is only used to obtain currents, torques, and potentials anywhere in the system, with easy access.

### XIII - 3 PACKAGE TOOLS

This package contains everything making the use of the code and writing scripts easier. It goes from data import/export function to useful mathematical functions.

## XIII - 4 SAMPLE CODE

We give here how a typical simulation looks like, for a 1D geometry, then for a 3D geometry. Note that a 1D geometry could very well be simulated through the use of CRMT3D. CRMT1D is however faster and better suited.

## XIII - 4.1 CRMT1D

First we give an example of usage of the Pillar class:

```

1 from CRMT.CRMT1D import Pillar , Layer
2 from math import pi
3 import numpy as np
4
5 P = Pillar ([ Layer ( "Cu" ,10) ,
6               Layer ( "Py" ,20 ,0) ,
7               Layer ( "Cu" ,2) ,
8               Layer ( "Py" ,5 ,0) ,
9               Layer ( "Cu" ,10) ])
10
11 for th in np.linspace (0 ,pi ,25) :
12     P.update_layer_angle (3 ,th)
13     print P.torques (layer_index=3)

```

Code sample 1: Usage of the Pillar class in CRMT1D

We first import everything we need, then build the `Pillar` by providing it with a list of `Layer` containing the material, its length, and the angle of the magnetization, when applicable. Then, in the loop, we update the third layer (Py) angle, and print the torque applied on it. It is an easy to measure the angular dependence of a quantity (here the torque), without having to rebuild the whole `Pillar`.

Next, an example for the `DomainWall` class:

In this example, we create the domain wall by providing it with a material (it is made up of only one ferromagnetic material), a length, the number of sections, and a dictionary `pfkwargs` containing information needed for the profile function (the function  $(\theta(x), \varphi(x))$ ). The fields given here correspond to the default profile function.

## ALGORITHM

```
1 from CRMT.CRMT1D import DomainWall
2 L=100
3 N = 20
4 DW = DomainWall(material="Py",
5                 length=L,
6                 pfkwargs={'length_wall':L/10., 'length_system':L},
7                 N=N)
8
9 for i in xrange(N):
10     print DW.currents(i)
11     print DW.torques(i)
```

Code sample 2: Usage of the DomainWall class in CRMT1D

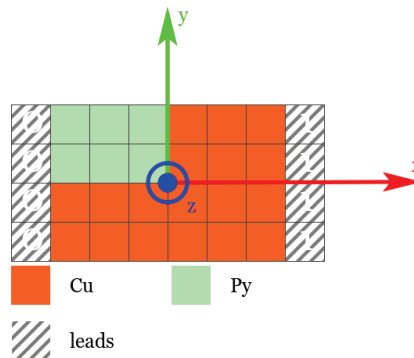


Figure 62.: Geometry used in the sample code using CRMT3D

The values used here are the default, used if no dictionary `pfkwargs` is provided. If another profile function is provided during the definition of the `DomainWall`, the dictionary is used to provide additional variables to the function, other than  $x$ . Finally in the loop, we print the currents (charge, spins) at each section, as well as the torque (in plane and out-of-plane).

### XIII - 4.2 CRMT3D

Here we give an example of use of the `CRMT3D` package, with a 2D system. At the end of the script, we export the geometry as a picture. Here is the output:

First, as usual in a Python script, we import everything that will be needed later on.

```

1 from CRMT.CRMT3D.geometry import Geometry, Atom, Lead
2 from CRMT.CRMT3D.finalized_system import System
3 from CRMT.CRMT3D.solver import solve
4 from CRMT.CRMT3D.observables import Observables
5 from CRMT.Illustrator.geometryIllustrator import
   GeometryIllustrator

```

Code sample 3: List of modules to import for a typical simulation using CRMT3D

Then, we create the geometry by first defining a few lengths, defining the discretization step, and finding out the number of cells needed for the geometry.

```

1 L_y = 4.
2 L_F_x = 3.
3 L_F_y = 2.
4 dl = 1.
5 matN = "Cu"
6 matF = "Py"
7
8 x_F = round(L_F_x/dl)
9 y_F = round(L_F_y/dl)
10 x = int(round(L_x/dl))+2    #+1 lead on each side
11 y = int(round(L_y/dl))
12 z = 1
13
14 geometry = Geometry(x,y,z)
15
16 geometry[:, :, :] = Atom(matN)
17 geometry[x_F+1, -y_F:, :] = Atom(matF, theta=0.)    #+1 is to
   include the lead
18 geometry[0, :, :] = Lead(lead=0, V=1.)
19 geometry[-1, :, :] = Lead(lead=1, V=0.)

```

Code sample 4: Creating and defining a geometry

## ALGORITHM

The next lines simply create the system from the geometry, and uses the solver. It detects automatically the convergence, by checking that the current is conserved up to the specified error. Current conservation is checked every N iterations.

```
1 sys = System(geometry , dl=dl)
2 solve (sys ,N=200 ,error=1e-8)
```

Code sample 5: Creating the system and applying the solver

Finally, an instance of `Observables` is created to measure the charge current at the leads (and display only the one corresponding to lead 0 in this case).

```
1 obs = Observables(sys)
2 print obs.jc_at_leads()[0]
```

Code sample 6: Basic use of the Observable class

The last two lines show how to create Fig. 62

```
1 I = GeometryIllustrator(geometry)
2 I.draw(name="basicCRMT3Dgeometry",cut=('z',0))
```

Code sample 7: Basic use of the Illustrator class

This concludes the presentation of the work flow with the CRMT package. We hopefully showed that it is a user-friendly, agile code. We now present its performance on real examples.

## XIII - 5 PERFORMANCE

In order to give an estimate of how fast CRTM3D is, we perform a simulation while varying a given parameter. Using the `timeit` module in python, we measure the time taken by the solver only (it is the longest part of any simulation, by far). Those simulations are performed on one core of an Intel ©Core™2 Duo, running at 2.4 GHz.

The first measurement is the time needed to perform 1000 iterations for an increasing number of cells. As Fig. 63 shows, the execution time is linear in the number

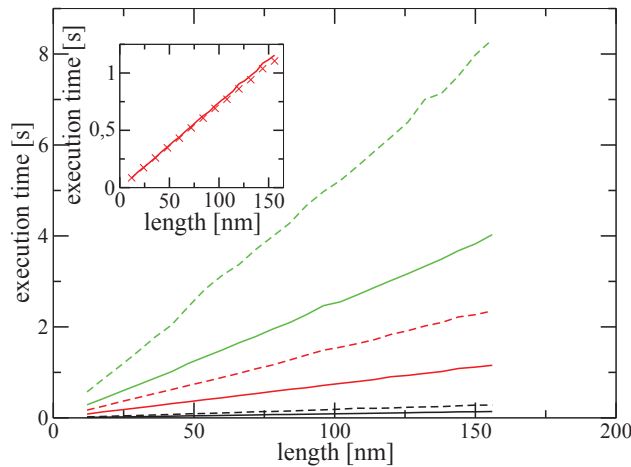


Figure 63.: Execution time in seconds for 1000 iterations vs the length of the bar. The transverse dimensions are  $12 \text{ nm} \times 12 \text{ nm}$ . The discretization step is  $6 \text{ nm}$  (black lines),  $3 \text{ nm}$  (red lines) and  $2 \text{ nm}$  (green lines). The results for the direct solver is represented in full lines while those for the sweeping solver are dashed. Inset: Execution time for the same simulation, for the direct solver, for a  $3 \text{ nm}$  step, where the increased dimension is along the  $y$  axis and not the  $x$  anymore. This illustrates that the execution time is dependent only on the number of cells, and not their organization.

of cells, and is independent on how those cells are organized. We also see that the sweeping solver takes roughly twice the time of the direct solver, which makes sense since it corresponds to applying it twice, the second time iterating over the cells in reverse order.

The second measurement shows the number of iterations needed (the time needed is proportional to this value) to reach convergence (with a relative error of  $10^{-6}$ ). This results in a square dependence in the length of the system. On one hand, we have the linear dependence mentioned simply for iterating over the cells, and on the other hand another linear dependence corresponding to the dependence of the convergence with the total length. The longer the distance between the two leads, the more the effect of each iteration is “diluted”. Fig. 64 clearly shows this quadratic dependence, and also exemplifies that the sweeping solver, while doing twice as many operations, is much more efficient.

The main message to take from those examples is that a full simulation can be performed in a matter of minutes, for the most demanding ones. This makes our

## ALGORITHM

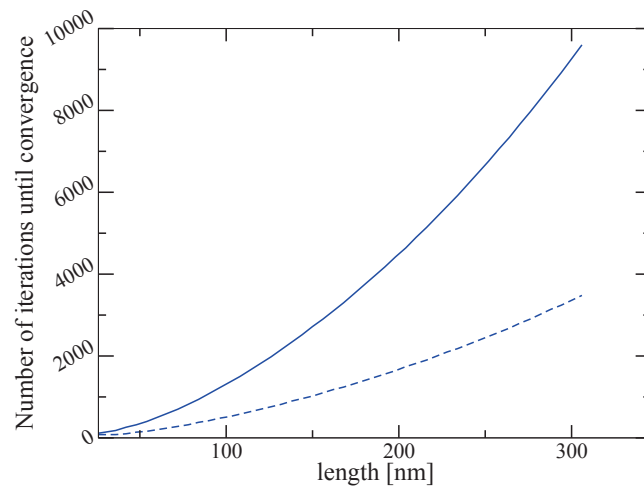


Figure 64.: Number of iterations to reach convergence vs the length of the bar. The transverse dimensions are  $12 \text{ nm} \times 12 \text{ nm}$ . The discretization step is  $6 \text{ nm}$ . The results for the direct solver is represented in full lines while those for the sweeping solver are dashed.

framework quite effective. The simple object architecture makes it easy to deploy a full simulation in a few lines, where most of it is actually the description of the geometry. Even better performances can be obtained by several techniques, such as increasing the discretization step (the diffusive nature of the equations allows for steps of several nanometers to be taken with barely any loss of precision), reducing the convergence precision (does one actually need a precision up to six digits ?) or skip one dimension altogether when the symmetry of the system allows it. The latter can be taken even further for unidimensional geometries, which can be simulated even more efficiently by using our 1D package.

---

## CONCLUSION

---

### WHAT HAS BEEN DONE

In this thesis, we investigated first the behavior of the spins transverse to their surrounding magnetization, and their impact on the giant magneto-resistance and spin-transfer torque. Then, we studied the feasibility of spin-valves (and more generally spintronics devices) powered by a temperature gradient rather than a bias voltage, through the dependence of the thermoelectric properties upon the spin species under consideration in ferromagnetic materials.

The first topic of investigation resulted in a semi-classical theory akin to the Valet-Fert theory, albeit including the non-collinear effects (our theory does reduce to the Valet-Fert theory within the correct set of approximations). In particular, it describes the fact that a spin transverse to its surrounding magnetization will precess around it, and be eventually absorbed. Both processes happen over very short distances, from a fraction to a few nanometers. These estimates come from an analysis we made from *ab initio* calculation of the mixing conductance we found in the literature. We proposed an experimental scheme capable of measuring those two lengths from simple GMR measurements. We also presented how those two phenomena can be related to the out-of-plane component of the spin-transfer torque in long (>10 nm) magnetic domain walls (which is strongly related to their dynamics).

The second topic resulted in an extension of the theory derived in the first part, in order to include the effects of the temperature (or rather the gradients thereof). To do so extensively, and in the same way as with the spin-dependent conductivity in ferromagnetic metals, we included the thermoelectric effects in our theory, as well as their spin-dependent part. This theory (as well as experimental results on the value of those spin-dependent thermoelectric coefficients) allowed us to predict that thermally powering spintronics devices is indeed possible, with reasonable temperature differences (down to a few degrees).

Our theory resulted also in a simulation tool, designed to be fast, easy to use, and reliable. This tool has been the cornerstone of our work, and is behind most of our numerical results.

## ALGORITHM

### WHAT ELSE CAN BEEN DONE

Future work can be done along a few directions. From a purely theoretical approach, taking into account the spin temperature might give a better understanding of some experiments where the assumption of thermalization fails. Another approach would be to investigate the thermoelectric properties of magnetic interfaces, rather only those of bulk materials. Taking those interfacial effects into account would be necessary to predict more accurately the temperature difference needed to power the device. Cleverly selecting materials and their interfaces may lead to even smaller requirements. One device in particular would benefit from this kind of technology: the nano-oscillators. Generating electromagnetic waves without the need of an external source of electricity would of course find applications in a lot of fields.

Finally, our simulation tool (and more generally our algorithm) is powerful enough that it might become possible to couple it to a micromagnetic simulation suite, without too much of a overhead. That would lead to two units computing the information the other needs: our tool would provide to the micromagnetic side the value of the torque (and in particular its usually poorly known out-of-plane component), while in exchange the micromagnetic side would give our tool the instantaneous magnetization state of the system. This would result in a one-of-a-kind piece of software with unmatched precision.

## APPENDICES



---

## MATERIAL PARAMETERS DATABASE

---

All of our simulations were based on some given materials, which properties had to be parametrized. We constituted a database of those parameters. In the Valet-Fert theory, interfaces and bulk materials have very similar properties, which explains why the parameter list is similar. Those parameters are, for a bulk material (see Table 8 for the values):

- $\rho_*$  the resistivity of the material, expressed in  $\Omega \cdot \text{nm}$
- $\beta$  the spin asymmetry (or polarization), describing the relative difference of resistivity between the majority and minority spin channels
- $\ell_{sf}$  the spin-flip length, expressed in nm, the characteristic length over which the spin orientation is maintained
- $\ell_L$  the Larmor precession length, expressed in nm, the characteristic length describing the precession of a spin transverse to the surrounding magnetization.
- $\ell_{\perp}$  the transverse penetration length, expressed in nm, the characteristic length describing how deep a spin transverse to the surrounding magnetization can penetrate in the material
- $s$ , the (reduced) Seebeck number, which is the non spin-dependent part of the Seebeck coefficient expressed in units of  $k_B/e$
- $\Delta s$  the (reduced) spin-dependent Seebeck number, which is the spin-dependent part of the Seebeck coefficient expressed in units of  $k_B/e$

For an interface, the list is shorter because we assume that no thermoelectric effects occur at interfaces. We also don't give here values for the mixing (transverse) properties of the interfaces, because they are highly dependent on the quality of the interface, and should be adjusted accordingly in the simulations. The parameters are (see Table 9 for the values):

- $r_b^*$  the resistivity of the interface, expressed in  $\Omega \cdot \text{nm}^2$

## MATERIAL PARAMETERS DATABASE

Name	$\rho_*$ [ $\Omega \cdot \text{nm}$ ]	$\beta$	$\ell_{sf}$ [nm]	$\ell_L$ [nm]	$\ell_{\perp}$ [nm]	$s$	$\Delta s$
Al	5	0	500	-	-	-0.017	0
Co	75	0.46	60	0.34	1.0	-0.23	-0.02
Cu	5	0	500	-	-	0.017	0
Fe	80	0.45	60	0.30	1.2	0.17	unknown
Py	291	0.76	5.5	0.8	1.7	-0.28	-0.44
Ag	17	0	30	-	-	0.017	0
Au	20	0	30	-	-	0.017	0
Cr	1250	0	6	-	-		0
Pt	42	0	14	-	-	-0.06	0
Ni	34	0.14	21	1.25	6		unknown
Ru	100	0	14	-	-	unknown	0

Table 8.: Table of the material parameters used by default for the simulations. When comparing to actual measurements, and if the material parameters were available, those had the precedence. Some parameters (especially the spin-dependent Seebeck coefficients) have not yet been measured, and therefore no value are reported yet. The transverse lengths  $\ell_L$  and  $\ell_{\perp}$  are obviously irrelevant for non-magnetic metals.

- $\gamma$  the spin asymmetry (or polarization), describing the relative difference of resistivity between the majority and minority spin channels (similar to the  $\beta$  of a bulk material)

Name	$r_b^*$ [ $\text{f}\Omega \cdot \text{m}^2$ ]	$\gamma$
Ag Co	0.56	0.85
Ag Py	0.56	0.1
Au Co	0.5	0.77
Au Py	0.5	0.77
Cu Au	0.5	0
Cu Co	0.51	0.77
Cu Cr	0.3	0
Cu Fe	5.8	0.22
Cu Ni	0.18	0.25
Cu Pt	0.5	0
Cu Py	0.5	0.7
Ru Co	0.5	-0.2

Table 9.: Table of the material parameters of common interfaces used in the simulations.



---

## BIBLIOGRAPHY

---

- [1] T. Valet and A. Fert. Theory of the perpendicular magnetoresistance in magnetic multilayers. *Phys. Rev. B*, 48(10):7099, 1993.
- [2] L. Berger. Emission of spin waves by a magnetic multilayer traversed by a current. *Phys. Rev. B*, 54:9353–9358, Oct 1996.
- [3] J C Slonczewski. Jmmm current-driven excitation of magnetic multilayers. *JMMM*, 62:L1, 1996.
- [4] Mark Johnson and R. H. Silsbee. Thermodynamic analysis of interfacial transport and of the thermomagnetolectric system. *Phys. Rev. B*, 35:4959–4972, Apr 1987.
- [5] Laurent Gravier, Santiago Serrano-Guisan, François Reuse, and Jean-Philippe Ansermet. Thermodynamic description of heat and spin transport in magnetic nanostructures. *Phys. Rev. B*, 73:024419, Jan 2006.
- [6] Laurent Gravier, Santiago Serrano-Guisan, François Reuse, and J.-Ph. Ansermet. Spin-dependent Peltier effect of perpendicular currents in multilayered nanowires. *Phys. Rev. B*, 73:052410, Feb 2006.
- [7] M. N. Baibich, J. M. Broto, A. Fert, F. Nguyen Van Dau, F. Petroff, P. Etienne, G. Creuzet, A. Friederich, and J. Chazelas. Giant magnetoresistance of (001)Fe/(001)Cr magnetic superlattices. *Phys. Rev. Lett.*, 61:2472–2475, Nov 1988.
- [8] G. Binasch, P. Grünberg, F. Saurenbach, and W. Zinn. Enhanced magnetoresistance in layered magnetic structures with antiferromagnetic interlayer exchange. *Phys. Rev. B*, 39:4828–4830, Mar 1989.
- [9] Simone Borlenghi, Valentin Rychkov, Cyril Petitjean, and Xavier Waintal. Multiscale approach to spin transport in magnetic multilayers. *Phys. Rev. B*, 84:035412, Jul 2011.

## Bibliography

- [10] Gerrit E. W Bauer, Yaroslav Tserkovnyak, Daniel Huertas-Hernando, and Arne Brataas. Universal angular magnetoresistance and spin torque in ferromagnetic/normal metal hybrids. *Phys. Rev. B*, 67(9):094421, 2003.
- [11] Arne Brataas, Gerrit E.W. Bauer, and Paul J. Kelly. Non-collinear magnetoelectronics. *Physics Reports*.
- [12] I Turek and K Carva. Spin-mixing conductances of metallic and half-metallic magnetic layers. *Journal of Physics: Condensed Matter*, 19(36):365203, 2007.
- [13] K. Carva and I. Turek. Spin-mixing conductances of thin magnetic films from first principles. *Phys. Rev. B*, 76:104409, Sep 2007.
- [14] M. D. Stiles and A. Zangwill. Anatomy of spin-transfer torque. *Phys. Rev. B*, 66:014407, Jun 2002.
- [15] A. Thiaville, Y. Nakatani, J. Miltat, and Y. Suzuki. Micromagnetic understanding of current-driven domain wall motion in patterned nanowires. *Europhys. Lett.*, 69(6):990–996, 2005.
- [16] F. K. Dejene, N. Vlietstra, D. Luc, X. Waintal, J. Ben Youssef, and B. J. van Wees. Control of spin current by a magnetic yig substrate in NiFe/Al nonlocal spin valves. *Phys. Rev. B*, 91:100404, Mar 2015.
- [17] Valentin S. Rychkov, Simone Borlenghi, Henri Jaffres, Albert Fert, and Xavier Waintal. Spin torque and waviness in magnetic multilayers: A bridge between valet-fert theory and quantum approaches. *Phys. Rev. Lett.*, 103:066602, Aug 2009.
- [18] S. S. P. Parkin, N. More, and K. P. Roche. Oscillations in exchange coupling and magnetoresistance in metallic superlattice structures: Co/Ru, Co/Cr, and Fe/Cr. *Phys. Rev. Lett.*, 64:2304–2307, May 1990.
- [19] S. S. P. Parkin. Systematic variation of the strength and oscillation period of indirect magnetic exchange coupling through the 3d, 4d, and 5d transition metals. *Phys. Rev. Lett.*, 67:3598–3601, Dec 1991.
- [20] P. Bruno and C. Chappert. Ruderman-kittel theory of oscillatory interlayer exchange coupling. *Phys. Rev. B*, 46:261–270, Jul 1992.

- [21] M. Lederman, S. Schultz, and M. Ozaki. Measurement of the dynamics of the magnetization reversal in individual single-domain ferromagnetic particles. *Phys. Rev. Lett.*, 73:1986–1989, Oct 1994.
- [22] Stuart S. P. Parkin, Masamitsu Hayashi, and Luc Thomas. Magnetic domain-wall racetrack memory. *Science*, 320(5873):190–194, 2008.
- [23] J. Grollier, V. Cros, A. Hamzic, J. M. George, H. Jaffrès, A. Fert, G. Faini, J. Ben Youssef, and H. Legall. Spin-polarized current induced switching in co/cu/co pillars. *Applied Physics Letters*, 78(23), 2001.
- [24] A. Fert, V. Cros, J.-M. George, J. Grollier, H. Jaffrès, A. Hamzic, A. Vaurès, G. Faini, J. Ben Youssef, and H. Le Gall. Magnetization reversal by injection and transfer of spin: experiments and theory. *Journal of Magnetism and Magnetic Materials*, 272–276, Part 3(0):1706 – 1711, 2004. Proceedings of the International Conference on Magnetism (ICM 2003).
- [25] O. Parcollet and X. Waintal. Spin torque in a nanomagnet coupled to non-collinear ferromagnetic electrodes. *Phys. Rev. B*, 73:144420, Apr 2006.
- [26] D.C. Ralph and M.D. Stiles. Spin transfer torques. *Journal of Magnetism and Magnetic Materials*, 2008.
- [27] S. I. Kiselev, J. C. Sankey, I. N. Krivorotov, N. C. Emley, R. J. Schoelkopf, R. A. Buhrman, and D. C. Ralph. Microwave oscillations of a nanomagnet driven by a spin-polarized current. *Nature*, 425(6956):380–383, Sep 2003.
- [28] D. V. Berkov, C. T. Boone, and I. N. Krivorotov. Micromagnetic simulations of magnetization dynamics in a nanowire induced by a spin-polarized current injected via a point contact. *Phys. Rev. B*, 83:054420, Feb 2011.
- [29] Stefano Bonetti, Pranaba Muduli, Fred Mancoff, and Johan Åkerman. Spin torque oscillator frequency versus magnetic field angle: The prospect of operation beyond 65 ghz. *Applied Physics Letters*, 94(10):-, 2009.
- [30] <http://www.wdc.com/wdproducts/library/other/2579-850121.pdf>.
- [31] W. P. Pratt, S.-F. Lee, J. M. Slaughter, R. Loloee, P. A. Schroeder, and J. Bass. Perpendicular giant magnetoresistances of Ag/Co multilayers. *Phys. Rev. Lett.*, 66:3060–3063, Jun 1991.

## Bibliography

- [32] Alan Kalitsov, Mairbek Chshiev, Ioannis Theodonis, Nicholas Kioussis, and W. H. Butler. Spin-transfer torque in magnetic tunnel junctions. *Phys. Rev. B*, 79:174416, May 2009.
- [33] Se-Chung Oh, Seung-Young Park, Aurelien Manchon, Mairbek Chshiev, Jae-Ho Han, Hyun-Woo Lee, Jang-Eun Lee, Kyung-Tae Nam, Younghun Jo, Yo-Chan Kong, Bernard Dieny, and Kyung-Jin Lee. Bias-voltage dependence of perpendicular spin-transfer torque in asymmetric mgo-based magnetic tunnel junctions. *Nat Phys*, 5(12):898–902, Dec 2009.
- [34] W.P. Pratt, S. D. Steenwyk, S. Y. Hsu, W.-C. Chiang, A C. Schaefer, R. Loloee, and J. Bass. Perpendicular-current transport in exchange-biased spin-valves. *Magnetics, IEEE Transactions on*, 33(5):3505–3510, Sep 1997.
- [35] Y. Jiang, T. Nozaki, S. Abe, T. Ochiai, A. Hirohata, N. Tezuka, and K. Inomata. Substantial reduction of critical current for magnetization switching in an exchange-biased spin valve. *Nat Mater*, 3(6):361–364, Jun 2004.
- [36] S. Zhang, P. M. Levy, and A. Fert. Mechanisms of spin-polarized current-driven magnetization switching. *Phys. Rev. Lett.*, 88:236601, May 2002.
- [37] M. AlHajDarwish, H. Kurt, S. Urazhdin, A. Fert, R. Loloee, W. P. Pratt, and J. Bass. Controlled normal and inverse current-induced magnetization switching and magnetoresistance in magnetic nanopillars. *Phys. Rev. Lett.*, 93:157203, Oct 2004.
- [38] R. Schad, C. D. Potter, P. Beliën, G. Verbanck, V. V. Moshchalkov, and Y. Bruynseraede. Giant magnetoresistance in Fe/Cr superlattices with very thin Fe layers. *Applied Physics Letters*, 64(25):3500–3502, 1994.
- [39] Jack Bass and William P Pratt Jr. Spin-diffusion lengths in metals and alloys, and spin-flipping at metal/metal interfaces: an experimentalist’s critical review. *Journal of Physics: Condensed Matter*, 19(18):183201, 2007.
- [40] Paul M. Haney, Hyun-Woo Lee, Kyung-Jin Lee, Aurélien Manchon, and M. D. Stiles. Current induced torques and interfacial spin-orbit coupling: Semiclassical modeling. *Phys. Rev. B*, 87:174411, May 2013.
- [41] L. Berger. Low-field magnetoresistance and domain drag in ferromagnets. *Journal of Applied Physics*, 49(3):2156–2161, 1978.

- [42] J. C. Slonczewski. Conductance and exchange coupling of two ferromagnets separated by a tunneling barrier. *Phys. Rev. B*, 39:6995–7002, Apr 1989.
- [43] E. B. Myers, D. C. Ralph, J. A. Katine, R. N. Louie, and R. A. Buhrman. Current-induced switching of domains in magnetic multilayer devices. *Science*, 285(5429):867–870, 1999.
- [44] J. A. Katine, F. J. Albert, R. A. Buhrman, E. B. Myers, and D. C. Ralph. Current-driven magnetization reversal and spin-wave excitations in Co /Cu /Co pillars. *Phys. Rev. Lett.*, 84:3149–3152, Apr 2000.
- [45] J. Grollier, V. Cros, A. Hamzic, J. M. George, H. Jaffrès, A. Fert, G. Faini, J. Ben Youssef, and H. Legall. Spin-polarized current induced switching in Co/Cu/Co pillars. *Applied Physics Letters*, 78(23):3663–3665, 2001.
- [46] Tao Yang, Takashi Kimura, and Yoshichika Otani. Giant spin-accumulation signal and pure spin-current-induced reversible magnetization switching. *Nat Phys*, 4(11):851–854, Nov 2008.
- [47] David Claudio-Gonzalez, André Thiaville, and Jacques Miltat. Domain wall dynamics under nonlocal spin-transfer torque. *Phys. Rev. Lett.*, 108:227208, Jun 2012.
- [48] Jan Manschot, Arne Brataas, and Gerrit E. W. Bauer. Nonmonotonic angular magnetoresistance in asymmetric spin valves. *Phys. Rev. B*, 69:092407, Mar 2004.
- [49] J. Barnaś, A. Fert, M. Gmitra, I. Weymann, and V. K. Dugaev. From giant magnetoresistance to current-induced switching by spin transfer. *Phys. Rev. B*, 72:024426, Jul 2005.
- [50] M. Gmitra and J. Barnaś. Current-driven destabilization of both collinear configurations in asymmetric spin valves. *Phys. Rev. Lett.*, 96:207205, May 2006.
- [51] O. Boulle, V. Cros, J. Grollier, L. G. Pereira, C. Deranlot, F. Petroff, G. Faini, J. Barnas, and A. Fert. Shaped angular dependence of the spin-transfer torque and microwave generation without magnetic field. *Nat Phys*, 3(7):492–497, Jul 2007.
- [52] Biodata. Microlink - thermocouple accuracy. <http://www.microlink.co.uk/tctable.html>, July 2012.

## Bibliography

- [53] NIST ITS-90 thermocouple database. <http://srdata.nist.gov/its90/main/>.
- [54] K. Uchida, S. Takahashi, K. Harii, J. Ieda, W. Koshibae, K. Ando, S. Maekawa, and E. Saitoh. Observation of the spin Seebeck effect. *Nature*, 455(7214):778–781, 2008.
- [55] K. Uchida, T. Ota, K. Harii, S. Takahashi, S. Maekawa, Y. Fujikawa, and E. Saitoh. Spin-Seebeck effects in NiFe/Pt films. *Solid State Communications*, 150(11–12):524 – 528, 2010.
- [56] K. Uchida, J. Xiao, H. Adachi, J. Ohe, S. Takahashi, J. Ieda, T. Ota, Y. Kajiwara, H. Umezawa, H. Kawai, G. E. W. Bauer, S. Maekawa, and E. Saitoh. Spin Seebeck insulator. *Nat Mater*, 9(11):894–897, Nov 2010.
- [57] <http://encyclopedia2.thefreedictionary.com/{P}eltier-{S}eebeck+effect>.
- [58] F. K. Dejene, J. Flipse, and B. J. van Wees. Spin-dependent Seebeck coefficients of Ni<sub>80</sub>Fe<sub>20</sub> and Co in nanopillar spin valves. *Phys. Rev. B*, 86:024436, Jul 2012.
- [59] J. Yang. Potential applications of thermoelectric waste heat recovery in the automotive industry. In *Thermoelectrics, 2005. ICT 2005. 24th International Conference on*, pages 170–174, June 2005.
- [60] Z.H. Dughaish. Lead telluride as a thermoelectric material for thermoelectric power generation. *Physica B: Condensed Matter*, 322(1–2):205 – 223, 2002.
- [61] Li-Dong Zhao, Shih-Han Lo, Yongsheng Zhang, Hui Sun, Gangjian Tan, Ctirad Uher, C. Wolverton, Vinayak P. Dravid, and Mercouri G. Kanatzidis. Ultralow thermal conductivity and high thermoelectric figure of merit in SnSe crystals. *Nature*, 508(7496):373–377, Apr 2014. Letter.
- [62] F. K. Dejene, J. Flipse, G. E. W. Bauer, and B. J. van Wees. Spin heat accumulation and spin-dependent temperatures in nanopillar spin valves. *Nat Phys*, 9(10):636–639, Oct 2013. Letter.
- [63] Moosa Hatami, Gerrit E. W. Bauer, Qinfang Zhang, and Paul J. Kelly. Thermal spin-transfer torque in magnetoelectronic devices. *Phys. Rev. Lett.*, 99:066603, Aug 2007.

- [64] Abraham Slachter, Frank Lennart Bakker, and Bart Jan van Wees. Modeling of thermal spin transport and spin-orbit effects in ferromagnetic/nonmagnetic mesoscopic devices. *Phys. Rev. B*, 84:174408, Nov 2011.
- [65] H Eckardt and L Fritsche. The effect of electron correlations and finite temperatures on the electronic structure of ferromagnetic nickel. *Journal of Physics F: Metal Physics*, 17(4):925, 1987.
- [66] Kimura. Private communication, 2014.
- [67] Gerrit E. W. Bauer, Eiji Saitoh, and Bart J. van Wees. Spin caloritronics. *Nat Mater*, 11(5):391–399, May 2012.
- [68] S. Bosu, Y. Sakuraba, K. Uchida, K. Saito, T. Ota, E. Saitoh, and K. Takahashi. Spin Seebeck effect in thin films of the Heusler compound  $\text{Co}_2\text{MnSi}$ . *Phys. Rev. B*, 83:224401, Jun 2011.
- [69] C. M. Jaworski, J. Yang, S. Mack, D. D. Awschalom, J. P. Heremans, and R. C. Myers. Observation of the spin-Seebeck effect in a ferromagnetic semiconductor. *Nat Mater*, 9(11):898–903, Nov 2010.
- [70] Xavier Waintal, Edward B Myers, Piet W Brouwer, and D. C Ralph. Role of spin-dependent interface scattering in generating current-induced torques in magnetic multilayers. *Phys. Rev. B*, 62(18):12317, 2000.
- [71] C. W. J. Beenakker. Random-matrix theory of quantum transport. *Rev. Mod. Phys.*, 69:731–808, Jul 1997.
- [72] Cyril Petitjean, David Luc, and Xavier Waintal. Unified drift-diffusion theory for transverse spin currents in spin valves, domain walls, and other textured magnets. *Phys. Rev. Lett.*, 109:117204, Sep 2012.
- [73] David Luc and Xavier Waintal. Thermally driven magnetic precession in spin valves. *Phys. Rev. B*, 90:144430, Oct 2014.
- [74] A. Slachter, F. L. Bakker, J-P Adam, and B. J. van Wees. Thermally driven spin injection from a ferromagnet into a non-magnetic metal. *Nat Phys*, 6, 2010.
- [75] W. Chen, G. de Loubens, J.-M. L. Beaujour, J. Z. Sun, and A. D. Kent. Spin-torque driven ferromagnetic resonance in a nonlinear regime. *Applied Physics Letters*, 95(17):172513, 2009.

## Bibliography

- [76] X. Waintal and M. Viret. Current-induced distortion of a magnetic domain wall. *EPL (Europhysics Letters)*, 65(3):427, 2004.
- [77] S. Zhang and Z. Li. Roles of nonequilibrium conduction electrons on the magnetization dynamics of ferromagnets. *Phys. Rev. Lett.*, 93:127204, Sep 2004.
- [78] J. Flipse, F. Bakker, A. Slachter, F. K. Dejene, and B. J. van Wees. Direct observation of the spin-dependent Peltier effect. *Nat Nano*, 7(3):166–168, Mar 2012.

---

## LIST OF FIGURES

---

1. The two types of domain walls . . . . .	7
2. Graphical representation of the terms in the LLG equation . . . . .	9
3. Hysteresis loop in magnetic switching . . . . .	13
4. Plot of the magnetoresistance by Fert <i>et al.</i> in 1988 . . . . .	17
5. Graph of the spin-resolved potentials in a Py Cu Py trilayer . . . . .	18
6. Two current model for a spin-valve without spin-flip . . . . .	19
7. Toy device for the calculation of GMR . . . . .	20
8. Sketch of the working principle of a spin-valve . . . . .	24
9. Sketch of the spin-filtering effect on an unpolarized current . . . . .	30
10. Sketch of the spin-filtering effect on a polarized current . . . . .	30
11. Torque, spin-filtering and multiple reflections in a spin-valve . . . . .	31
12. Examples of wavy and non-wavy torques . . . . .	34
13. Geometric criterion for waviness . . . . .	36
14. Experimental setup used by Seebeck . . . . .	38
15. Working principle of a thermocouple . . . . .	39
16. Cartoon of a scatterer with two reservoirs and their respective potential and temperature . . . . .	40
17. Thermoelectric efficiency as a function of $ZT$ . . . . .	46
18. Values of $Z$ against $T$ for common thermoelectric materials . . . . .	46
19. Sketch of the device used by van Wees <i>et al.</i> to measure the spin-dependent Seebeck coefficient . . . . .	49
20. Spin-split density of states for Nickel . . . . .	51
21. Spin Seebeck geometries . . . . .	52
22. Evolution of CRMT . . . . .	59
23. Theory A: Scattering theory . . . . .	61
24. Sketch of the wave functions in a scattering system . . . . .	62
25. Poles of $\mathbb{T}_{AB}$ for the residue theorem . . . . .	64
26. Theory B: Random matrix theory . . . . .	65
27. Drawing of an incoming transverse spin on a polarized layer . . . . .	66
28. Origin of the finite transverse spin penetration length . . . . .	68
29. Theory C: Circuit theory . . . . .	71
30. Theory D: Continuous theory . . . . .	75

## List of Figures

31. Theory E: Drift-diffusion theory . . . . .	77
32. Theory F: From 1D to 3D . . . . .	81
33. Sketch of the nodes and links in CRMT3D . . . . .	82
34. Theory G: Adding thermoelectric effects . . . . .	84
35. <i>ab initio</i> calculation of the mixing conductance of a Cu Co Cu trilayer and its fit with Eq. (246) . . . . .	99
36. GMR signal for a spin-valve with transverse layer . . . . .	102
37. $\beta_\tau$ ratio in domain walls . . . . .	106
38. Non-local resistance in a YIG device . . . . .	111
39. Sketch of a generic non-local spin valve . . . . .	112
40. Magnetic sweep in the YIG non-local spin valve . . . . .	113
41. Non-local resistance vs the YIG magnetization orientation . . . . .	113
42. Non-local GMR signal in the YIG system vs $R_{mx}$ . . . . .	116
43. The three processes occurring at a YIG interface . . . . .	117
44. Non-local magnetoresistance vs YIG magnetization orientation . . . . .	118
45. $\Delta R_{31}$ vs $R$ . . . . .	119
46. $\Delta R_{31}$ vs $R_{sf}/R$ . . . . .	120
47. $\Delta R_{31}$ vs $L_{gap}$ (as indicated on Fig. 38b) for various values of $R_{mx}$ . . . . .	121
48. $\lambda_{mx}$ vs the Cu thickness . . . . .	121
49. $\Delta R_0$ vs the Cu thickness . . . . .	122
50. The three configurations of a spin-valve subjected to a temperature gradi- ent and/or a voltage . . . . .	129
51. STT angular dependence for an input voltage, or an input temperature difference . . . . .	134
52. Waviness angle and domains against ferromagnet thicknesses . . . . .	136
53. Critical temperature vs ferromagnet thicknesses for various configurations . . . . .	138
54. Dependence on $\Delta s_B$ of the critical temperature . . . . .	139
55. Value of $\beta_\tau$ when applying a voltage or a temperature difference to a Py domain wall . . . . .	142
56. Device used to measure the spin polarization of the Seebeck coefficient . . . . .	146
57. Simulated version of the spin-dependent Seebeck measurement device . . . . .	147
58. Temperature profile in the spin-dependent Seebeck measurement . . . . .	148
59. GMR vs spin-dependent Seebeck coefficient of the ferromagnet . . . . .	149
60. Sketch of the nodes and links in CRMT3D . . . . .	156
61. Creation time (in seconds) of the CRMT1D systems versus length of the system . . . . .	158
62. Geometry used in the sample code using CRMT3D . . . . .	162

## List of Figures

- 63. Execution time in seconds for 1000 iterations vs the length of the bar . . . . 165
- 64. Number of iterations to reach convergence vs the length of the bar . . . . 166



---

## LIST OF TABLES

---

1. Values of the spin-flip length for usual magnetic and non-magnetic metals . . . . .	25
2. Values of the Seebeck coefficients for a variety of metals and common thermoelectric alloys. . . . .	44
3. Reduced material parameters for bulk and interface materials . . . . .	91
4. Values of $\ell_L$ and $\ell_{\perp}$ . . . . .	100
5. Conductance value for the transverse lengths measurement . . . . .	101
6. Values of $\beta_{\tau}$ . . . . .	107
7. Measured values of the non-local resistance on YIG devices . . . . .	114
8. Table of the material parameters used by default for the simulations . . . . .	172
9. Table of the material parameters of common interfaces used in the simulations. . . . .	173



Dans cette thèse, nous étudions le transport diffusif de la charge, du spin et de la chaleur dans les structures métalliques incluant des métaux ferromagnétiques. En particulier, nous nous sommes intéressés à la partie de ce transport dont la polarisation n'est pas colinéaire à l'aimantation ambiante.

Par exemple un courant polarisé en spin arrivant sur une couche magnétique dont l'aimantation pointe dans une autre direction verra sa partie transverse (i.e. non colinéaire à l'aimantation) précesser et être absorbée par l'aimantation sur une distance de quelques nanomètres au plus. Nous présentons un état de l'art sur ces deux distances caractéristiques, de précession et d'absorption transverse. Nous montrons aussi que ce comportement a un impact majeur sur la dynamique, notamment des murs de domaines magnétiques "longs" (plus de dix nanomètres).

Nous étudions aussi le torque de transfert de spin dans ces structures magnétiques. Cette étude a porté sur deux aspects majeurs. Tout d'abord l'amplitude du torque, pour savoir s'il est capable de démarrer une des dynamiques magnétiques connues : l'inversion magnétique, ou la précession en état stationnaire. Ensuite, la dépendance du torque avec l'angle relatif des aimantations : dans certains cas, une configuration non-colinéaire peut-être stabilisée. Deux sources d'énergies ont été considérées, une différence de potentiel, ou une différence de température (en incluant les effets thermoélectriques dépendant du spin).

Toute cette étude est réalisée dans le cadre de notre théorie, la Continuous Random Matrix Theory, que nous présentons dans son intégralité, de son origine avec la théorie de scattering, jusqu'aux équations différentielles de diffusion, résultat majeur de cette thèse, et enfin son implémentation en tant qu'outil numérique.

In this thesis we study the diffusive transport of the charge, spin and heat in metallic structures involving ferromagnets. In particular, we focused on the part of the transport which polarization is not collinear to the surrounding magnetization.

For example, a spin-polarized current arriving on a magnetic layer with a magnetization pointing in another direction will have its transverse part (i.e. non-collinear to the magnetization) precess and be absorbed by the magnetization, over a distance of up to a few nanometers. We present a state-of-the-art collection of values for those two characteristic lengths, of precession and transverse absorption. We also show that this behavior has a tremendous impact over the dynamics, notably that of "long" magnetic domain walls (over ten nanometers).

We also study the spin-transfer torque in those magnetic structures, and focus on two major aspects. First the amplitude of the torque, to know if it is strong enough to start one of the known dynamics: magnetic switching or steady-state precession. Second, the dependence of the torque with the relative angle between the magnetizations: in some cases, a non-collinear configuration may be stabilized. Two driving forces have been considered, a voltage bias or a temperature difference (by including spin-dependent thermoelectric effects).

This whole study is performed within the framework of our theory, the Continuous Random Matrix Theory, that we present in its entirety, from its origin with the scattering theory, to the diffusion differential equations, one of the main results of this thesis, and eventually its implementation as a numerical tool.